



REFERENCE ONLY

UNIVERSITY OF LONDON THESIS

Degree *Pho*

Year *2005*

Name of Author *CARLEY, N.C.*

COPYRIGHT

This is a thesis accepted for a Higher Degree of the University of London. It is an unpublished typescript and the copyright is held by the author. All persons consulting the thesis must read and abide by the Copyright Declaration below.

COPYRIGHT DECLARATION

I recognise that the copyright of the above-described thesis rests with the author and that no quotation from it or information derived from it may be published without the prior written consent of the author.

LOANS

Theses may not be lent to individuals, but the Senate House Library may lend a copy to approved libraries within the United Kingdom, for consultation solely on the premises of those libraries. Application should be made to: Inter-Library Loans, Senate House Library, Senate House, Malet Street, London WC1E 7HU.

REPRODUCTION

University of London theses may not be reproduced without explicit written permission from the Senate House Library. Enquiries should be addressed to the Theses Section of the Library. Regulations concerning reproduction vary according to the date of acceptance of the thesis and are listed below as guidelines.

- A. Before 1962. Permission granted only upon the prior written consent of the author. (The Senate House Library will provide addresses where possible).
- B. 1962 - 1974. In many cases the author has agreed to permit copying upon completion of a Copyright Declaration.
- C. 1975 - 1988. Most theses may be copied upon completion of a Copyright Declaration.
- D. 1989 onwards. Most theses may be copied.

This thesis comes within category D.

This copy has been deposited in the Library of *UCL*

This copy has been deposited in the Senate House Library, Senate House, Malet Street, London WC1E 7HU.

DEVELOPMENT OF A NEW APPARATUS
FOR COHERENT CONTROL IN
SODIUM ATOMS AND ~~MOLECULES~~ *DIATOMS*

Robert Edward Carley

A thesis submitted in partial
fulfilment of the degree of
Doctor of Philosophy

University College London
University of London
June 2005

UMI Number: U592663

All rights reserved

INFORMATION TO ALL USERS

The quality of this reproduction is dependent upon the quality of the copy submitted.

In the unlikely event that the author did not send a complete manuscript and there are missing pages, these will be noted. Also, if material had to be removed, a note will indicate the deletion.



UMI U592663

Published by ProQuest LLC 2013. Copyright in the Dissertation held by the Author.
Microform Edition © ProQuest LLC.

All rights reserved. This work is protected against
unauthorized copying under Title 17, United States Code.



ProQuest LLC
789 East Eisenhower Parkway
P.O. Box 1346
Ann Arbor, MI 48106-1346

DEVELOPMENT OF A NEW APPARATUS FOR COHERENT CONTROL IN SODIUM ATOMS AND MOLECULES

R E Carley

University College London, University of London, 2005

ABSTRACT

This thesis presents original work contributing to the understanding of coherent control of wave packet dynamics in atomic and molecular systems excited by sequences of ultrafast laser pulses.

An introduction to coherent control and a review of the literature is presented in chapter 1. Different approaches to coherent control are considered from the perspective of the phase complexity of the light fields used to achieve them, starting with a single transform-limited pulse, advancing through two-colour and multi-pulse schemes to chirped pulses, and finally arbitrarily shaped pulses. The purpose of this literature review is to position the work described in this thesis within the context of contemporary coherent control. In particular, our approach is seen to be in line with the current trend towards understanding the physics underlying coherent control processes.

In chapter 2, development of a sodium atom and dimer beam source for use in optical coherent control experiments is described. The concepts of molecular beams are introduced along with a brief review of the literature on sodium atom and dimer beams. The beam source is considered in two parts. Firstly the sodium oven and nozzle are described in detail, along with the vacuum chamber that houses them. This is followed by a description of the experimental chamber, which contains a time-of-flight mass spectrometer. Finally a number of potential improvements to the system are discussed.

Experiments to control the angular momentum composition of Rydberg electronic wave packets in atomic sodium are reported in chapter 3. The control scheme uses phase-locked pairs of transform-limited picosecond laser pulses to create pairs of identical radial wave packets in the Rydberg states. Quantum interference between the wave packets, or the excitation pathways to them, is manipulated to control the total angular composition of the resultant wave packet, which is detected either by the optical

Ramsey method or by state-selective field ionisation. The results are interpreted both from the perspective of time evolution of the wave packet and the frequency content of the laser fields. The control strategy is then extended theoretically by the inclusion of linear chirp in one of the laser pulses.

Chapter 4 describes progress towards a novel experiment for optical coherent control of vibrational wave packet dynamics in the sodium dimer. A coherent superposition of high-lying Rydberg states of the Na_2 is excited by the broad bandwidth of a femtosecond laser pulse. The Rydberg states converge to several vibrational ionisation limits of the dimer, so the excitation effectively forms a vibrational wave packet in the $X^+ \ ^2\Sigma_g^+$ ionic potential. Excitation of several wave packets by a series of phase-locked transform-limited pulses allows control over the composition and dynamics of the wave packet, and its detection using a combination of the optical Ramsey method and pulsed-field ionisation techniques adapted from ZEKE spectroscopy.

A simple genetic algorithm is presented in chapter 5. It has been implemented to investigate the suitability of this type of optimisation procedure in simulations of Rydberg electronic wave packet coherent control in atomic sodium. The operation of the algorithm is described in detail. It is then tested against known solutions for two experimental scenarios: coherent control based on pairs of transform-limited laser pulses; and transform-limited first pulse followed by a chirped second pulse. The behaviour of the algorithm is discussed in detail for each of these cases. Finally, the potential for application of the algorithm to unknown problems is briefly discussed.

ACKNOWLEDGEMENTS

Firstly I must thank Professor Helen Fielding for her guidance and supervision for the last five years or so, and for devising all these horribly difficult experiments for us to do.

In addition to suffering the highs and lows of this project, Liz has had to put up with working with me. I know now that I really shouldn't have tweaked the interferometer that day.... I am truly grateful for her company and friendship.

With out the kind help of Rakhee and Russell with the picosecond laser system, none of the sodium atom experiments would have been possible. They have been great colleagues and even better friends.

Thanks to Eva for difficult answers to my questions, and for helpful, interesting and funny conversations. Thanks to Nick for his surreal imaginings and Dorian for good arguments.

Thanks to Paul for coffee trips to Starbucks and for exploring the darker sides of so many things.

Lastly, and most importantly, thanks to my wife Julie and my parents for their love and support.

The work in this thesis has contributed to the following publications:

- CHAPTER 1 R E Carley, E Heesel and H H Fielding
Femtosecond lasers in gas phase chemistry.
Chem. Soc. Rev. **34** (11) 949-969 (2005)
- CHAPTER 3 R E Carley, E D Boléat, R S Minns, R Patel and H H Fielding.
Interfering Rydberg wave packets in Na.
J. Phys. B: At. Mol. Opt. Phys. **38** 1907-1922 (2005)
- E D Boléat, R E Carley, R S Minns, R Patel and H H Fielding.
Optical control of the quantum state distribution of Rydberg wave
packets in Na and NO.
Central Laser Facility Annual Report 2003/2004
- CHAPTER 5 The work in Chapter 5 is currently being extended and will be written up
as,
Use of a genetic algorithm to correct dispersion in atomic electronic
Rydberg wave packets.

LIST OF CONTENTS**CHAPTER 1 INTRODUCTION TO COHERENT CONTROL**

1.1 INTRODUCTION	1
1.2 COHERENT CONTROL USING A SINGLE TRANSFORM-LIMITED LASER PULSE	2
1.3 TWO-LASER FIELD COHERENT CONTROL	2
1.4 PHASE-LOCKED LASER PULSES	5
1.5 CHIRPED-PULSE COHERENT CONTROL	8
A. MULTIPLE CHIRPED PULSES	11
1.6 PULSE SHAPING	12
A. REGULAR PHASE FUNCTIONS	14
B. IRREGULAR PHASES AND GENETIC ALGORITHMS	15
1.7 CONCLUSION	17
1.8 REFERENCES	17

CHAPTER 2 DEVELOPMENT OF A BEAM SOURCE FOR SODIUM ATOMS AND DIMERS

2.1 INTRODUCTION	25
2.2 INTRODUCTION TO ATOMIC AND MOLECULAR BEAMS	26
A. THE FREE JET	26
B. SODIUM ATOM AND DIMER EXPANSIONS	30
C. CLUSTERING	31
D. QUANTUM STATE DISTRIBUTION	35
E. INTERNAL ENERGY RELAXATION	36
F. MIXED EXPANSIONS: THE ROLE OF THE CARRIER GAS	37
G. SKIMMERS	38
H. CONCLUSION OF INTRODUCTION TO MOLECULAR BEAMS	40
2.3 OUR SODIUM ATOMIC AND MOLECULAR BEAM: SYSTEM OVERVIEW	41
A. THE SODIUM OVEN	42
I. INTRODUCTION	42
II. SODIUM OVEN: PHYSICAL DESCRIPTION	43
III. HEATING OF THE OVEN AND NOZZLE	45

LIST OF CONTENTS

IV. OVEN SUPPORT	50
III. THE NOZZLE	56
IV. THE SKIMMER	59
V. SODIUM SOURCE VACUUM CHAMBER	62
VI. VACUUM PUMPS, GAUGES AND CONNECTIONS	66
2.4 EXPERIMENTAL CHAMBER	68
A. TIME-OF-FLIGHT MASS SPECTROMETER	68
I. OPERATION OF A LINEAR TIME-OF-FLIGHT MASS SPECTROMETER	68
II. PHYSICAL DESCRIPTION OF TOF APPARATUS	70
III. ELECTRON/ION DETECTOR	74
IV. EXPERIMENTAL SIDE VACUUM CHAMBER	76
V. THE COLD TRAP	78
VI. VACUUM PUMPS ON THE EXPERIMENTAL CHAMBER	79
2.5 THOUGHTS ON FUTURE DESIGNS AND MODIFICATIONS	80
A. OVEN DESIGN	80
B. OVEN MOUNTING	81
C. NOZZLE - SKIMMER DISTANCE ADJUSTMENT	82
D. THERMAL SHIELDING AND COOLING	82
E. TRAPPING SODIUM IN THE SOURCE CHAMBER	82
F. IMPROVEMENTS TO THE EXPERIMENTAL SIDE OF THE VACUUM SYSTEM	83
G. IMPROVEMENTS TO THE TIME-OF-FLIGHT APPARATUS	83
2.6 REFERENCES	84
 CHAPTER 3 COHERENT CONTROL OF RYDBERG ELECTRON WAVE PACKETS IN ATOMIC SODIUM	
3.1 INTRODUCTION	87
A. SODIUM ATOM SPECTROSCOPY	87
B. ATOMIC RYDBERG STATES	88
C. RYDBERG ELECTRON WAVE PACKETS	90
D. INTERFEROMETRIC CONTROL OF RYDBERG ELECTRON WAVE PACKETS	94
I. WAVE PACKETS SEPARATED BY T_{cl}	94
II. WAVE PACKETS SEPARATED BY $3T_{cl}/2$	95

LIST OF CONTENTS

3.2 EXPERIMENTAL	99
A. MOLECULAR BEAM	99
B. LASERS	99
I. LASERS FOR FREQUENCY-RESOLVED SPECTRA	101
II. LASERS FOR COHERENT CONTROL EXPERIMENTS	102
III. MICHELSON INTERFEROMETER	104
C. THE INTERACTION REGION	106
D. DATA COLLECTION	108
I. FREQUENCY SPECTRA	108
II. RECURRENCE SPECTRA AND OPTICAL RAMSEY METHOD	
COHERENT CONTROL	110
III. STATE SELECTIVE FIELD IONISATION	113
3.3 RESULTS AND DISCUSSION	119
A. FREQUENCY SPECTRA	119
B. DYNAMICS OF SINGLE WAVE PACKETS	119
C. COHERENT CONTROL OF WAVE PACKETS SEPARATED BY T_{cl} DETECTED	
BY STATE SELECTIVE FIELD IONISATION	121
D. WAVE PACKET INTERFEROMETRY	128
3.4 CHIRPED WAVE PACKET INTERFEROMETRY	130
3.5 CONCLUSION	136
3.6 REFERENCES	136
CHAPTER 4 OPTICAL CONTROL OF VIBRATIONAL WAVE PACKET DYNAMICS IN THE SODIUM DIMER	
4.1 INTRODUCTION	139
A. SODIUM DIMER SPECTROSCOPY	140
B. VIBRATION WAVEFUNCTIONS	141
C. VIBRATIONAL WAVE PACKETS	142
D. FORMATION AND DETECTION OF VIBRATIONAL WAVE PACKETS IN	
THE $X^+ 2\Sigma_g^+$ STATE OF Na_2^+	144
4.2 PROPOSED COHERENT CONTROL SCHEME	147

LIST OF CONTENTS

4.3 EXPERIMENTAL	151
A. LASERS	151
B. DATA COLLECTION	154
C. EXPERIMENTAL ARRANGEMENT FOR FREQUENCY RESOLVED SPECTROSCOPY OF Na ₂	157
4.4 RESULTS AND DISCUSSION	159
A. PROGRESS IN THE PROPOSED DATA COLLECTION METHOD	159
B. Na ₂ A – X FREQUENCY SPECTRA	161
4.5 CONCLUSION	164
4.6 REFERENCES	164

CHAPTER 5 DEVELOPMENT OF A GENETIC ALGORITHM TO OPTIMISE SIMPLE COHERENT CONTROL IN RYDBERG WAVE PACKETS IN ATOMIC SODIUM

5.1 INTRODUCTION	166
5.2 THE USE OF GENETIC ALGORITHMS IN CHEMICAL PHYSICS	168
5.3 A GENETIC ALGORITHM FOR SIMPLE COHERENT CONTROL SCHEMES	171
A. OVERVIEW OF OUR GENETIC ALGORITHM	172
B. STEPS IN THE GENETIC ALGORITHM	172
I. GENERATION OF THE INITIAL POPULATION.	173
II. EXTRACTION OF OUTPUT PARAMETERS	173
III. PERFORMING THE CALCULATION	174
IV. EVALUATING THE FITNESS	174
V. RANKING THE INDIVIDUALS	175
VI. CONVERGENCE TESTING	175
VII. SELECTING THE BREEDING SET	175
VIII. BREEDING	176
IX. MUTATION	176
C. RUNNING THE GENETIC ALGORITHM	176
I. OPTIMISATION OF THE DELAY AND PHASE OF A PAIR OF TRANSFORM- LIMITED PICOSECOND LASER PULSES	177
II. OPTIMIZATION OF THE DELAY, PHASE AND CHIRP OF A PAIR OF PICOSECOND LASER PULSES	183

LIST OF CONTENTS

III. APPLICATION TO OTHER PROBLEMS	186
5.4 CONCLUSION	187
5.5 REFERENCES	187
CHAPTER 6 SUMMARY AND OUTLOOK	
6.1 ATOMIC AND MOLECULAR BEAM SOURCE	189
6.2 COHERENT CONTROL IN SODIUM ATOMIC RYDBERG ELECTRONIC WAVE PACKET DYNAMICS	189
6.3 VIBRATIONAL WAVE PACKET COHERENT CONTROL IN Na ₂	190
6.4 DEVELOPMENT AND USE OF GENETIC ALGORITHMS COMBINED WITH ULTRA FAST PULSE SHAPING	191
6.5 REFERENCES	191
APPENDIX	
A1 INTRODUCTION	192
A2 CODE LISTINGS	192
A3 REFERENCES	212

LIST OF FIGURES

LIST OF FIGURES

CHAPTER 1 INTRODUCTION TO COHERENT CONTROL

Figure 1.1	Schematic representation of an ideal $(\omega + \omega + \omega) + 3\omega$ frequency domain coherent control scheme.	3
Figure 1.2	Schematic representation of STIRAP for an ideal three level system.	5
Figure 1.3	Schematic representation of the single chirped pulse pump-dump coherent control scheme for large solution phase molecules.	11
Figure 1.4	Schematic layout of a zero-dispersion (4- <i>f</i>) pulse shaper.	13

CHAPTER 2 DEVELOPMENT OF A SODIUM ATOMIC AND MOLECULAR BEAM

Figure 2.1	Cross-section of the continuum free-jet axis-symmetric expansion.	29
Figure 2.2	Plots of equilibrium vapour pressure of sodium atoms and dimers as a function of temperature.	32
Figure 2.3	Elevation of the vacuum chamber, drawn to scale, showing the separate source and experimental chambers.	41
Figure 2.4	Scale drawing of the sodium oven.	44
Figure 2.5	Variable transformer circuit used to power the oven heaters.	47
Figure 2.6	Circuit diagram for a single thermocouple.	48
Figure 2.7	Circuit diagram for a cold-junction compensated thermocouple pair.	49
Figure 2.8	Plot of the error in reading a single thermocouple compared to a thermocouple pair with one thermocouple held at 0 °C.	49
Figure 2.9	Side and end elevations of the first oven mount.	51
Figure 2.10	Positioning of the oven in its first mount in the source vacuum chamber.	52
Figure 2.11	Sodium oven mounted on an <i>xyz</i> translator.	53
Figure 2.12	Cross-section of the sodium source chamber showing the position of the oven when suspended from an <i>xyz</i> translator.	54

LIST OF FIGURES

Figure 2.13	Partial cutaway of the source chamber showing the most recent oven support.	55
Figure 2.14	Scale drawing of the first nozzle used in the sodium atomic/molecular beam source.	57
Figure 2.15	Exploded view of the carrier used to hold the 3/8 in. diameter molybdenum disk in the sodium oven.	58
Figure 2.16	Cross-section of the latest nozzle, currently under test in the sodium oven.	59
Figure 2.17	Collimator used to reduce the flux of sodium into the experimental chamber.	60
Figure 2.18	Dimensional drawing of the skimmer.	61
Figure 2.19	Cross-section of the mounting assembly for the skimmer.	62
Figure 2.20	End and side elevations of the sodium source vacuum chamber.	63
Figure 2.21	Symbolic representation of the vacuum system.	66
Figure 2.22	Operation of a linear time-of-flight mass spectrometer.	69
Figure 2.23	Cross-section through the electron/ion time-of-flight apparatus.	72
Figure 2.24	Cross-section detail of the time-of-flight apparatus and detail of an electrostatic lens.	73
Figure 2.25	Schematic representation of the operation of a microchannel plate detector (MCP).	74
Figure 2.26	Circuit diagrams for the microchannel plate detectors.	75
Figure 2.27	Assembly drawing of the microchannel plate (MCP) support.	76
Figure 2.28	Elevation of the experimental vacuum chamber.	77
Figure 2.29	Angled mounts for laser input and output windows.	78

CHAPTER 3 COHERENT CONTROL OF RYDBERG ELECTRON WAVE PACKETS IN ATOMIC SODIUM

Figure 3.1	Laser excitation scheme for coherent control in atomic sodium.	89
Figure 3.2	Experimental and calculated recurrence spectra of a radial Rydberg electronic wave packet in sodium excited around $n = 35$.	93
Figure 3.3	Cartoon showing the relative phases of two wave packets arising after the first has performed $1\frac{1}{2}$ orbits.	97

LIST OF FIGURES

Figure 3.4	Cartoon illustrating two opposite instances of coherent control using wave packet interference at the second order partial revival.	98
Figure 3.5	Laser bench for wave packet interferometry experiments.	100
Figure 3.6	Cross-section through a Bethune cell.	103
Figure 3.7	Synchronization of the picosecond and nanosecond lasers and data collection electronics.	104
Figure 3.8	Schematic of the stabilized nested Michelson-type interferometer.	105
Figure 3.9	Schematic of the laser – sodium atomic beam interaction.	107
Figure 3.10	Schematic interconnection of data collection instruments.	109
Figure 3.11	Calculated optical Ramsey fringes for a pair of wave packets	111
Figure 3.12	Sample of raw data from an ORM experiment in atomic sodium and its reduction to a recurrence spectrum.	112
Figure 3.13	Cartoon illustrating state-selective field ionisation.	114
Figure 3.14	Calculated Stark manifold for the $m = 0$ states of sodium.	115
Figure 3.15	CR circuit seen by a high-voltage pulse.	116
Figure 3.16	High voltage pulse shapes for different loads and voltages.	117
Figure 3.17	Frequency resolved spectrum of the Rydberg states of sodium.	119
Figure 3.18	Experimental and calculated recurrence spectra and Rydberg state populations for a wave packet excited around $n = 31$.	120
Figure 3.19	Dependence of the classical orbit period of a Rydberg electron wave packet on the average principal quantum number.	121
Figure 3.20	SSFI data for control of the angular momentum composition of a Rydberg electronic wave packet in sodium.	122
Figure 3.21	Composite of SSFI traces for individual Rydberg states.	123
Figure 3.22	Enlargement of the experimental SSFI data compared to calculated values.	124
Figure 3.23	Calculated s and d Rydberg state populations for the most significant phases between the laser pulses.	125
Figure 3.24	Comparison of calculated and experimental SSFI traces for individually excited Rydberg states.	127
Figure 3.25	Experimental and calculated recurrence spectrum and calculated Rydberg state population for a single wave packet around the time of the second order partial revival.	128

LIST OF FIGURES

Figure 3.26	Experimental and calculated recurrence spectra around the time of the second order partial revival resulting from excitation of two wave packets with different phases.	130
Figure 3.27	Spectra of pairs of laser pulses as used in the sodium atom experiments with different time delays and phases.	132
Figure 3.28	Spectra of transform-limited pump-chirped-probe pulse pairs for different delays, phases and chirps.	135

CHAPTER 4 OPTICAL CONTROL OF VIBRATIONAL WAVE PACKET DYNAMICS IN THE SODIUM DIMER

Figure 4.1	Excitation scheme used in the sodium dimer coherent control experiment.	140
Figure 4.2	Calculated recurrence spectrum of a vibrational wave packet in the $X^+ 2\Sigma_g^+$ state of Na_2^+ .	144
Figure 4.3	Cartoon of the phases at the second order partial.	148
Figure 4.4	Cartoon showing the relative phases of two second order partial revivals of two wave packets.	148
Figure 4.5	Cartoons illustrating the effect of phase differences between two wave packets.	149
Figure 4.6	Layout of the femtosecond laser table.	152
Figure 4.7	Spectrum of the output pulse train from the Ti:S laser.	153
Figure 4.8	Nested Michelson interferometer for vibrational wave packet experiments.	155
Figure 4.9	Data collection timing for vibrational wave packet experiments.	156
Figure 4.10	Optical fringes generated by 400 nm \approx 100 femtosecond laser pulses.	159
Figure 4.11	Optical interference fringes from photoelectrons from atomic sodium.	160
Figure 4.12	Time-of-flight mass spectrum recorded following excitation the sodium beam at 637 nm.	162
Figure 4.13	Possible A – X frequency spectra for Na_2 .	163
Figure 4.14	Calculated $A(v' = 0-20) \leftarrow X(v'' = 0)$ spectrum of Na_2 .	163

LIST OF FIGURES

CHAPTER 5 DEVELOPMENT OF A GENETIC ALGORITHM TO OPTIMISE SIMPLE COHERENT CONTROL IN RYDBERG WAVE PACKETS IN ATOMIC SODIUM

Figure 5.1	Schematic operation of a genetic algorithm.	167
Figure 5.2	Schematic of the current genetic algorithm.	172
Figure 5.3	Representation of the GA population as a three dimensional array.	173
Figure 5.4	Storage of the output parameters and fitness parameter for one individual.	174
Figure 5.5	Results of five consecutive GA runs maximising either the d or s Rydberg states population.	178
Figure 5.6	Rydberg state populations generated prior to any optimisation.	179
Figure 5.7	Dependence of the optimisation rate on the convergence criterion.	181
Figure 5.8	Improvement of the best fitness parameter (convergence) with each generation for 7 runs.	182
Figure 5.9	Population of s and d Rydberg states generated from output parameters from five non-optimal individuals in the final population.	183
Figure 5.10	Comparison of an optimised spectrum with the objective and an analytically optimised spectrum.	185
Figure 5.11	Values of delay, phase and chirp for 10 runs of the GA.	186

APPENDIX CODE LISTINGS FOR GENETIC ALGORITHM

Figure A1	Hierarchy of subroutines in the genetic algorithm	192
------------------	---	-----

CHAPTER 1 INTRODUCTION TO COHERENT CONTROL**ABSTRACT**

This chapter introduces coherent control and briefly reviews the literature. Different approaches to coherent control are considered from the perspective of the phase complexity of the light fields used to achieve them, starting with a single transform-limited pulse, advancing through two-colour and multi-pulse schemes to chirped pulses and finally arbitrarily shaped pulses. The purpose of this literature review is to position the work described in this thesis within the context of contemporary coherent control. In particular, our approach is seen to be in line with the current trend towards understanding the physics underlying coherent control processes.

1.1 INTRODUCTION

Having recognised the quantum mechanical nature of matter at the atomic and molecular level, it is inevitable that attempts would be made to manipulate, and if possible fully dictate, the quantum state distribution of such systems. This endeavour has become known as coherent control or quantum control.

Targets for coherent control tend to be atomic and small molecular systems in all states of matter. The ideas do however extend to more exotic systems, for instance quantum dots [1], solutions of large molecules, for example azulene in cyclohexane [2], laser dyes and biological molecules [3, 4] and semiconductors [5].

At present, coherent control is largely of interest as a piece of fundamental science. There have been model chemical reaction control schemes (for example [6, 7]) but their value as synthetic tools is limited by cost. Perhaps ironically however, coherent control is finding applications within spectroscopy and laser physics. It has been used to reduce the natural linewidth of transitions in Rb vapour [8]. In laser physics coherent control has been used in the generation of femtosecond pulses over wide wavelength ranges [9], including high-order harmonic generation [10], and in the phase control of femtosecond pulses using molecular rotational wave packets [11].

The high coherence and intensity of laser light has meant that most coherent control efforts have involved their use, although now it is extending to using the coherent properties of Bose-Einstein condensates to control reaction dynamics on surfaces, at least in theory [12]. The earliest experiments attempted to utilise the high intensity and monochromaticity of laser light to cleave chemical bonds selectively by exciting their vibrational overtones. This was unsuccessful because the energy put into the bond is rapidly redistributed among other vibrational modes of the molecule.

Approaches to coherent control usually fall into either the frequency domain or the time domain, roughly along the lines of the division between narrow band and broad band lasers. However, the two approaches are in fact equivalent, as shown by Shapiro and Brumer [13] and in many ways overlap [14, 15]. For this reason, here they are considered from the point-of-view of the phase complexity of the laser fields used.

1.2 COHERENT CONTROL USING A SINGLE TRANSFORM-LIMITED LASER PULSE

The simplest laser-matter interaction is probably an atom excited by a monochromatic continuous-wave (CW) laser field, but it is useless as a quantum control strategy. In principle a single transform-limited laser pulse should be able to achieve a π -pulse. For a two-level system, if the product of the Rabi frequency, $\Omega_0 = E_0\mu/\hbar$ (where E_0 is the amplitude of the electric field of the laser pulse and μ is the dipole moment [16]), and the pulse duration is an odd integer multiple of π , total inversion of the population occurs. In reality the π -pulse is impracticable because it is impossible to satisfy simultaneously the conditions for multiple states.

1.3 TWO-LASER FIELD COHERENT CONTROL

Frequency domain coherent control was proposed in 1986 by Shapiro and Brumer [17]. The central idea is that in order to control the population of a final quantum state, it must be simultaneously accessed by multiple independent excitation paths [18]. The net excitation results from interference between the competing pathways, and control is achieved by altering the relative phases and amplitudes of

those pathways. There are numerous ways to implement these ideas using combined single photon and multi photon excitations. The most frequently discussed is a control scheme involving simultaneous excitation by three photons at frequency ω and one photon at frequency 3ω [19], which is illustrated in figure 1.1.

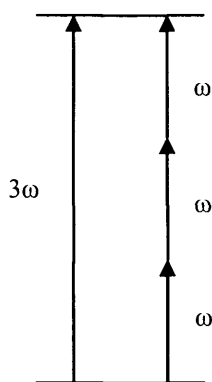


Figure 1.1 Schematic representation of an ideal $(\omega + \omega + \omega) + 3\omega$ excitation scheme for frequency domain coherent control. Two excitation pathways exist between the lower level and the upper level. One pathway excites the transition with a single photon of frequency 3ω , while the other requires 3 photons with $1/3$ the frequency. Which excitation dominates is controlled by the phase difference between the pathways and is manipulated by the phases between the light.

Combining one- and three-photon transitions means that the angular momentum selection rules allow both routes to access the same final state. The popularity of this formulation stems from the ease with which it can be implemented by tripling the output of a pulsed narrow band (nanosecond) laser. The phase between the beams is controlled by passing them through a gas cell containing, for example, H_2 [20], or H_2 and argon [21, 22], in which the gas pressure is altered, or by exploiting the phase shift occurring at a focus [23].

There are many experiments demonstrating $(\omega + \omega + \omega) + 3\omega$ control over ionisation/excitation ratios in atoms and molecules, and product branching ratios in molecules. Excitation of two paths into degenerate continuum states has allowed control of the ionisation/excitation ratio in Hg atoms [24] and Ca atoms [22]. Likewise ionisation/excitation control has been achieved in molecules, for example in HCl and CO [21] and CH_3I [25]. In these experiments competition between two paths to a Rydberg state followed by photoionisation effected control. Experiments involving

reaction product branching ratios include HCl and CO [21], CH₃I [26] and HI (and DI). In the HI work the relative excitation of HI⁺ and I⁺ was the control objective.

A related approach is $(\omega + \omega) + 2\omega$ excitation. This scheme has been applied to slightly different problems, mostly in the high field regime, because optical selection rules preclude accessing the same state with both one and two photons. Above-threshold ionisation rates in Kr and Xe have been shown to exhibit phase dependence [27, 28]. In a molecular systems this method has been used to control the yield of spin-orbit excited I from IBr [29]; and the direction of photoionisation fragments in HD⁺ [30] and photoelectrons in rubidium [31] and NO [32]. Recently, rotational coherent control has been achieved with the $(\omega + \omega) + 2\omega$ scheme in the iodine-containing molecules IBr, CH₃I and C₃H₅I [15]. It is interesting to note that, with lasers now capable of generating pulses with a spectral width spanning more than an octave of frequency [14], it should be possible to perform these experiments with a single laser pulse.

In another variation, control over ionisation/excitation has also been demonstrated in barium [33, 34] and NO [35] using a resonant $(\omega_1 + \omega_2) + (\omega_2 + \omega_1)$ excitation. These experiments revealed interferences between the resonant intermediates that could be controlled by detuning the lasers from resonance, in addition to the control achieved by altering the laser phase and amplitude.

A whole series of frequency domain coherent control methodologies fall into the category of adiabatic population transfer, and they are beautifully reviewed by Vitanov *et.al.* [36]. Although these do not rely on optical or molecular phase to achieve control, they are very powerful techniques and included here for completeness. Adiabatic population transfer can achieve efficiencies very close to 100 % for some systems.

The most versatile variant appears to be stimulated Raman adiabatic passage (STIRAP) and its derivatives. In STIRAP two lasers are used to couple three states as shown in figure 1.2. The objective is to transfer population from state $|1\rangle$ to state $|3\rangle$. It has been found that to achieve high population transfer the Stokes pulse, with frequency ω_{23} , has to come before the pump pulse, which has frequency ω_{12} .

STIRAP experiments have been reported on atomic and molecular systems. Bergmann and co-workers were able to control the $^3P_0 \rightarrow ^3P_1 \rightarrow ^3P_2$ excitation in neon atoms [37], and were the first to report STIRAP in a molecule, NO [38]. The STIRAP

scheme was also used to excite from the S_0 ground state of benzene to the 6_2 state via the $S_1 6^1$ [39].

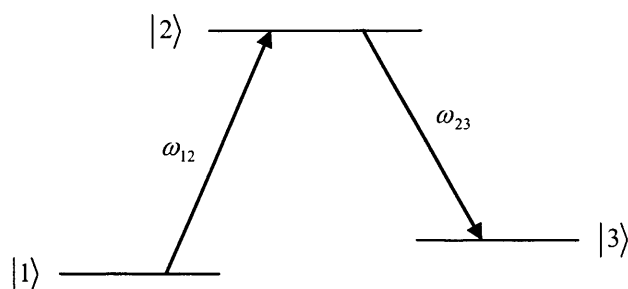


Figure 1.2 Schematic representation of STIRAP for an ideal three-level system sometimes referred to as a Λ -atom. The laser fields, ω_{12} (the pump pulse) and ω_{23} (the Stokes pulse), lead to time dependent mixing of the stationary states $|1\rangle$, $|2\rangle$ and $|3\rangle$. Population is transferred from state $|1\rangle$ to state $|3\rangle$ without ever populating state $|2\rangle$.

A quantum control process closely related to STIRAP is electromagnetically induced transparency (EIT), which also includes light-slowing. EIT has been studied widely, but was first demonstrated by Harris *et al.* in strontium vapour [40]. EIT involves essentially a three-level system where two narrow linewidth lasers couple an excited state to two non-degenerate low-lying states, one of which is populated and the other not. Scanning the wavelength of the laser coupling the excited and populated lower state through resonance reveals no absorption at resonance.

1.4 PHASE-LOCKED LASER PULSES

The development of ultrafast lasers has driven the development of time-dependent coherent control. The field really started with lasers producing pulses lasting a few picoseconds and continues to expand as laser pulses get shorter. Pulses of 30 fs duration are now routine in many laboratories round the world, and the shortest experimentally realisable pulse is just 250 attoseconds in duration [41], so there are enormous opportunities for coherent control.

The first experiments in, and theoretical treatment of, short pulse excitation were pump-probe and pump-dump schemes. A short laser (pump) pulse excites a coherent superposition of stationary states of the system – a wave packet. Although coherent,

and therefore phase synchronised, this work was not primarily concerned with phase evolution. The stationary states can be rotational, vibrational or electronic, or combinations of them. The excitation is impulsive – the duration of the excitation is small compared to the timescales of the wave packet evolution. The wave packet evolves in time and its behaviour can be monitored by a second, time delayed short laser pulse, the probe. Pump-probe investigation of wave packet dynamics continues to be applied to increasing complex systems [2].

The first control experiments and theory developed from this idea. Instead of simply monitoring wave packet evolution, in some systems controlling the timing of the second pulse can select between excitation of two or more final states. The classic demonstration of this approach was made by Gerber and co-workers [42] in the sodium dimer. From the $\text{Na}_2 \text{ X } ^1\Sigma_g^+$ ($v'' = 10$) ground state, a one photon excitation with a 70 fs laser pulse at 627 nm created a vibrational wave packet in the $\text{A } ^1\Sigma_u^+$ ($v' = 10-14$) state of with a period of 306 fs. A two photon excitation simultaneously formed a wave packet in the $2 ^1\Pi_g$ ($v' = 11-18$) state, which has a period of 363 fs. A time-delayed but otherwise identical laser pulse was used to probe the wave packet motion. Two-photon ionisation by the probe laser from the inner turning point of the A state wave packet generated the $^2\Sigma_g^+$ state of the Na_2^+ ion. From the outer turning point of the $2 ^1\Pi_g$ wave packet the probe laser made a single photon excitation to a doubly excited Rydberg state, which autoionised to Na_2^+ ($^2\Sigma_g^+$), and dissociated to give Na^+ and $\text{Na}(3s)$.

The related pump-dump approach was formalised by Tannor, Kosloff and Rice. [43, 44]. Their model is based on a ground state potential energy surface of a molecule ABC featuring a minimum separated from two product channels, say $\text{AB} + \text{C}$ and $\text{A} + \text{BC}$, by saddle points. Above the ground state surface is an excited state surface with a minimum that is displaced from that of the ground state, and has rotated normal coordinates. An ultrafast (femtosecond) laser pulse excites vertically from the ground state, forming a vibrational wave packet on the excited surface. The wave packet evolves on the excited state surface and at some later time is pumped back down to the ground state surface by a second ultrafast laser pulse. If the wave packet on the excited surface takes the molecule to geometries corresponding to those in the product channels of the ground state, vertical transitions from these points will place the wave packet in a product channel of the ground state. The second laser pulse can be timed, therefore, so that it causes de-excitation into specific products.

Pulse sequence experiments where the relative phase of the electric field between the pulses, and between the pulses and the wave packets they excite were first used to study wave packet evolution. Zewail and co-workers performed the first experiments in iodine [45] and anthracene [46], controlling the relative pulse phase and delay with an acousto-optic modulator. Scherer *et al.* [47] measured fluorescence to follow the temporal behaviour of rovibrational wave packets in iodine vapour generated by phase-locked pulse pairs from Michelson and Mach-Zender interferometers. That work led to the first demonstration of control by the same group [48]. The total excited state population of the iodine molecule was monitored by fluorescence as a function of the phase difference between the two pulses for a fixed time delay.

Noel and Stroud [49] proposed and executed a coherent control scheme in the Rydberg states of potassium that is the prototype for the work described in this thesis. They excited two identical time-delayed phase-locked wave packets centred around $n = 66$ with a 15 cm^{-1} bandwidth (picosecond) laser. The second wave packet was excited after a delay of one half the classical orbit period. The system was then allowed to evolve until the second order partial revival. This ensured that the two wave packets overlapped spatially and could therefore interfere. The phase of the second wave packet determined the outcome of the interference, which was monitored interferometrically using the optical Ramsey method. Three key phase differences were identified. If the phase was $\pi/2$ the interference completely removed the sub-wave packet at the outer turning point at the time of the second order partial revival. If the phase was $-\pi/2$ the sub wave packet at the inner turning point was destroyed. A phase difference of π left both sub-wave packets intact but shifted their phases. Removing one sub-wave packet effectively shifts the time of the full revival. State-selective field ionisation (see chapter 3) allowed the same workers to measure directly the Rydberg state distributions resulting from the above wave packet interference [50].

Employing wave packet interference to exploit *accumulated* phase relationships between constituents of Rydberg wave packets in atoms and molecules, Fielding and co-workers were able to manipulate the electronic angular momentum in xenon atoms [51], the ratio of predissociation to autoionisation in NO [52], and rotational angular momentum in NO [53]. The xenon work exploited the phase shift that arises as a result of the different quantum defects of the Rydberg series comprising the wave packet. As the wave packet orbits, this phase difference increases. By exciting a second wave

packet, phase matched to the first, one or other angular component (s or d) could be selectively enhanced or diminished. In the NO rotation control experiments, a phase contribution from the different rotational series of a Rydberg wave packet was utilised in a similar way. In this case the researchers were able to create, from an initial superposition of both, a wave packet comprising only $N^+ = 0$ or $N^+ = 2$, where N^+ is the rotational quantum number of the core.

Girard *et al.* [54] have used phase-shifted transform-limited pulses to control interference between matter wave packets in Na^+ formed by predissociation from NaI . Suitably phased pulses could be used to control the kinetic energy of the fragments. Free particle wave packet interference was also demonstrated for electrons ionised from potassium [55]. A pair of time-delayed 30 fs pulses ionised potassium from the $5p$ state. Two ionisation pathways occurred: one-photon threshold ionisation, and two-photon continuum ionisation. The two pathways interfered, depending on the delay between the ionisation pulses, allowing manipulation of the free-electron wave packet dynamics.

Control over bound-bound and bound-free transitions (but not their branching ratios) was reported in NO by Faucher *et al.* [56] using phase-locked non-transform-limited pulses. They made a two-photon excitation from the ground state to an intermediate (A) state, and from there ionised with another two photons. Oscillations were observed in the ion yield as a function of delay between various combinations of intermediate and ionisation steps.

1.5 CHIRPED-PULSE COHERENT CONTROL

The next step in increasing phase complexity brings us to the use of frequency-chirped laser pulses. In a chirped laser pulse there is a change of phase with frequency or, equivalently, a change in wavelength with time. Thus the instantaneous frequency of an up- (or positively) chirped pulse increases as the pulse passes, i.e. it becomes bluer, whereas that of a down- (or negatively) chirped pulse decreases, i.e. it becomes redder. The simplest case of chirping is linear, characterised by a quadratic phase shift, followed by increasingly higher orders, cubic and so on. Most work in coherent control uses linear chirp but cubic phase shifts have been considered recently [57].

A single chirped pulse has been used extensively to manipulate quantum state amplitudes and is often combined with a transform-limited probe pulse. A simplification of STIRAP replaces the pair of pulses with a single chirped ultra fast pulse [58] for population transfer in a three-level Λ -atom (see figure 1.2). The π -pulse approach discussed for atomic excitation in section 1.2 was extended theoretically to molecules by Wilson and co-workers [16] by considering a chirped pulse. The chirp ensures the π -pulse condition is met for all the rovibrational states of the molecule by providing a range of Rabi frequencies. Warren *et al.* [59] used a chirped picosecond laser pulse to selectively excite the transitions $^2P_{3/2} \leftarrow ^2S_{1/2}$ or $^2P_{1/2} \leftarrow ^2S_{1/2}$ in atomic sodium – a quasi three-level system. A positive chirp preferentially excited $^2P_{1/2}$ whereas a negative chirp only excited $^2P_{3/2}$. The same group has also extended this approach to I_2 , a multi-level system [60, 61]. Chelkowski proposed a vibrational ladder-climbing approach to dissociate H_2 [62] using a chirped pulse. Vibrational levels are sequentially excited as the negatively chirped pulse comes into resonance with the decreasing vibrational transition energies. Eventually the asymptotic levels are reached and the molecule dissociates. Their view was that this approach should be applicable to polyatomics provided the pulse was short compared to the vibrational relaxation time.

The ladder-climbing approach has been extended theoretically to pure vibrational excitation of ground state potentials by Raman adiabatic passage (ARP) [63-66], and in conjunction with rotational alignment with the laser field [67]. Chelkowski *et al.* [68] have also formulated the non-adiabatic case for H_2 , which they called Raman chirped non-adiabatic passage (RCNAP).

Experimentally vibrational ladder-climbing has been demonstrated in the $X^2\Pi_{1/2}$ state of NO [69] where the excitation $v'' = 0 \rightarrow v' = 1 \rightarrow v = 2$ lead to enhanced $v = 2$ population when the chirp follows the reduction in vibrational energy levels. A chirp-dependant oscillation in the population was also observed due to interferences between different rotational pathways in the excitation. Electronic ladder climbing has been seen in $5s \rightarrow 5p \rightarrow 5d$ excitation of atomic rubidium by a chirped pulse [70]. The ‘intuitive’ case, where the chirped pulse comes into resonance first with the $5s \rightarrow 5p$ transition followed by the $5p \rightarrow 5d$ transition, leads to population inversion. Surprisingly the ‘counter intuitive’ case, where the resonances are reversed, works equally well. Gerber *et al.* [71] found that in Na_2 , multiphoton excitation by a

negatively chirped pulse lead to enhanced final state population compared to excitation by a positively chirped pulse, but the positively chirped pulse gave a higher Na^+ yield upon multiphoton ionisation. The group of Girard have studied several systems using single chirped pulses. In the two-level system formed by the $5p \leftarrow 5s$ transition of atomic rubidium excited by a weak chirped pulse [72], chirp-dependent oscillations occur in the population of the excited state. These resulted from interference between resonant and non-resonant excitation pathways and occurred only after the pulse passed through resonance. Similar results were reported for multiphoton excitation of Na [57] leading to enhancement of the final population compared to excitation with a transform-limited pulse. Using interference between wave packets in the $4\ ^2\text{P}_{1/2}$ and $4\ ^2\text{P}_{3/2}$ states of potassium formed by a chirped pulse and a transform-limited pulse [73], the same group were able to shape the wave packets and alter their dynamics.

Bardeen *et al.* demonstrated a pump-dump experiment to control vibrational and electronic population in the laser dyes LDS690 and LDS750 [74] and bacteriorhodopsin [3] in solution using excitation by a single chirped pulse. A similar approach was used in 3-3'-diethylthiatricarbocyanine iodide (DTTCI) in ethanol [4]. Figure 1.3 shows schematically how a vibrational wave packet is formed on the excited state potential energy surface by the blue leading edge of the chirped pulse. The wave packet moves to the outer turning point of the potential and, in a stimulated emission process, is pumped back down to the ground state potential surface by the trailing red edge of the pulse.

Other studies also take the perspective of wave packet motion. Wilson *et al.* studied vibrational wave packets in the B-state of I_2 in the gas [75] and condensed (in solid Kr) [76] phases. The same group also revisited an early Zewail coherent control experiment in NaI [77]. They found that a chirped pulse could pre-compensate for dispersion of the wave packet over its trajectory in such a way that it was 'focussed' into an optimal Frank-Condon window for subsequent excitation. For I_2 this increased the ionisation yield, and for NaI the Na^* yield.

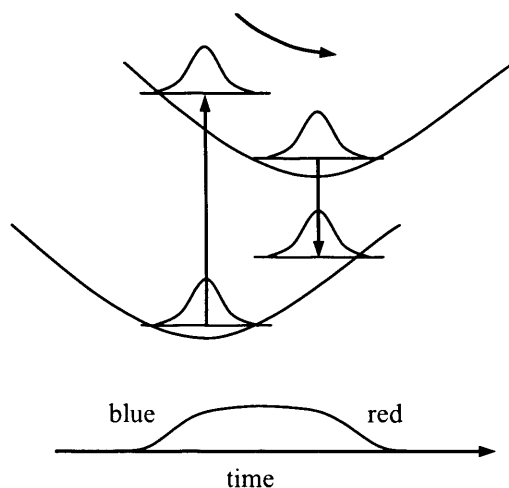


Figure 1.3 Schematic representation of the single chirped pulse pump-dump coherent control scheme for large solution phase molecules. The blue edge of the chirped laser pulse (bottom) excites a vibrational wave packet on the upper surface. The wave packet quickly relaxes (curved arrow) and is then pumped down to the ground state again by the red end of the laser pulse.

Although carried out in a Rydberg electron wave packet, a similar model was used by Arlt and co-workers [78]. The chirped pulse created an initially dispersed wave packet that becomes temporally narrower with time until it resembled a wave packet generated by a transform-limited laser pulse. Having first narrowed, the wave packet then dispersed in the normal way. Effectively the dynamics of the wave packet had been temporally shifted.

Rotational wave packets have also been manipulated. This was demonstrated experimentally by Faucher *et al.* [79] for N_2 . The shape of ground state rotational wave packet recurrences was found to be highly sensitive to the chirp. Higher rotational terms were excited after lower ones, leading to altered dynamics.

A. MULTIPLE CHIRPED PULSES

Warren and Davis [80] considered theoretically a Raman chirped adiabatic passage scheme using two chirped pulses. This allows selective population of ground-state vibrational levels. Bhattacharyya [81] extended these ideas theoretically to two oppositely chirped pulses making a non-resonant stimulated Raman excitation of H_2 from $\nu'' = 0, J'' = 0$ to $\nu' = 1, J'$. A negatively chirped pump pulse combined with a positively chirped Stokes pulse placed all the population in the S-branch if the pulse

was long and the chirp slow. Reversing the chirps of the pump and Stokes pulses populates only the Q-branch. If the pulse is short and the chirp is fast, then the S/Q branching ratio can be controlled by the chirp.

Sauerbrey *et al.* [82] created a very simple technique to selectively excite one or other of the $5^2P_{1/2}$ and $5^2P_{3/2}$ states of rubidium. Interference between two phase-locked chirped pulses leads to modulation of the frequency spectrum of the pulse pair. The positions of peaks and troughs in the spectrum can be controlled simply by phase shifting two replicas of the chirped pulse with a Michelson interferometer. Selective excitation was achieved by placing a spectral hole at one resonant frequency and a peak at the other.

Additional theoretical proposals for the use of multiple chirped pulses include chirped adiabatic passage by two-photon absorption (CAPTA) [83]. This allows selective excitation of *single* rovibrational states of a diatomic by non-resonant excitation via an electronic intermediate. Very recently Dunning and co-workers [84] proposed an extension of the half-cycle pulse control of Rydberg electron wave packets to include trains of chirped pulses that, modulated in the right way, control the dynamics of the wave packet.

1.6 PULSE SHAPING

The advent of pulse shaping of ultrafast laser pulses has made it possible to generate laser pulses with regular phase functions that are much more complex than simple linear chirps. These have included phase steps [85-87], sine functions [85] and square waves [88] and arbitrary phases output by feedback-based optimisation.

There are several different designs of pulse shaper reported in the literature, but most are based on a zero-dispersion, or $4f$, compressor [89] (also known as a null stretcher). The layout of a typical pulse shaper is shown in figure 1.4 [90]. Variations of the optical arrangement of the pulse shaper include replacement of the lenses with cylindrical mirrors and different input and output geometries, but the concept of operation is the same. The grating – lens – lens – grating arrangement performs a Fourier transform of the laser pulse from time to frequency and back to time. The pulse shaping operation occurs in the frequency domain.

The pulse-shaping device itself can be a liquid crystal spatial light modulator (LC-SLM) [91, 92], an acousto-optic modulator (AOM) [93, 94], or less commonly, a deformable mirror [10, 95] or reflective SLM (the parallel aligned nematic liquid crystal, PAL-SLM [96]). Liquid crystal spatial light modulators comprise a linear array of pixels (typically 128, but recently extended to 640 [97]) containing a liquid crystal. The array is connected so that a different electrical potential can be applied to each pixel. The refractive index of the liquid crystal depends on the applied potential. The difference in refractive index between pixels shifts the relative phase of the laser light passing through them. When the pulse is reformed the phase shifts imprinted by the SLM are retained, and the pulse is shaped. The degree of shaping available depends on how well separated are the frequency components of the pulse. Often two such arrays are stacked together, one altering the phase and the other adjusting the amplitude.

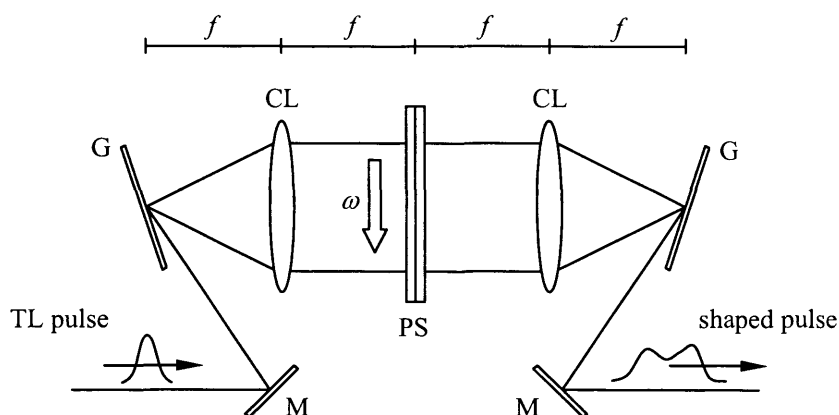


Figure 1.4 Schematic layout of a zero-dispersion ($4f$) pulse shaper. A transform-limited laser pulse enters the pulse shaper from the left and is dispersed by a grating (G). Gratings for this application typically have around $1800 \text{ lines mm}^{-1}$. The grating separates spatially the spectral frequency (ω) components of the pulse. A cylindrical lens (CL) positioned at its focal length (f) from the grating serves to collimate the beam coming off the grating, and focus the frequency components into the SLM pixels [98]. A second identical lens is located two focal lengths from the first. The pulse-shaping (PS) device is placed half way between the lenses, as this is the Fourier plane, where the spectral resolution is highest. The second lens focuses the light onto the second grating where it is recombined to form a temporally shaped pulse.

Acousto-optic modulators comprise a photonic crystal (usually TeO_2 , but fused silica was recently used to shape 400 nm pulses [99]) attached to a piezoelectric actuator to which is applied a shaped radio-frequency (RF) potential. This sets up a shaped

acoustic wave in the material that presents a frequency dependent diffraction grating to the laser pulse [93]. AOMs can be used without the 4-f arrangement, in which case they are known as acousto-optic programmable dispersive filters (AO-PDF) [100]. Although originally developed for use at the fundamental wavelengths of titanium sapphire lasers (around 800 nm), these devices have recently been extended to below 500 nm [101], and will doubtless be extended into the UV.

A. REGULAR PHASE FUNCTIONS

Meshulach and Silberberg [87, 102] demonstrated coherent control of the two-photon transition $8S_{1/2} \leftarrow 6S_{1/2}$ in atomic Cs using a 30 fs laser pulse with a π phase step. The π -step is generated by having the phases $\varphi = 0$ for all frequencies $\omega < \omega_\pi$, and $\varphi = \pi$ for $\omega \geq \omega_\pi$, and leads to a “dark pulse” [85], where for $\omega_\pi \approx \omega_{8S \leftarrow 6S} / 2$, i.e. near the two-photon resonance, no excitation occurs, whereas for $\omega_\pi = \omega_{8S \leftarrow 6S} / 2$ the 8S population is maximal, as if excited by a transform-limited pulse. The same approach was found to be applicable also in the laser dye Coumarin 6H, in which the absorption forms a broad continuum as opposed to discrete atomic levels. The Silberberg experiment was repeated in sodium by Baumert and co-workers [85] and extended by the addition of a transform-limited “pre-pulse”. By exciting the system first with a phase-locked transform-limited pulse the effect of the π -step pulse could be controlled, and even inverted, depending on the relative phases.

Meshulach and Silberberg [102] used a cosine phase function to shape 31 fs pulses at 822 nm to generate dark pulses in the same transition in Cs as their π -step work. Motzkus and co-workers [103] also generated dark pulses in a two-photon excitation of atomic sodium using a cosine phase function, but combined it with a feedback algorithm (discussed below). A cosine function applied to the spectral phase of the laser pulse was studied in detail by the Baumert group [85]. A single pulse shaped by a sine phase function generates a train of pulses. The relative phases between the pulses can be controlled by the phase of the sine function. For the two-photon excitation of atomic sodium ($4s \leftarrow 3s$), changing the phase of the function lead to enhancement or reduction of the 4s population. If the shaped pulse was preceded by a transform-limited pulse, the role of the shaped pulse could itself be controlled,

depending on the relative phases between them. Pastirk *et al.* [104] were able to select single fluorescent marker species for excitation in solution mixture by applying a cosine phase function in femtosecond two-photon microscopy.

A square-step phase function was employed by Renard *et al.* [88] to shape 100 fs pulses to control ground state rotational wave packet dynamics in N₂ in a stimulated Raman process. Altering the spectral phase reduced or accentuated interference between contributions from odd and even rotational states.

Perhaps the most sophisticated pulse shaping experiment not to include experimental feedback (discussed in the following section) was performed by the Bucksbaum group [105]. A Rydberg wave packet was excited in atomic caesium by a shaped optical pulse. The initial wave packet included the states 24*p* to 29*p*, the populations of which were redistributed by a shaped THz half-cycle pulse to include only the 27*s* state.

B. IRREGULAR PHASES AND GENETIC ALGORITHMS

The real power of ultrafast optical pulse shaping has come from its combination with feedback optimisation. In this arrangement, a genetic algorithm (GA) or other automatic optimisation algorithm optimises the shape of the laser field using feedback from the experiment to select a particular objective. The objective can be any of the normal coherent control products, for instance ionisation yield, particular dissociation products or generation of a particular harmonic order. This section reviews some examples of coherent control using pulse shaping coupled with feedback optimisation. Chapter 5 discusses in greater detail what these experiments have revealed about coherent control physics and the algorithms themselves.

The GA combined with a pulse-shaper was first realised by Gerber *et al.* in 1997. In a proof-of-principle experiment, second harmonic generation in a BBO crystal [91] was optimised by correcting a pre-chirped 60 fs laser pulse. The first molecular coherent control was reported by Warren and co-workers [106]. Their experiment monitored the population of the first excited state of the laser dye IR125 in methanol, and demonstrated maximisation of both the efficiency (excited state population/laser power) and efficacy (total excited state population) using feedback from fluorescence. Since that time there have been many studies using these techniques to control

excitation of atoms and molecules ranging from homonuclear diatomics to biological macromolecules in the gas and solution phases, and even *in vivo* (at least in principle [107]). In atomic physics the GA and pulse shaping approach has selected a particular harmonic order (the 27th) from its neighbours in high-order harmonic coherent XUV generation in argon in a 175 μm diameter capillary waveguide [10]. More recently, resonant two-photon absorption was maximised in rubidium atoms [96]. In diatomics, Pearson *et al.* were able to select the relative ratios of dissociative ionisation and non-dissociative ionisation in Na_2 [94]. Bartelt *et al.* maximised single pulse multiphoton ionisation in NaK (and Na_2K) [108]. In Li_2 , Leone and co-workers [92] optimised the delay between a shaped pump and a transform-limited probe to maximise the photoionisation yield. The Motzkus group selected arbitrary vibrational states the potassium dimer by stimulated Raman scattering in a degenerate four-wave mixing experiment [109]. A recent development from the established techniques of phase and amplitude shaping by Brixner *et al.* enhanced the three-photon K_2^+ signal by incorporating polarisation shaping with phase shaping.

Work on polyatomic molecules has included control of the self-phase modulation spectrum of CCl_4 [110], selection of individual vibrational modes in methanol [94, 111] and benzene [94], SF_6 and CO_2 [95], and polydiacetalene [112]. Selective bond cleavage was first demonstrated in $\text{CpFe}(\text{CO})_2\text{Cl}$ (where Cp is cyclopentadiene) and $\text{Fe}(\text{CO})_5$ by Gerber's group [113], and has now been extended to include fragmentation of CH_3COCF_3 [93] and $\text{CpMn}(\text{CO})_3$ [114]. Rabitz and co-workers [7] used pulse-shaping coupled to a learning algorithm in an impressive set of high field experiments in simple organic molecules. Working in the high field, they argued, offers more powerful control over chemical reactions as it allows ac-Stark shifting of energy levels and multiphoton ionisation, which overcome the limitations imposed by the laser bandwidth in weak field experiments. They were able to selectively enhance photofragmentation products from acetone, trifluoroacetone and acetophenone. In addition, the dissociative rearrangement product of acetophenone could be optimised. Other studies in polyatomics include simultaneous optimisation of absorption by solution phase DCM and $[\text{Ru}(\text{dpb})_3](\text{PF}_6)_2$ [115], and multiphoton excitation of $[\text{Ru}(\text{dpb})_3](\text{PF}_6)_2$ [90].

Extending both the molecular size and the utility of coherent control, Motzkus *et al.* have studied electron transfer in a bacterial light harvesting complex [107], and the

Dantus group have demonstrated that in principle coherent control could be used as a probe *in vivo* [116].

1.7 CONCLUSION

This chapter has introduced coherent control and reviewed particular instances from the literature. There are many approaches to coherent control ranging from simple schemes to complex multiple shaped pulses and feedback optimisation by machine learning. The enormous power of ultrafast pulse shaping coupled with genetic algorithms has altered the path of coherent control research. However, it is no longer sufficient simply to select the outcome of photoexcitation. The objective now is to understand the physics of the interactions between light and matter so that our reliance on the genetic algorithm to find optimal pulses is removed. The work presented in this thesis is a contribution to such understanding. By returning to simpler systems, atomic sodium and sodium dimers, we have been able to relate the properties of the laser pulses required to achieve particular control objectives to the properties of the system, such as its anharmonicity.

1.8 REFERENCES

1. J.M. Villas-Boas, A.O. Govorov, and S.E. Ulloa, *Phys. Rev. B (Condens. Matt. Mat. Phys.)* **69** (12), 125342. (2004).
2. A.J. Wurzer, S. Lochbrunner, and E. Riedle, *Appl. Phys. B (Lasers Opt.)* **71** (3), 405-409. (2000).
3. C.J. Bardeen, Q. Wang, and C.V. Shank, *J. Phys. Chem. A* **102** (17), 2759-2766. (1998).
4. K. Misawa and T. Kobayashi, *J. Chem. Phys.* **113** (17), 7546-7553. (2000).
5. S. Kundermann, M. Saba, C. Ciuti, T. Guillet, U. Oesterle, J.L. Staehli, and B. Deveaud, *Phys. Rev. Lett.* **91** (10), 107402. (2003).
6. L. Banares, T. Baumert, M. Bergt, B. Kiefer, and G. Gerber, *Chem. Phys. Lett.* **267** (1-2), 141-148. (1997).
7. R.J. Levis, G.M. Menkir, and H. Rabitz, *Science* **292** (5517), 709-713. (2001).

8. U.D. Rapol, A. Wasan, and V. Natarajan, *Phys. Rev. A (At. Mol. Opt. Phys.)* **67** (5), 053802. (2003).
9. M. Wittmann, A. Nazarkin, and G. Korn, *Phys. Rev. Lett.* **84** (24), 5508-5511. (2000).
10. R. Bartels, S. Backus, E. Zeek, L. Misoguti, G. Vdovin, I.P. Christov, M.M. Murnane, and H.C. Kapteyn, *Nature* **406** (6792), 164-166. (2000).
11. R.A. Bartels, T.C. Weinacht, N. Wagner, M. Baertschy, C.H. Greene, M.M. Murnane, and H.C. Kapteyn, *Phys. Rev. Lett.* **8801** (1), 013903. (2002).
12. S. Jorgensen and R. Kosloff, *Phys. Rev. A* **70** (1), 015602. (2004).
13. M. Shapiro and P. Brumer, *J. Chem. Phys.* **84** (1), 540-541. (1986).
14. S.T. Cundiff and J. Ye, *Rev. Mod. Phys.* **75** (1), 325-342. (2003).
15. H. Ohmura and T. Nakanaga, *J. Chem. Phys.* **120** (11), 5176-5180. (2004).
16. J.S. Cao, C.J. Bardeen, and K.R. Wilson, *Phys. Rev. Lett.* **80** (7), 1406-1409. (1998).
17. M. Shapiro and P. Brumer, *J. Chem. Phys.* **84** (7), 4103-4104. (1986).
18. M. Shapiro and P. Brumer, *Int. Rev. Phys. Chem.* **13** (2), 187-229. (1994).
19. M. Shapiro, J.W. Hepburn, and P. Brumer, *Chem. Phys. Lett.* **149** (5-6), 451-454. (1988).
20. L. Zhu, K. Suto, J.A. Fiss, R. Wada, T. Seideman, and R.J. Gordon, *Phys. Rev. Lett.* **79** (21), 4108-4111. (1997).
21. S.P. Lu, S.M. Park, Y.G. Xie, and R.J. Gordon, *J. Chem. Phys.* **96** (9), 6613-6620. (1992).
22. D. Xenakis, N.E. Karapanagioti, O. Faucher, E. Hertz, and D. Charalambidis, *J. Phys. B (At. Mol. Opt. Phys.)* **32** (2), 341-348. (1999).
23. C. Chen and D.S. Elliott, *Phys. Rev. Lett.* **65** (14), 1737-1740. (1990).
24. C. Chen, Y.Y. Yin, and D.S. Elliott, *Phys. Rev. Lett.* **64** (5), 507-510. (1990).
25. G.Q. Xing, X.B. Wang, X. Huang, R. Bersohn, and B. Katz, *J. Chem. Phys.* **104** (3), 826-831. (1996).
26. V.D. Kleiman, L.C. Zhu, J. Allen, and R.J. Gordon, *J. Chem. Phys.* **103** (24), 10800-10803. (1995).
27. H.G. Muller, P.H. Bucksbaum, D.W. Schumacher, and A. Zavriyev, *J. Phys. B (At. Mol. Opt. Phys.)* **23** (16), 2761-2769. (1990).

28. D.W. Schumacher and P.H. Bucksbaum, *Phys. Rev. A* **54** (5), 4271-4278. (1996).
29. H. Ohmura, T. Nakanaga, H. Arakawa, and M. Tachiya, *Chem. Phys. Lett.* **363** (5-6), 559-566. (2002).
30. B. Sheehy, B. Walker, and L.F. Dimauro, *Phys. Rev. Lett.* **74** (24), 4799-4802. (1995).
31. Y.Y. Yin, C. Chen, D.S. Elliott, and A.V. Smith, *Phys. Rev. Lett.* **69** (16), 2353-2356. (1992).
32. Y.Y. Yin, D.S. Elliott, R. Shehadeh, and E.R. Grant, *Chem. Phys. Lett.* **241** (5-6), 591-596. (1995).
33. F. Wang, C. Chen, and D.S. Elliott, *Phys. Rev. Lett.* **77** (12), 2416-2419. (1996).
34. F. Wang and D.S. Elliott, *Phys. Rev. A* **56** (4), 3065-3076. (1997).
35. S.T. Pratt, *J. Chem. Phys.* **104** (15), 5776-5783. (1996).
36. N.V. Vitanov, T. Halfmann, B.W. Shore, and K. Bergmann, *Annu. Rev. Phys. Chem.* **52**, 763-809. (2001).
37. K. Bergmann, H. Theuer, and B.W. Shore, *Rev. Mod. Phys.* **70** (3), 1003-1025. (1998).
38. S. Schiemann, A. Kuhn, S. Steuerwald, and K. Bergmann, *Phys. Rev. Lett.* **71** (22), 3637-3640. (1993).
39. R. Sussmann, R. Neuhauser, and H.J. Neusser, *J. Chem. Phys.* **100** (7), 4784-4789. (1994).
40. K.J. Boller, A. Imamoglu, and S.E. Harris, *Phys. Rev. Lett.* **66** (20), 2593-2596. (1991).
41. P.M. Paul, E.S. Toma, P. Breger, G. Mullot, F. Auge, P. Balcou, H.G. Muller, and P. Agostini, *Science* **292** (5522), 1689-1692. (2001).
42. T. Baumert, M. Grosser, R. Thalweiser, and G. Gerber, *Phys. Rev. Lett.* **67** (27), 3753-3756. (1991).
43. D.J. Tannor, R. Kosloff, and S.A. Rice, *J. Chem. Phys.* **85** (10), 5805-5820. (1986).
44. D.J. Tannor and S.A. Rice, *J. Chem. Phys.* **83** (10), 5013-5018. (1985).
45. W.S. Warren and A.H. Zewail, *J. Chem. Phys.* **75** (12), 5956-5958. (1981).
46. W.R. Lambert, P.M. Felker, and A.H. Zewail, *J. Chem. Phys.* **75** (12), 5958-5960. (1981).

47. N.F. Scherer, A.J. Ruggiero, M. Du, and G.R. Fleming, *J. Chem. Phys.* **93** (1), 856-857. (1990).
48. N.F. Scherer, R.J. Carlson, A. Matro, M. Du, A.J. Ruggiero, V. Romero-Rochin, J.A. Cina, G.R. Fleming, and S.A. Rice, *J. Chem. Phys.* **95** (3), 1487-1511. (1991).
49. M.W. Noel and C.R. Stroud, *Phys. Rev. Lett.* **75** (7), 1252-1255. (1995).
50. M.W. Noel and C.R. Stroud, *Phys. Rev. Lett.* **77** (10), 1913-1916. (1996).
51. J.R.R. Verlet, V.G. Stavros, R.S. Minns, and H.H. Fielding, *Phys. Rev. Lett.* **89** (26), 263004. (2002).
52. R.S. Minns, J.R.R. Verlet, L.J. Watkins, and H.H. Fielding, *J. Chem. Phys.* **119** (12), 5842-5847. (2003).
53. R.S. Minns, R. Patel, J.R.R. Verlet, and H.H. Fielding, *Phys. Rev. Lett.* **91** (24), 243601. (2003).
54. J. Degert, C. Meier, B. Chatel, and B. Girard, *Phys. Rev. A (At. Mol. Opt. Phys.)* **67** (4), 041402. (2003).
55. M. Wollenhaupt, A. Assion, D. Liese, C. Sarpe-Tudoran, T. Baumert, S. Zamith, M.A. Bouchene, B. Girard, A. Flettner, U. Weichmann, and G. Gerber, *Phys. Rev. Lett.* **89** (17), 173001. (2002).
56. C. Doule, E. Hertz, L. Berguiga, R. Chaux, B. Lavorel, and O. Faucher, *J. Phys. B (At. Mol. Opt. Phys.)* **34** (6), 1133-1142. (2001).
57. B. Chatel, J. Degert, and B. Girard, *Phys. Rev. A (At. Mol. Opt. Phys.)* **70** (5), 053414. (2004).
58. G.P. Djotyan, J.S. Bakos, Z. Sorlei, and J. Szigeti, *Phys. Rev. A (At. Mol. Opt. Phys.)* **70** (6), 063406. (2004).
59. J.S. Melinger, S.R. Gandhi, A. Hariharan, J.X. Tull, and W.S. Warren, *Phys. Rev. Lett.* **68** (13), 2000-2003. (1992).
60. J.S. Melinger, S.R. Gandhi, A. Hariharan, D. Goswami, and W.S. Warren, *J. Chem. Phys.* **101** (8), 6439-6454. (1994).
61. J.S. Melinger, A. Hariharan, S.R. Gandhi, and W.S. Warren, *J. Chem. Phys.* **95** (3), 2210-2213. (1991).
62. S. Chelkowski, A.D. Bandrauk, and P.B. Corkum, *Phys. Rev. Lett.* **65** (19), 2355-2358. (1990).

63. S. Chelkowski and A.D. Bandrauk, *J. Raman Spectrosc.* **28** (6), 459-466. (1997).
64. S. Chelkowski and G.N. Gibson, *Phys. Rev. A* **52** (5), R3417-R3420. (1995).
65. J.T. Lin and T.F. Jiang, *Phys. Rev. A* **6301** (1), 013408. (2001).
66. K. Mishima and K. Yamashita, *J. Chem. Phys.* **110** (16), 7756-7769. (1999).
67. F. Legare, S. Chelkowski, and A.D. Bandrauk, *Chem. Phys. Lett.* **329** (5-6), 469-476. (2000).
68. F. Legare, S. Chelkowski, and A.D. Bandrauk, *J. Raman Spectrosc.* **31** (1-2), 15-23. (2000).
69. D.J. Maas, M.J.J. Vrakking, and L.D. Noordam, *Phys. Rev. A* **60** (2), 1351-1362. (1999).
70. B. Broers, H.B.V. Vandenheuvell, and L.D. Noordam, *Phys. Rev. Lett.* **69** (14), 2062-2065. (1992).
71. A. Assion, T. Baumert, J. Helbing, V. Seyfried, and G. Gerber, *Chem. Phys. Lett.* **259** (5-6), 488-494. (1996).
72. J. Degert, W. Wohlleben, B. Chatel, M. Motzkus, and B. Girard, *Phys. Rev. Lett.* **89** (20), 203003. (2002).
73. M.A. Bouchene, C. Nicole, and B. Girard, *J. Phys. B (At. Mol. Opt. Phys.)* **32** (21), 5167-5177. (1999).
74. G. Cerullo, C.J. Bardeen, Q. Wang, and C.V. Shank, *Chem. Phys. Lett.* **262** (3-4), 362-368. (1996).
75. B. Kohler, V.V. Yakovlev, J.W. Che, J.L. Krause, M. Messina, K.R. Wilson, N. Schwentner, R.M. Whitnell, and Y.J. Yan, *Phys. Rev. Lett.* **74** (17), 3360-3363. (1995).
76. C.J. Bardeen, J.W. Che, K.R. Wilson, V.V. Yakovlev, V.A. Apkarian, C.C. Martens, R. Zadoyan, B. Kohler, and M. Messina, *J. Chem. Phys.* **106** (20), 8486-8503. (1997).
77. C.J. Bardeen, J.W. Che, K.R. Wilson, V.V. Yakovlev, P.J. Cong, B. Kohler, J.L. Krause, and M. Messina, *J. Phys. Chem. A* **101** (20), 3815-3822. (1997).
78. J. Arlt, C. Weiss, G. Torosyan, and R. Beigang, *Phys. Rev. Lett.* **79** (24), 4774-4777. (1997).
79. M. Kubasik, A. Cebo, E. Hertz, R. Chauv, B. Lavorel, and O. Faucher, *J. Phys. B (At. Mol. Opt. Phys.)* **34** (12), 2437-2446. (2001).

80. J.C. Davis and W.S. Warren, *J. Chem. Phys.* **110** (9), 4229-4237. (1999).
81. S. Sen, S. Ghosh, S.S. Bhattacharyya, and S. Saha, *J. Chem. Phys.* **116** (2), 581-588. (2002).
82. R. Netz, A. Nazarkin, and R. Sauerbrey, *Phys. Rev. Lett.* **90** (6), 063001. (2003).
83. B.Y. Chang, I.R. Sola, V.S. Malinovsky, and J. Santamaria, *J. Chem. Phys.* **113** (12), 4901-4911. (2000).
84. S. Yoshida, C.O. Reinhold, E. Persson, J. Burgd, and F.B. Dunning, *J. Phys. B (At. Mol. Opt. Phys.)* **38** (2), S209. (2005).
85. A. Prakelt, M. Wollenhaupt, C. Sarpe-Tudoran, and T. Baumert, *Phys. Rev. A (At. Mol. Opt. Phys.)* **70** (6), 063407. (2004).
86. T.C. Weinacht, J. Ahn, and P.H. Bucksbaum, *Phys. Rev. Lett.* **80** (25), 5508-5511. (1998).
87. D. Meshulach and Y. Silberberg, *Phys. Rev. A* **60** (2), 1287-1292. (1999).
88. M. Renard, E. Hertz, B. Lavorel, and O. Faucher, *Phys. Rev. A* **69** (4), 043401. (2004).
89. O.E. Martinez, *IEEE J. Quantum Electron.* **24** (12), 2530-2536. (1988).
90. T. Brixner, N.H. Damrauer, B. Kiefer, and G. Gerber, *J. Chem. Phys.* **118** (8), 3692-3701. (2003).
91. T. Baumert, T. Brixner, V. Seyfried, M. Strehle, and G. Gerber, *Appl. Phys. B (Lasers Opt.)* **65** (6), 779-782. (1997).
92. J.B. Ballard, H.U. Stauffer, Z. Amitay, and S.R. Leone, *J. Chem. Phys.* **116** (4), 1350-1360. (2002).
93. D. Cardoza, F. Langhojer, C. Trallero-Herrero, O.L.A. Monti, and T. Weinacht, *Phys. Rev. A (At. Mol. Opt. Phys.)* **70** (5), 053406. (2004).
94. B.J. Pearson, J.L. White, T.C. Weinacht, and P.H. Bucksbaum, *Phys. Rev. A* **6306** (6), 063412. (2001).
95. T.C. Weinacht, R. Bartels, S. Backus, P.H. Bucksbaum, B. Pearson, J.M. Geremia, H. Rabitz, H.C. Kapteyn, and M.M. Murnane, *Chem. Phys. Lett.* **344** (3-4), 333-338. (2001).
96. T. Ando, T. Urakami, H. Itoh, and Y. Tsuchiya, *Appl. Phys. Lett.* **80** (22), 4265-4267. (2002).
97. A. Monmayrant and B. Chatel, *Rev. Sci. Instrum.* **75** (8), 2668-2671. (2004).
98. A.M. Weiner, *Rev. Sci. Instrum.* **71** (5), 1929-1960. (2000).

99. M. Roth, M. Mehendale, A. Bartelt, and H. Rabitz, *App. Phys. B (Lasers Opt.)* **80** (4-5), 441-444. (2005).
100. F. Verluise, V. Laude, Z. Cheng, C. Spielmann, and P. Tournois, *Opt. Lett.* **25** (8), 575-577. (2000).
101. A. Monmayrant, A. Arbouet, B. Girard, B. Chatel, A. Barman, B.J. Whitaker, and D. Kaplan, *App. Phys. B.* (in press.).
102. D. Meshulach and Y. Silberberg, *Nature* **396** (6708), 239-242. (1998).
103. T. Hornung, R. Meier, D. Zeidler, K.-L. Kompa, D. Proch, and M. Motzkus, *App. Phys. B (Lasers Opt.)* **71** (3), 277-284. (2000).
104. I. Pastirk, J.M. Dela Cruz, K.A. Walowicz, V.V. Lozovoy, and M. Dantus, *Opt. Express* **11** (14), 1695-1701. (2003).
105. C. Rangan, J. Ahn, D.N. Hutchinson, and P.H. Bucksbaum, *J. Mod. Opt.* **49** (14-15), 2339-2347. (2002).
106. C.J. Bardeen, V.V. Yakovlev, K.R. Wilson, S.D. Carpenter, P.M. Weber, and W.S. Warren, *Chem. Phys. Lett.* **280** (1-2), 151-158. (1997).
107. J.L. Herek, W. Wohlleben, R.J. Cogdell, D. Zeidler, and M. Motzkus, *Nature* **417** (6888), 533-535. (2002).
108. A. Bartelt, S. Minemoto, C. Lupulescu, S. Vajda, and L. Woste, *Eur. Phys. J. D* **16** (1-3), 127-131. (2001).
109. T. Hornung, R. Meier, R. de Vivie-Riedle, and M. Motzkus, *Chem. Phys.* **267** (1-3), 261-276. (2001).
110. T.C. Weinacht, J.L. White, and P.H. Bucksbaum, *J. Phys. Chem. A* **103** (49), 10166-10168. (1999).
111. J.L. White, B.J. Pearson, and P.H. Bucksbaum, *J. Phys B (At. Mol. Opt. Phys.)* **37** (24), L399. (2004).
112. D. Zeidler, S. Frey, W. Wohlleben, M. Motzkus, F. Busch, T. Chen, W. Kiefer, and A. Materny, *J. Chem. Phys.* **116** (12), 5231-5235. (2002).
113. A. Assion, T. Baumert, M. Bergt, T. Brixner, B. Kiefer, V. Seyfried, M. Strehle, and G. Gerber, *Science* **282** (5390), 919-922. (1998).
114. C. Daniel, J. Full, L. Gonzalez, C. Lupulescu, J. Manz, A. Merli, S. Vajda, and L. Woste, *Science* **299** (5606), 536-539. (2003).
115. T. Brixner, N.H. Damrauer, P. Niklaus, and G. Gerber, *Nature* **414** (6859), 57-60. (2001).

116. J.M. Dela Cruz, I. Pastirk, M. Comstock, and M. Dantus, *Opt. Express* **12** (17), 4144-4149. (2004).

CHAPTER 2 DEVELOPMENT OF A BEAM SOURCE FOR SODIUM ATOMS AND DIMERS

ABSTRACT

This chapter describes development of a sodium atom and dimer beam source for use in optical coherent control experiments. The concepts of molecular beams are introduced along with a brief review of the literature on sodium atom and dimer beams. The beam source is considered in two parts. Firstly the sodium oven and nozzle are described in detail, along with the vacuum chamber that houses them. This is followed by a description of the experimental chamber, which contains a time-of-flight mass spectrometer. Finally a number of potential improvements to the system are discussed.

2.1 INTRODUCTION

A large part of this research project has been the development of a source for molecular beams of sodium atoms and sodium dimers. This chapter details the system we have built and describes how it has been developed and used. The chapter starts with an introduction to molecular beams, focussing on the particular characteristics that have been found to pertain to beams of alkali metals, especially sodium. Our molecular beam is then presented, starting with the sodium source, which comprises an oven, nozzle and vacuum system. That is followed by a description of the experimental chamber, where we make use of the molecular beam in coherent control experiments. The experimental side includes a time-of-flight mass spectrometer and micro-channel plate detector and the vacuum pumps. Finally, some lessons learnt and suggestions for improvements are noted.

2.2 INTRODUCTION TO ATOMIC AND MOLECULAR BEAMS

A. THE FREE JET

Chapter 2 of Atomic and Molecular Beam Methods by D. R. Miller [1] is an excellent introduction to free jet sources. This section follows its structure, starting with an ideal analysis of the free jet expansion, but then concentrates on expansions and beams of alkali metals atoms and dimers.

An atomic or molecular beam source like ours is driven by the pressure difference between the high pressure P_0 inside an oven separated by a small aperture from a lower background pressure P_b . Gas escaping from the oven is accelerated by the pressure difference and its approach to the aperture. If,

$$\frac{P_0}{P_b} > \left(\frac{\gamma + 1}{2} \right)^{\gamma/\gamma-1}, \quad (2.1)$$

where $\gamma = C_p/C_v$, the flow velocity of the gas will reach the local speed of sound in the aperture. The gas flow velocity is expressed by the Mach number,

$$M = \frac{V}{a} = 1, \quad (2.2)$$

where V is the flow velocity and a is the local speed of sound. Expansion of the gas into the vacuum accelerates it further, to $M > 1$, so the expansion is called supersonic.

The expansion does flow work so enthalpy is the natural thermodynamic quantity to use. Within the source the gas has a stagnation enthalpy h_0 . The expansion is divided notionally into *streamlines* along which h_0 is constant. The first law of thermodynamics then gives,

$$h + \frac{V^2}{2} = h_0 \quad (2.3)$$

along a streamline. For an ideal gas $dh = \hat{C}_p dt$, where \hat{C}_p is the heat capacity at constant pressure, so velocity and flow can be related by,

$$V^2 = 2(h_0 - h) = 2 \int_T^{T_0} \hat{C}_p dt, \quad (2.4)$$

which gives,

$$V = \sqrt{2\hat{C}_p(T_0 - T)}, \quad (2.5)$$

if \hat{C}_p is constant over the temperature range T_0 to T . This gives the final velocity reached by the gas molecules during expansion,

$$V_\infty = \sqrt{\frac{2RT_0}{W} \left(\frac{\gamma}{\gamma-1} \right)} \quad (2.6)$$

if $T \ll T_0$ (i.e. the gas is cooled), and the gas is ideal with molar mass W and $C_p = RW\gamma/(\gamma-1)$. Taking the ideal local speed of sound $a = \sqrt{\gamma RT/W}$, equation 2.5 can be recast in terms of just γ and M to give temperature, velocity, pressure, and density characteristics throughout the expansion normalised to the source conditions. Thus,

$$\frac{T}{T_0} = \left(1 + \frac{\gamma-1}{2} M^2 \right)^{-1}, \quad (2.7)$$

so,

$$V = M \sqrt{\frac{\lambda RT_0}{W} \left(1 + \frac{\gamma-1}{2} M^2 \right)^{-1/2}}. \quad (2.8)$$

For an isentropic (constant entropy) expansion pressure and density are then,

$$\frac{P}{P_0} = \left(\frac{T}{T_0} \right)^{\gamma/\gamma-1}, \text{ and } \frac{\rho}{\rho_0} = \frac{n}{n_0} = \left(\frac{T}{T_0} \right)^{1/\gamma-1}, \quad (2.9)$$

where ρ is the mass density, n the number density and R is the gas constant.

For these expressions to be useful it is necessary to calculate the velocity or Mach number behaviour of the expansion. A fluid mechanical continuum (high collision frequency) model can be used to calculate these. The expansion is assumed to be isentropic and starts from a steady state. Viscosity and heat conduction are neglected. The fluid mechanics equations to be solved are for the conservation of mass, momentum and energy, given respectively by,

$$\nabla \cdot (\rho \mathbf{V}) = 0 \quad (2.10)$$

$$\rho \nabla \cdot \nabla \mathbf{V} = -\nabla P \quad (2.11)$$

$$\mathbf{V} \cdot \nabla h_0 = 0 \quad (2.12)$$

where $P = \rho RT/W$. These equations can be solved numerically but the details lie outside the scope of the work presented here. The numerical results have been fitted to

equations which can be conveniently used to calculate properties of an expansion. The most useful of these for this work describes the Mach number as a function of distance from the nozzle for an axis-symmetric ideal expansion,

$$M = A \left(\frac{x - x_0}{d} \right)^{\gamma-1} - \frac{1}{2} \left(\frac{\gamma+1}{\gamma-1} \right) \bigg/ A \left(\frac{x - x_0}{d} \right)^{\gamma-1} \quad (2.13)$$

where, for $\gamma = 5/3$, the constant $A = 3.26$, x is distance from the nozzle aperture along the centreline and d is the nozzle diameter. The term $x_0/d = 0.075$ is the effective position of the source aperture, and lies slightly in front of the real aperture. This expression is applicable to distances greater than 2.5 diameters from the aperture. Having calculated the Mach number, equations (2.7) to (2.9) can then be evaluated at any point along the centreline of the expansion.

The behaviour of the ideal isentropic expansion can be summarised as follows. The velocity reaches its terminal value V_∞ within a short distance (< 4 nozzle diameters) after leaving the nozzle. Temperature, pressure and density, on the other hand, fall much more slowly and only approach their terminal values after > 20 nozzle diameters. Eventually however the collision rate falls to a level where the continuum model breaks down and collision-free molecular flow prevails. The distance to the transition to free-molecular flow is important when the expansion is being used to cool the internal degrees of freedom of a molecule, as in our experiment. Once free-molecular flow occurs there is no further cooling.

Figure 2.1 summarises a supersonic expansion near the nozzle. As the gas accelerates towards the nozzle the Mach number reaches 1. Outside the nozzle the gas expands and accelerates until its velocity is higher than the local speed of sound ($M \gg 1$). Since information about the surrounding, background, pressure is transmitted through the expanding gas at the local speed of sound, the expansion region cannot adjust to background pressure. The deceleration to $M < 1$ is achieved by shock structures. These are thin regions (with a thickness of about the mean free path) where density, pressure, temperature and velocity change rapidly. Around the outside of the expansion is a cylindrical ‘barrel shock’, and perpendicular to the beam axis is the ‘Mach disk shock’. Between the barrel shock and the jet boundary is a viscous, heat conducting, non-isentropic region. Downstream of the Mach disk is a collision-free

region that gives the system its name. The position of the Mach disk x_M is given approximately by,

$$\frac{x_M}{d} = 0.67 \left(\frac{P_0}{P_b} \right)^{1/2}. \quad (2.14)$$

For diffusion-pumped systems, it is possible to have pressure ratios so large that the Mach disk lies outside the apparatus and there is a smooth transition from continuum to free-molecular flow.

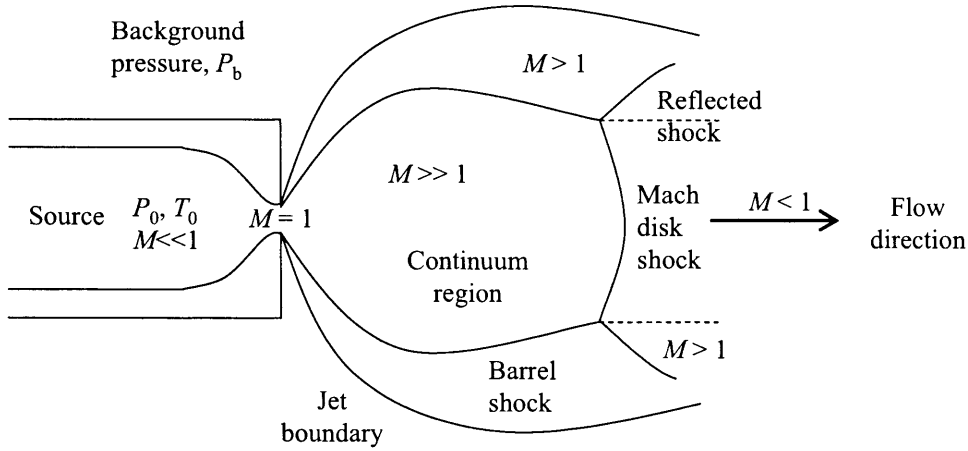


Figure 2.1 A cross-section of the continuum free-jet axis-symmetric expansion. For a short converging nozzle like this the flow is approximately isentropic with negligible viscosity and heat conduction. Approaching the nozzle, material is accelerated by the diminishing area from very low velocity within the source to the local speed of sound. Once outside the nozzle the acceleration continues as the gas expands (continuum region). Eventually the flow decelerates to local conditions by developing regions of shock. Adapted from [1].

Since most molecular beams are ‘used’ far downstream from the nozzle it is useful to know the characteristics of the expansion in that region. In addition to the terminal temperatures and densities, a useful parameter to come out of this analysis is the terminal speed ratio – the mean terminal velocity divided by the spread in velocity. Beijerinck and Verster [2] have correlated the terminal speed ratio to the source conditions,

$$S_{\parallel\infty} = A \left[\sqrt{2} n_0 d C^{1/3} \right]^B, \quad (2.15)$$

where A and B are parameters dependent on γ , n_0 is the number density of particles in the source and d is the nozzle diameter. C is the collision cross section, which for heated sources like ours, can be taken as $\pi\sigma^2$, where σ is a hard-sphere cross section. From $S_{\parallel\infty}$ the parallel temperature can be calculated. In the molecular free-flow region the average terminal perpendicular speed ratio can be expressed as,

$$S_{\perp} = \frac{V}{\sqrt{2kT_{\perp}/m}}. \quad (2.16)$$

For an expansion of a mixture of light and heavy molecules with a given average velocity V and perpendicular temperature T_{\perp} , the lighter component will have smaller S_{\perp} .

The centreline characteristics of the expansion are the most important for molecular beam systems because this section is often skimmed off and used downstream. The ideal centreline intensity I_0 can be calculated from the flow rate through the nozzle [2],

$$I_0 = \frac{\kappa\dot{N}}{\pi}, \quad (2.17)$$

where κ is a gas-dependant peaking factor. $\dot{N} = \dot{m}/WN_{av}$ where, from equations (2.7) to (2.9) the mass flow rate is,

$$\dot{m} = P_0 A^* \left[\frac{\gamma W}{RT_0} \left(\frac{2}{\gamma+1} \right)^{\gamma+1/\gamma-1} \right]^{\frac{1}{2}}, \quad (2.18)$$

which gives,

$$\dot{N} = F(\gamma)n_0 \sqrt{\frac{2kT_0}{m}} \left(\frac{\pi d^2}{4} \right), \text{ and } F(\gamma) = \left(\frac{\gamma}{\gamma+1} \right)^{\frac{1}{2}} \left(\frac{2}{\gamma+1} \right)^{\frac{1}{\gamma-1}} \quad (2.19)$$

where $A^* = \pi d^2/4$ is the effective nozzle area, which is significantly smaller than its physical area.

B. SODIUM ATOM AND DIMER EXPANSIONS

Real systems exhibit deviations from ideal isentropic expansion because the approximations it uses are incomplete. Firstly, as the collision rate falls, non-

equilibrium kinetic effects within the continuum region alter the temperature and velocity distributions. Secondly the beam intensity is usually reduced from ideal by scattering from background gas molecules, and by the presence of skimmers. Finally co-expansion of gas mixtures presents another set of properties. Since we have been concerned with constructing a sodium atom and dimer molecular beam, discussion of non-ideal effects in the expansion are confined as far as possible to sodium and the other alkali metals.

The continuum approximation in the isentropic supersonic expansion depends on the collision rate being high enough to maintain equilibrium. As the collision rate falls the equilibrium (and continuum) assumption fails and velocity and temperature distributions are altered from equilibrium. The continuum model can be used to estimate where in the expansion non-equilibrium effects start to appear. Since most atomic and molecular beams are ‘used’ in the molecular free-flow region it is the terminal velocity and temperature distributions that are of interest. Their determination requires solution of the Boltzmann equation for the velocity and temperature in the expansion taking account of the changing collision rates. Both calculations and experiments have found the velocity distribution in the direction parallel to the expansion to be more or less Gaussian. Velocity perpendicular to the expansion is distributed in a double Gaussian: one forming a sharp peak and the other a broad tail [1, 2].

C. CLUSTERING

The two most important kinetic effects for the current study are clustering and internal energy relaxation. It was noticed early in the use of molecular beams that the dimer concentration in supersonic expansions is increased above equilibrium levels [3]. This offers greater signal intensities for molecular beams over closed cells for spectroscopic studies. The equilibrium dimer fraction, such as might occur in a heated closed cell, can be calculated from its tabulated vapour pressure. Atomic and dimer vapour pressures tabulated by Nesmeyanov [4] are commonly referenced in the literature and are plotted in figure 2.2. Alternatively the dimer fraction can be calculated from the thermal equilibrium constant for dimer formation. The equilibrium

constant can be calculated from atomic vapour pressure data and the X $^1\Sigma_g^+$ state of Na_2 [5, 6],

$$K_{eq} = \frac{g_X}{g_{3S_0}} \int_0^\infty \exp\left[\frac{-V_X(R)}{kT}\right] \Gamma\left(\frac{3}{2}, V_X/kT\right) d^3R, \quad (2.20)$$

where g_X and g_{3S_0} are the multiplicities of the molecular and atomic states, $V_X(R)$ is the X $^1\Sigma_g^+$ potential, and $\Gamma\left(\frac{3}{2}, V_X/kT\right)$ is the normalised incomplete gamma function.

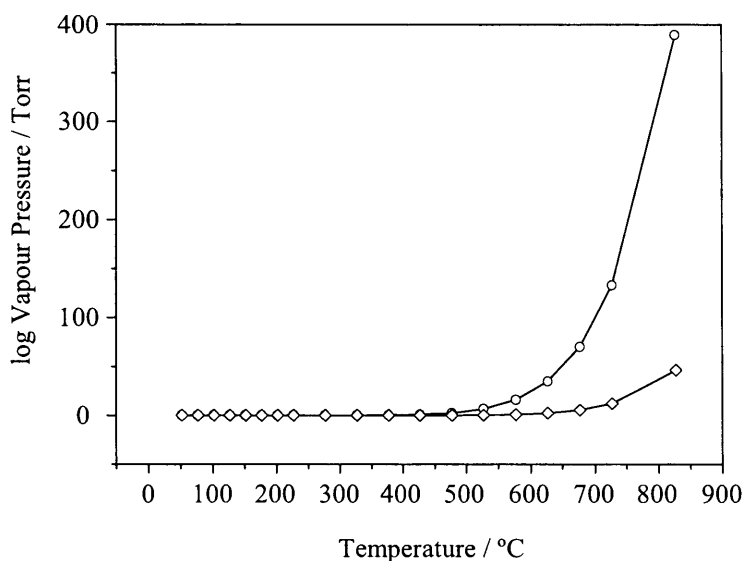


Figure 2.2 Equilibrium vapour pressure of sodium atoms and dimers as a function of temperature from [4]. Na data is indicated by circles, Na_2 is represented by diamonds.

Gordon, Lee and Herschbach [3] performed a detailed study of the oven pressure and nozzle diameter dependence of alkali metal (Rb and Cs) dimer fraction in molecular beams with high source pressures. Their short converging (approximately ideal) nozzles ranged in diameter from 0.04 mm to 0.16 mm, and the source pressure was varied from ~ 0.3 mbar to ~ 470 mbar by changing the oven temperature from ~ 500 K to ~ 880 K. Their experiment measured the frozen (terminal) atom and dimer intensity and velocity approximately 80 cm downstream from the nozzle. The dimer fraction was found to increase with nozzle diameter and oven pressure, levelling off at a maximum of $\sim 5 \times 10^{17} \text{ sr}^{-1} \text{ s}^{-1}$ due to scattering from background metal atoms. For larger nozzles the dimer fraction increased faster with oven pressure than for smaller ones. The dimer fraction fell slightly when the nozzle temperature was more than 70°C greater than the oven. Optimising these conditions allowed generation of 30% mole fraction dimers. Higher order clusters were found to have $< 1\%$ fractions. Zare *et al.* [7] reported a

dimer fraction between 15% and 45% for a similar experimental arrangement. The concept that dimers are formed in the expansion is supported by the work of Whitehead and Grice [8]. Their crossed beam experiments on reactive collisions between alkali dimers and different alkali metal atoms showed that the formation of dimers is highly favourable.

In reference [7] the parallel velocity distributions of the atoms and dimers were both very sharp, corresponding to translational temperatures of 26 K and 37 K respectively. There was a small velocity ‘slip’: the atom and dimer velocities differed by only about 1%, with the dimer having a slightly lower velocity and slightly narrower distribution. The velocities, and therefore terminal Mach numbers, increased with nozzle diameter and oven pressure, again the pressure dependence being steeper for the larger nozzles. Significantly for the current work, the terminal velocities of the atoms and dimers did not exceed the isentropic limit. This indicated that the heat of condensation of dimers was not transferred to the expansion and must therefore have remained as vibrational excitation of the dimers.

The process of dimer formation was modelled by Gordon *et al.* as a two step process [3, 9], valid under equilibrium or expansion conditions, where a ‘virtual-orbiting collision state’, A_2^* , is stabilised by collision with a third body M,



where M can be another A atom or a carrier gas atom. The forward and reverse rate constants, k_f and k_r , scale as $P_0 d^2$ and $P_0 d$ respectively [1] so increasing the nozzle diameter strongly favours dimer formation, but of course also increases the required pumping speed.

Knuth [9] used the ‘quitting surface’ or ‘freezing surface’ analysis of expansions of rare gases to correlate terminal dimer mole fraction to parameters and measurable quantities of the system, such as the nozzle diameter and temperatures in the expansion. Thus the dimer fraction x_{A_2} is given by,

$$x_{A_2} \approx 0.5 \left[n_0 \sigma^3 (\varepsilon/kT_0)^{\frac{7}{5}} (d^*/\sigma)^{\frac{2}{5}} \right]^{\frac{5}{3}}, \quad (2.23)$$

where n_0 is the source number density, σ is the zero-potential interaction radius, ε is the potential-well depth of the dimer, d^* is the effective source diameter, k is the

Boltzmann constant and T_0 is source temperature. While this expression was not applied to either alkali metals or heated sources, there was no indication that it cannot be, and given the wealth of data available on sodium potential energy curves, it seems potentially useful.

The dimerisation process in the continuum region of a nozzle expansion of sodium was studied by laser-induced fluorescence by Aerts and co-workers [10, 11]. Fluorescence from a small range of rovibrational transitions in the $B \ ^1\Pi_u - X \ ^1\Sigma_g$ excitation were studied in an expansion from a 0.5 mm nozzle at 800 K into a vacuum of $\leq 10^{-6}$ mbar. This work indicated that dimerisation was almost complete within the first 0.7 nozzle diameters of the expansion and that higher source pressures lead to higher dimer fractions at large distances from the nozzle.

Experiments using time-of-flight mass spectrometry with optical pumping by Bergmann, Hefter and Hering [12, 13] revealed that the velocity of dimers in a pure sodium expansion is strongly correlated with the internal energy. The vibrational ground state was found to have a higher terminal velocity than the atoms, whereas higher rovibrational states had lower velocity and a wider velocity distribution than lower lying states, corresponding to a fall in the speed ratio with vibrational excitation.

A laser-induced fluorescence (LIF) study conducted further out in the expansion [14] found that for $P_0 d < 1$ the off-axis dimer population decreased with increasing $P_0 d$ and with increasing internal energy of the dimer, whereas for $P_0 d > 1$ the situation reversed. The dependence on source conditions indicates that molecules formed in the expansion, as opposed to those formed inside the nozzle, have excess kinetic energy and rapidly move away from the beam centre. More highly excited molecules move further from the axis, leaving the beam centreline populated by molecules in low vibrational states. Molecules formed in the oven or nozzle are more likely to be found in the beam centre. Of the high percentage dimer fractions (15% to 45%) reported by Zare *et al.* [7], between 2% and 17% were estimated to have formed downstream of the nozzle respectively.

Measurements of fluorescence polarisation from dimers in a sodium expansion showed that there is partial (around 10 %) alignment of the molecular angular momentum perpendicular to the flow direction [15]. The degree of alignment was found to increase linearly with the logarithm of oven pressure. This was explained by

Visser and co-workers [16] in terms of the molecule – atom interaction potential and their relative velocities. The potential is anisotropic for a diatomic molecule so the scattering cross section depends on the orientation of the molecule to the relative velocities of the molecule and atom (or another molecule). Lower vibrational states were found to align more strongly; an observation attributed their velocity more closely matching that of the atoms.

D. QUANTUM STATE DISTRIBUTION

The quantum state distribution in sodium dimer expansions has been studied widely. Gordon *et al.* [3] and Whitehead *et al.* [8] both interpreted the absence of translational excitation to indicate the energy of bond formation must remain as vibrational excitation. The work of Aerts *et al.* [10] on the very start of the expansion (out to 1.5 nozzle diameters) showed that, on the contrary, dimers were not formed in highly excited vibrational states, but were Boltzmann distributed about the equilibrium temperature. Further away from the nozzle the distribution became non-Boltzmann as the collision rate fell. Work by the same group [17] revealed that low vibration and rotation states reside in the beam centreline, whereas higher lying states have angular distributions that broaden with v and J . These propensities are amplified as the source pressure increases.

Sinha, Schultz and Zare [7] measured the vibrational and rotational state distribution of the ground state of Na_2 as a function of nozzle diameter and source conditions using white light and laser-induced fluorescence. No evidence was found for highly excited vibrational states. In fact the optimal beam, emanating from a 0.5 mm nozzle at 970 K had a vibrational temperature of 153 ± 5 K and a rotational temperature of 55 ± 10 K. The state distributions were found to be insensitive to source pressure.

Fluorescence studies on the source pressure dependence of rovibrational state occupancy by Visser *et al.* [16] indicated that at low source pressures dimers were formed vibrationally excited, but cooled efficiently as the source pressure increased.

E. INTERNAL ENERGY RELAXATION

In addition to generating nearly collision-free environments, cooling of rotational and vibrational degrees of freedom in supersonic expansion makes them highly attractive as a spectroscopy tool. If the molecules are in a much smaller number of rotational and vibrational states than room temperature or, in the case of alkali metals, elevated temperatures then experimental signals are likely to improve.

Most of the collisions in a free jet expansion occur within the first few tens of nozzle diameters from the nozzle. The collision rate for two body collisions falls off rapidly with distance and scales as $P_0 d/T_0$. Molecules in a typical supersonic expansion will undergo in the region of 100 to 1000 collisions before the flow becomes free-molecular. The key question is how far will rotational and vibrational degrees of freedom relax before collisions cease and they ‘freeze’? Rotations of a small diatomic molecule require between 10 and 100 collisions to relax, so rotational cooling is extensive [1].

Vibrational cooling of a diatomic will take approximately 10^4 collisions to relax [1], so might not be expected to occur in typical supersonic nozzle expansions. However the failure to observe any evidence of highly excited vibrational states in, for example, the LIF experiments discussed above lead Bergmann *et al.* to conclude that molecules formed in the expansion convert their heat of formation to kinetic energy in a very efficient cooling mechanism [12].

The details of rotational and vibrational relaxation in Na/Na₂ expansions have been studied by several groups [18-20]. Kompitsas and co-workers [21] excited the 3²P state of atomic sodium and analysed fluorescence from B ¹Π_u → X ¹Σ_g⁺ of Na₂ excited by collisions with the excited atoms. A strong correlation was observed between the oven temperature, i.e. source pressure and thus density of collision partners, and population of higher rovibrational states. The collision rate fell off very fast with distance from the nozzle: a molecule made less than one collision once it travelled more than a nozzle diameter from the nozzle. From such low collision rates it was concluded that each collision must involve a large exchange of energy, probably by reactive collision, but possibly also non-reactive inelastic collision.

Aerts, Hulsman and Willems [18] studied relaxation of vibration and rotation along the molecular beam axis from the nozzle (in the equilibrium region) to far out in

the molecular free-flow region using LIF of several rovibrational states. The population of states was found to be Boltzmann distributed in the continuum region, becoming non-Boltzmann as the collision rate fell with distance. Everywhere in the expansion, higher vibrational and rotational states were less populated. Populations of lower internal states were found to be fairly constant along the beam axis, whereas for higher states it fell with distance. The decrease was faster for higher states. Effective inelastic collision cross-sections were enumerated and found to increase with the source pressure (and therefore with the gas density) and collision number. The change in internal state population was found to occur gradually with distance from the nozzle, not abruptly at a shock structure, for their experimental conditions. Nonetheless Gundlach *et al.* [19] analysed translational and rotational relaxation in a Na/Na₂ expansion in terms of a ‘sudden-freeze’ model. In this picture the expansion is divided into two regions: the continuum region where collisions are common and relaxation is efficient, and the free-molecular flow region where there are negligible collisions, no relaxation and the internal states are ‘frozen’. The transition from continuum flow to frozen flow is abrupt and described by a surface lying some distance from the nozzle orifice. Although apparently a significant approximation, the experimental data can be well modelled using it.

F. MIXED EXPANSIONS: THE ROLE OF THE CARRIER GAS

Binary collision rates scale as P_0d so can be adjusted to increase cooling to some extent [1]. A more useful method though is the use of mixed species expansions. The ideal continuum expansion can be cast in terms of molar average heat capacity $\bar{C}_p = \sum X_i C_{pi}$ and molecular weight $\bar{W} = \sum X_i W_i$, where X_i is the mole fraction. This gives $\hat{C}_p = \bar{C}_p / \bar{W}$ in equations 2.4 and 2.6. Equation 2.6 shows that the terminal velocity depends inversely on the molar average mass if C_{pi} and γ_i are equal and constant. The practical consequences are that expansion of a heavy gas can be accelerated by a light one, creating a narrower velocity distribution, or a light gas can be slowed down by addition of a heavier one. A heavy carrier gas added to the sodium expansion extends the equilibrium region further from the nozzle, leading to more collisions and increase vibrational and rotational cooling.

Pritchard *et al.* [22] reported a 30 % dimer fraction of Na_2 in sodium expanding through a 70 μm nozzle from an oven at 800 $^\circ\text{C}$ ($p_{\text{Na}} \approx 400$ mbar) with argon or krypton at 2670 mbar as a carrier gas. These conditions correspond to $P_0d = 21.5$ mbar cm. Although the vibration and rotation temperatures were not reported, the beam was described as cold and the dimer fraction was used in molecular interferometry, which suggests high population of a few rovibrational states.

Bergmann *et al.* [23] reported a sodium dimer source operated at 930 K (giving a sodium vapour pressure of 65 mbar) with 500 mbar argon as a carrier gas and expanded through a 0.2 mm diameter orifice. This gave estimated translational, rotational and vibrational temperatures of 10 K, 30 K and 70 K respectively.

Very recently, Vigué *et al.* [24] discovered lower than expected parallel velocity distribution for an expansion of lithium in argon at low lithium densities. If the effect they report scales linearly with the mass of the seed molecule, it suggests krypton or xenon might be a more suitable carrier than argon for sodium expansions where vibrational and rotational cooling are desirable.

Data on alkali metal seeded beams of rare gases is surprisingly scarce in the literature. It may be possible to make use of a model proposed by DePaul and co-workers [25] for mixed gas expansions. Their objective was to provide convenient expressions for important beam quantities such as terminal temperatures, velocity slip, enrichment and beam intensity without recourse to complex numerical methods. They applied their model to the expansion of iodine diluted by rare gases and demonstrate excellent agreement to experiment. It would be very interesting to adapt this approach to our system.

G. SKIMMERS

A skimmer selects a small diameter sample from the centreline of an expansion to isolate it from the rest of the expansion. This is done mostly to move the sample to a region of lower pressure where it can be utilised without interference. In principle a skimmer can be any small aperture but usually skimmers are approximately conical, thin-walled structures with sharp-edged orifices.

Three characteristics of the skimmer require attention: its shape, its position in relation to the nozzle and beam target (a detector or, in our case, lasers), and its

diameter. Campargue [26] argued that for molecular beams operating with low background pressure, such as diffusion pumped systems, the internal and external angles of the skimmer have weak effects on the beam intensity downstream. This is because the low pressure means there is little scattering off the inside of the skimmer, and there are only infrequent collisions within the beam because it is cold. Miller agrees [1] but considers gas molecules scattered into the centreline before the skimmer, and suggests long narrow skimmers with total exterior angles of around 30° .

The optimum position for a skimmer depends on several factors, including the allowable flux of material into the second chamber, the beam divergence after skimming, and interference from material scattered into the expansion before skimming. Broadly, skimmers can be placed in one of two regions of the expansion: in the continuum region, in which case the system is described as a Campargue type source; or in the free-molecular flow region, when it is called a Fenn type source. Most sodium sources for atoms or dimers are of the latter type.

The effect of a skimmer on the intensity of an atomic or molecular beam can be understood by consideration of the perpendicular velocity components in the expansion. In the molecular free-flow region the average terminal perpendicular speed ratio can be expressed as shown in equation (2.16). For an expansion of a mixture of light and heavy molecules with a given average velocity V and perpendicular temperature T_\perp . The lighter molecules have a smaller perpendicular velocity and spread more than the heavier ones. Therefore the intensity of lighter molecules downstream of the skimmer is lower than that of the heavier ones. Such fractionation is not expected to be a problem for an expansion of sodium dimers in argon as their masses are so similar, indeed it might be expected to concentrate dimers in the beam centre at the expense of sodium atoms. In addition, consider the effect of the wall on which the skimmer is mounted. Molecules that will not pass through the skimmer, but which have perpendicular velocities such that they *would* have reached the detector if there was no wall, are blocked by the wall, so the intensity at the detector falls. The effect of a skimmer on the centreline beam intensity I can be related to its ideal value I_0 for diffusion pumped systems by [1],

$$\frac{I}{I_0} \cong 1 - \exp \left[S^2 \left(\frac{r}{x_q} \right)^2 \left(\frac{x_d}{x_d - x_s} \right)^2 \right], \quad (2.24)$$

where S is the speed ratio at the quitting surface; x_q , x_s and x_d are the distances of the nozzle to the quitting surface, skimmer aperture and detector respectively. To include background interference a Beer - Lambert attenuation can be added in the form,

$$\frac{I}{I_0} = e^{-nQl}, \quad (2.25)$$

where n is the number density of background gas, l is the path length and Q is the total collision cross section.

Beijerinck and Verster [2] investigated the shielding effects of skimmers in expansions of rare gases, diatomics and small polyatomics, including the role of the skimmer diameter. They proposed that for monatomic gases the radius of a circular skimmer should be $20R_n$, and for a diatomic it should be $40R_n$, where R_n is the nozzle radius.

H. CONCLUSION OF INTRODUCTION TO MOLECULAR BEAMS

The expansion of gas to form a molecular beam is well understood. Beams of alkali metals and their dimers have been studied extensively. Important characteristics of these beams, such as their intensity, velocity, and temperatures of translation, vibration and rotation can be expressed conveniently in terms P_0d , the product of the source stagnation pressure P_0 and the nozzle diameter d . Likewise the roles of nozzle geometry, skimmer shape and position and detector position have all been investigated thoroughly and well characterised into simple expressions which the experimentalist can easily utilise. Molecular beam apparatus have a range of formats and configurations and there appears to be considerable latitude in the exact details that will generate suitable beams, notwithstanding the need to be able to attain high P_0d values. It should be noted that LIF experiments conducted near nozzles usually operate at low source pressures to avoid radiation trapping caused by the high density of sodium in that region. In general, LIF experiments can be operated at much lower particle density than we require.

2.3 OUR SODIUM ATOMIC AND MOLECULAR BEAM: SYSTEM OVERVIEW

Having reviewed the literature on sodium molecular beams, this section details the system we have developed, and continue to develop, for use in our coherent control experiments. It is convenient to consider our molecular beam apparatus in two parts: a sodium atom or dimer beam source and an attached experimental chamber. This is justified on the basis of their operating conditions and the way they are used, but slightly artificial in so far as they are closely interconnected. The sodium atom or dimer source comprises an oven mounted inside a diffusion-pumped vacuum chamber. Sodium vapour, and sometimes a carrier gas, expands through a small aperture in the oven into the surrounding vacuum. The central portion of the expanding vapour/gas is selected by a skimmer and passes into the experimental chamber. Within the experimental chamber the sodium beam is crossed by the laser beams at the base of a time-of-flight mass spectrometer. The mass spectrometer is fitted with a micro-channel plate detector sensitive either to ions or electrons. The layout of the beam source and experimental chambers is shown in figure 2.3

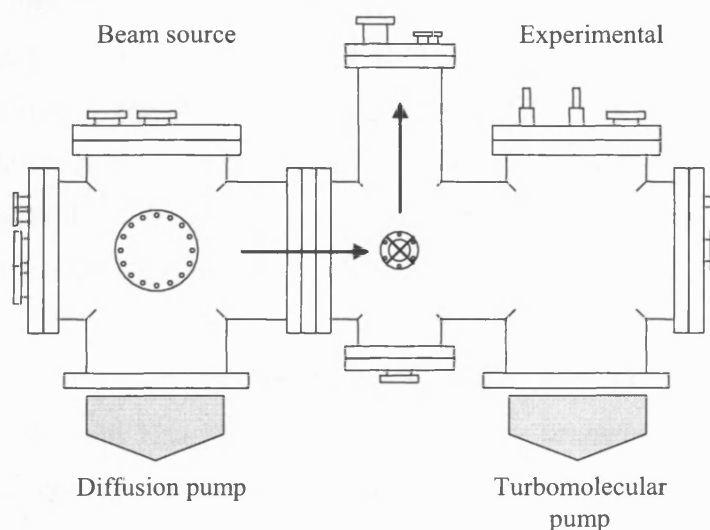


Figure 2.3 An elevation of the vacuum chamber, drawn to scale, showing the separate source and experimental chambers. The sodium oven lies horizontally in the left-hand chamber. The sodium atomic/molecular beam passes through a skimmer mounted on the flange between the chambers in the direction indicated by the horizontal arrow. The cross indicates where the laser beams pass through the experimental chamber coming out of the plane of the page. Ions or electrons travel vertically up a time-of-flight mass spectrometer (vertical arrow). The vacuum pumps are connected as indicated.

A. THE SODIUM OVEN

I. INTRODUCTION

Several classes of molecular beam sources for alkali metals appear in the literature and they are briefly reviewed here. The simplest consist of a cylindrical crucible with a hole in it through which sodium vapour escapes [27, 28]. More sophisticated designs include a simple [29] or complex nozzle assembly including high precision molybdenum apertures [30] that can be heated independently of the main body. The crucibles can be made from stainless steel or graphite and are heated using coaxial cable, tantalum-ceramic heaters, resistive heating of the crucible by a large direct current, or inductive heating by high frequency alternating current. These sources often allow for a carrier gas to be introduced into the space above the liquid metal to control the properties of the molecular beam. A high capacity development of this type of source was reported in [31]. The apparatus was constructed from 4.5 in. diameter Conflat standard parts (a T-piece and a cross) and included a skimmer. It was heated by mantles placed round the outside of the tubing and was attached to two diffusion pumps. This design could be easily included in or added to an existing vacuum system.

Similar systems are used where very large clusters are required [32, 33]. In these devices however the sodium vapour diffuses through a large aperture into a chamber filled with the seed gas (He). The mixture then passes into a 'condensation channel' where clusters form, before escaping into the vacuum chamber as a molecular beam.

The 'Candlestick' is a very elegant and apparently reliable design developed by Burns, Golovchenko and Hau [34]. An outer cylinder (outside diameter ~ 30 mm), heated at its base, contains a reservoir of liquid sodium. A thin inner tube lined with metal gauze wicks liquid sodium up its length by capillary action. The top of this tube is heated to a much higher temperature causing the sodium to vaporise and expand through a small hole in its side. A hole in the outer cylinder allows sodium atoms/dimers to pass through, forming a collimated molecular beam. Any atoms which miss this aperture are returned to the reservoir by wicking down another metal gauze. The outer cylinder insulates the high temperature heater from the outside. This design has also been used for rubidium [35].

A non-thermal source for a sodium molecular beam which also readily allowed for pulsing and mixed beams is laser ablation from a solid surface [36]. The surface was made by sputtering a mixture of Na and Au or Na and F to a depth of 1000-3000 Å on top of vacuum-evaporated vanadium (300 Å thick) on a fused silica glass slide. The molecular beam was formed by irradiating this surface with a Nd:YAG laser at 1.06 μm, 0.6-0.7 J cm⁻² with pulse length of 10 ns full-width at half-maximum.

II. SODIUM OVEN: PHYSICAL DESCRIPTION

We have opted for an oven comprising two independently heated cylindrical sections similar to one described by [37] and [3] and many others. This is not strictly a double-chamber design because the small and large diameter sections are not thermally isolated. Rather it is a single oven with a nozzle that can be held at a higher temperature (50 to 100 K) to prevent clogging.

The oven was machined to our specifications by VacWeld Ltd. from a single piece of 316 stainless steel. While this is an expensive approach it allows for thick walls and avoids welded joints, both features we felt would better withstand thermal cycling between room temperature and approximately 700 °C. The oven, complete with door, nozzle and heaters, is shown in cross-section in figure 2.4. The larger chamber on the left is a reservoir for liquid sodium. The narrower section on the right transmits the sodium vapour (or sodium vapour plus carrier gas mixture) to the nozzle. The dimensions of the reservoir were chosen so that it could hold enough sodium to run for a reasonable length of time before refilling. This is important because refilling is time-consuming; involving cleaning sodium off most of the inside of the vacuum chamber. Such cleaning was necessary because reaction of sodium with air forms hygroscopic products (probably peroxides) that, if not removed, might have made re-evacuating the chamber very slow. The level of sodium has to be kept below the smaller diameter section otherwise liquid metal will block the nozzle aperture. This limits the maximum volume of sodium that can be put into the oven to approximately 72 cm³. In practice the most sodium we put in the oven was about 25 cm³. On one occasion even this relatively small amount wetted the inside surface of the oven enough to reach the nozzle and block it.

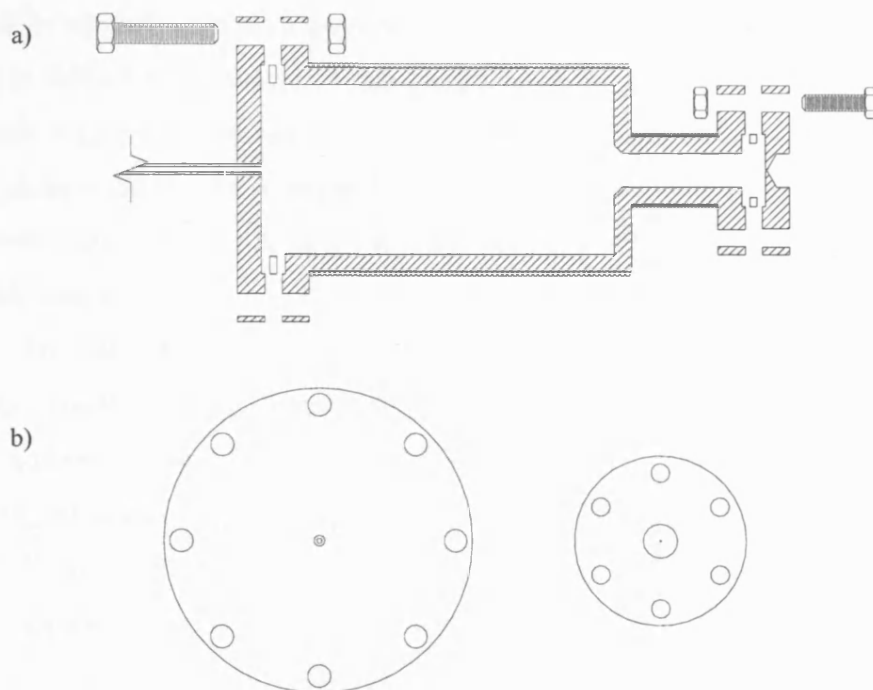


Figure 2.4 Scale drawing of the sodium oven. a) Cross-section through the sodium oven showing attachment of the nozzle and rear flange. The larger diameter section is the sodium reservoir. The narrower section to the right is referred to as the nozzle section. The walls of the whole oven are 5 mm thick throughout, except where the nozzle and rear flanges attach, where it thickens to 8 mm. The internal diameter of the reservoir is 50 mm, that of the nozzle section 10 mm. The reservoir and nozzle sections are 98 mm and 38 mm in length respectively. The small circles along the walls of the reservoir and nozzle section indicate Thermocoax heaters. b) shows outside views of the rear flange (left) and nozzle (right).

The thinner section of the oven has to be thin enough not to reduce the capacity of the reservoir but not so thin as to be readily blocked. The outer diameter of this section has to be big enough to wrap heaters round, but this was easily achieved by having thick walls. This section had to be long enough to carry a heater with sufficient power output to keep the nozzle hotter than the oven.

The oven is sealed at both ends by bolting on modified Conflat flanges (shown in figure 2.4b). For the reservoir this flange is a blank with a tube (1/8 in. outside diameter) welded into its centre to admit the carrier gas. When the carrier gas was not used this was sealed using a stainless steel Swagelok fitting. The knife-edges are the

same as for an 85 mm diameter Conflat (this is no longer a standard size flange) but the eight M6 bolt holes are on a slightly larger diameter (80 mm versus 72.4 mm), and the flange is thinner than normal (8 mm compared to the 16 mm standard). For the nozzle the knife-edges are standard DN16CF but there are eight M5 bolt holes instead of six M4, and they are also on a larger diameter (40 mm compared to 27 mm). In both cases this modification was made to allow clearance between the heater elements and the nuts and bolt heads.

The rear door and nozzle flanges are sealed using standard copper Conflat gaskets. The literature is contradictory on the effect of liquid sodium on copper gaskets. Some authors use copper gaskets [28] while others avoid them [38]. However the solubility of copper in liquid sodium is not very high [39]: 3.7 ppm at 385 °C, 5.0 ppm at 485 °C and 7.7 ppm at 530 °C. At no time did sodium ever noticeably corrode a copper gasket, and certainly these seals did not leak. Equally we have not seen evidence that copper contamination of the sodium was a problem for our experiments. To start with we used spectroscopic grade sodium (Aldrich 99.95%), breaking the phial inside the oven under an argon stream before sealing the rear door. This was replaced by reagent grade sodium (Aldrich 99%) when it was realised how quickly the sodium was exhausted during operation, and that in all probability the small contamination (< 1%) would not affect our experiments. In this case the oxidised surface of the sodium was cut off under the paraffin oil, kerosene or hexane in which the sodium is stored. The oil or hexane was rinsed off using ethanol before the sodium was put in the oven. This was done in air as an inert gas atmosphere was found to be ineffective at preventing re-oxidation. In any case the oxide appears to be refractory and remains in the oven when the sodium has been exhausted.

III. HEATING OF THE OVEN AND NOZZLE

Both sections of the oven were initially heated by Thermocoax mineral-insulated coaxial wire resistive heaters. The heaters comprised an Inconel (an alloy of 76% Ni, 17%Cr and 7% Fe) wire core and sheath separated by compacted MgO powder. The heater on the larger section of the oven had an outer diameter of 1.5 mm and a heating length of 315 cm. This heater dissipated a maximum of 700 W at 120 V, and was specified to heat the oven to 800 °C. There was an additional 100 cm of non-heating

wire on each end of the heating section. These ‘cold ends’ were not attached to the oven. A threaded stainless steel and ceramic connector was brazed onto each end of the wire for electrical connection. The heater for the smaller section of the oven was similar but only 1 mm in diameter. It had 100 cm of heating wire with 100 cm cold ends, and connectors like the larger heater. It produced a maximum power of 184 W at 42 V, and was specified to heat the nozzle to 850 °C. The smaller section is maintained at a slightly higher temperature (50 K to 100 K) to prevent the nozzle blocking.

Thermocoax heaters can be bent to very small radii and withstand very high power densities, but proved to be inappropriate for our first oven design. To prevent the high power density we required (approximately 4.5 W cm^{-1} for the reservoir) damaging the heaters, they were brazed to the outside of the oven using a high-melting nickel alloy (Nicobrase). Unfortunately, because we had to regularly remove the whole oven from the chamber, disassemble, clean, refill and reassemble it, the points of connection of the heater to the oven were constantly flexed, suffered fatigue and broke. Without specialised tools it is almost impossible to splice this type of coaxial cable, especially where it joins to a surface. Instead, the brazed-on remnants of the heaters were removed on a lathe and the heaters replaced. For the sodium reservoir a larger diameter (8 mm) coaxial heater was used. This was approximately one tenth the cost of a replacement Thermocoax heater and much more robust in these circumstances. It was first coiled around a slightly smaller cylinder then ‘sprung’ onto the oven to ensure good thermal contact. Connection to this heater is less convenient than the Thermocoax. The heating element protrudes about 30 mm from the end of the sheath and is threaded (4BA). Ring terminals can be retained between two nuts tightened on the thread to attach electrical power. This brings the connecting wires into close proximity with the heater and required that glass-fibre insulated cable be used. This is a workable solution but ceramic ‘fish spine’ beads would probably be better.

The smaller heater was replaced with a 2 mm diameter Thermocoax heater (SEI 20/100). This was thin enough to bend round the tube but thick enough to withstand more flexing than the 1 mm diameter heater. The heater was simply wound round the oven and held in place by a stainless steel worm-drive (Jubilee) hose clip. This fixing is more flexible than the brazed joint so there is less stress on the heater where it joins the oven. To stop the clamp damaging the heater, and to retain the whole heater winding, a

thin sheet of copper (*ca.* 1 mm) was placed between them. The replacement heaters have survived many cycles of filling, cleaning and refilling.

Power is supplied to the two oven heaters from the mains (240 VAC, 50 Hz) using two variable autotransformers (Carroll and Meynell CMV8E-1 and CMV5E-1 for the reservoir and nozzle heaters respectively). These are rated at 15 A and 8 A for the larger and smaller heaters respectively. The voltage supplied is measured on a voltmeter connected in parallel as shown in figure 2.5.

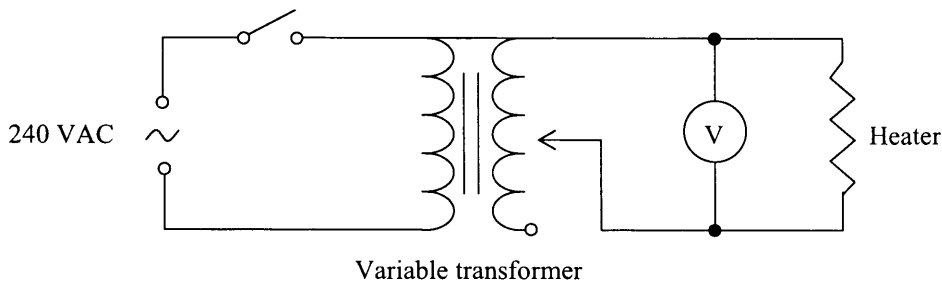


Figure 2.5 The circuit used to power the oven heaters. These are not isolating transformers so there is a danger of short circuit within the windings. Each heater has a separate power supply. The larger heater can withstand having full line voltage across it. The smaller heater is rated for a maximum of approximately 40 V so a 10:1 stepdown transformer (not shown) is connected in series with the autotransformer to prevent accidental overload.

The heater temperature is controlled by increasing the voltage applied to each heater until the desired temperature is reached. Typically it would take about one hour for the oven to stabilise at an operating temperature of around 600 °C.

Each section of the oven has a thermocouple attached near the centre of the heater to monitor the temperature. These have a coaxial construction much the same as the heaters and have the same respective diameters. The coaxial wire extends from the oven for 50 cm before a connection to 15 cm of PTFE insulated thermocouple extension wire. The pins from a standard miniature thermocouple connector have been attached to the ends of the extension wire. These are used to connect to a K-type thermocouple feed-through. Like the brazed-on heaters, the attached thermocouples snapped off and were replaced by loose ones of much the same construction. These are held in close contact with the heating elements.

We use K-type thermocouples formed by the junction of Chromel and Alumel. Chromel is an alloy of chromium (10%) and nickel (90%); Alumel is an aluminium

(2%), manganese (2%) and nickel (95%) alloy. These materials are the same colour but can be distinguished with a permanent magnet: Alumel is magnetic while Chromel is not. Thermocouple wires are colour coded: Chromel is green; Alumel is white. The connectors are marked for polarity: Chromel is positive; Alumel is negative; and colour coded for type: K-type thermocouple connectors are green. The temperature range for a K-type thermocouple is $-200\text{ }^{\circ}\text{C}$ to $+1200\text{ }^{\circ}\text{C}$ [40].

Temperature measurements using thermocouples measure the junction potential generated between two dissimilar metals in contact. The junction potential varies (non-linearly) with temperature by approximately $41\text{ }\mu\text{V K}^{-1}$. The temperature is found by comparing the measured potential against the known and tabulated behaviour of the thermocouple. It is not good practice to simply measure the voltage across a thermocouple as shown in figure 2.6. This is because where the thermocouple wires connect to the voltmeter two more thermocouples will be established. The measured potential is the sum of all the active thermocouples in the circuit. Since thermocouple potentials are small ($< 20\text{ mV}$ at 1000 K) incorrect potentials can give significant errors in temperature. There are two ways round this problem. The first is to add another thermocouple of the same type that is held at a known temperature. Thermocouple data tables give voltages for a circuit where the second thermocouple is held at $0\text{ }^{\circ}\text{C}$, figure 2.7.

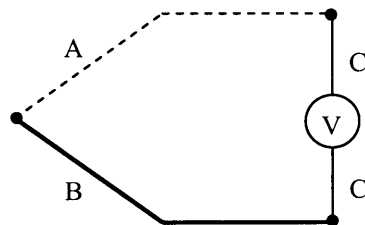


Figure 2.6 Circuit diagram for a single thermocouple. The voltage measured is the sum of the junction potentials of the thermocouple A-B at the temperature to be measured and the junctions A-C and B-C at a different temperature.

The second solution to the problem of unwanted thermocouples is as follows. If all the junctions in figure 2.6 are at the same temperature then the potentials from the AC and BC junctions is equal to the AB potential.

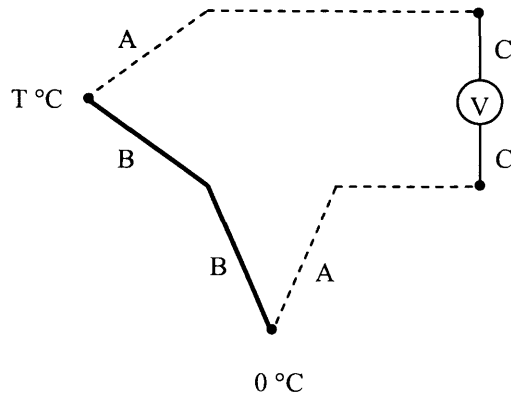


Figure 2.7 Circuit diagram for a cold-junction compensated thermocouple pair. An additional thermocouple means that it is the temperature difference between the temperature to be measured and the one held at 0 °C. The connections to the voltmeter (A-C junctions) cancel each other. Adapted from ref. [40].

This is because the intermediate metal (C) has no effect if all the junctions are at the same temperature. It is possible to measure the temperature of the AC and BC junctions with a thyristor or semiconductor transducer and subtract the potential expected for an AB thermocouple at that temperature from the measured potential. The difference is the potential of the AB thermocouple at the temperature being measured.

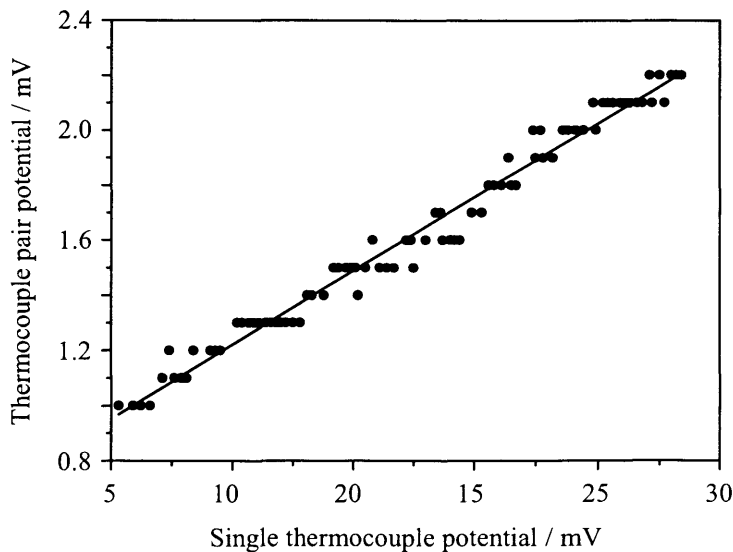


Figure 2.8 The potential difference between a single thermocouple and a pair of thermocouples (one of which was at 0 °C) plotted against the single thermocouple potential from root temperature to the operating range of the sodium oven (approximately 650 °C). The linear fit to the data can be used to estimate the correct temperature when measuring with a single thermocouple.

CHAPTER 2

We actually operated the thermocouples without a cold junction because, without using commercial thermocouple readers, it is more convenient. While this is poor practice it can be justified somewhat because it is more important for us to be able to repeat a particular set of oven and nozzle temperatures than to know exactly what the temperature is. Operated in this way there is an offset to the measured potential compared to the cold-compensated set up. This was measured on one occasion to quantify the error in our normal practice with a digital voltmeter on 2 mV and 20 mV scales. The results are shown in figure 2.8.

IV. OVEN SUPPORT

Like the oven heating, the way the oven is mounted inside the vacuum chamber has undergone several changes. The first arrangement is shown in figure 2.9. It was made to our specification by VacWeld Ltd. from 316 stainless steel.

The oven was fixed inside the vacuum chamber by two rings (10) which braced against the inside walls of the smaller vacuum chamber with six screws each (as shown in figure 2.13). The rings supported two horizontal rails (9) on to which the water-cooled jacket was bolted (8). The cooling jacket comprised two vertical end walls (3 and 4) supporting a cylinder (2) with a 1/4 in. diameter tube (11) tack welded round it for cooling water. The rear end wall (3) had a hole in its centre large enough for the oven to fit through. The front wall (4) had a 10 mm diameter hole in it aligned with the nozzle to act as a collimator. A coiled tube (1/4 in. outside diameter, not shown) was tack-welded onto the outside of this wall (4). Two rings bolted onto the inside of the cylinder suspended the oven (6 and 7). Where they touch the oven the edges of the disks were thinner to minimise conduction of heat away from the oven. Two rods (5) screwed into the front disk stopped the oven moving forwards in its mount. It was prevented from moving backward by two screw clamps in the rear disk (not shown). The tubing on the end wall and round the cylindrical section were connected together and the two remaining ends connected to a water feed-through so that mains water could be circulated round the oven support to cool it. These connections were made using stainless steel Swagelok compression fittings and required three additional lengths of tubing. All the connections were leak-tested before the chamber was evacuated.

In principle supporting the oven in this way allowed it to be aligned to point precisely to the interaction region. The horizontal rails had six sets of holes so that the oven could be positioned nearer or further from the interaction region as required.

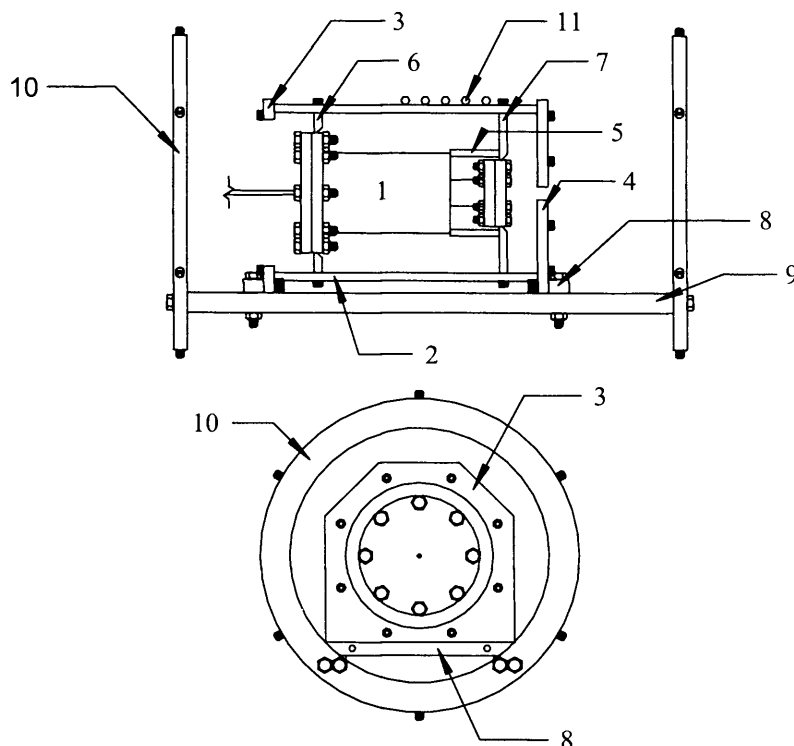


Figure 2.9 Side (upper) and rear end (lower) elevations of the first oven mount. Numbered parts are described in the text. The oven (1) is shown solid with the nozzle and rear flange in place, but without heaters. The large rings and horizontal rails (8, 9 & 10) and the oven depth stops (5) are shown solid. The end walls (3 & 4), oven support rings (6 & 7), cylindrical water jacket (2) and cooling water tubing (11) are shown in cut away.

Vertical adjustment and tilt, while not easy, was made by moving the bracing screws that hold the whole assembly in the vacuum chamber. Alignment was achieved by directing a HeNe laser beam into the diffusion pump chamber, through the nozzle and out of the far end of the experimental chamber. In practice this whole arrangement lead to very poor alignment and was abandoned in favour of one which allowed some adjustment from outside while the chamber was under vacuum.

The next oven support was developed to allow the oven to be aligned from outside the vacuum chamber. This was necessary because we started using a 1 mm diameter skimmer between the source and experimental chambers. The oven hung on a 1/4 in. diameter rod mounted on a commercial xyz manipulator (ThermoVacuum Generators

Miniax) as shown in figures 2.11 and 2.12. A home-made aluminium framework attached the oven to the rod.

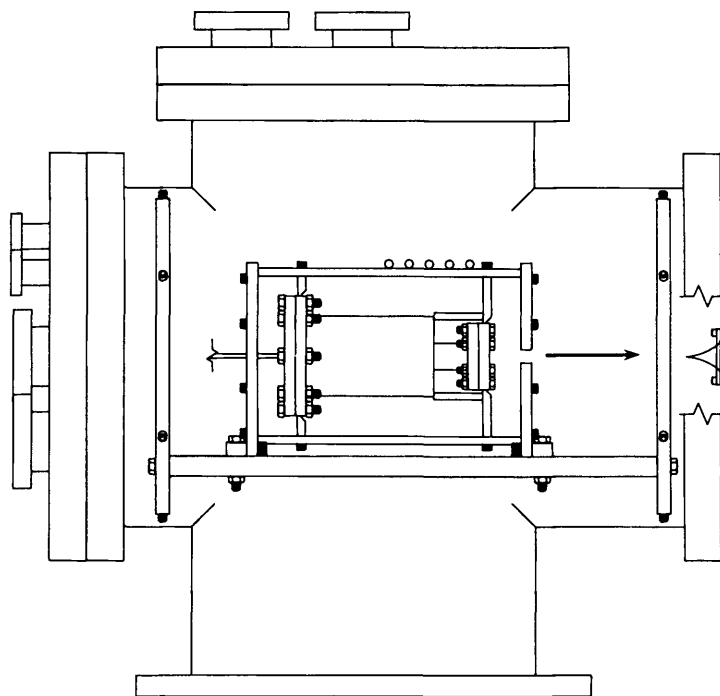


Figure 2.10 Positioning of the oven in its first mount in the source vacuum chamber. Only one half of the chamber is shown. The sodium beam travelled rightwards (as indicated by the heavy arrow) through the skimmer and into the experimental chamber. Connections for thermocouples and heater power were made through the cluster flange on the left. Cooling water for the oven entered through a flange directly in front of the oven (not shown).

Aluminium is too low melting ($660\text{ }^{\circ}\text{C}$) and too soft for this purpose but it was expedient to use it at the time and it worked quite well, indeed all the experiments carried out in atomic sodium (described in chapter 3) used it. Provided it was not badly misaligned in rotation about the suspension rod, moving the manipulator allowed the oven to be aligned adequately with respect to the skimmer. Clearly however there was no facility to correct errors of rotation or elevation. The distance between the nozzle and skimmer (shown in figure 2.12) could be moved only $\pm 12\text{ mm}$, which is not enough to be useful.

The rod on which the oven hung was kept thin to retain as much movement as possible, even though this made it prone to swinging if the chamber was knocked, susceptible to vibration and to being displaced by tension in the heater and thermocouple wires. There was no water-cooling inside the chamber so the outside of

the chamber became very hot. Eventually the bolts were pulled through the aluminium and it had to be discarded.

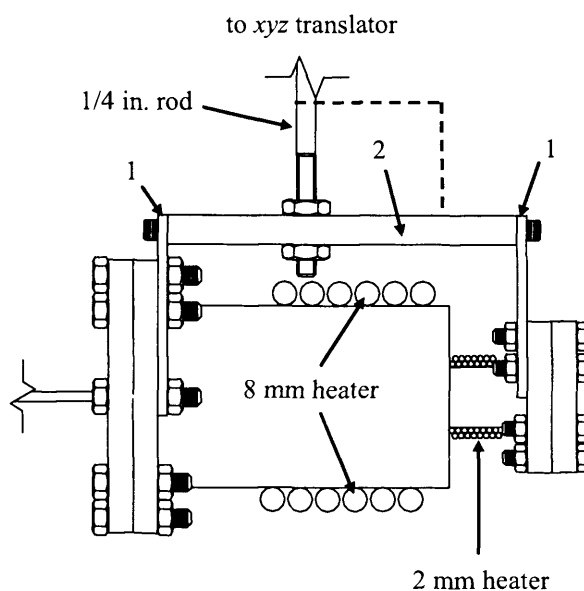


Figure 2.11 The sodium oven mounted on an xyz translator. The verticals (1) at either end of the oven were made from 1/8 in. thick aluminium and were retained by the oven sealing bolts. The horizontal beam (2) was also made from aluminium ($3/8 \times 1$ in.) and attached to the verticals with two M4 cap screws at each end. The 1/4 in. diameter vertical rod passed through a hole in the beam positioned in line with the centre of gravity to reduce its tendency to tip. Nonetheless the oven always had a slight front-down tilt. A second L-shaped bar was later added (dashed line) to stop the oven rotating around the 1/4 in. rod. The second generation of heaters (with diameters 8 mm and 2 mm) are shown in cross-section.

A final configuration was developed for sodium dimer experiments. It is described here as it is the on-going set-up but has been used relatively little to date. The objective was to reduce both the nozzle-skimmer distance and the skimmer-interaction region distance with a view to increasing the beam intensity in the interaction region. Figure 2.13 shows how this was achieved. Firstly the flange between the source and experimental chambers was replaced by a top hat shaped structure that projects towards the time-of-flight apparatus. This served to move the wall separating the two chambers towards the interaction region. The skimmer was attached to this wall (as detailed later) so the effect of this change was to move the skimmer closer to the interaction region.

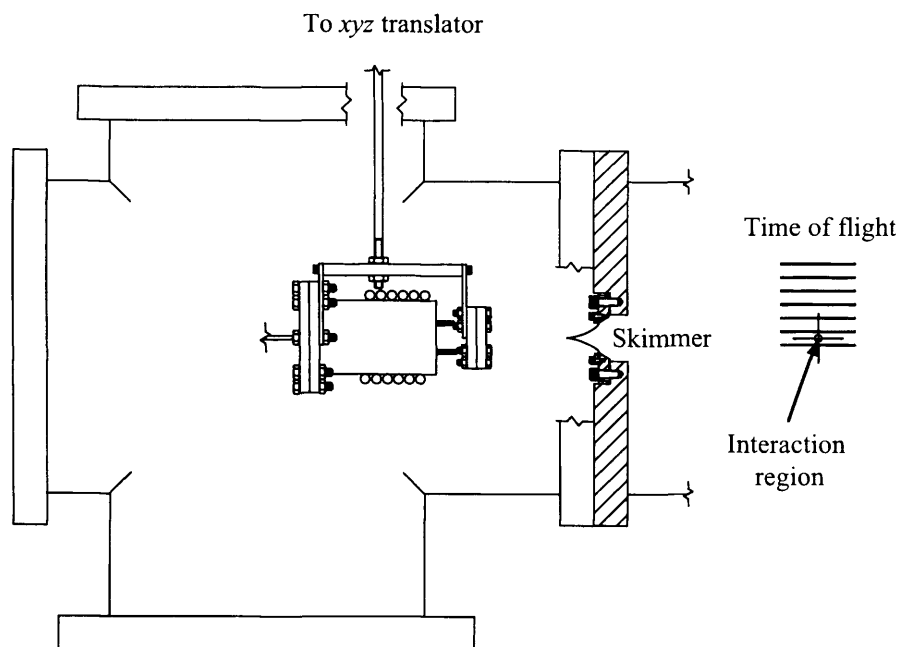


Figure 2.12 Cross-section of the sodium source chamber showing the position of the oven when suspended from an *xyz* translator (not shown) with respect to the skimmer and laser interaction region. The skimmer and its mounting flanges (hatched areas) are shown in cross-section.

Moving the skimmer closer to the interaction region meant that the oven also had to be moved. At the same time it was decided to reduce the nozzle – skimmer distance. The oven support made to achieve these objectives is shown in figure 2.13. The nozzle - skimmer distance was set to between 5 mm and 10 mm. At point (6) in the figure a vertical rod from an *xyz* translator attached to the frame. By moving the translator up and down or in and out of the page the nozzle could be aligned accurately with the skimmer.

Judging from the strong Na^+ ion signals and the sensitivity of the ion signal to adjustments of the *xyz* translator, this arrangement appears to be fairly effective. This is not surprising as the shorter nozzle-skimmer-interaction region distance can be expected to have increased the signal intensity, and the nozzle does not have to move far before the beam misses the skimmer completely. Pivoting the oven support at the rear and at such a large distance from the nozzle effectively removed misalignment of the molecular beam axis with respect to the skimmer. On the other hand, the top hat has a number of rather serious problems.

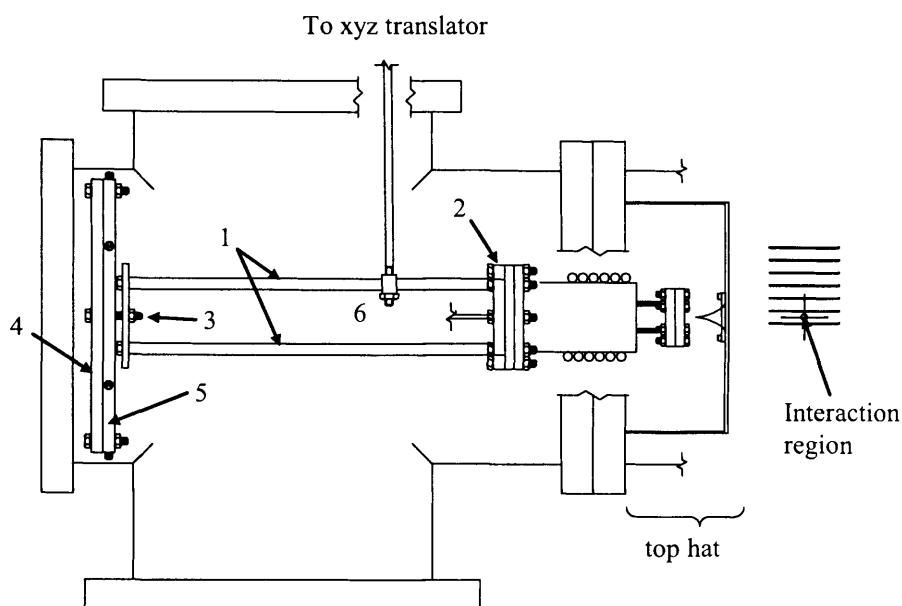


Figure 2.13 A partial cutaway of the source chamber showing the most recent oven support. The oven is projected toward the interaction region on four horizontal bars (1) screwed into a ring (2) that bolts to the back of the oven. The structure is pivoted at the central bolt (3) on the left and supported in the middle (6) by the vertical bar (shown cut) connected to an xyz translator (not shown). The pivot is formed from a bar (4) bolted across a ring (5) (see figure 2.12) braced by six screws against the inside of the vacuum chamber. On the far right is a section of the time of flight apparatus, shown to illustrate the nozzle – skimmer and skimmer – laser distances.

The pressure in the experimental chamber increased from mid 10^{-7} mbar to low 10^{-5} mbar, which is close to the maximum operating pressure of the MCP. It proved very difficult to get the oven in the chamber after refilling. Crucially for a configuration with the nozzle so close to the skimmer, there was no possibility to change the nozzle – skimmer distance while the oven was operational. The thin rod attached to the xyz translator was still susceptible to vibration and tension in the heater and thermocouple wires. Finally given the requirement for high nozzle throughput in sodium dimer experiments, extending the chamber with a narrower tube which is partially filled by the oven will have significantly reduced the pumping speed and raised the background pressure the sodium expands into. These are probably not ideal conditions for a sodium dimer beam.

III. THE NOZZLE

There are an enormous number of different nozzle designs for gas expansions in the chemical physics literature, varying in geometry and materials of construction. Nozzle materials span the range of metals from brass to stainless steel to molybdenum and tantalum. One group made a high temperature nozzle entirely from ceramics, using a ruby watch bearing for the aperture [41], another was cleverly heat shielded and water-cooled [42]. Nozzle geometries vary in sophistication from converging-diverging Laval nozzles to ideal short-converging nozzles, capillary nozzles and sharp-edged orifices. Laval nozzles are largely confined to cluster work and CRESU experiments [43], but they have also been used for sodium beams [44]. Gordon and co-workers [3] used approximately ideal (short converging) stainless steel nozzles made by electric discharge to study alkali metal dimer formation. Campargue found that ‘capillary’ nozzles give close to ideal expansion without clustering when $l/d \geq 2$, where l is the capillary length and d its diameter [26]. Capillary geometry also has the benefit of reducing the net flux in the beam in all but the direction along the nozzle axis [45]. Sharp-edged nozzles are often used because they can be readily made by laser or mechanical drilling, or chemical etching. These nozzles have the advantage of requiring lower source pressure to achieve the same throughput of material than do supersonic ones, but they can be mechanically frail and the number of collision occurring in the nozzle throat is reduced.

Murphy and Miller [46] studied the effects of nozzle geometry using Pitot tube pressure measurements as a function of position from the nozzle in a free-jet of argon. They compared the temperature profile, velocity and nucleation rate (which relates to collision rate) from the orifice to about 16 nozzle diameters away for a sharp-edged orifice, an ideal (short converging) orifice and a long capillary. All three gave similar translational temperatures, and Mach numbers, however the nucleation rates differed considerably. For the sharp-edged and ideal orifices there is no nucleation before the gas leaves the orifice. On the other hand nucleation peaks inside the capillary. Within the expansion the nucleation rate falls sharply with distance, fastest for the sharp-edged orifice and slowest for the ideal orifice by a factor of about 2. It seems likely that this will have implications for vibrational and rotational cooling in our work, and suggests a short-converging ideal nozzle geometry should be used.

In practice the choice of nozzle is influenced strongly by manufacturing constraints. The first nozzle we used was machined directly into the centre of a modified 316 stainless steel Conflat flange. To fit the smaller flange on the oven this flange had a standard DN16CF knife-edge but eight M5 clearance holes on a diameter of 40 mm instead of the standard six M4 holes on 27 mm. At the time this nozzle was made we were unable to find anyone able to drill hole less than 0.5 mm diameter in stainless steel. This drilling was also confined to making holes as long as they are wide. Consequently our first nozzle comprised a hole 0.5 mm long and 0.5 mm in diameter bored in the centre of the flange. The hole enlarged to 10 mm diameter on the outside as shown in figure 2.14. A positive feature of this design is that it was relatively inexpensive to replace – an important consideration as sodium is corrosive to stainless steel. Gerber has reported erosion of the nozzle after only a few hours of operation [47].

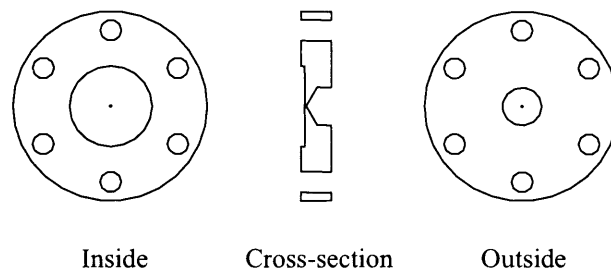


Figure 2.14 The first nozzle used in the sodium atomic/molecular beam source. The aperture was drilled directly into the flange used to seal the front end of the oven. Like the front flange of the oven, the knife-edges (not shown) are those of a standard DN16CF flange, but there are eight bolt holes on a diameter of 40 mm instead of six on 27 mm.

The 0.5 mm diameter nozzle proved to be too large. In the mean time a supplier called Lenox Laser Inc. was found who could laser-cut very small holes in all kinds of materials. They were able to produce 10 μm , 50 μm and 100 μm diameter holes in molybdenum disks 250 μm thick and 3/8 in. in diameter. Holes of these diameters can be photo-etched in molybdenum, but its thickness is limited to the hole diameter. We felt they would be fragile and difficult to seal.

To carry the thicker molybdenum disks one of the nozzles discussed above was modified as shown in figure 2.15. This nozzle is something of a hybrid. It is long compared to its diameter so it has some characteristics of a capillary nozzle, but the insert creates an approximately short-converging section.

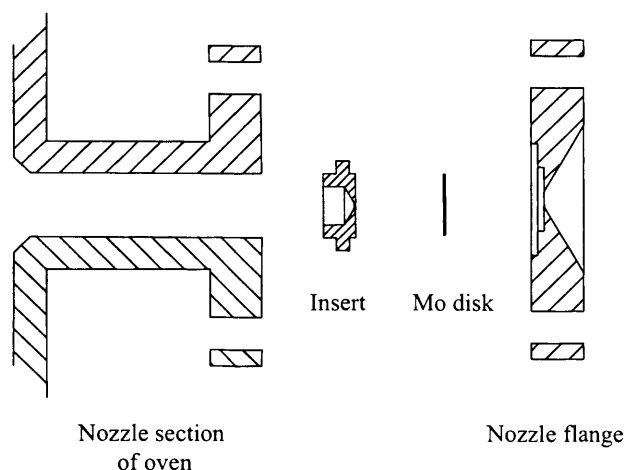


Figure 2.15 Cross-section of the holder for the 3/8 in. diameter molybdenum disk nozzle. The disk sits in a recess in the outer flange. It was compressed between the outer flange and a small stainless steel insert. The insert was made so that tightening the flange bolts formed a seal between the stainless steel and molybdenum faces, in addition to the copper gasket. The flange has the same dimensions as the nozzle described above, indeed it was made from one of them. In addition to the recess for the Mo disk, the outside of the flange was opened out to allow the sodium to expand freely.

The molybdenum aperture has worked extremely well. It has withstood many months of daily cycling from room temperature to about 650 °C. It shows no sign of having been etched by sodium. There was no evidence that sodium leaked between the molybdenum and the stainless steel. However, some sodium did appear to leak round the outside of the insert. This could be remedied easily by placing a tantalum gasket between the insert and the oven [3]. The only other improvement would be to better accommodate the different thermal expansion coefficients of stainless steel and molybdenum. The disk has become embedded in the edge of the recess it sits in and its front face is slightly bowed outward. Embedding could be simply rectified by enlarging slightly the diameter of the recess.

A third nozzle variation, shown in figure 2.16, was briefly tested but its behaviour remains mostly unknown, but it did appear to deposit a smaller diameter of sodium on the chamber wall. In an attempt to initiate more dimerisation at lower source temperatures and nozzle throughput, an approximately Laval nozzle was made. The nozzle was machined directly in a flange used to seal the front end of the oven in the same way as the first nozzle we used (figure 2.14). The flange was made by the UCL Chemistry mechanical workshop and bored by Drill Service Ltd.

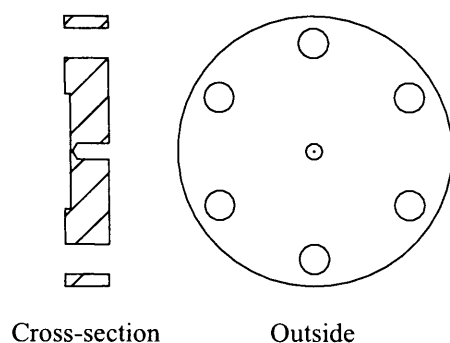


Figure 2.16 Cross-section of the nozzle currently under test in our system. It approximates a Laval nozzle but has no internal converging section. It was machined directly into a stainless steel blank flange made to fit on the front of the oven. The nozzle aperture is 250 μm in diameter and opens out to a 3 mm diameter section approximately 6 mm in length.

IV. THE SKIMMER

Our first designs did not include a skimmer in the normal sense of the term. Instead we used a simple collimator placed in the centre of the wall separating the source and experimental chambers. Kappas and Leutwyler [48] report a liquid nitrogen cooled collimator comprising an array of disks of decreasing diameter arranged perpendicularly to the beam axis to collimate a lithium expansion. It condenses all but the central portion of the expansion, which is transmitted to another chamber. Gordon *et al.* [3] used a simpler collimator to investigate dimerisation in rubidium and caesium. Three disks with central holes of diameter 6.2 mm, 3.1 mm and 3.1 mm were positioned 30 mm, 50 mm and 110 mm from the nozzle respectively. This was used instead of a skimmer to avoid having to put the nozzle about 1 mm from the skimmer, and fabricate a nozzle with an aperture of about 100 μm diameter, which they thought would become blocked. Liquid nitrogen cooling of this collimator was found to significantly increase the dimer intensity, an observation attributed to reduced interference by molecules scattering of it.

Our collimator was perhaps a little too simple, comprising a commercial Conflat flange (Thermo Vacuum Generators DN35CF) with a bevelled 10 mm diameter hole bored through its centre. Figure 2.17 shows the geometry of this collimator. It was mounted in the centre of the flange separating the source and experimental chambers.

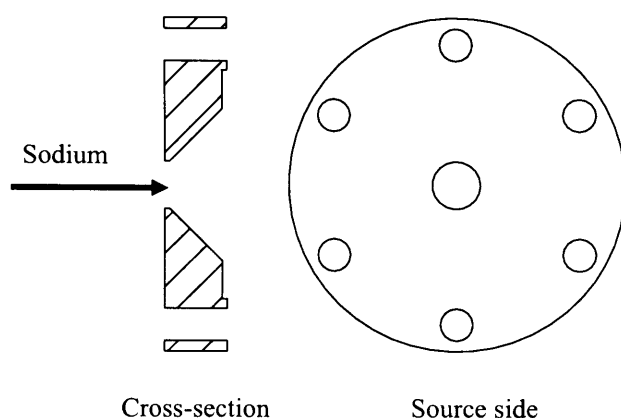


Figure 2.17 The collimator used to reduce the flux of sodium into the experimental chamber shown in cross-section (left) and from the side facing the sodium oven (right). The collimator was bolted into the centre of the flange separating the source and experimental chambers (see figure 2.15). The sodium approached the collimator from the left of the cross-section.

The aperture diameter of this collimator was much too big for this system, especially when used in conjunction with the 0.5 mm diameter nozzle, as it allowed too much gas into the experimental chamber. It was replaced with a nickel skimmer of the design of Gentry and Giese [49], purchased from Beam Dynamics Inc., with the dimensions shown in figure 2.18. The skimmer is designed to project into the impinging beam and sample only the central portion, which is then isolated from interference from the rest of the expansion. The exact shape is a compromise between a small external angle at the orifice facing the beam and a wide angle on the down-stream side. The small external angle ensures that the shock wave at the orifice is ‘attached’. The large internal angle minimises beam intensity loss by scattering off the inside of the skimmer. The thin walls of this skimmer are an excellent realisation of these conflicting requirements. The orifice rim is electrochemically sharpened to minimise scattering of impinging atoms and molecules. The polished surface resists any build up of beam material during operation. After running the system for several weeks at a time we would find the shiny surface of the skimmer only slightly dulled by a coating of sodium. The skimmer mount on the other hand was always coated in several millimetres of sodium.

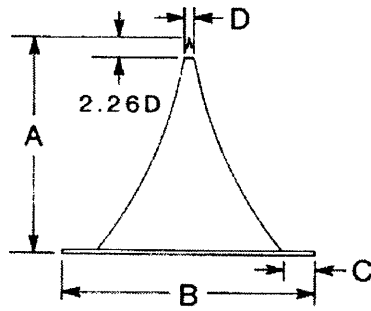


Figure 2.18 A dimensional drawing of the Beam Dynamics Model-2 nickel skimmer. $A = 25.4$ mm, $B = 27.9$ mm, $C = 2.5$ mm (rim width), $D = 1.0 \pm 0.05$ mm. The height is reduced by 2.26 times the orifice diameter, D . The wall thickness is $50 \mu\text{m}$ to $80 \mu\text{m}$ and the orifice edge thickness is less than $10 \mu\text{m}$. The internal and external angles at the orifice are 25° and 30° respectively. The angle at the base is 70° . Image reproduced from the manufacturer's web site: <http://www.beamdynamicsinc.com>.

The skimmer was mounted in place of the collimator, clamped to a modified DN35CF flange, shown in figure 2.19. Clearly the structure of the skimmer means that it must be treated with great care. The body is fairly robust and it has survived quite large pressure differences across it. It was routinely operated with 1×10^{-4} mbar difference in pressure, and occasionally 1×10^{-3} mbar. While venting and pumping down from atmospheric pressure care was taken to keep both sides of the skimmer at approximately the same pressure. The sharpened tip is easily damaged by any contact. The manufacturers report that damage to the tip of a skimmer has a very deleterious effect on its performance.

When the source chamber was modified to reduce the nozzle-skimmer and skimmer-laser distances, the skimmer was clamped directly to the wall separating the chambers by a ring shown in figure 2.13, but without the intervening 70 mm Conflat that is shown in figure 2.19.

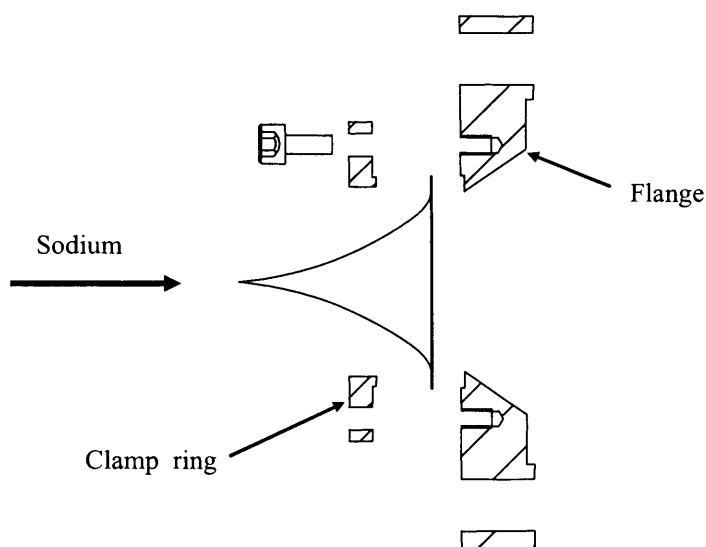


Figure 2.19 A cross-section of the mounting assembly for the skimmer. The base of the skimmer sits in a recess 0.5 mm deep to centre it in the larger flange. It is clamped down by a stepped ring held in place by six M3 cap screws. The down stream side of the larger flange is bevelled to match the angle at the base of the skimmer. The molecular beam approaches from the left.

V. SODIUM SOURCE VACUUM CHAMBER

The sodium oven is housed in a vacuum chamber to provide a low background pressure for the expansion. The high vacuum pump is a diffusion pump. Rough vacuum, and backing for the diffusion pump, is provided by a rotary-vein pump. This section details the chamber, feedthroughs, vacuum pumps, gauges and connections. The sodium source chamber is shown in figure 2.20 with all cluster flanges in place.

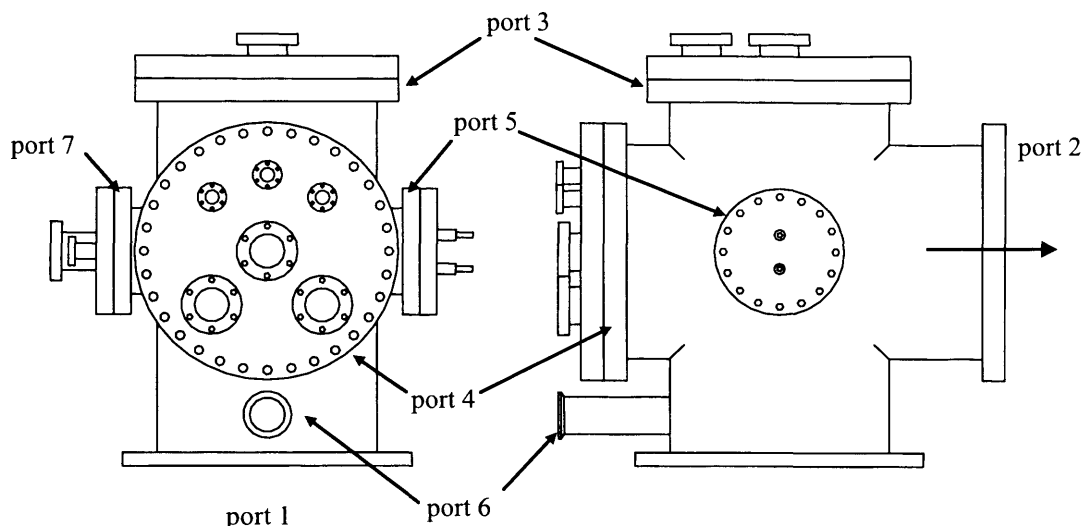


Figure 2.20 End and side elevations of the sodium source vacuum chamber. Small flanges on the cluster flange on port 4 carry thermocouple, oven power and gas feedthroughs. The small flanges on port 3 have been used for a viewing window and pressure gauge, and currently for the *xyz* translator. Port 5 was initially a water feedthrough but is currently blanked off. The pressure gauge is now attached to a right-angle valve and extension on the DN35CF flange on Port 7. The diffusion pump is connected at port 1, the experimental chamber connects to port 2, and the sodium expansion travels in the direction shown by the bold arrow. Port 6 is a DN40KF roughing vacuum connection.

The chamber is essentially a 250 mm diameter four-way cross. A third 100 mm diameter pipe crosses at the same point, perpendicular to the other two. The chamber comprises an asymmetric 250 mm diameter tube terminated by 300 mm (nominal) diameter Conflat flanges, with the exception of the connection to the diffusion pump (port 1). The diffusion pump connection is an DN 250 ISO-F flange. Port 2 is the connection to the experimental chamber. Electrical and gas feedthroughs are attached to a cluster flange which seals port 4. Port 3 is closed by a cluster flange used for an *xyz* translator (when one is used). Port 7 carries a pressure sensor and a spare port. Port 5 was initially a water feedthrough for the cooling jacket for the oven, but is currently blanked off.

Connection between the sodium source and the experimental chamber took two forms. The first, used in all the atom experiments, was a blank flange with a recess in its center for a DN35CF flange shown in figure 2.19. The collimator and later the

skimmer were mounted at this point. More recently, in an effort to reduce the skimmer – laser distance, the blank flange was replaced by one with a top-hat shape. This is sandwiched between the two chambers and projects towards the time-of-flight tube by 15 cm. Figures 2.12 and 2.13 make a comparison between these two arrangements.

The cluster flange at port 4 is used for feedthroughs for the oven. Two power feedthroughs (Thermo Vacuum Generators ZEFT34A) connect the oven heater power supplies. These comprise four ceramic-insulated conductors in a DN35CF flange. The pins are stainless steel with M5 threads on each end. Each pin is rated at 40 A and 15 kV, easily meeting our requirements. Connections are made using M5 ring crimp terminals, both inside and outside the chamber. A single four-conductor thermocouple feedthrough allows connection of the nozzle and oven thermocouples. These are ceramic-insulated conductors through a DN16CF flange. Two of the conductors are Chromel and two Alumel to match the K-type thermocouples. Vacuum side connection uses a miniature standard thermocouple connector. The air side connection uses terminal blocks.

The carrier gas feedthrough was made to our specification by VacWeld Ltd. from 316L stainless steel. It is DN16CF blank flange with a tube (1/8 in. outside diameter) welded through its centre. As with most welding in vacuum systems the joint is made on the vacuum side. The tubing extends approximately 150 mm on each side of the flange. The vacuum end is connected to the oven with an intervening length of tube. This has been a problematic item. The first was a length of 1/8 in. diameter stainless steel tube bent into a hairpin to give it some springiness. Although very fiddly during assembly, this worked for the fixed oven mount. When the oven was mounted on a translator the tube was replaced first with 1/8 in. diameter copper tubing and finally 1/16 in. stainless steel tube. Both of these were supple enough not to push the oven out of alignment, but the stainless steel was more resistant to corrosion by sodium.

A control valve for the carrier gas attached to the air side of the gas feedthrough. A variety of valves were tried, including a Nupro M-series needle valve, a General Valve solenoid valve, a UHV dosing valve (Vacuum Generators MD5-series), and finally a Nupro SS-4BMW-TSW bellows-sealed metering valve. Except for the last one none of the valves had fine enough control of low flow rates. The Nupro SS-4BMW-TSW has a flow range around 1 std. L min⁻¹ (approximately 20 mbar L s⁻¹). A micrometer on the valve allows it to be set reproducibly. Using this valve enabled us to

control the argon flow from levels so low the chamber pressure hardly increased ($<1 \times 10^{-6}$ mbar), right up to the limit of the pump ($<1 \times 10^{-4}$ mbar). The argon (BOC Pureshield) fitted with a 12 bar output pressure multistage regulator (BOC Saffire [sic]). Typically the output pressure was set at 2 bar when using the Nupro SS-4BMW-TSW valve.

A venting valve (Whitey 43-series ball valve) is fitted to a 1/4 in. diameter tube welded through a DN16CF flange at port 4. The tube simply opens into the vacuum chamber and is used to admit air or other gas. The air side has a Swagelok compression fitting so that inert gases can be used. Although we have never seen it, others report spontaneous ignition of deposited sodium on venting with air. In addition to preventing fire, venting with inert gas (usually nitrogen) allowed us to vent, open and reseal the chamber without the risk of sodium reacting with atmospheric water vapour and blocking the nozzle.

A DN35CF on the cluster flange on port 7 is used for a vacuum gauge. The sensor is fitted at the end of an UHV extension attached to a UHV right-angle valve (Vacuum Generators CR-series). Although this reduces the reliability of the pressure reading, both fittings keep the gauge away from the sodium vapour. Exposure to operational levels of sodium vapour while the gauge was turned on was found to prevent it working properly. Once exposed the gauge would not function again until cleaned. The right-angle valve was used to isolate the gauge for removal and cleaning without venting the whole chamber. Turning the gauge off while the sodium oven was hot mostly avoided this problem. Condensing the sodium on cold surfaces inside the chamber would be a better solution.

The gauge is a Penning (or cold-cathode) ionisation type (Leybold PTR225). These operate by ionising gas molecules in the gauge volume and measuring the ion current. Ionisation at low pressures is maintained by the presence of a magnetic field. The magnetic field is arranged so that it forces electrons emitted by the cathode into a spiral path. The long path increases the likelihood of collision with a molecule. The pressure is displayed on a Leybold Combivac IT23. Connection to the chamber is by a DN25KF HV flange and FPM o-ring seal.

VI. VACUUM PUMPS, GAUGES AND CONNECTIONS

This section details the vacuum pumps and fittings forming part the sodium source chamber. The vacuum pumps of the experimental chamber are dealt with later. It is slightly artificial to separate the vacuum system in this way as they are, as figure 2.21 shows, interdependent and interconnected.

The high vacuum pump is a diffusion pump fitted with a water-cooled baffle. Between the chamber and the baffle is a gate valve. The gate valve is used to isolate the pump from the chamber. A rotary-vein pump backs the diffusion pump. This pump also evacuates the chamber to rough vacuum after venting.

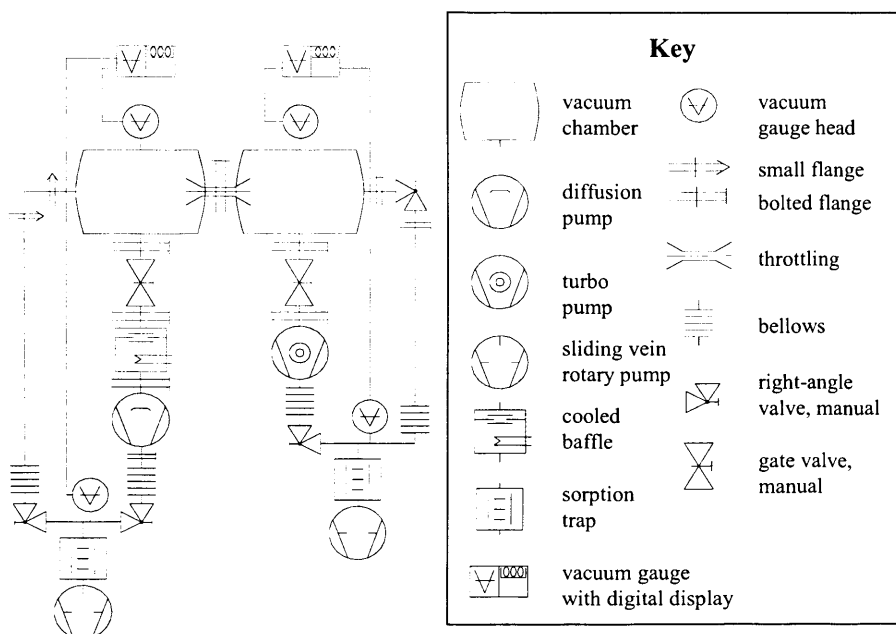


Figure 2.21 Left: a symbolic representation of the vacuum components of the whole system. The vacuum components of the sodium source are on the left of the figure; those of the experimental chamber are on the right. The skimmer is represented as a throttle between the two chambers. Most of the small flange interconnections have been omitted for clarity. Right: key to the vacuum symbols, which are from DIN 28401.

The diffusion pump is a Leybold DIP 3000 specified to pump air at 3000 L s^{-1} in its operating pressure range of $< 1 \times 10^{-4}$ mbar. The pump operates by evaporating oil (about 1.5 L) in a boiler at the base. Two cartridge heaters operating at 240 VAC and 5.4 A generate a total of 2.6 kW. The oil vapour ascends the height of the stack to a

water-cooled cap which deflects it downwards and towards to water-cooled outer walls. Any gas molecules that have diffused into the pump from the chamber are entrained in the oil vapour jet. The oil vapour condenses on the cooled outer wall, carrying the gas to the boiler where, on reheating, it escapes and is removed from the exhaust port by the rotary pump. We chose to use a silicone oil (DC 705, trimethylpentaphenyltrisiloxane) because it is better able to withstand oxidative chemical attack than other pump oils. This proved to be a somewhat inappropriate choice. The oil was destroyed by sodium and crystallised round the top of the pump (where it is cool) and in the baffle.

The baffle (Leybold Astrotaurus) attaches to the top of the diffusion pump using a DN 250 ISO-K flange and FPM o-ring seal. Its purpose is to reduce the inevitable 'backstreaming' (diffusion) of diffusion pump oil vapour into the vacuum chamber and thus reduce the ultimate pressure attained by the diffusion pump from $< 5 \times 10^{-7}$ mbar to $< 1 \times 10^{-8}$ mbar. It has a chevron interior construction that blocks all optical paths through the baffle. This increases the likelihood that any oil will hit a cooled surface before reaching the vacuum chamber. The compromise is that this inevitably reduces the throughput of the pump. Although this baffle has a quoted conductance of 3000 L s^{-1} , it also throttles the pump by approximately 30%.

The gate valve (VAT) is manually operated. It uses FPM O-rings for shaft seals and to seal the valve when closed. Like the diffusion pump, the connections between the gate valve and the baffle and vacuum chamber use DN 250 ISO flanges and FPM o-ring seals.

The backing (or forevacuum) pump is a two-stage oil-sealed Leybold Trivac D40B rotary vein pump. The specifications of this pump indicate it displaces $40 \text{ m}^3 \text{ h}^{-1}$ and can achieve pressures lower than 5×10^{-4} mbar. It must keep the pressure at the exhaust port of the diffusion pump below 6×10^{-1} mbar and has proved more than adequate. All connections between the inlet port of the rotary pump and the diffusion pump are made with the same size fittings (DN40KF and FPM o-rings) to conserve conductance. An absorption trap containing alumina pellets is fitted to the inlet port of the pump to prevent backstreaming of rotary pump oil into the diffusion pump. However we find that (presumably damaged) diffusion pump oil travels to the rotary pump. A cross piece connects the pump to two valves and a pressure gauge. The pressure gauge is a Pirani type (Leybold TTR90) connected to the same reader as the Penning gauge on the chamber. The valves isolate the connections to the chamber and

diffusion pump. When roughing the chamber it is necessary to close the valve on the backing line of the diffusion pump. This is to stop the sudden high pressure at the rotary pump causing the diffusion pump to backstream oil. It is also necessary to close the roughing line once the diffusion pump is pumping the chamber. Otherwise the lower pressure above the diffusion pump draws rotary pump oil vapour into the chamber. The connections between the rotary pump and the diffusion pump and the chamber are made with flexible stainless steel hose to reduce transmitted vibration. The rotary pump is also mounted on rubber feet designed to minimise vibration transmitted to the floor.

2.4 EXPERIMENTAL CHAMBER

The experimental chamber is where our wave packet coherent control experiments are conducted. The atomic/molecular beam interacts at right angles with the laser beams between two electric field plates at the base of a linear time-of-flight mass spectrometer. Following laser excitation a pulsed electric field is applied to the plates to ionise the target atoms or molecules and accelerate them to a microchannel plate detector. This apparatus is housed in a vacuum chamber attached to the molecular beam source chamber. The following paragraphs detail the time-of-flight mass spectrometer, detector, vacuum chamber and pumps, and associated instrumentation.

A. TIME-OF-FLIGHT MASS SPECTROMETER

I. OPERATION OF A LINEAR TIME-OF-FLIGHT MASS SPECTROMETER

The linear time-of-flight mass spectrometer separates ions by their charge to mass ratio. The principle of operation (shown in figure 2.22) is simple: an ion or electron is accelerated by an external electric field, it then passes into and through a field-free region to a detector. If the accelerating field is constant and applied for the whole time the ion is in the acceleration region, all the ions will increase in energy by the same amount [50]. Neglecting the time to leave the extraction region, the flight time for an ion of mass m and charge z can be readily derived from the kinetic energy, U , imparted by the field,

$$t = d \left(\frac{m}{2zU} \right)^{\frac{1}{2}}, \quad (2.26)$$

which can be expressed in convenient units [51],

$$t_{\mu s} = \frac{d_{mm}}{13.89} \left(\frac{m_{amu}}{2zU_{eV}} \right)^{\frac{1}{2}}, \quad (2.27)$$

where $t_{\mu s}$ is the flight time in μs , d_{mm} is the length of the free-flight region in mm, m_{amu} is the ionic mass in atomic mass units, z is the charge in units of electronic charge and U_{eV} is the kinetic energy in electron volts taken to equal the applied electric field in volts cm^{-1} . Clearly, starting at the same point in space, for a given field and the same charge, an ion with mass $2m$ will have a flight time $\sqrt{2}$ longer than an ion of mass m and an electron will have a very much shorter flight time than any ion.

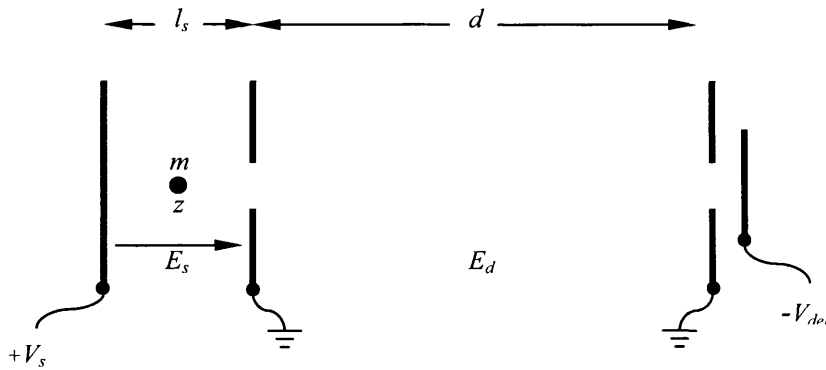


Figure 2.22 Operation of a linear time-of-flight mass spectrometer. The left hand pair of plates are commonly referred to as the ion source, although we use the term interaction region. In either case a positive ion formed there, indicated by a black dot, will experience an electric field $E_s = V_s/l_s$ V cm^{-1} . The ion is accelerated by the field through the hole in the grounded plate into the field free region $E_d = 0$ V cm^{-1} . Having traveled a distance d , the ion passes through the hole in the second grounded plate and is accelerated into the detector by the field from its attractive potential V_{det} . Acceleration of the ion is discussed in the text.

Accordingly, the flight times for Na^+ and Na_2^+ calculated by equation (2.27) for a 2000 V accelerating field are 1.26 μs and 1.78 μs respectively, so these ions can be easily distinguished by mass in our system. For comparison, to achieve a 1 μs flight time an electron would need to be accelerated by approximately only 13 V cm^{-1} (although this field would be insufficient to ionise in our experiments).

Our time-of-flight apparatus has been used in several different ways. In chapter 3 frequency-resolved experiments and time-resolved wave packet experiments in sodium atoms are described. In these experiments high fields (between 500 V cm^{-1} and 2000 V cm^{-1}) were applied to the interaction region as square pulses to field ionise Na and accelerate the ions to a detector. Later in the same chapter ramped electric fields were used to field ionise atoms state selectively and accelerate the electrons to a detector. Chapter 4 describes our plans for the sodium dimer experiments, which will be a ZEKE experiment where time-varying shaped fields as low as 10 V cm^{-1} will be used to ionise very high-lying Rydberg states.

II. PHYSICAL DESCRIPTION OF TOF APPARATUS

The time of flight apparatus was designed following ones used in this group [52], and others [53]. The layout of electrostatic lenses was modelled in Simion [51, 54], but since we are ionising with a pulsed electric field the behaviour is very simple and the simulations revealed no useful information, aside from accurate flight times. All the components were made by Thermo Vacuum Generators to our specifications. Figure 2.23 shows the key components. A field plate lies in the plane of the molecular and laser beams with its centre 5 mm below the point where they cross. 10 mm above the field plate is the first of six electrostatic lenses, each separated by 10 mm. A field-free flight tube starts 10 mm higher than the last electron lens. There is a final lens 5 mm above the top of the free flight tube. A micro-channel plate (MCP) detector lies approximately 5 mm above the last electron lens.

The field plate, electron lenses and free-flight tube are made from 316 stainless steel. The field plate, lenses and the ends of the flight tube are disks 60 mm in diameter and 1 mm thick. The field plate is a solid disk, whereas the electron lenses have a 10 mm diameter hole in the centre (see figure 2.24b). High transmission stainless steel mesh provided and spot-welded in place by Thermo Vacuum Generators covers the central hole. Four holes 5 mm diameter on a diameter of 50 mm carry the rods that hold the assembly together. The free flight tube is 150 mm long and the tubular section has an internal diameter of 14.4 mm (this is a standard tube size). The time-of-flight components are assembled outside the vacuum chamber. The PTFE (polytetrafluoroethylene) base of the assembly rests on a 3 mm thick stainless steel plate

CHAPTER 2

welded into the vacuum chamber just inside port 10. PTFE spacers maintain the height of the field plate above the base and the 10 mm spacing between the plates. The whole assembly is held together by four rods (4 mm diameter, 316 stainless steel) which pass through the plates and spacers and are secured with M4 nuts at each end. The ends of the rods pass through holes in the base plate so that the whole assembly can be secured to the vacuum chamber. When the apparatus was first assembled and put into the vacuum chamber the field plate was too low by about 2 mm. The height was adjusted by adding washers to the rods between the PTFE base and the plate on which it rests. Consequently the PTFE does not rest on the plate as intended. Instead an additional nut was added so that the whole assembly could be jacked up to the correct height then locked in place by another nut on the outside of the base plate.

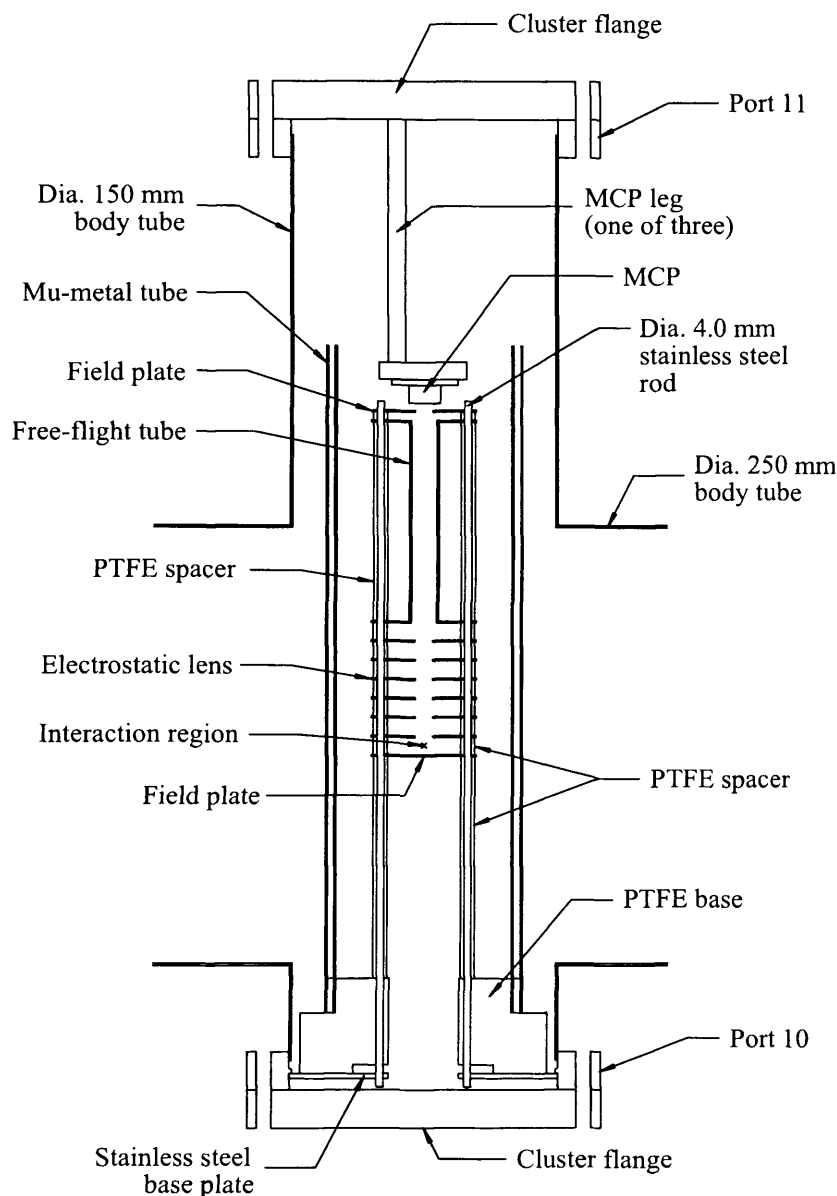


Figure 2.23 A cross-section through the electron/ion time-of-flight apparatus showing its position in the chamber body and the position of the MCP detector. The molecular beam passes through the interaction region in the plane of the page. The laser beams cross the molecular beam as they pass through the interaction region coming out of the page. Ions or electrons are accelerated upwards in the plane of the page to the micro-channel plate detector.

The PTFE spacers isolate the plates and free flight tube electrically so that each can be held at different potentials as required. The spacers are stepped so that they create a continuous insulation between the lenses and the rods. A detail of the spacers, lenses and rods is shown in figure 2.24.

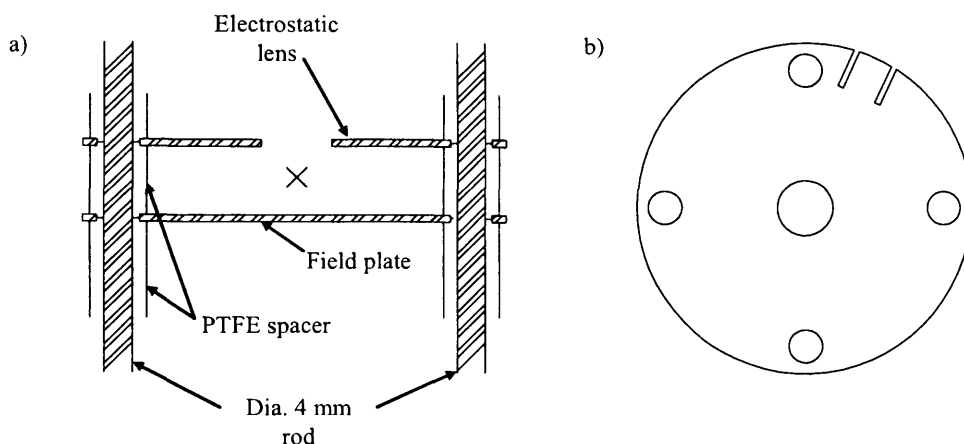


Figure 2.24 a) Cross-section detail of the interconnection between ion/electron lenses, PTFE spacers and rods in the time-of-flight apparatus. The sodium – laser interaction region is marked by an cross. b) An electrostatic lens showing the central hole through which ions or electrons pass, the four holes for PTFE spacers and the support rods, and the slots used for electrical connection.

Each of the plates and the free flight tube has two slots cut in its edge for $\frac{1}{4}$ in. push-on electrical connectors. The connectors are soldered onto wires that connect to electrical devices outside the vacuum chamber via a commercial feed-through located in the cluster flange at the bottom of the base of flight tube (port 10, figure 2.23). Initially this was a 19-pin instrumentation feed-through (Thermo Vacuum Generators ZEFT19) and this would be sufficient for experiments using low voltages (< 50 V), such as ZEKE. It was replaced with an 11-pin high-voltage instrumentation feed-through (Thermo Vacuum Generators ZEFT16) when our experiments required 2000 V square pulses or ramped high voltages applied to the field plate. It is specified up to 1000 V but had been used successfully to 2000 V. The feedthrough has gold plated pins on the vacuum side which accept push-on sockets soldered on the wires from the field plate and lenses. The air-side connection is to a removable plug (Thermo Vacuum Generators ZEFT17SK). Wires are soldered to the pins in the plug and connected to electrical devices described later.

The vacuum chamber has been designed so that a synchronous detector such as a counter-propagating ion time-of-flight mass spectrometer can be built below the electron time-of-flight if future experiments demand it.

III. ELECTRON/ION DETECTOR

At the top of the time of flight tube the electrons are detected on a microchannel plate detector (MCP). Two different models of detector were employed. For experiments where sodium ions were detected we used a Hamamatsu F4566-10. To detect electrons we fitted a Hamamatsu F4566-12. The latter is capable of detecting electrons or ions depending how it is connected.

The operation of both detectors is essentially the same and is shown in figure 2.25. The microchannel plate itself is a thin ceramic material perforated diagonally by many tiny holes. MCPs can detect charged or neutral particles, and photons. Electrons or ions are accelerated into the plate by the high bias potential.

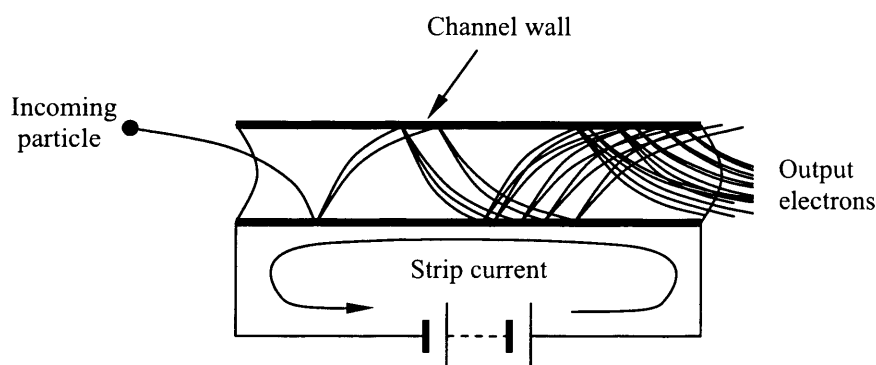


Figure 2.25 A schematic representation of the operation of a single channel of a microchannel plate detector seen in cross-section. A particle arriving from the left causes a cascade of ejected electrons from the biased channel wall. The strip current is provided by the external DC power supply that biases the channel. Adapted from Hamamatsu product literature.

On hitting the channel wall the particle causes a cascade of secondary electrons to be ejected. This is repeated along the channel length amplifying the arrival of one particle to a measurable current. At the end of the channel the electrons are emitted towards an anode (or a phosphor screen in imaging detectors). The current at the anode is transmitted to instruments outside the vacuum chamber.

Both the F4566-10 and -12 comprise two microchannel plates with the angle of their channels arranged in a chevron. Both models have the same effective diameter (14.5 mm) and channel diameter (12 μm). Electrical connection, plate arrangement and anode position of the two models of detector is shown in figure 2.26. The F4655-10 has

a rise time of 250 ps, a fall time of 750 ps and a gain of 5×10^7 when biased at 2400 V. The F4655-12 has is specified to have a rise time of 370 ps, a fall time of 910 ps and a FWHM of 720 ps when connected for negative ion or electron detection. When biased at 2400 V its gain is at least 10^7 . Hamamatsu claim both detectors generate 3 dark counts per second when biased at 2400 V. Both the detectors generate a maximum anode voltage of 500 V and current of 1 μA , and they are both output impedance matched to 50 Ω . We operate the detectors with a bias of between 2000 V and 2500 V, usually around 2200 V.

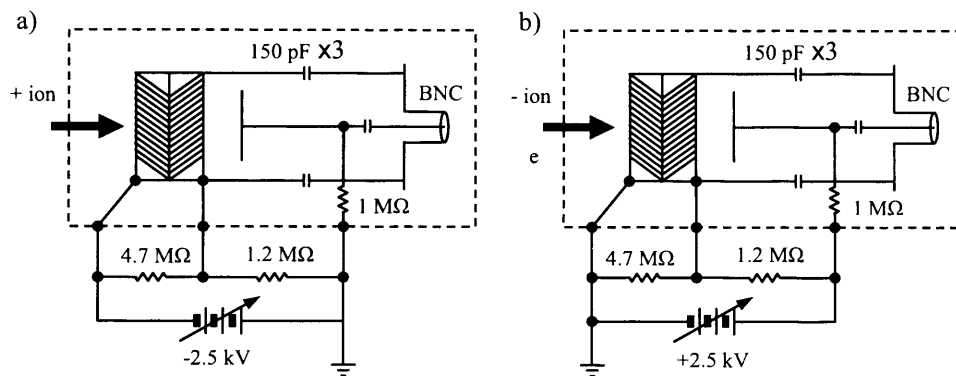


Figure 2.26 Circuit diagrams for a) the F4566-10 and b) F4566-12 (set up for negative ions or electrons) microchannel plate detectors. The angled lines indicate the two microchannel plates arranged in a chevron. The dashed line indicates components that are built in to the detector assembly. The external resistors (0.5W at 70 °C, $\pm 5\%$, 2500 VAC max.) are connected inside the vacuum chamber. A SRS PS325 provides high voltage bias, with the ground side of the circuit formed by the vacuum chamber. The signal connector is a BNC chassis plug.

The detector is mounted on the inside face a cluster flange at the top of the time-of-flight tube (port 11, figure 2.23). Figure 2.27 shows the detector mount, which can accept either model of MCP and electrically isolate the detector from the vacuum chamber if required (although this option was never used).

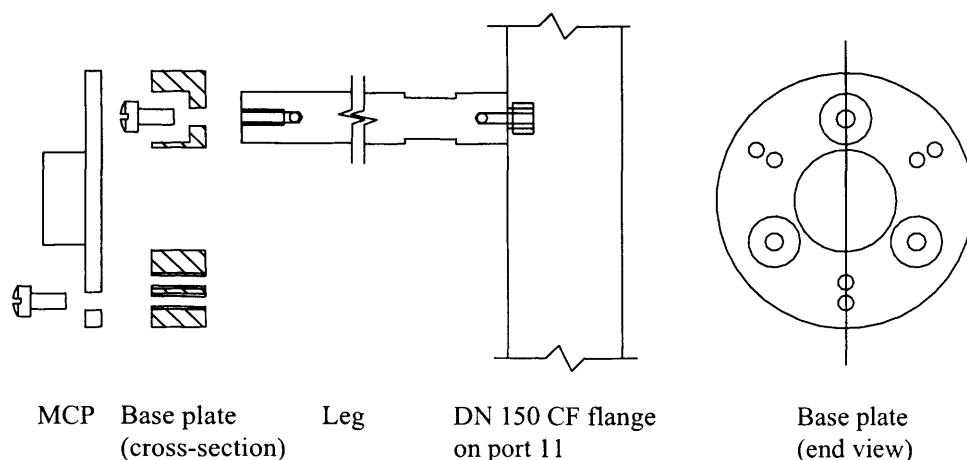


Figure 2.27 Left: an assembly drawing of the microchannel plate (MCP) support. Right: the stainless steel disk to which the microchannel plate attaches. The vertical line in this image indicates the shaded cross-section on the right hand image. The ring has tapped holes at two diameters so that either the F4655-10 or F4655-12 (shown) can be bolted to it. The ring bolts to three legs (one shown), which in turn screw into tapped holes in the vacuum flange at the top of the time-of-flight apparatus (see figure 2.23).

Both the high voltage DC biasing supply and the detector output signal use chamber-grounded BNC feedthroughs (Thermo Vacuum Generators ZEFT920). Internally the high voltage supply is wired using the thickly insulated solid conductor core of a BNC cable with a push terminal onto the feedthrough. Connection to the F4655-10 is made with M2 screws, and to the F4655-12 with solder and M2 screws. The signal output is wired using PVC insulated instrumentation wire with a push terminal on the feedthrough end and the central pin of a BNC terminal on the other.

IV. EXPERIMENTAL SIDE VACUUM CHAMBER

The above instrumentation is housed in a vacuum chamber arranged so that the molecular beam and laser beams cross at right angles 5 mm above the field plate. The laser beams are able to pass right through the chamber through windows on either side. A liquid nitrogen-cooled trap lies in the molecular beam path, behind the time-of-flight mass spectrometer, to condense sodium and stop it reaching the turbomolecular pump that evacuates this section.

The vacuum chamber, shown in figure 2.28, was fabricated by Thermo Vacuum Generators Ltd. to our design. The chamber is basically a horizontal tube 250 mm in diameter.

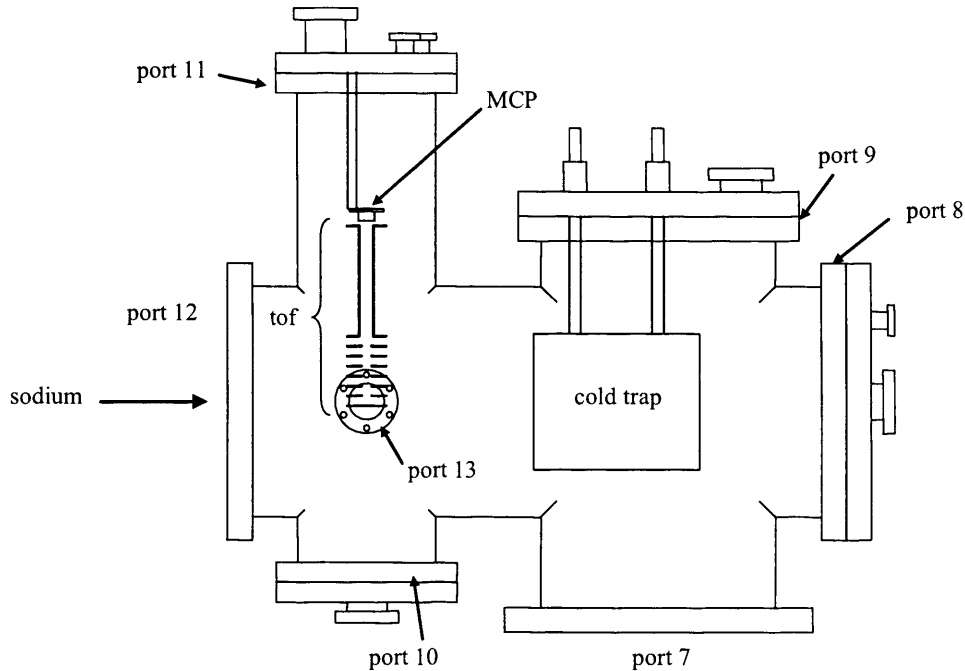


Figure 2.28 An elevation of the experimental vacuum chamber. The sodium beam approaches through port 12. The time-of-flight apparatus is shown in the vertical tube to the left, partly obscured by port 13 through which the laser beams pass. The pulsed voltages to the field plates are connected via a feedthrough on the cluster flange at port 10. The electrical connections to the MCP are made via feedthroughs at port 11. The liquid nitrogen cooled trap at port 9 is indicated by the square in the centre of the chamber suspended by the tubes used to fill it. A vacuum gauge attaches to the small flange on port 9. The small flanges on port 8 are connected to a roughing line and a venting valve. The turbomolecular pump attaches to a gate valve attached to port 7.

The time-of-flight apparatus is housed in a 150 mm diameter vertical tube which crosses the main tube near the connection to the molecular beam source. A vertical 250 mm diameter tube crosses the other and this attaches the cold trap and the vacuum pump. With the exception of the connection to the vacuum pump all flanges on these tubes are Conflats: 300 mm diameter on the 250 mm tube, and DN150CF on the 150 mm tube. The pump is connected with an DN 250 ISO-K flange.

The laser beams pass through the chamber in a perpendicular direction to the sodium (out of the plane of figure 2.28) through port 13. The vacuum connection is a

DN35CF on a 73 mm tubulation from the wall of the main chamber. Mounts (figure 2.29) for angled input and output windows were fabricated to our specification by Thermo Vacuum Generators Ltd.

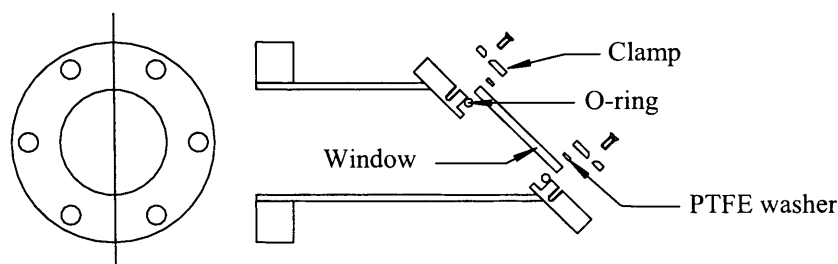


Figure 2.29 Angled mounts for laser input and output windows. Right: horizontal cross-section through a window mount showing its assembly. The Viton o-rings were purchased from James Walker Ltd.. They have an inside diameter of 34.50 mm and a section of 3.00 mm. The windows are 3 mm thick fused silica. The PTFE washer prevents the stainless steel clamp from damaging the window. Eight M2 countersunk screws secure the clamp. Left: view of the DN35CF connection showing the orientation of the bolt holes with respect to the window angle. The vertical line indicates the cross-section shown on the left. A rotating flange either on the chamber or the window mount would have allowed the window to be rotated to accept different laser polarisations.

From the centre of the window to the interaction region is approximately 300 mm. This distance prevents tight focussing of the laser beams, which is probably not a problem for the femtosecond lasers, but had to be addressed when nanosecond and picosecond lasers were used as they have to be focussed. It would be sensible to minimise the length of both the input and output ports of the chamber, and the window mounts. As an interim measure we replaced the input window mount with a flat Kodial window (Thermo Vacuum Generators ZVPZ38), which appears to have performed adequately for experiments with nanosecond and picosecond lasers.

V. THE COLD TRAP

Figure 2.28 shows the liquid nitrogen cooled trap and its feedthroughs in a 300 mm diameter cluster flange. The flange also has a DN35CF flange where a Penning gauge (Leybold PTR225) is attached using a CF to KF adaptor. The cold trap presents a cold surface directly in the path of the molecular beam after it has passed through the

interaction region on to which sodium can condense. This reduces the amount of sodium vapour passing into either of the vacuum pumps. The trap also operates as a cryopump – reducing the pressure in the chamber by around 3×10^{-7} mbar when filled with liquid nitrogen.

The cold trap is a cylindrical vessel 150 mm in diameter and 200 mm long with its axis lying horizontally. It is suspended from the cluster flange by two tubes (0.5 in. outside diameter). As the figure shows, the cold trap projects slightly towards the time-of-flight apparatus to intercept as much of the molecular beam as possible. The tubes are used to fill and vent the liquid nitrogen. Their connection to the flange is a standard liquid nitrogen feedthrough, designed to minimise the conduction of heat from the flange to the tubes. The 0.5 in. tubes are welded into 1 in. diameter tube, which in turn is welded into the flange. In this way there is very little direct contact between the flange and cold tube.

The flange on port 8 of the experimental chamber attaches a roughing connection via a DN35CF and a right-angle valve (Vacuum Generators CR-series), and a DN16CF connection taken by a venting valve (Thermo Vacuum Generators CR-series).

VI. VACUUM PUMPS ON THE EXPERIMENTAL CHAMBER

The experimental chamber is pumped by a Leybold Turbovac 1000C turbomolecular pump. It is specified to pump 1000 L s^{-1} of nitrogen at 10^{-5} mbar and can achieve pressure lower than 10^{-10} mbar. We operate it in the range 3×10^{-7} mbar to $< 1 \times 10^{-6}$ mbar. This pump contains a series of rotating turbines and fixed chevrons. Gas molecules entering the pump are deflected further inwards by consecutive collisions with the rapidly rotating turbine blades and the chevrons until they reach the exhaust. The rotation speed of the turbines is controlled electronically by a Leybold Turbotronic controller. We eventually decided to fit a nitrogen purge valve to the turbo pump to reduce further the possibility of sodium vapour reaching the bearings. The purge valve has a predetermined leak rate when supplied at 1 bar input pressure. The leak rate is determined to keep laminar flow of nitrogen in the bearings to exclude any gas or vapour. Even with this precaution the bearings have started to ‘sing’ a little.

Since the throughput of the turbo pump was expected to be small we started out backing it with a relatively small rotary pump (Leybold Trivac D16B). This displaces a volume of $16 \text{ m}^3 \text{ h}^{-1}$ and can achieve an ultimate pressure of $< 5 \times 10^{-4}$ mbar, and was more than adequate until the purge gas was introduced. The leak rate of the purge valve is intended for a larger backing pump and increased the exhaust pressure of the turbo pump above its operating range ($< 1 \times 10^{-2}$ mbar). We replaced the backing pump with a bigger one (Leybold Trivac D40BCS). The exhaust pressure has still always run higher than optimal ($\sim 1 \times 10^{-1}$ mbar), even with the gas supply pressure to the purge valve reduced to ~ 0.5 bar, but this does not appear to affect the ultimate pressure achieved by the turbo pump. Connection to the turbo pump and chamber is similar to that for the backing pump on the molecular beam source, incorporating an alumina absorption trap, a four-way cross, right angle valve and bellows. The roughing line is also attached to the four-way cross. Backing pressure is measured with an identical Pirani gauge which shares a display (Leybold Combivac IT23) with the high vacuum gauge on this chamber.

2.5 THOUGHTS ON FUTURE DESIGNS AND MODIFICATIONS

A. OVEN DESIGN

The most serious problem with the oven design concerns the nozzle heating. The nozzle flange is not directly heated and heat conduction between the heated part and the flange is probably not ideal. There have been indications of periodic clogging of the nozzle when using a carrier gas, and even without a carrier gas if the nozzle was not hot enough. If this proves to be a serious problem it could be quite a difficult to solve, involving a third heater attached directly to the nozzle flange.

We opted for an oven machined from a single piece of stainless steel. This was a costly choice made because we feared a welded oven would not survive the thermal stress of daily temperature cycling. We briefly tried an oven made from a standard UHV extension (Thermo Vacuum Generators ZBS19) which has Conflat flanges (DN16CF) welded onto the ends of a thin walled tube (1.22 mm). This did not appear to suffer any damage from thermal cycling. Gerber also reported using a welded cartridge in a lithium source [48]. It seems likely therefore that a welded oven would be

adequate and cost less than a one-piece construction. In addition a welded construction would more easily allow for complex oven layouts. For instance to connect the nozzle off-centre in a welded construction is no harder than having it centrally placed. In a machined oven, having the nozzle off-centre adds considerable complexity to the machining process.

Given a certain diameter for the sodium reservoir, having the nozzle attached off-centre and higher than in the cylindrical design would allow more sodium to be stored. This would lead to less frequent refills.

For our work, contamination of sodium by copper from the gaskets used to seal the oven and nozzle was not a problem. However it would be interesting to investigate other methods of sealing heated sources, particularly ones where only one material is used.

B. OVEN MOUNTING

The oven mounting is where most improvement could be made to the current set up. Ideally the oven should be held rigidly (which rules out the type of *xyz* translator we used) and be able to be moved in the three Cartesian coordinates aligned with the beam axis, as well as rotating around a vertical and a horizontal axis. Probably the easiest way to achieve this in the current chamber would be to upgrade the system used in the sodium atom experiments. If the source was suspended from an *xyz* translator with rotation and tilt adjustments, any misalignment could be corrected from outside the chamber while the source was operating. The bar on which the oven hangs would have to be much thicker than 1/4 in. in diameter, more like 20 mm. To reduce the nozzle – skimmer distance and reduce the cantilever load of the heavy oven on the translation stage, the flange connecting to the experimental chamber (Port 3 in figure 2.20) should be moved towards the diffusion pump. This would have the added advantage of increasing the pumping speed of the chamber – always a desirable feature in molecular beams.

C. NOZZLE - SKIMMER DISTANCE ADJUSTMENT

When the nozzle – skimmer distance is very small (< 10 mm), as it is in many experiments, it would be highly desirable to be able to see the separation to avoid hitting the skimmer and to know the distance precisely. A view port at the front of the molecular beam chamber would allow such observation. This arrangement would also permit laser excitation of the expansion very close to the nozzle, as is sometimes desirable.

D. THERMAL SHIELDING AND COOLING

During our sodium atom experiments there was no thermal shielding or cooling jacket round the oven. This made the vacuum chamber wall dangerously hot and would probably have rendered useless the baffle on the diffusion pump. Ideally we should incorporate a combination of both thermal shielding, using tantalum foil or thin stainless steel [7], and a thin-walled water-cooled jacket to reduce heat loss from an oven. This will be imperative if sodium is cold-trapped within the source chamber (see below).

E. TRAPPING SODIUM IN THE SOURCE CHAMBER

Subject to the installation of water cooling of the oven, it would be advantageous to condense sodium onto liquid nitrogen cooled surfaces surrounding the expansion and the skimmer wall. Condensed sodium would not then attenuate the beam by scattering off the chamber walls. In addition, not only would this reduce the flux of sodium into the diffusion pump, but it would also reduce the gas load on the pump and allow for higher source pressures (and P_0d), especially when a carrier gas is used. The simplest way to cool the skimmer wall would be to create a hollow, sealed from the vacuum, in the flange separating the two chambers that can be filled with liquid nitrogen from outside. For the chamber walls, passing liquid nitrogen (or liquid nitrogen cooled nitrogen gas) through channels on the outside of the chamber is preferable as there are no internal structures to reduce pumping speed and it does not require costly liquid nitrogen feedthroughs.

One final comment on the sodium source side concerns the sealing technology used. The operating pressures in the source chamber do not require UHV compatible vacuum components, and in any case the diffusion pump, gate valve and baffle do not use them. In a new system it would be cost effective to use the HV ISO system.

F. IMPROVEMENTS TO THE EXPERIMENTAL SIDE OF THE VACUUM SYSTEM

The first improvement would be to move the flange connecting to the source chamber towards the time-of-flight tube. This would reduce the distance from the skimmer to the interaction region and lead to higher beam intensity, without recourse to the top hat and its associated problems. Combined with moving the mirror flange on the source chamber, this change would make for a much improved molecular beam chamber.

G. IMPROVEMENTS TO THE TIME-OF-FLIGHT APPARATUS

The most significant improvement to the TOF apparatus would be to build the whole system on to a single flange (as is the case for many commercial devices), and could be easily implemented. This would allow electrical connections to be made on the bench and would facilitate alignment.

A related modification would be to attach the microchannel plate detector to the top of the TOF apparatus. The distance between the TOF and the detector is then known and does not depend on the rather poor tolerances of vacuum chamber fabrication. Thermo Vacuum Generators quote a port length tolerance of ± 1 mm, and an angular tolerance of $\pm 1^\circ$. Although we did not experience problems of this nature, it could be easily eliminated as a potential problem.

A suggestion for another time-of-flight apparatus is the use of ceramic or PEEK spacers in place of PTFE. Both ceramics and PEEK have better dimensional integrity, especially for long tubes and small machined features like the steps shown in figure 2.24.

The final improvement suggested is to the electron/ion lenses. Unless mesh is spot-welded wire by wire there are inevitably some 'strays' that lift off the surface of the lens. This has not manifested problems for us but it could if the lenses were used to

focus electrons, as in photoelectron spectroscopy, or when smaller accelerating fields are applied, as in ZEKE spectroscopy. If it is possible to perform resistance welding with a ring electrode instead of a point, all wires would then be welded simultaneously. This is a possibility that can be easily investigated with the support facilities at UCL.

2.6 REFERENCES

1. D.R. Miller, *Free Jet Sources*, in *Atomic and Molecular Beam Methods*, G. Scoles, Editor. 1988, Oxford University Press: New York. p. 14-53.
2. H.C.W. Beijerinck and N.F. Verster, *Physica B & C* **111** (2-3), 327-352. (1981).
3. R.J. Gordon, Y.T. Lee, and D.R. Herschbach, *J. Chem. Phys.* **54** (6), 2393-2409. (1971).
4. A.N. Nesmeyanov, *Vapour Pressures of the Chemical Elements*, ed. R. Gary. 1963, Amsterdam: Elsevier.
5. L.K. Lam, T. Fujimoto, A.C. Gallagher, and M.M. Hessel, *J. Chem. Phys.* **68** (8), 3553-3561. (1978).
6. R.E.M. Hedges, Gallaghe.A, and D.L. Drummond, **6** (4), 1519-&. (1972).
7. M.P. Sinha, A. Schultz, and R.N. Zare, *J. Chem. Phys.* **58** (2), 549-556. (1973).
8. J.C. Whitehead and R. Grice, *Faraday Discuss.* (55), 320-330. (1973).
9. E.L. Knuth, *J. Chem. Phys.* **66** (8), 3515-3525. (1977).
10. F. Aerts, H. Hulsman, and P. Willems, *Chem. Phys.* **68** (1-2), 233-249. (1982).
11. F. Aerts and H. Hulsman, *Chem. Phys. Lett.* **72** (2), 237-241. (1980).
12. K. Bergmann, U. Hefter, and P. Hering, *J. Chem. Phys.* **65** (1), 488-490. (1976).
13. K. Bergmann, U. Hefter, and P. Hering, *Chem. Phys.* **32** (3), 329-348. (1978).
14. K. Bergmann, R. Engelhardt, U. Hefter, and P. Hering, *Chem. Phys.* **44** (1), 23-32. (1979).
15. M.P. Sinha, C.D. Caldwell, and R.N. Zare, *J. Chem. Phys.* **61** (2), 491-503. (1974).
16. A.G. Visser, J.P. Bokooy, L.K. Vandermeij, C. Devreugd, and J. Korving, *Chem. Phys.* **20** (3), 391-408. (1977).
17. F. Aerts, P. Willems, and H. Hulsman. in *13th International Conference on Rarefied gas dynamics*. 1985. Novosibirsk, Russia: Plenum Press, New York.
18. F. Aerts, H. Hulsman, and P. Willems, *Chem. Phys.* **83** (3), 319-332. (1984).

19. G. Gundlach, E.L. Knuth, H.G. Rubahn, and J.P. Toennies, *Chem. Phys.* **124** (1), 131-142. (1988).
20. F. Aerts, H. Hulsman, and P. Willems, *Chem. Phys.* **89** (2), 307-312. (1984).
21. M. Kompitsas, K. Kolwas, and H.G. Weber, *Chem. Phys.* **55** (2), 221-227. (1981).
22. M.S. Chapman, C.R. Ekstrom, T.D. Hammond, J. Schmiedmayer, S. Wehinger, and D.E. Pritchard, *Phys. Rev. Lett.* **74** (24), 4783-4786. (1995).
23. U. Gaubatz, P. Rudecki, S. Schiemann, and K. Bergmann, *J. Chem. Phys.* **92** (9), 5363-5376. (1990).
24. A. Miffre, M. Jacquy, M. Büchner, G. Tréneç, and J. Vigué, *Phys. Rev. A* **70**, 030701. (2004).
25. S. Depaul, D. Pullman, and B. Friedrich, *J. Phys. Chem.* **97** (10), 2167-2171. (1993).
26. R. Campargue, *J. Phys. Chem.* **88** (20), 4466-4474. (1984).
27. S. Skowronek and A.G. Urena, *Rev. Sci. Instrum.* **67** (7), 2463-2465. (1996).
28. V. Tarnovsky, M. Bunimovicz, L. Vuskovic, B. Stumpf, and B. Bederson, *J. Chem. Phys.* **98** (5), 3894-3904. (1993).
29. L. Banares and A.G. Urena, **22** (12), 1046-1047. (1989).
30. W.P. Lapatovich, R. Ahmad-Bitar, P.E. Moskowitz, I. Renholm, R.A. Gottscho, and D.E. Pritchard, *J. Chem. Phys.* **73** (11), 5419-5431. (1980).
31. W. DeGraffenreid, J. Ramirez-Serrano, Y.M. Liu, and J. Weiner, *Rev. Sci. Instrum.* **71** (10), 3668-3676. (2000).
32. T. Bergen, X. Biquard, A. Brenac, F. Chandezon, B.A. Huber, D. Jalabert, H. Lebius, M. Maurel, E. Monnard, J. Opitz, A. Pesnelle, B. Pras, C. Ristori, and J.C. Rocco, *Rev. Sci. Instrum.* **70** (8), 3244-3253. (1999).
33. S. Nonose, H. Tanaka, T. Mizuno, N.J. Kim, K. Someda, and T. Kondow, *J. Chem. Phys.* **105** (20), 9167-9174. (1996).
34. L.V. Hau, J.A. Golovchenko, and M.M. Burns, *Rev. Sci. Instrum.* **65** (12), 3746-3750. (1994).
35. M.R. Walkiewicz, P.J. Fox, and R.E. Scholten, *Rev. Sci. Instrum.* **71** (9), 3342-3344. (2000).
36. C.H. Ching, J.E. Bailey, P.W. Lake, A.B. Filuk, R.G. Adams, and J. McKenney, *Rev. Sci. Instrum.* **68** (1), 354-357. (1997).

37. A. Assion, T. Baumert, J. Helbing, V. Seyfried, and G. Gerber, *Chem. Phys. Lett.* **259** (5-6), 488-494. (1996).
38. L. Bewig, U. Buck, C. Mehlmann, and M. Winter, *Rev. Sci. Instrum.* **63** (8), 3936-3938. (1992).
39. H.E. Evans and W.R. Watson, *The Solubility of Copper in Sodium*. 1971, Central Electricity Generating Board.
40. P.A. Kinzie, *Thermocouple Temperature Measurement*. 1973, New York: Wiley. 278.
41. A. Danon and A. Amirav, *Rev. Sci. Instrum.* **58** (9), 1724-1726. (1987).
42. B. Brutschy and H. Haberland, *J. Phys. E (Sci. Instrum.)* **13** (2), 150-151. (1980).
43. I.R. Sims, J.L. Queffelec, A. Defrance, C. Rebrionrowe, D. Travers, P. Bocherel, B.R. Rowe, and I.W.M. Smith, *J. Chem. Phys.* **100** (6), 4229-4241. (1994).
44. O. Abraham, J.H. Binn, B.G. Deboer, and G.D. Stein, *Phys. Fluids* **24** (6), 1017-1031. (1981).
45. N.F. Ramsey, *Molecular Beams*. International Series of Monographs on Physics. 1986: Oxford University Prss. 466.
46. H.R. Murphy and D.R. Miller, *J. Phys. Chem.* **88** (20), 4474-4478. (1984).
47. G. Gerber, *Personal Communication*, 2001
48. M. Kappas and S. Leutwyler, *Molecular Beams of Clusters*, in *Atomic and Molecular Beam Methods*, G. Scoles, Editor. 1988, Oxford University Press: New York. p. 380.
49. W.R. Gentry and C.F. Giese, *Rev. Sci. Instrum.* **46** (1), 104-104. (1975).
50. W.C. Wiley and I.H. McLaren, *Rev. Sci. Instrum.* **26** (12), 1150-1157. (1955).
51. A.D. Applehans and D.A. Dahl, *Ion optics through the eyes of Simion 6.0*. 1996.
52. H.H. Fielding, R.A.L. Smith, V.G. Stavros, and J.R.R. Verlet, *Abstr. Pap. Am. Chem. Soc.* **221**, 156-PHYS. (2001).
53. F. Merkt and T.P. Softley, *High Resolution Laser Photoionization and Photoelectron Studies*. Wiley Series on Ion Chemistry and Physics, ed. I. Powis, T. Baer, and C.-Y. Ng. 1995: Wiley.
54. D.A. Dahl, *Int. J. Mass Spectr.* **200** (1-3), 3-25. (2000).

CHAPTER 3 COHERENT CONTROL OF RYDBERG ELECTRON WAVE PACKETS IN ATOMIC SODIUM

ABSTRACT

This chapter describes experiments to control the angular momentum composition of Rydberg electronic wave packets in atomic sodium. The control scheme uses phase-locked pairs of transform-limited picosecond laser pulses to create pairs of identical radial wave packets from the Rydberg states. Quantum interference between the wave packets, or the excitation pathways to them, is manipulated to control the total angular composition of the resultant wave packet, which is detected either by the optical Ramsey method or by state-selective field ionisation. The results are interpreted both from the perspective of time evolution of the wave packet and the frequency content of the excitation laser fields. The control strategy is then extended by the inclusion of linear chirp in one of the laser pulses.

3.1 INTRODUCTION

A. SODIUM ATOM SPECTROSCOPY

The sodium atom is a classic spectroscopic model exhibiting many simple features that make it an ideal system in which to test coherent control schemes. The electronic structure of ground state sodium is $[\text{Ne}](3s)^1$ giving the term $3^2S_{1/2}$. Excitation of the $3s$ electron gives $[\text{Ne}](3p)^1$, which has terms $3^2P_{1/2}$ and $3^2P_{3/2}$. These states lie $16956.1(72) \text{ cm}^{-1}$ and $16973.3(68) \text{ cm}^{-1}$ [1] above the ground state and can be excited in an optically allowed ($\Delta l = \pm 1$) transition. Here and below, wavenumbers are quoted to the linewidth of the nanosecond lasers (0.1 cm^{-1}) with the remaining higher precision terms in brackets. Degeneracy makes the transition amplitude to the $3^2P_{3/2}$ level a factor of 2 larger than the $3^2P_{1/2}$ level so, in the experiments discussed in this chapter, the $3^2P_{3/2}$ level was chosen as the intermediate from which to excite high-lying Rydberg states.

B. ATOMIC RYDBERG STATES

In general Rydberg states are defined as electronic configurations of atoms and molecules that behave hydrogenically. This often, but not exclusively, corresponds to excitation to high principal quantum number. Far from the nucleus, where the Rydberg electron spends most of its time, it experiences a simple $-1/r$ Coulomb potential. In sodium the nuclear charge is shielded by the remaining electrons, so the Coulomb potential the Rydberg electron feels is modified compared to the hydrogen atom. Rydberg electrons with low angular momentum penetrate the inner electron cloud more than higher angular momentum states and, as a result, experience increased nuclear charge and binding energy. This lowers the energy of low angular momentum states from the hydrogenic case by an amount accounted for by the quantum defect, μ_l , which depends on the orbital angular momentum l . The Rydberg state energies are then given by the familiar Rydberg formula,

$$E_n = IP - \frac{R_{Na}}{(n - \mu_l)^2}, \quad (3.1)$$

where $IP = 41449.4(51) \text{ cm}^{-1}$ is the ionisation potential and $R_{Na} = 109734.6(97) \text{ cm}^{-1}$ is the Rydberg constant for sodium calculated from accurate electron and sodium atomic masses, n is the principal quantum number and μ_l is the quantum defect [2]. For sodium the quantum defects are 1.35 for the s Rydberg series and 0 for the d series [3].

Rydberg states have characteristics that are very different from low-lying electronic states. The orbital radius is large and scales as n^2 , so the $35d$ state of sodium has an orbital radius of approximately 95 nm [2]. The orbital period is very long compared to the ground state, 6.5 ps at $n = 35$ compared to ≈ 24 attoseconds ($1 \text{ as} = 10^{-18} \text{ s}$) at $n = 1$, which brings the electronic motion into the reach of picosecond lasers. The spacing between adjacent energy levels scales as n^{-3} , giving a spacing of approximately 5 cm^{-1} between $35s$ and $36s$. This allows several Rydberg states with different principal quantum numbers to be excited within the bandwidth of a picosecond laser pulse. Finally, the binding energy is low, approximately 90 cm^{-1} for a $35d$ electron, and scales with n^{-2} . Rydberg states are therefore readily ionised by external electric fields, which facilitates their detection.

In the following experiments we have excited high-lying Rydberg states of atomic sodium, as shown in figure 3.1.

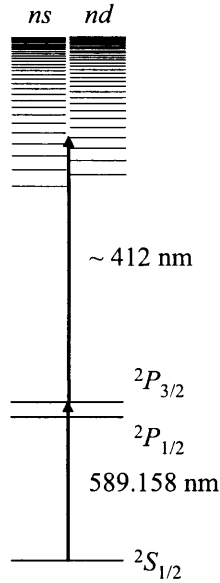


Figure 3.1 Laser excitation scheme for sodium for the experiments in this chapter. Excitation from the $3^2S_{1/2}$ ground state to the $3^2P_{1/2}$ or $3^2P_{3/2}$ level is made with a narrow bandwidth nanosecond dye laser. Excitation to the Rydberg states is made either using a narrow bandwidth nanosecond dye laser (for frequency resolved experiments), or a broad bandwidth picosecond dye-laser (giving time-resolved data). The angular momentum selection rules dictate that from a $3^2P_{3/2}$ state ns and nd Rydberg series are excited. The energy levels of both series converge to the same ionisation limit ($41449.4(51) \text{ cm}^{-1}$). The broad bandwidth of the picosecond laser excites coherently several Rydberg states, forming a wave packet. Wave packets are discussed in section 3.1 B. A description of the lasers is given in section 3.2 A.

Excitation of the $3s$ electron into the high-lying Rydberg states leaves the neon closed shell electronic configuration, which makes this effectively a one-electron system.

The oscillator strengths for excitation of the s and d Rydberg series from the $3^2P_{3/2}$ level in sodium differ. The d oscillator strength is double that of the s , so the d series is excited with twice the probability. This can be seen clearly in the frequency resolved spectra of the Rydberg series (see figure 3.16). The average oscillator strength for a transition from state $|nl\rangle$ to state $|n'l'\rangle$ can be written [2],

$$\bar{f}_{n'l',nl} = \frac{2}{3} \omega_{n'l',nl} \left(\frac{l_{\max}}{2l+1} \right) \left| \langle n'l' | r | nl \rangle \right|^2 \quad (3.2)$$

where $\omega_{n'l',nl} = (E_{n'l'} - E_{nl})/\hbar$ is the transition angular frequency, l_{\max} is the larger of l and l' , and E_{nl} and $E_{n'l'}$ are the energies of the lower and upper states in Joules

respectively. The bra-ket is the same for both transitions, giving an oscillator strength ratio $d/s = 2$ (see figure 3.17).

C. RYDBERG ELECTRON WAVE PACKETS

A Rydberg electron wave packet is formed by excitation of a coherent superposition of stationary Rydberg eigen states. In our experiments, this excitation is made by a picosecond dye laser. The broad bandwidth of the laser (around 21 cm^{-1}) simultaneously and coherently excites between 5 and 8 Rydberg states. Considering first the interaction of just the launch state $|1\rangle$, in this case the $3^2P_{3/2}$, and one Rydberg state $|2\rangle$ and the electric field of the laser light allows an understanding of the excitation. Solution of the time-dependent Schrödinger equation,

$$\hat{H}\Psi(r,t) = i\hbar \frac{d\Psi(r,t)}{dt}, \quad (3.3)$$

with the Hamiltonian $\hat{H} = \hat{H}_{atom} + \hat{H}_i$, where $\hat{H}_{atom}\psi_j(r) = E_j\psi_j(r)$ is the time-independent atomic Hamiltonian and \hat{H}_i is the interaction Hamiltonian. Solution of equation (3.3) gives the time-dependent wavefunctions

$$\Psi_j(r,t) = \psi_j(r) \exp\left(-\frac{iE_j t}{\hbar}\right) \quad (3.4)$$

where the radial wavefunctions $\psi_j(r)$ and energies E_j come from \hat{H}_{atom} . The wave function for the two-level system can then be written as a linear combination,

$$\Psi(r,t) = a_1(t)\Psi_1(r,t) + a_2(t)\Psi_2(r,t) \quad (3.5)$$

where the a_i are the time dependent amplitudes, and $|a_1(t)|^2 + |a_2(t)|^2 = 1$. The transition angular frequency between states $|1\rangle$ and $|2\rangle$ is

$$\omega_0 = (E_2 - E_1)/\hbar. \quad (3.6)$$

Application of equation (3.3) and the atomic Hamiltonian to equation (3.5), multiplying through by the complex conjugates, $\psi_1^*(r)$ and $\psi_2^*(r)$, integrating over all space and noting the orthogonality between eigenstates,

$$\int \psi_n^* \psi_m dV = \delta_{nm} \quad (3.7)$$

gives expressions for the amplitudes,

$$a_1 M_{11} + a_2 \exp(-i\omega_0 t) M_{12} = i \frac{da_1}{dt} = i\dot{a}_1 \quad (3.8)$$

$$a_1 \exp(-i\omega_0 t) M_{21} + a_2 M_{22} = i \frac{da_2}{dt} = i\dot{a}_2 \quad (3.9)$$

where the transition matrix elements are,

$$\hbar M_{nm} = \int \psi_n^* \hat{H}_i \psi_m dV \quad (3.10)$$

The interaction Hamiltonian \hat{H}_i derives from the potential energy felt by the induced electric dipole $e\mathbf{D} = e \sum r_j$ because of the electric field of the light. For a laser pulse with a full-width at half-maximum duration of τ_p , the electric field can be written

$$E(t) = E_0 \cos(\omega t) f(t), \quad (3.11)$$

where $f(t) = \exp[-2 \ln 2 (t/\tau_p)^2]$ is the pulse envelope and assumed to be Gaussian.

The interaction Hamiltonian becomes,

$$\hat{H}_i = e\mathbf{D} \cdot \mathbf{E}_0 \cos(\omega t) f(t), \quad (3.12)$$

and from symmetry,

$$M_{11} = M_{22} = 0 \quad \text{and} \quad M_{12} = M_{21}^* = \frac{1}{\hbar} e E_0 X_{12} \cos(\omega t) \quad (3.13)$$

where $X_{12} = \int \psi_1^* X \psi_2 dV = \langle \psi_1 | X | \psi_2 \rangle$ is the dipole matrix element. Equations (3.8) and (3.9) can now be written,

$$\dot{a}_1 = -\frac{i}{2} a_2 \Omega_{Rabi} [\exp(-i(\omega - \omega_0)t) + \exp(-i(\omega + \omega_0)t)] \quad (3.14)$$

$$\dot{a}_2 = -\frac{i}{2} a_1 \Omega_{Rabi} [\exp(i(\omega - \omega_0)t) + \exp(i(\omega + \omega_0)t)] \quad (3.15)$$

where $\Omega_{Rabi} = eE_0 X_{12}/\hbar$ is the Rabi frequency. For frequencies of light such that $|\omega - \omega_0| \ll \omega$, i.e. near resonance, the fast oscillating term $\exp(-i(\omega + \omega_0)t)$ can be neglected as it does not contribute to the amplitude. This is known as the rotating wave approximation (RWA) and gives,

$$\dot{a}_1 = -\frac{i}{2} a_2 \Omega_{Rabi} [\exp(-i(\omega - \omega_0)t)] \quad (3.16)$$

$$\dot{a}_2 = -\frac{i}{2} a_1 \Omega_{Rabi} [\exp(i(\omega - \omega_0)t)] \quad (3.17)$$

We are primarily interested in the amplitude of the excited state a_2 , so to make equation (3.14) tractable an assumption is made, known as the weak field approximation, that the lower state population is not depleted by the excitation and can be ignored. Equation (3.16) can then be integrated to give the upper state amplitude after the perturbation has been removed, i.e. after the laser pulse,

$$a(t) = -\frac{1}{2}\Omega_{Rabi} \int_{-\infty}^{\infty} f(t)e^{-i\omega_0 t} dt = -\frac{1}{2}\Omega_{Rabi}g(\omega) \quad (3.18)$$

where $g(\omega) = \exp[-(\omega - \omega_0)^2 \tau_p^2 / 8 \ln 2]$ is the Fourier transform of the laser pulse. The experimental observable, discussed in later sections, is $S \propto |a(t)|^2$.

If the excitation is made by a broad bandwidth picosecond laser pulse coupling a launch state $|g\rangle$ with several Rydberg states $|n\rangle$, the resulting wave function may be expressed,

$$\Psi(r, t) = a_g \psi_g(r) e^{-i\omega_g t} + \sum_n a_n(t) \psi_n(r) e^{-i\omega_n t}, \quad (3.19)$$

where $a_{g,n}$ are, respectively, the time-dependant amplitudes of the launch and Rydberg states with stationary radial wavefunctions $\psi_{g,n}(r)$, and angular frequencies $\omega_{g,n}$. Thus, following excitation by $k + 1$ pulses, the population of each Rydberg state $|n\rangle$ becomes,

$$a_n(t) = -\frac{i}{2}\Omega_n g_n \left[1 + \sum_k e^{i\Delta_n t_k} e^{i\omega_k t} \right], \quad (3.20)$$

where $\Delta_n = \omega_n - \omega_g - \omega$ is the *detuning* frequency. The term in square brackets oscillates with an angular frequency $\omega = \omega_g - \omega_n$, the angular frequency of the laser pulse resonant with the transition. When multiple Rydberg states have been excited these terms beat in and out of phase with each other. For a wave packet excited in a single Rydberg series, this beating can be understood by casting the frequency as a Taylor expansion about the average, or central, principal quantum number,

$$\omega_n = -\frac{1}{2n^2} = -\frac{1}{2\bar{n}^2} \left[1 - 2\frac{\delta n}{\bar{n}} + \left(\frac{\delta n}{\bar{n}}\right)^2 - \dots \right] \quad \text{for } \delta n \ll \bar{n}, \quad (3.21)$$

where $\delta n = (\bar{n} - n)$ and \bar{n} is the central principal quantum number of the wave packet, which corresponds to the central angular frequency of the laser field, $\omega = -1/2\bar{n}^2$. The first term in the expansion corresponds to the average oscillation of the population

amplitude of the wave packet. The second term is linear in δn and gives rise to a harmonic phase evolution of the population amplitudes. This is the classical oscillation of the wave packet with period $T_{cl} = 2\pi\bar{n}^3$, and can be understood as follows. In the time taken for its excitation by a laser pulse the wave packet essentially does not move, i.e. the excitation is impulsive. The radial distribution of the 3s electron, which is close to the core, is mapped into the much larger distribution of the Rydberg states. Therefore it immediately starts to move away from the core to sample the full spatial extent of the Rydberg states. When it reaches the edge of the Coulomb potential it is reflected back towards the core. This oscillation would continue indefinitely were it not for the anharmonicity of the Coulomb potential, which causes the wave packet to de-phase and spread as described by the third term in equation (3.21), which is quadratic in δn . The dispersion spreads the wave packet over the whole radial coordinate. This leads to interference that generates partial revivals – sub-wave packets that are distributed around the radial coordinate and visit the core at equal time intervals. At time $T_R = \bar{n}T_{cl}/3$ there is a full revival where the single wave packet reforms. This revival structure was first seen in calculations by Parker and Stroud [4], and elucidated by Averbukh and Perelman [5]. Typical temporal evolution of a radial Rydberg electronic wave packet is shown in figure 3.2.

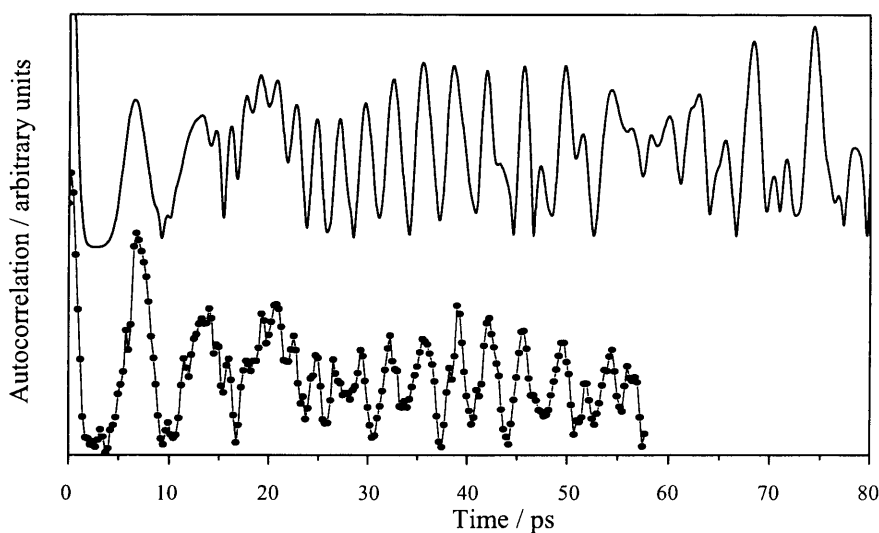


Figure 3.2 Experimental (lower trace) and calculated (upper trace) recurrence spectra of a radial Rydberg electronic wave packet in sodium excited around $n = 35$ showing its classical-like recurrence at 6.51 ps, dispersion of the recurrence, a third order partial revival around 20 ps, a second order partial revival around 40 ps and a full revival around 70 ps.

Although it is not obvious in the above figure, there is a quantum beat between the angular momentum states in addition to the obvious oscillation of the wave packet. The beat period depends on the difference between the quantum defects $\Delta\mu$ of Rydberg series,

$$t_{ang} = -\frac{T_{cl}}{\Delta\mu}. \quad (3.22)$$

In the case of the sodium s and d Rydberg series excited here, the quantum defect difference is 0.35 (in modulo 1) giving an angular beat period of 18.6 ps.

D. INTERFEROMETRIC CONTROL OF RYDBERG ELECTRON WAVE PACKETS

The presence of phase properties of a wave packet suggests that it may be possible to engineer interference effects to exert control, and that is exactly the approach taken in this work. This type of coherent control was first demonstrated by Noel and Stroud [6, 7]

I. WAVE PACKETS SEPARATED BY T_{cl}

The phase behaviour we shall examine first derives from the difference between the quantum defects of the two Rydberg series that are excited in the wave packet. Consider the Rydberg state component of the wave function shown in equation (3.3),

$$\Psi(r, t) = \sum_{nl} a_{nl} \psi_{nl}(r) \exp(-i\omega_{nl}t), \quad (3.23)$$

where $\psi_{nl}(r)$ is the radial wavefunction of the eigenstate $|nl\rangle$ with amplitude a_{nl} in the wave packet and angular frequency $\omega_{nl} = -1/2(n - \mu_l)^2$. Defining an effective principal quantum number, $\nu_{nl} = n - \mu_l$ and making the substitution $\omega_{nl} = -1/2\nu_{nl}^2$ allows expansion of the frequency about the central state of the wave packet $\bar{\nu}$,

$$\begin{aligned} \omega_j &= -\frac{1}{2\bar{\nu}^2} \left[1 - 2\left(\frac{\delta\nu}{\bar{\nu}}\right) + 3\left(\frac{\delta\nu}{\bar{\nu}}\right)^2 - \dots \right] \\ &= -\frac{1}{2\bar{\nu}^2} - \frac{(\nu_j - \bar{\nu})}{\bar{\nu}} - \dots \end{aligned} \quad (3.24)$$

Substituting this back into the time dependent term of equation (3.6) gives,

$$\exp(i\omega_{nl}t) = \exp\left[-\frac{i(n_j - \bar{n})t}{\bar{n}^3} + \frac{i\mu t}{\bar{n}^3}\right] \quad (3.25)$$

$$= \exp\left[-2\pi i(n_j - \bar{n})\frac{t}{t_{cl}}\right] \exp\left[2\pi i\mu\frac{t}{t_{cl}}\right] \quad (3.26)$$

The first term corresponds to the classical recurrence of the wave packet dictated by the spacing of the energy levels in the superposition. The second exponential shows a phase shift of $2\pi\mu$ accumulating for every orbit of the wave packet. This idea can be easily extended to two Rydberg series, as required by the current work, giving an accumulated phase difference between the angular momentum components of $2\pi\Delta\mu$ for each orbit of the wave packet, where $\Delta\mu$ is the difference (in modulo 1) between the quantum defects of the s and d Rydberg series.

If a second wave packet, identical to the first, is then excited it can be phase-matched to either one or other angular component of the existing wave packet. By suitable phase matching, the quantum state of the system can be controlled. For example, if the second wave packet is excited exactly in phase with the d component of the first, the population of the d Rydberg states of the system will be enhanced. Alternatively if the second wave packet is exactly out of phase with the d component of the first, the result will be zero d -state population. It would be nice if while enhancing the population of one angular component we could simultaneously depopulate the other. This situation is possible but not with the quantum defects of sodium.

To observe the result of coherent control discussed here the Rydberg state populations were analysed using state-selective field ionisation. This experimental technique allows the relative populations of the Rydberg states in the wave packet to be observed directly by ionising them sequentially. The experimental details are discussed in section 3.2B and the results in section 3.3C.

II. WAVE PACKETS SEPARATED BY $3T_{cl}/2$

In addition to the phase contribution from the quantum defect, there is a phase evolution arising in all wave packets in anharmonic potentials. Averbukh and Perelman [5, 8] showed that around the time of the second order partial revival, the wave function of the wave packet can be written

$$\psi(r, t = T_{rev}/2) = \frac{1}{\sqrt{2}} [\exp(-i\pi/4)\psi_{cl}(r, t) + \exp(i\pi/4)\psi_{cl}(r, t + t_{cl}/2)] \quad (3.27)$$

where $\psi_{cl}(r, t)$ and $\psi_{cl}(r, t + t_{cl}/2)$ are the two sub wave packets, separated in time by half the classical orbit period. The exponents show there exists a phase difference of $\pi/2$ between the two sub-wave packets forming a second order partial revival. These ideas have been used to develop an additional coherent control scheme [9, 10], developing the ‘Young’s Double-Slit Interferometry’ approach of [6]. To utilise the phase behaviour of wave packet revivals, it must be combined with the phase accumulation arising from the quantum defect. Equation (3.26) can be used to find when the accumulated phase difference between the two angular momentum components of the wave packet is exactly π , i.e. when

$$\phi = 2\pi\Delta\mu \frac{t}{t_{cl}} = \pi \quad (3.28)$$

The difference in quantum defects for the s and d states in sodium are 0.35 (modulo 1). If this is approximated to $1/3$ it is clear from equation (3.28) that $t/t_{cl} = 3/2$ is required for the two series to be out of phase. That is, the two angular momentum components will be exactly out of phase after $1\frac{1}{2}$ orbits of the wave packet. If a second identical wave packet is launched at this time they will not immediately interfere because they occupy different regions of space. Figure 3.3 illustrates the situation and resulting interference.

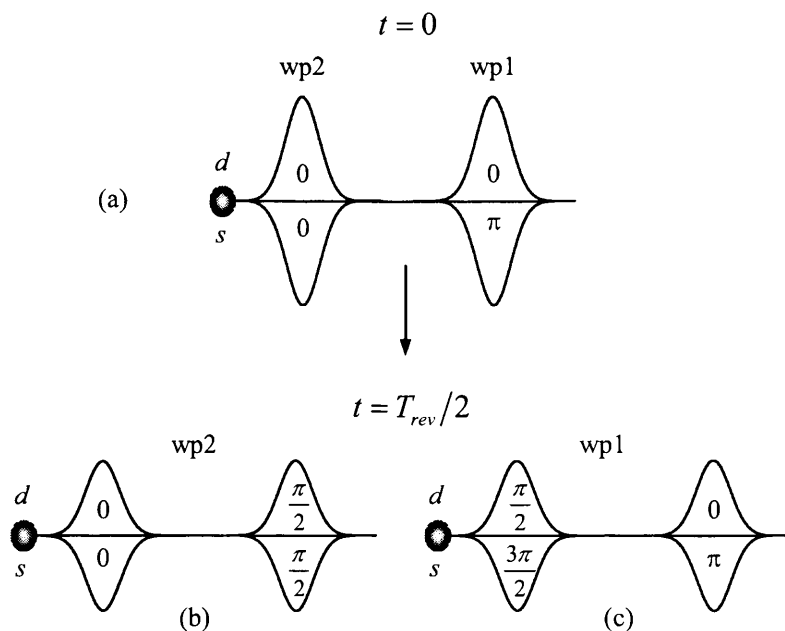


Figure 3.3 Cartoon showing the relative phases of two wave packets that arise when the second wave packet (wp2) is excited in phase with the d component of the first (wp1), after the first has performed $1\frac{1}{2}$ orbits, (a). Both wave packets are allowed to evolve to the second order partial revival, (b) and (c), at which time their sub-wave packets have the indicated phases. Labelling the d state phase of wp1 at the outer turning point as 0 fixes the phase of the d part of wp2 at the inner turning point. The relative phases between d and s parts of the same wave packet is retained from (a). The phases of the partial revivals derive from the $\pi/2$ rule. Inspection of the phases for the s and d components between wp1 and wp2 at the inner and outer turning points reveals neither fully constructive nor destructive interference.

The first wave packet is at the outer turning point and the second is formed near the nucleus. If the system is allowed to evolve until the second order partial revival ($T_R/2 = nT_{cl}/6$), the two wave packets will occupy the same regions of space and can interfere. In the special case that $n/6 = 3k$, where $k = 1, 2, \dots$, the relative phases of the first and second wave packets retains the value it had when the second wave packet was formed, and the partial revivals have the phase relationships discussed above. Since the relative phases of the two wave packets are fixed when the second is excited, by controlling this initial phase difference we can engineer a phase relationship at the second order partial revival that results in constructive or destructive interference. Figure 3.4 illustrates the principle of this coherent control strategy.

(a)

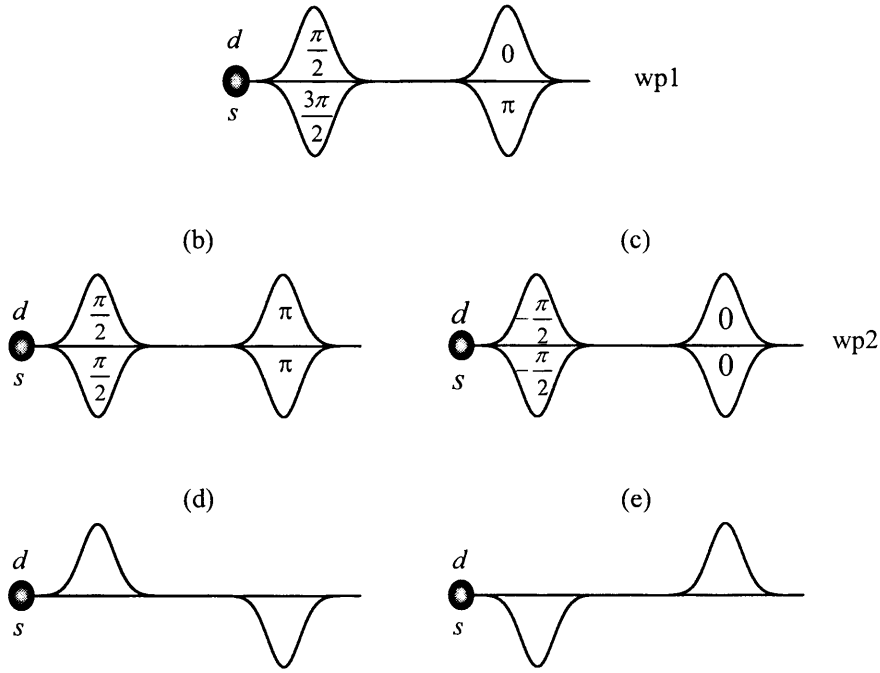


Figure 3.4 Cartoon illustrating two opposite instances of coherent control using wave packet interference at the second order partial revival. If the second wave packet is excited with an initial phase difference of $\pi/2$ to the first, by the second order partial revival the sub-wave packets will have phases shown in (a) and (b). Sub-wave packets from wp1 and wp2 with the same angular momentum interfere where they overlap spatially. Where there is zero phase difference they interfere constructively to enhance the amplitude. Where there is a π phase difference destructive interference removes the wave packet amplitude. The resulting wave packet (d) has a d component localised at the inner turning point, and an s component at the outer. The location of the constructive and destructive interference is inverted (e) if the second wave packet is initially shifted by $-\pi/2$ with respect to the first (c).

By phase shifting the second wave packet by $\pi/2$ from the first, by the time of the second order partial revival the phases of the angular components of the sub wave packets will have evolved such that the d components interfere constructively at the inner turning point but destructively at the outer turning point, and vice versa for the s component. By shifting the phase of the second wave packet by $-\pi/2$, the positions of constructive and destructive interference are reversed.

In summary, the wave packet resulting from the interference of two identical wave packets phase shifted and separated in time by the classical orbit period of the wave packet is divided into two, each with different angular momentum character. The

control approach discussed above requires monitoring of alterations in the dynamical behaviour of the wave packet. This is done using a phase sensitive wave packet interferometry technique known as the optical Ramsey method. Experimental and theoretical aspects of the approach are discussed in section 3.3D.

3.2 EXPERIMENTAL

A. MOLECULAR BEAM

The molecular beam apparatus was described in detail in Chapter 1. The particular setup used in all the sodium atom experiments is shown in figure 2.15. The distance between the nozzle and the skimmer tip was approximately 70 mm. The interaction region was approximately 200 mm from the skimmer tip. The oven was operated at approximately 600 °C, with the nozzle held approximately 50 °C higher to prevent blocking by sodium. The pressure in the source chamber was difficult to measure as sodium appears to interfere with operation of the Penning gauge, but was approximately 5×10^{-5} mbar. The pressure in the experimental chamber was typically around 3×10^{-7} mbar.

Simple geometric considerations of the relative positions of the nozzle, skimmer and interaction region indicate that the sodium beam had a diameter of approximately 4 mm in the interaction region. Evaluation of equation (2.13) indicates the Mach number in the interaction region would be around 650 if the expansion was ideal and there was no skimmer. From this it is possible to calculate the number density from equation (2.9) and consideration of the source pressure and temperature. The calculated number density at the interaction region was estimated to be $7.5 \times 10^{15} \text{ m}^{-3}$.

B. LASERS

The lasers used in these coherent control experiments are part of an existing set-up, shown schematically in figure 3.5, that has been successfully employed in Rydberg electron wave packet dynamics and coherent control in xenon [9, 10] and NO [11]. The

frequency spectra (section 3.3B) were recorded using a nanosecond dye laser, which is also described in this section.

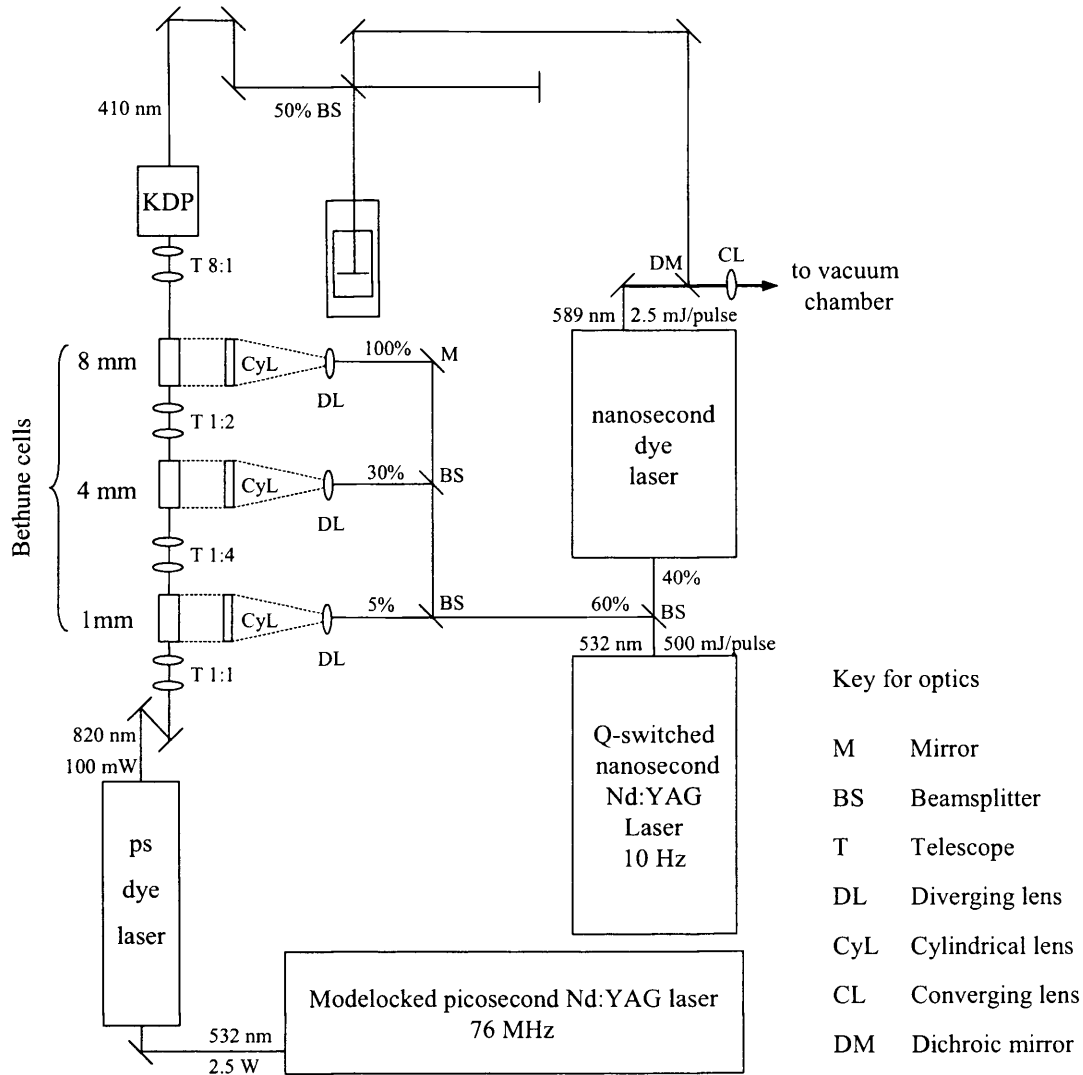


Figure 3.5 Schematic layout of the laser bench for wave packet interferometry experiments. The output of a picosecond Nd:YAG-pumped dye laser is amplified in a series of three Bethune cells using part of the output from a nanosecond Nd:YAG laser operating at 10 Hz. The amplified picosecond beam is frequency-doubled and passed through either a single or a nested Michelson interferometer. The resulting phase-locked pulse pair or pulse triplet crosses the sodium molecular beam to excite the Rydberg electron wave packet. The remainder of the nanosecond YAG beam pumps a narrow linewidth dye laser, which is used to excite the $3^2P_{1/3}$ and $3^2P_{3/2}$ states from the ground state.

I. LASERS FOR FREQUENCY-RESOLVED SPECTRA

High-resolution frequency-resolved spectra were recorded prior to attempting time-resolved experiments to establish the accessible energy levels. The excitation scheme is shown in figure 3.1 and is the same as that for time-resolved spectra. A nanosecond dye laser was used to excite from the ground $3^2S_{1/2}$ state to the intermediate $3^2P_{3/2}$ state. From there a second dye laser excited the Rydberg states. Frequency spectra were recorded by scanning the wavelength of the second laser, pulsed-field ionising the excited Rydberg states and detecting either the resulting ions or electrons on an MCP.

To excite from the $3^2S_{1/2}$ ground state of sodium to the intermediate $3^2P_{1/2}$ or $3^2P_{3/2}$ states in both frequency and time-resolved studies, we used a Continuum ND6000 dye laser. Rhodamine 610 dye at concentrations of 0.11 g L^{-1} in methanol for the oscillator and 0.02 g L^{-1} for the amplifier was pumped by the 10 Hz Nd:YAG with around $200 \text{ mJ pulse}^{-1}$ at 532 nm and generated approximately 2 mJ pulse^{-1} at 589 nm with a bandwidth specified at 0.05 cm^{-1} .

Excitation of the sodium Rydberg states for frequency spectra (section 3.2A) and for signal analysis of the state-selective field ionisation data (section 3.2D) was made by the output of a Sirah Precisionscan dye laser (not shown in figure 3.5) on loan from the Rutherford Appleton Laboratory. This was operated with Exalite 411 dye (0.15 g L^{-1} in *p*-dioxane in the oscillator and pre-amplifier and 0.04 g L^{-1} in the amplifier). Around 410 nm the dye laser generated $10 \text{ }\mu\text{J pulse}^{-1}$ with a bandwidth of 0.1 cm^{-1} (0.0024 nm). Wavelength tuning is by means of a variable angle grating ($1800 \text{ lines mm}^{-1}$) under computer control. The beams from both dye lasers were combined on a dichroic beam splitter and focussed collinearly into the sodium atomic beam with a 300 mm lens.

The two dye lasers were pumped by a Continuum Powerlite II 8000 Nd:YAG laser borrowed from the Rutherford Appleton Laboratory. The Powerlite is a Q-switched Nd:YAG laser operating at 10 Hz. It generates 5-8 ns pulses with 1100 mJ per pulse at 1064 nm and 1 cm^{-1} bandwidth. It was operated in two modes: to pump red (Rhodamine 610) and infrared (Staryl 9) dyes, the 1064 nm output was frequency doubled in KDP to give 532 nm with $500 \text{ mJ pulse}^{-1}$. To pump Exalite 411 dye, which

emits around 410 nm, the 532 nm light was mixed with the fundamental to give 355 nm at 280 mJ pulse⁻¹.

II. LASERS FOR COHERENT CONTROL EXPERIMENTS

For the coherent control experiments, excitation from the ground $2^1S_{1/2}$ state of sodium to the intermediate state ($3^2P_{1/2}$ or $3^2P_{3/2}$) was by the Continuum nanosecond dye laser as above. Rydberg electron wave packets were excited by the output of an amplified picosecond dye laser. This system starts with the frequency doubled output of an actively modelocked picosecond Nd:YAG laser (Coherent Antares 76s) generating 2 W output power at a repetition rate of 76 MHz at 532 nm. This was used to pump Staryl 9 (LDS 821) dye (2 g L^{-1}) dissolved in propylene carbonate (300 mL) and ethylene glycol (700 mL) in a synchronously pumped picosecond dye laser (Coherent 700). An intracavity birefringent filter (BRF) allows for wavelength selection by manually turning a micrometer screw gauge. For these experiments a three-plate BRF was fitted that limited the output bandwidth to approximately 21 cm^{-1} around 810 nm. The output power was typically 50 mW at 76 MHz repetition rate. The pulse duration was monitored periodically by taking its autocorrelation with a commercial autocorrelator (Femtochrome Research FR103).

The beam then passed, via two steering mirrors, through a lab-built amplifier comprising three Bethune [12] cells as indicated in figure 3.5. A cross section of a Bethune cell is shown in figure 3.6. The amplification is maximised when $\alpha r = 1$, where α is the absorption coefficient of the dye solution at the pump wavelength (532 nm in this case) and r is the radius of the channel. This determines for each cell the diameter of the beam being amplified, the dye concentration and the pump energy. In our amplifier the first cell has a diameter of 1 mm, the second 4 mm and the third 12 mm. The cell lengths are 30 mm, 40 mm and 40 mm respectively. Before each cell is a collimating telescope, which also expands the beam for cells 2 and 3. The concentrations of Staryl 9 dye in methanol were approximately 50 mg L^{-1} , 12.5 mg L^{-1} and 4.2 g L^{-1} for cells 1, 2 and 3 respectively. 60 % ($300 \text{ mJ pulse}^{-1}$) of the 10 Hz Nd:YAG laser output was directed to the amplifier and directed to the Bethune cells by the beam splitters shown in figure 3.5.

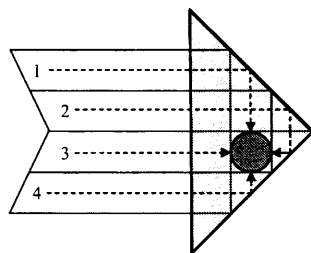


Figure 3.6 A cross-section through a Bethune cell (shaded triangle) showing the position of the channel for the dye solution (off-centre circle) and its diameter relative to the whole cell. The beam being amplified must be collimated and of the same diameter as the channel. It passes through the dye solution in the channel in the same direction as the dye. The pump laser beam approaches from the right and is expanded to four times the diameter of the dye channel so that its internal reflection pumps the channel from all sides, as shown by the numbered blocks.

The pump pulse energies were 15 mJ, 85 mJ and 200 mJ for cells 1, 2 and 3. To effect the pumping shown in figure 3.6, before impinging on the cell each pump beam was expanded to four times the channel diameter by a diverging lens, and collimated using a cylindrical lens.

The output of the amplifier is a train of picosecond pulses of 300 μJ with a repetition rate of 10 Hz. After the final Bethune cell the beam diameter is reduced to approximately 1 mm by a collimating telescope before frequency doubling in an 18 mm long KDP crystal, yielding $\approx 20 \mu\text{J}$ pulses around 410 nm with a bandwidth of approximately 21 cm^{-1} .

Careful synchronisation is required if this amplification is to be successful. A pulse from the 10 Hz pump laser has to coincide exactly with one of the pulses in the 76 MHz pulse train from the picosecond dye laser. This is achieved, as figure 3.7 shows, by locking the trigger timing of the nanosecond YAG to the optical pulse timing of the picosecond YAG. In addition to optical alignment, the Q-switch timing of the nanosecond laser must be optimised to maximise the frequency-doubled pulse energy. The 10 Hz pulse timing is used to synchronise data collection electronics to the laser pulses, which is discussed in section 3.2C

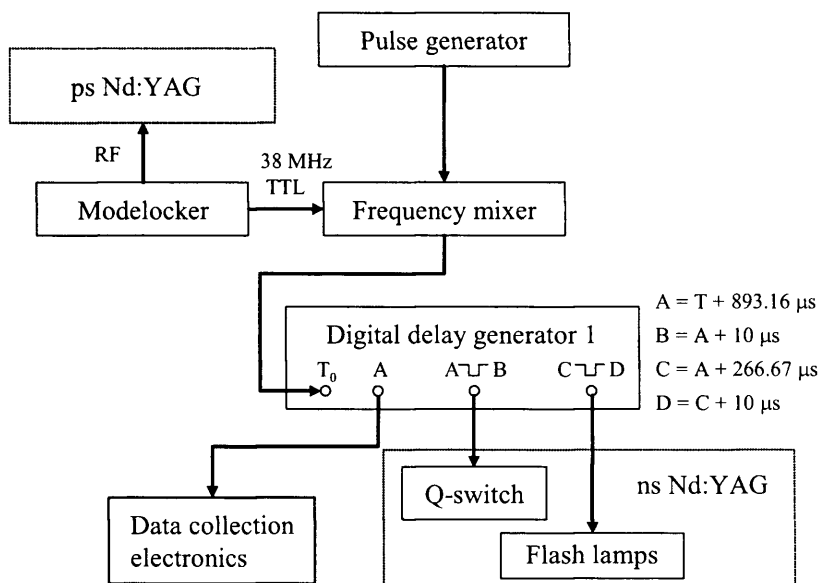


Figure 3.7 Synchronisation of the picosecond and nanosecond lasers and data collection electronics. A 10 Hz TTL from a function generator (Thandar TG105) is synchronised with a 38 MHz TTL from the modelocking electronics for the picosecond Nd:YAG laser by frequency mixing (Hatfield 1750). The 38 MHz signal is synchronous with the laser output. The locked 10 Hz TTL is then time-delayed by a digital delay generator (SRS DG535) and used to generate triggering TTL pulses for the nanosecond Nd:YAG laser and data collection instrumentation via a second delay generator (see figure 3.10). Typical delays are shown relative to the trigger T for each output of the delay generators.

III. MICHELSON INTERFEROMETER

To generate sequences of phase-locked picosecond laser pulses, the frequency doubled picosecond beam is directed into a nested or three-path Michelson-type interferometer. The layout and operation of the interferometer are shown in figure 3.8.

The interferometer generates three phase-locked picosecond pulses with variable phase and timing between them for use in time-resolved coherent control experiments. Time delay and relative phase are altered by moving the mirrors MM1 and MM2. Coarse time delays are achieved by moving computer controlled DC motor-driven translation stages (Physik Instrumente M510.12). The range of the stages is 100 mm, which corresponds to a 670 ps pulse delay. To minimise the distance the stages have to be moved the relative path lengths are adjusted so that the second pulse comes from

path 1 in the figure. Phase control is effected by piezoelectric linear translators (Physik Instrumente P780.00 and P753.31C) mounted on the translation stages, and upon which the mirrors are mounted.

The time-resolved single wave packet experiments and the coherent control experiments detected by state-selective field ionisation require only two phase-locked pulses. The interferometer can be quickly reconfigured to generate two pulses instead of three by blocking one of the moving arms, or by using the normally wasted beam from BS2.

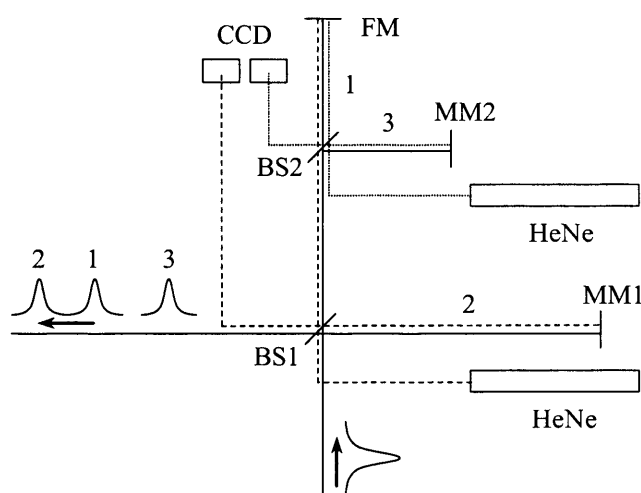


Figure 3.8 Schematic of the nested Michelson-type interferometer. The incoming picosecond laser pulse (solid line) divides equally at the first beamsplitter (BS1). The pulse in path 2 is reflected off a moving mirror (MM1) back to BS1, where it divides in half again. The transmitted half is pulse 2 and the reflected half is wasted. The pulse in path 1 passes through the second 50% beamsplitter (BS2) to the fixed mirror (FM), then back to BS1 where it is reflected as pulse 1. Pulse 3 is generated by reflection at BS2 and at a moving mirror (MM2), re-reflection at BS2, and finally reflection at BS1. Half of each pulse reflected off MM2 and FM is lost on returning to BS2. To ensure all the pulses have the same energy after the interferometer, MM1 is therefore only 25% reflecting. Each of the output pulses has $1/16^{\text{th}}$ of the input pulse energy. Stabilisation for each moving mirror is made with reference to the fixed mirror with interference fringes from a separate HeNe laser. Interference fringes from the paths shown in dotted and dashed lines are collected separate CCD arrays.

In order that the three (or two) output pulses from the interferometer be phase-locked, it is necessary to stabilise the interferometer from vibrations that alter the

relative path lengths. Each moving mirror is stabilised independently with reference to the fixed mirror by monitoring interference fringes from a HeNe laser beam that passes through the interferometer as shown in figure 3.8. Two different stabilisation systems are in use: a home-built analogue instrument that stabilises path 2 in figure 3.8, and a digital system controlled by a personal computer (PC) that stabilises path 3. The analogue system samples HeNe (Carl Zeiss Jena LGK7628) interference fringes (from the paths shown as a dashed lines) that are expanded onto a 1-dimensional CCD array. The electronics monitors the position of the fringes on the CCD and a PID feedback loop moves the piezoelectric actuator to correct any movements.

The digital system operates in essentially the same way, but uses commercial hardware controlled by software running on a PC. HeNe (Plasma 303) interference fringes (from the paths indicated by dotted lines in figure 3.6) are expanded onto a CCD camera (Basler L101k-1k) and digitised by a PCI expansion card in the PC (Bitflow RoadRunner CL). A lab-written software PID loop running in LabView (National Instruments LabView v5.1) monitors the fringes and generates a signal to move the piezoelectric actuator (Physik Instrumente P753.31C) to correct for movements. This signal is sent to the piezo driver (Physik Instrumente E501.00, a $\times 10$ voltage amplifier) by a 16-bit analogue output PC expansion card (National Instruments PCI 6703).

C. THE INTERACTION REGION

Both for frequency-resolved and time-resolved experiments, the laser beams (either two nanosecond beams or one nanosecond and one picosecond beam) were focussed into the sodium atomic beam using a 250 mm lens. The atomic and laser beams crossed at 90° in a horizontal plane half way between the extractor and repeller plates at the base of the time-of-flight mass spectrometer, as shown in figure 3.9.

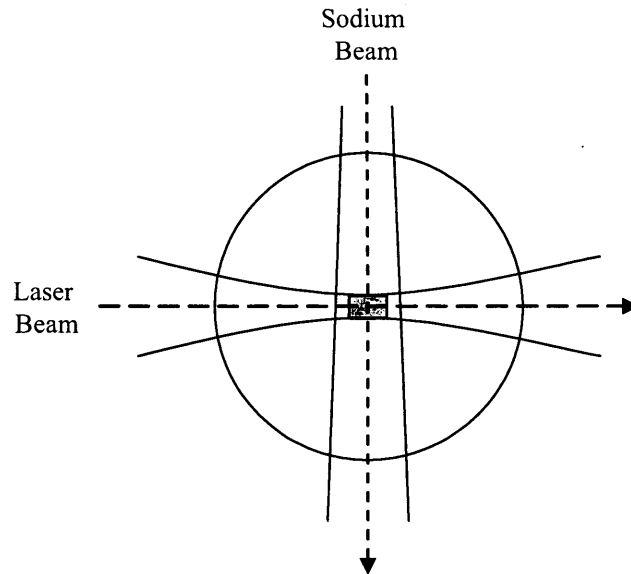


Figure 3.9 A schematic representation of the interaction region viewed along the electron/ion time-of-flight axis. The slightly diverging sodium atomic beam has a diameter estimated as 4 mm and is crossed by the focussed laser beam at 90° in the plane of the page. The curved lines indicate the extent of the laser beam perpendicular to the propagation axis and mark where the laser intensity falls to $1/e^2$ of its value at the beam centre. The beam radius reaches a minimum, w_0 , at the waist. The distance along the propagation axis before and after the beam waist, where the beam radius reaches $\sqrt{2}w_0$ defines the interaction volume (shaded region), which is limited by the laser beams not the atomic beam. The circle indicates the 10 mm diameter hole in the centre of the extractor plate through which ions or electrons (depending on the field polarity) are accelerated towards the detector (out of the plane of the page).

Both the nanosecond and picosecond lasers operating at around 410 nm had a beam diameter estimated by eye to be approximately 6 mm prior to focussing. Under the assumption of a diffraction-limited Gaussian beam, this leads to a beam waist radius at the focus of $w_0 = f\lambda/\pi w_s \approx 11\ \mu\text{m}$, where f is the focal length of the lens, λ is the wavelength and w_s is the unfocussed beam radius. The beam radius is taken as the distance from the beam centre to the point where the intensity falls to $1/e^2$ of the peak intensity. The confocal parameter, defined as twice the Rayleigh range $2z_R = 2\pi w_0^2/\lambda \approx 2\ \text{mm}$ and is the distance along the beam propagation direction from the position of the minimum beam waist, w_0 , where the beam waist has expanded to

$\sqrt{2}w_0$. This defines an interaction volume of approximately $7.6 \times 10^{-13} \text{ m}^3$. The number density of sodium atoms discussed in section 3.2A is $7.5 \times 10^{15} \text{ m}^{-3}$, so each laser pulse interacts with approximately 5000 atoms.

The PrecisionScan nanosecond dye laser used to excite Rydberg states for frequency spectra generates $10 \text{ }\mu\text{J}$ pulses of approximately 5 ns duration. The power density at the interaction region for this excitation is approximately $5 \times 10^8 \text{ W cm}^{-2}$. After the Michelson interferometer, the energy of the picosecond laser pulses reaching the interaction region is approximately $5 \text{ }\mu\text{J}$ and their duration is around 1 ps , giving a power density of approximately $1 \times 10^{12} \text{ W cm}^{-2}$.

D. DATA COLLECTION

Data collection for all the experiments described in this chapter is done with the same basic arrangement of instruments, which is shown in figure 3.10. Each experiment also has its own details and these are discussed here. All data collection is controlled by lab-written software running under LabView on a Windows PC.

I. FREQUENCY SPECTRA

Frequency resolved spectra of the Rydberg states were collected using the above set-up but the interferometers were not used so the software does not move the motor or piezoelectric translators. For this work the Rydberg states were pulsed-field ionised by a square high voltage (HV) pulse of 2000 V , generating a field in the interaction region of 2000 V cm^{-1} . The HV pulse was switched on between 50 ns and 100 ns after the laser pulse and lasted for $30 \text{ }\mu\text{s}$. The timing and rise of the HV pulse was monitored by a 1:1000 image signal from the pulser. The HV pulse timing was compared to a photodiode signal from the laser pulse on the oscilloscope and set using the variable delay generator (Stanford Research Instruments DG535) prior to running the experiment.

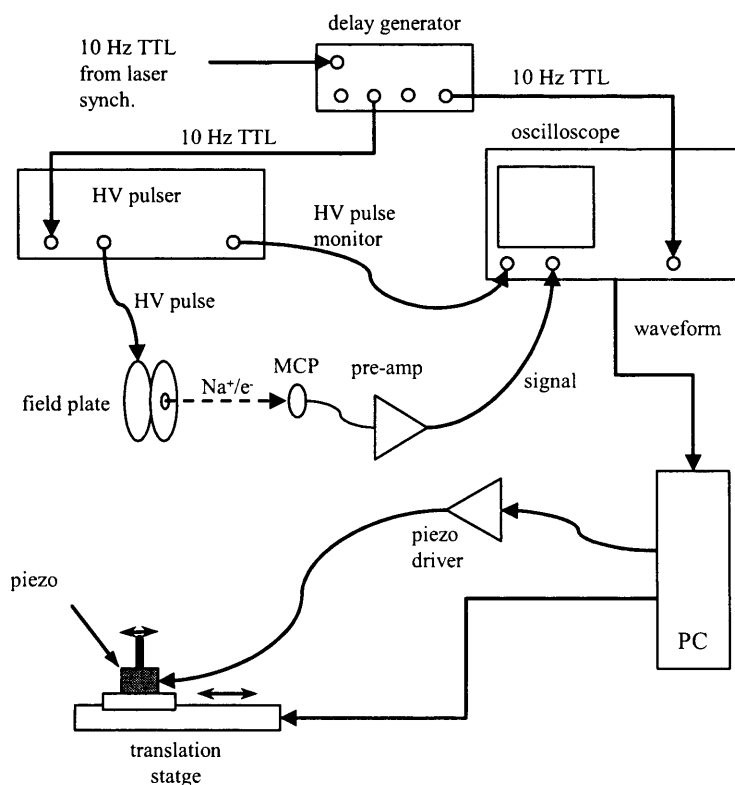


Figure 3.10 Schematic showing the interconnection of data collection instruments. Straight connectors carry digital signals, curved connectors are for analogue signals. Timing of data collection events derives from the laser-synchronized 10 Hz TTL described in figure 3.7. This signal triggers a delay generator (SRS DG535), which triggers the high-voltage pulse generator (Directed Energy PVX4140) and waveform capture by the oscilloscope (LeCroy Waverunner LT372). The HV pulse is triggered after a delay of $266.46 \mu\text{s}$ and the pulse lasts for $300 \mu\text{s}$. The oscilloscope is triggered $2.48 \mu\text{s}$ after the HV pulse is triggered. The high voltage pulse ionises the sodium atoms and repels the ions or electrons towards the MCP. The MCP output is pre-amplified (Ortec-EG&G VT120) and then sampled by the oscilloscope. The digital waveform is recorded on a PC, which also controls the oscilloscope (via GPIB), and movement of the piezoelectric and motor driven mirror translators. For clarity only one of the two motor plus piezo translation setups is shown.

The data collection software downloads the current waveform from the oscilloscope (LeCroy Waverunner LT372) every 100 ms, integrates it to give the total ion or electron signal for each laser shot, and writes this to file. It is possible to average the integrated data over several laser shots if required, and we typically averaged over 5 laser shots. The laser was typically set to scan at 0.01 nm s^{-1} for these spectra, so

averaging leads to a very small error. The software does not communicate with the dye laser or control its scanning. Instead, it simultaneously records the wavelength from a wavelength meter (Angstrom WS7) running on a separate PC. There is only one wavelength data point for every four spectral data points so, in order to plot the spectrum against wavelength, the wavelength data is interpolated to have the same number of points as the spectrum.

II. RECURRENCE SPECTRA AND OPTICAL RAMSEY METHOD COHERENT CONTROL

Recurrence spectra of single wave packets and two-wave packet coherent control are detected by the *optical Ramsey method* (ORM). This approach was developed by Noordam, Duncan and Gallagher [13] and, like the coherent control strategies described here, relies on phase and interference effects of wave packets.

Formally, the optical Ramsey method shares the same basis as the coherent control scheme discussed in section 3.1C. The probe pulse forms a wave packet that is identical to the first (and second, in the control experiments). For the case of a single existing wave packet being probed by an identical probe wave packet, the amplitude of Rydberg states $|n\rangle$ can be written [14],

$$a_n(\tau_d) = -\frac{i}{2}\Omega_n g_n [1 + \exp(i\Delta_n \tau_d) \exp(i\omega \tau_d)] \quad (3.31)$$

where τ_d is the time delay between the pump and probe wave packets and other terms have the definitions given above. The $\Delta_n \tau_d$ term in the exponent is a slow oscillation corresponding to the wave packet overlap, underneath which is a fast oscillation caused by interference term between the wave packets $\omega \tau_d$. This indicates that, since the probe wave packet is formed at the core, the existing wave packet is probed only in the vicinity of the core. The interference term causes the population to oscillate from 0 to $|2a^2| = 4|a|^2$ and this is seen as an oscillation on top of the constant signal from the incoherent sum of the two wave packets. In order to make a measurable signal from the Rydberg state population, a short time (typically $50 \leq t \leq 100$ ns) after the probe laser pulse the system is pulsed field ionised. The low field ionisation thresholds of Rydberg states assure nearly unit efficiency. Figure 3.11 shows the fast and slow oscillations in the total Rydberg population $P(\tau_d) = \sum_n |a_n|^2$ for a wave packet excited around $n = 35$

in sodium. The optical Ramsey signal is proportional to the time autocorrelation of the existing $\Psi(\tau)$ and probe $\Psi(0)$ wave packets [16, 17],

$$\langle \Psi(0) + \Psi(\tau) | \Psi(0) + \Psi(\tau) \rangle = \langle \Psi(0) | \Psi(0) \rangle + \langle \Psi(\tau) | \Psi(\tau) \rangle + 2\text{Re}[\langle \Psi(0) | \Psi(\tau) \rangle] \quad (3.32)$$

The first two terms on the right do not depend on the delay and contribute to the background ion (electron) signal. The last term gives the Ramsey fringes shown in figure 3.12. The optical Ramsey method thus provides two measurements of the existing wave packet: whether or not it is at the core, and the extent to which it resembles the probe wave packet. From this we can ascertain the temporal behaviour of the wave packet – the classical orbit period, dispersion and revival evolution, which allows observation of the temporal results of our coherent control experiments.

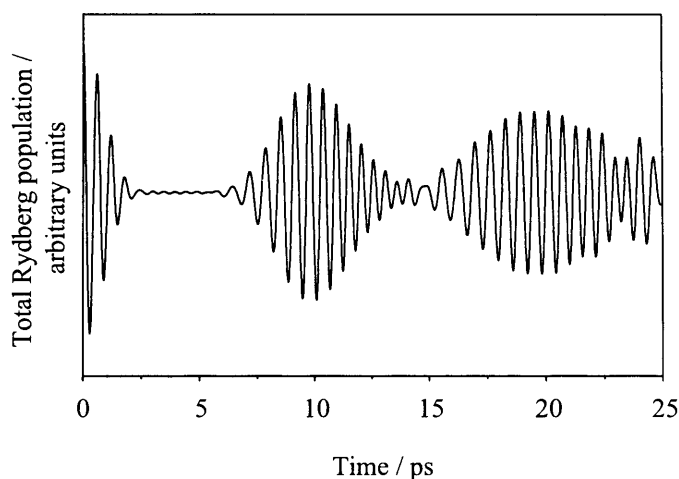


Figure 3.11 Calculated optical Ramsey fringes for a pair of wave packets excited around the $40p$ state of hydrogen. The fast oscillations indicate interference between the wave packets. Since the second wave packet is excited at the core, the slowly oscillating envelope originating from the spatial overlap of the wave packets indicates when both wave packets are at the core. The fast oscillation has been scaled by 2000 to facilitate plotting [15].

The instrumentation shown in figure 3.10 was used to record these spectra. To achieve the required pulsed-field ionisation, between 50 ns and 100 ns after the probe laser pulse the HV pulser applied a ± 2000 V square pulse (rise time ≤ 25 ns, duration 30 μ s) to the field plate. For these spectra, either Na^+ ions or electrons can be detected, but they were mostly done with ion detection using the Hamamatsu F4655-10 MCP. The ion signal from the MCP is sampled by the oscilloscope, transferred via GBIP to

the PC at 10 Hz, integrated, averaged, and written to file. It was found that averaging over 7 laser shots typically gave the best spectra. The software also controls the position of the motor and piezoelectric translators. The motor stages are controlled by an ISA format PC expansion card (Physik Instrumente C842). To acquire the spectrum of a single wave packet, where there is only one moving mirror in the interferometer, the spectrum starts with the moving arm of the interferometer shorter than the fixed arm and steps till the moving arm is longer. This shifts the timing of the laser pulse from the moving arm of the interferometer from (typically) -2 ps to $+70$ ps relative to the pulse from the fixed arm. Starting at 'negative time' allows us to clearly identify zero time, the point where the pulses arrive simultaneously. Data are collected at intervals of typically 0.2 ps, which corresponds to moving the motor driven translator by approximately $30\ \mu\text{m}$. At each interval a series of ion signal Ramsey fringes is recorded by stepping the piezoelectric translator through about 3 optical cycles in (typically) 40 steps. For light at 410 nm this corresponds to a step size of around 15 nm. The data written to file therefore comprises blocks of 40 data points, one block for each 0.2 ps step. To extract the recurrence spectrum, the raw data undergoes non-linear filtering by fitting a sine function to the interference fringes and taking the root mean square (RMS) value of each block of 40 data points, as shown in figure 3.12. Each block of 40 data points then gives one point in the recurrence spectrum.

Data collection in coherent control experiments using optical Ramsay method detection (three pulse experiments) is the same as above but there are two moving mirrors in the interferometer, as in figure 3.8. To keep the movement of the motor driven translators to a minimum, and so that each delay is measured from the fixed mirror rather than from another moving mirror, pulse 1 (pump pulse) comes from path 1 (the outer moving arm of the interferometer), pulse 2 (the control pulse) comes from the fixed arm and pulse 3 (detection pulse) from the inner moving arm.

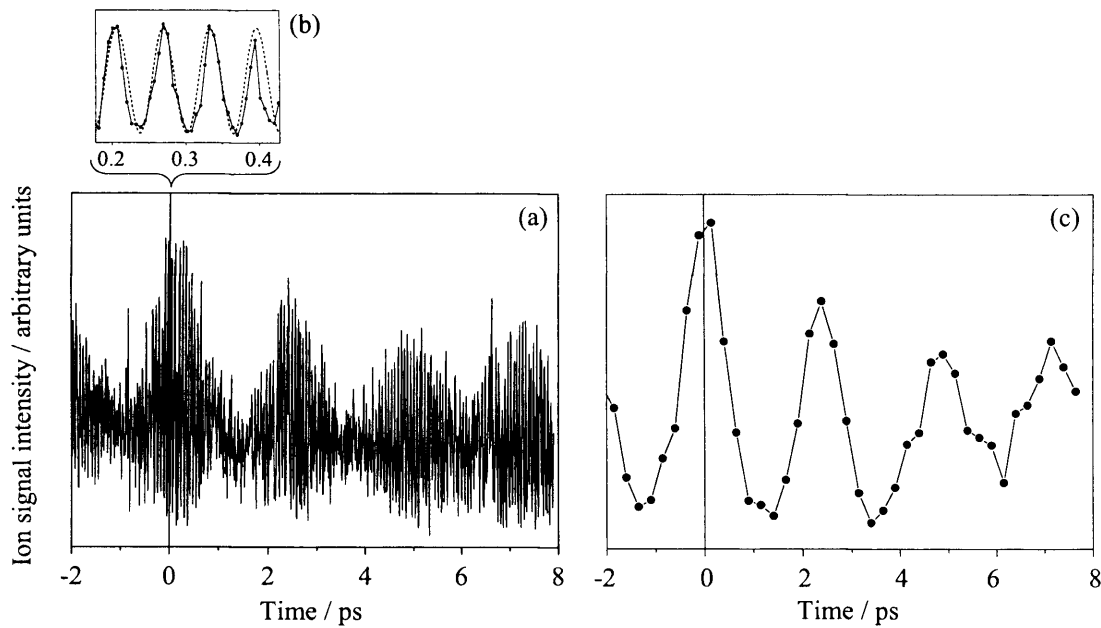


Figure 3.12 A sample of raw data from an ORM experiment in atomic sodium and its reduction to a recurrence spectrum. The raw data (a) comprises blocks from each coarse pump - probe delay. Each block samples the Ramsey fringes made by scanning the phase through approximately 8π in 40 steps. The trace also shows a superimposed sine wave used to extract the wavelength. Non-linear filtering, by taking the RMS of a fit of the fringes to a sine function, generates one data point in the recurrence spectrum (c) for each block of fringes.

Experience has revealed that the analogue stabilizer is more stable than the digital one in the long term. We therefore arrange that the timing between the first (pump) and second (control) laser pulses in three pulse coherent control experiments is stabilized by the analogue system. On the other hand the digital system is easier to use and has better short-term stability so it is used for two pulse experiments.

III. STATE SELECTIVE FIELD IONISATION

An alternative method to observe the effects of coherent control in Rydberg wave packets is state-selective field ionisation (SSFI). SSFI has been applied widely to state-selective detection of Rydberg states (see for example [18-21]), and Rydberg wave packets [7, 22-24], particularly those excited using half-cycle pulses [25, 26]. SSFI measures directly the population of the Rydberg states in the wave packet so

complements the optical Ramsay method, which monitors dynamical changes brought about by coherent control. The utility of SSFI in the current work is that it allows comparison between experimental results and calculated Rydberg state populations from equation (3.20).

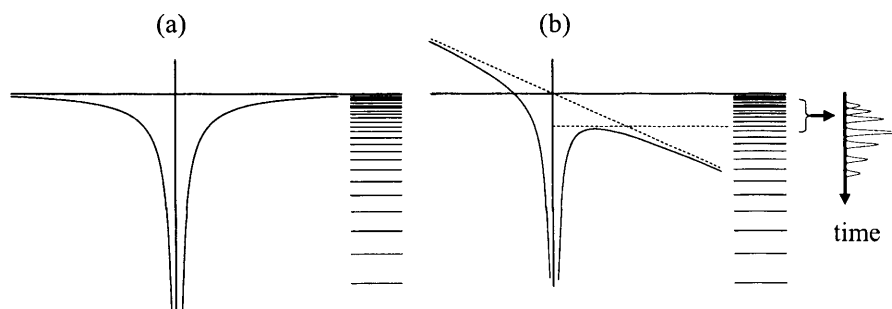


Figure 3.13 A schematic representation of state-selective field ionisation. The field-free Coulomb potential, (a), is tilted in the direction of the applied field, (b), creating a saddle point that falls as the field increases. Only electrons below the saddle point are classically bound and those above it ionize. If the field rises quickly, as in pulsed-field ionisation, all the states ionise effectively simultaneously. In state-selective field ionisation the field is increased sufficiently slowly that the states ionize sequentially and separately, as indicated on the far right.

The principle of state-selective field ionisation can be understood simply in terms of the Coulomb potential and is shown in figure 3.13 [2]. The tilted Coulomb potential is a classical picture but it provides a useful indication of the field required to ionise a particular Rydberg state [2]. The potential experienced by an electron moving along the z axis is,

$$V = -\frac{1}{4\pi\epsilon_0|z|} + Ez \quad (3.33)$$

where E is the applied field and ϵ_0 is the permittivity of free space. The potential at the saddle point is given by,

$$V_s = -2\sqrt{E/4\pi\epsilon_0} . \quad (3.34)$$

Equating this to the Rydberg state energy $-R/n^2$ gives the classical field required to ionise the Rydberg state $|n\rangle$,

$$E_{classical} = \frac{R^2\pi\epsilon_0}{n^2}, \text{ or} \quad (3.34)$$

$$E_{a.u.} = \frac{1}{16n^4} \text{ in atomic units.} \quad (3.36)$$

This level of detail is sufficient for calculating the field required for pulsed-field ionisation in optical Ramsey experiments and frequency resolved experiments and is often expressed, $E_{cm^{-1}} = -6.12\sqrt{F}$ where F is the field in $V\text{ cm}^{-1}$. This figure represents the adiabatic limit and corresponds the lowest field at which ionisation will occur. The opposite extreme is the diabatic case, in which classical ionisation occurs at $E_{a.u.} = 1/9n^4$ [15].

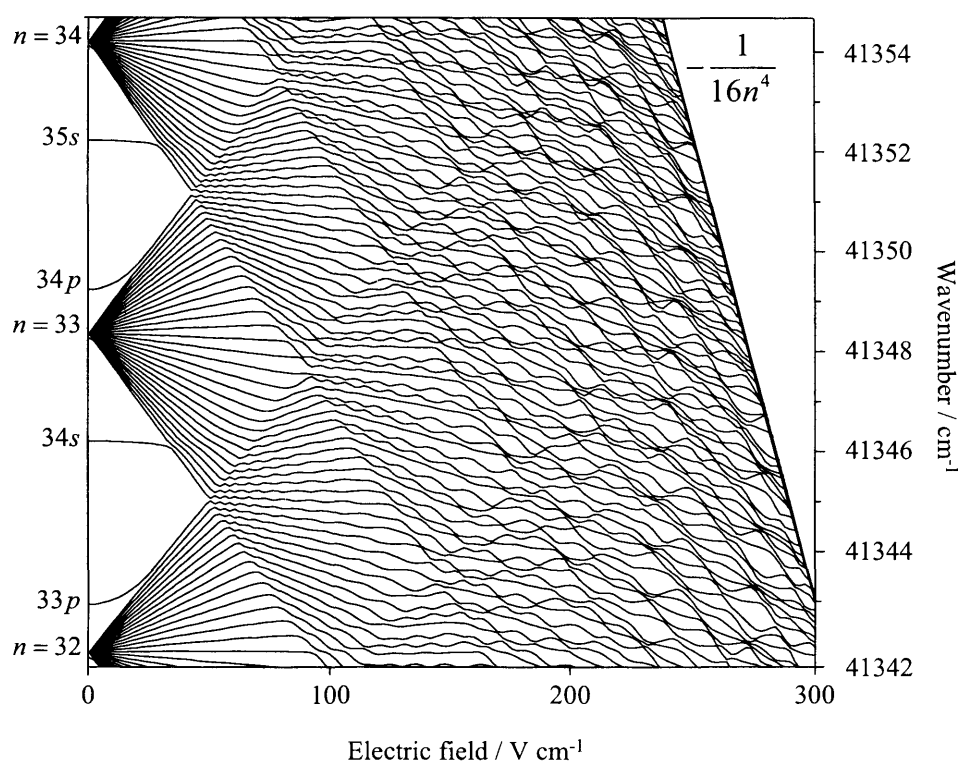


Figure 3.14 Calculated Stark manifold for the $m = 0$ states of sodium around $n = 33d$. The field free Rydberg states split into $n|k\rangle$ states in an applied electric field. The splitting increases with the field and avoided crossing form when the manifolds overlap. The field-free quantum numbers are shown along the vertical axis. Classical (adiabatic) ionisation occurs at the heavy curved line given by equation (3.36).

The applied electric field splits each field-free state $|n\rangle$ into a manifold of n Stark states. The angular momentum quantum number l ceases to be a good quantum number and the states are labelled by a new quantum number k . As the field increases, the splitting

between $|k\rangle$ states increases. Eventually blue-shifted states from the $n - 1$ manifold cross red-shifted states from the n manifold, forming avoided crossings. The resulting Stark ‘map’, shown in figure 3.14, can be calculated by solving the time-independent Schrödinger equation for the system as the field increases.

The Landau-Zenner approximation can be used to find the trajectory of the system from a field-free state to ionisation. The probability of a crossing between two states $|1\rangle$ and $|2\rangle$ being traversed *adiabatically* is given by,

$$P_{dia} = \exp\left(-2\pi|V_{12}|^2 / \dot{F} \left| \frac{dE_1}{dF} - \frac{dE_2}{dF} \right| \right), \quad (3.37)$$

where V_{12} is the coupling between the states and $E_{1,2}$ are their energies. $\dot{F} = dF/dt$ is the field ramp rate. If the coupling is small, the field ramps quickly, or the slopes of the states on the Stark map differ greatly, then the crossing will probably be crossed adiabatically. It is possible to evaluate equation (3.37) at each crossing to establish the spread of field strength over which each state ionises, and hence the shape of the SSFI signal [21]. This approach, although it provides ready insight into the ionisation process, has been superseded by direct solution of the Schrödinger equation for the atom in the applied field (which is discussed in section 3.3C).

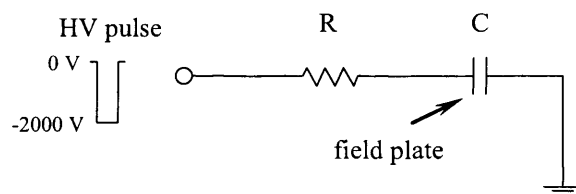


Figure 3.15 The circuit seen by a HV pulse. The resistors are discrete electronic components ($1 \times 10 \text{ k}\Omega$ and $1 \times 4.7 \text{ k}\Omega$, $\pm 5\%$, 2 W carbon film) soldered into a break in the BNC cable. The capacitance derives from the BNC cable (100 pF m^{-1}), which was kept to minimum length (approximately 60 cm), and the face-to-face arrangement of the field plate and first ion lens. Knowing the resistance and fitting equation (3.38) gave a system capacitance of 72 pF.

The optical set-up for SSFI is that in figure 3.5, and the instrumentation is shown in figure 3.10. An electron MCP (Hamamatsu F4655-12) was used to detect electrons ionised by a ramped-field. The electric field was switched on approximately 50 ns after

the laser pulse as before, but was made to rise much more slowly by addition of two series resistors in the BNC cable between the HV pulser and the field plate. This has the effect of increasing the RC time constant of the resistor-capacitor circuit seen by the high voltage pulse (figure 3.15). The mathematical form of the potential, $V(t)$, applied to the field plate is that of a charging capacitor,

$$V(t) = V_0 \left(1 - e^{-\frac{t}{CR}} \right), \quad (3.38)$$

where V_0 is the amplitude of the square pulse (in this case -1000 V), C is the capacitance in Farads, R is the resistance in ohms and t is time in seconds. Increasing the time constant, CR , increases the rise time of the otherwise square pulse generated by the HV pulser, as shown in figure 3.16.

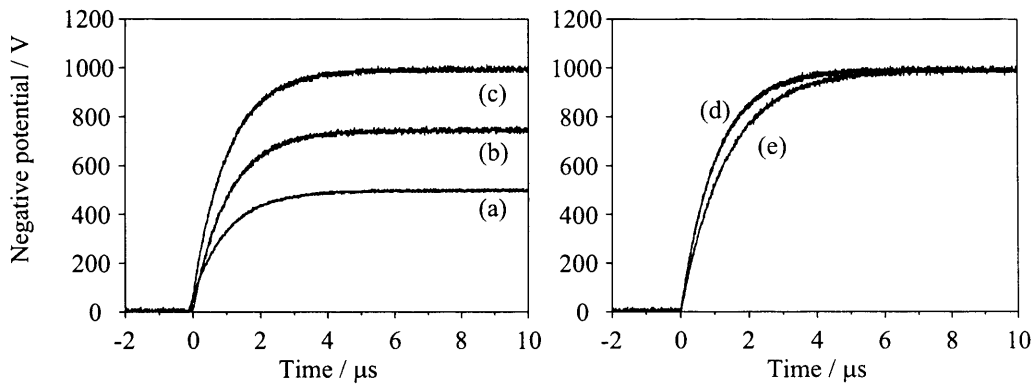


Figure 3.16 Left panel: The shape of HV pulse applied to the field plate with (a) $V_0 = -500$ V, (b) $V_0 = -750$ V and (c) $V_0 = -1000$ V with a load of 14.57 k Ω . Changing V_0 alters the ramp rate in the key time interval, 0 to 2 μ s. $V_0 = -1000$ V was found to be most suitable. Right panel: pulse shape for $V_0 = -1000$ V with loads of (d) 14.57 k Ω and (e) 18.97 k Ω . The 14.57 k Ω load was used for the SSFI coherent control experiments. The polarity of the potentials has been reversed to facilitate plotting.

The ramp-rate of the field, and thus the rise-time and resistance, required to separate the signals depended on the Rydberg states being ionised. Around $n = 35$ a suitable rise-time (defined as the time taken for the potential to change from 0.1 to 0.9 of the maximum) was found to be 2.37 μ s, which was achieved by adding 14.57 k Ω load to the pulser. In addition, to optimise the resistance value, the maximum applied potential was altered to achieve the best separation of states on the oscilloscope.

The integrated electron signal from all the Rydberg states ionised by the ramped electric field was probably of the same magnitude as for a pulsed-field ionisation experiment using fast-rising pulses, as in the frequency resolved and optical Ramsey method experiments above. However the signal from each state in the SSFI experiments was much smaller and it was necessary to accumulate data for many laser shots in order to see the spectrum. Initially this was done using a summing function on the oscilloscope, but superseded by accumulating the data in software (National Instruments LabView). We found that summing the data from between 500 to 1000 laser shots gave good results.

3.3 RESULTS AND DISCUSSION

A. FREQUENCY SPECTRA

Frequency resolved spectra of the Rydberg states of sodium excited in a two colour (1 + 1) photon process via the $3^2P_{3/2}$ state recorded to identify unequivocally the states involved in subsequent wave packet experiments are shown below.

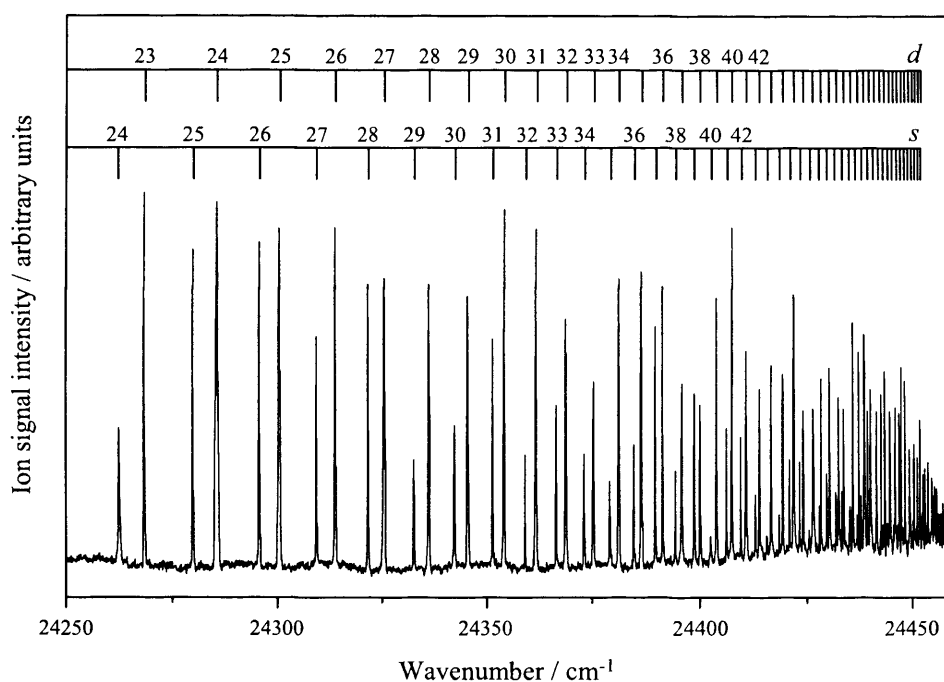


Figure 3.17 Frequency resolved spectrum of the Rydberg states of sodium excited from the $3^2P_{3/2}$ state with a narrow linewidth nanosecond laser. The combs along the top assign the s and d Rydberg series. The difference in peak heights between the two Rydberg series can be clearly seen. The integrated peak area for the s and d series are in a 1:2 ratio (see section 3.1B).

B. DYNAMICS OF SINGLE WAVE PACKETS

Figure 3.18a shows the experimental (lower trace) and calculated (middle trace) recurrence spectrum of a single Rydberg electron wave packet excited around $n = 31$ in sodium detected using the optical Ramsey method. This wave packet was excited by a laser pulse with a wavelength in vacuum centred around 410.48 nm with 21 cm^{-1} bandwidth (corresponding to a 0.7 ps transform-limited Gaussian pulse) and is

composed of both s and d angular momentum states with relative populations shown in figure 3.15b. The wave packet has a classical orbit period $T_{cl} = 4.5$ ps, exhibits a clear second order partial revival at about 23 ps a full revival at 47 ps. The 12.9 ps quantum beat between the angular components is shown in the top trace of figure 3.18a, and derives from the quantum defect difference between the s and d Rydberg series.

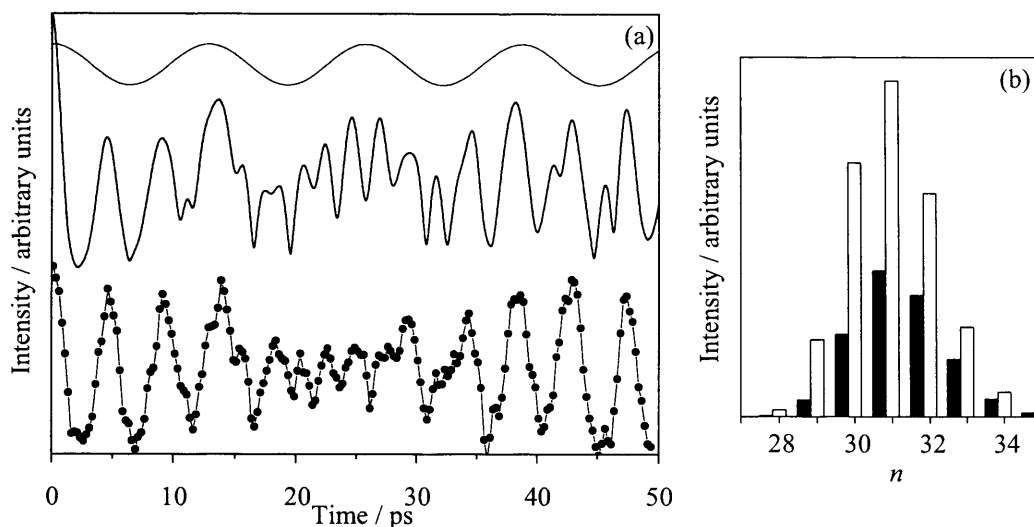


Figure 3.18 (a) Experimental (lower trace) and calculated (middle trace) dynamics of a Rydberg electron wave packet in sodium excited around $n = 31$. $T_{cl} = 4.5$ ps, a second order partial revival can be seen around 23 ps and a full revival at 47 ps. The top trace shows the 12.9 ps calculated angular quantum beat between the s and d states. b) Calculated relative Rydberg state populations of the wave packet excited in a), with s states shown in black and d states in white.

Similar recurrence spectra were recorded for wave packets centred over a range of principal quantum numbers from $n = 25$ to 40. It has been found that for Rydberg wave packets in NO [27, 28] a plot of the classical orbit period versus n reveals the influence of the core on the electron dynamics. If this is used as a measure of the hydrogenicity of the system we see from figure 3.19 that sodium is, as we expect, a highly hydrogenic system.

Having established the typical behaviour of a Rydberg electron wave packet in sodium we can go on to apply our control schemes. These are reported in the following two sections in order of increasing complexity of the control mechanism.

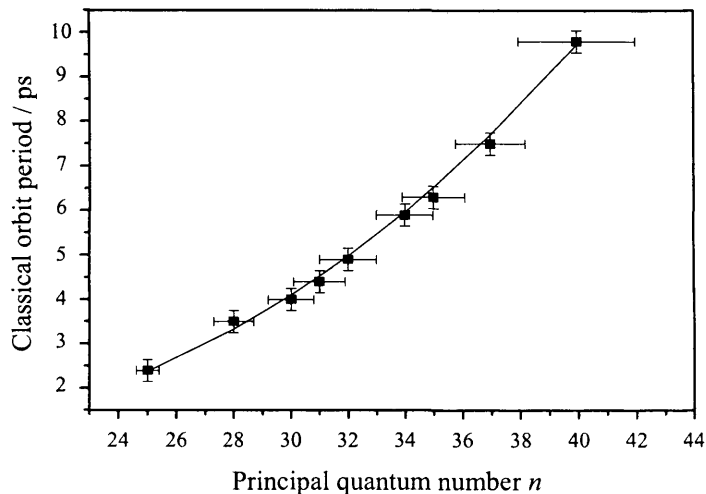


Figure 3.19 The dependence of the classical orbit period on the average principal quantum number for experimental (circles) Rydberg electron wave packets in sodium compared to the classical case, hydrogen (solid line). Measurement of the ps laser wavelength (to ± 0.1 nm) leads to an error in the principal quantum number which increases at higher n , as shown by the horizontal error bars. The classical orbit time can be estimated from recurrence spectra to approximately one experimental step of 0.25 ps.

C. COHERENT CONTROL OF WAVE PACKETS SEPARATED BY T_{cl} DETECTED BY STATE SELECTIVE FIELD IONISATION

As discussed in section 3.1D, if a Rydberg electron wave packet is allowed to evolve for one classical oscillation, on its return to the core we can exploit phase differences between the angular momentum components to achieve control over the final quantum state distribution. By stepping the phase of a second identical wave packet so that it sequentially moves in and out of phase with the existing wave packet, the different angular momentum components can be selectively enhanced or reduced in population. Results for this experiment, where the final quantum state distribution was detected by state-selective field ionisation, are shown in figure 3.20. The phase of the second wave packet was stepped through 3π in steps of approximately 0.07π . As the phase changes each Rydberg states is enhanced then reduced, and so on. At each phase angle the SSFI trace was collected and summed for between 500 and 1000 laser shots.

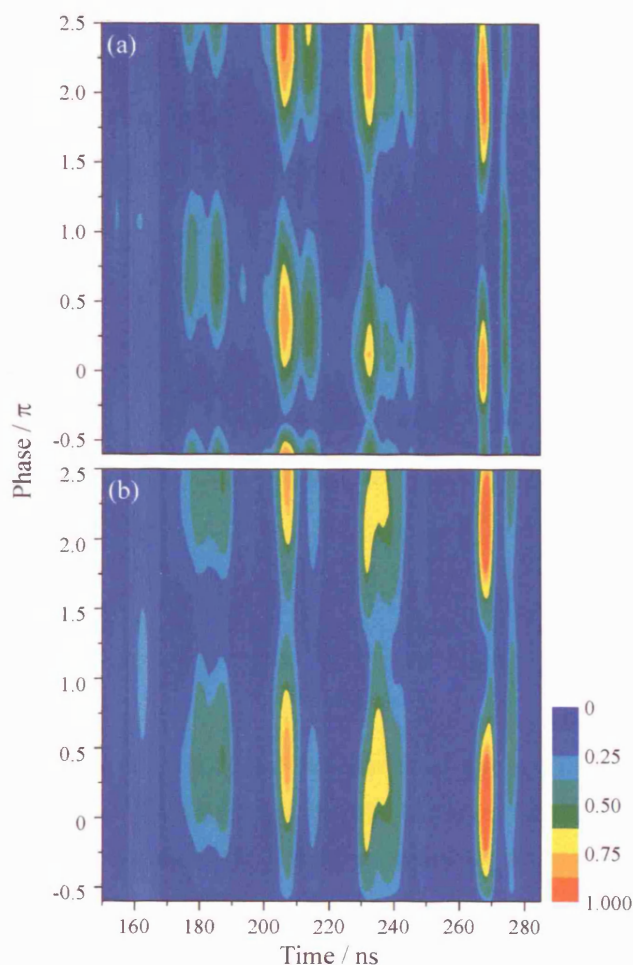


Figure 3.20 SSFI data for control of the angular momentum composition of a Rydberg electronic wave packet in sodium. Panel (a) shows the experimental control data. As the phase (ordinate) of the second wave packet is changed the relative population of the states is modulated. The phase angle has been arbitrarily zeroed at the maximum of the $34d$ state. The separation of s and d components is clearest for the $34d$ and $35s$ states along the right-hand side of the figure. $34d$ is maximal at 0π and 2π , whereas $35s$ is maximised at 0.7π . Panel (b) is modelled data generated by convolving the SSFI traces of separately excited Rydberg states (see figure 3.21) with the populations found from equation (3.39), and shows clear qualitative agreement with the experimental data.

Assignment of the wave packet SSFI data (figure 3.20b) required that we perform frequency-resolved SSFI experiments. Each state was excited individually using a narrow line-width ns laser instead of the ps laser used in the wave packet experiments then field-ionised under exactly the same conditions as in the wave packet experiments so that its SSFI trace could be unambiguously assigned. The traces from all the states

were combined to make figure 3.21. The data was collected on a digital oscilloscope, which has only a limited time base. To record the traces with sufficient resolution it was necessary to alter the timing of the scope trigger signal to catch the signal. Great care had to be taken to repeat the time delays and position of the signal on the scope in order that the composite trace could be made. As for the wave packet SSFI data, each trace was made by summing over 500 to 1000 laser shots.

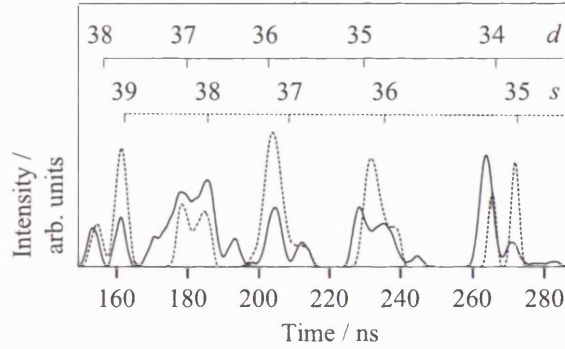


Figure 3.21 A composite of SSFI traces for individual Rydberg states excited a narrow linewidth nanosecond laser. Apart from the nanosecond laser, the experiment was identical to the wave packet experiments and allowed unambiguous assignment of the states, as indicated in the figure. *s* and *d* states are indicated by dashed and solid lines respectively.

Having assigned the wave packet SSFI traces by reference to the frequency data it was possible to compare the coherent control experimental results with calculated values. The populations were calculated from equation (3.22), rewritten to include two pulses (same as equation (3.31)),

$$a_n(\tau_d) = -\frac{i}{2} \Omega_n g_n [1 + \exp(i\Delta_n \tau_d) \exp(i\omega \tau_d)], \quad (3.39)$$

and evaluated for small steps of phase angle to give relative populations of the quantum states after the second laser pulse. These values were then convolved with the frequency resolved SSFI traces for each state to model the experimental data. Figure 3.20b shows that the resulting SSFI spectra agree well with the experimental data.

The SSFI traces in figure 3.20a show overlapping *s* and *d* signals so it is difficult to see the control result on first inspection. A fortunate exception is the trace for $34d$ and $35s$, which are shown enlarged in figure 3.22. There is a phase shift between the maximum of the *d* state population and that of the *s* state of approximately $2\pi/3$,

indicating control of the angular momentum composition of the wave packet if the population of those states is reflected in the other s and d states.

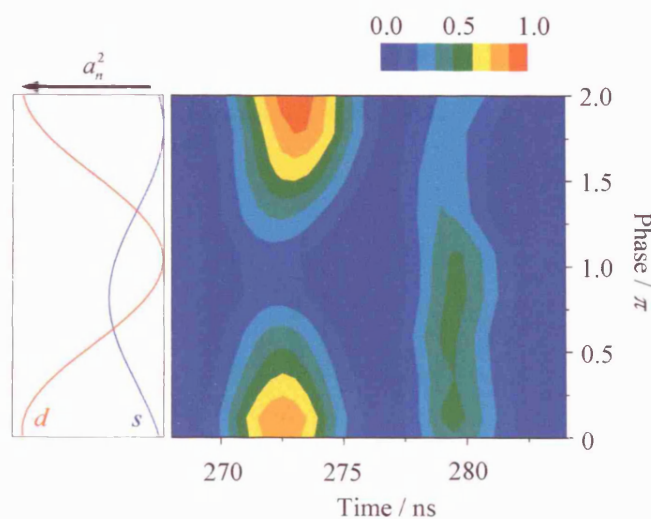


Figure 3.22 Right panel: Enlargement of the experimental SSFI data showing the populations of the $34d$ and $35s$ states as a function of the phase between the two laser pulses. The right hand vertical band is the SSFI signal arising from the $35s$ state. The two intense peaks on the left are from the $34d$ state. Left panel: Calculated populations for the $35s$ and $34d$ Rydberg states as a function of the phase between the laser pulses. The population increases to the left, as indicated by the arrow. The maxima in the calculated and experimental data show clear agreement.

From the calculated populations we can see exactly the effects of coherent control we have achieved, and that the populations of the $35s$ and $34d$ states discussed above are indeed representative of the series as a whole. Figure 3.23 shows the calculated populations of s and d states at key phase angles of the second wave packet.

To determine the size of the phase steps in the experiment, the SSFI data can be summed to include all states for each step (i.e. across figure 3.20). This gives the Ramsey fringe that would be recorded in an optical Ramsay experiment, where the electric field rises much faster. We know how many steps were made by the piezoelectric translator in the interferometer, and the Ramsey fringes show how many optical cycles this corresponded to. It is then straightforward to calculate the size (and phase change) of each step. This can also be cross-referenced to the HeNe interference fringes used to stabilise the interferometer. In this case the steps corresponded to 0.07π (approximately 29 nm).

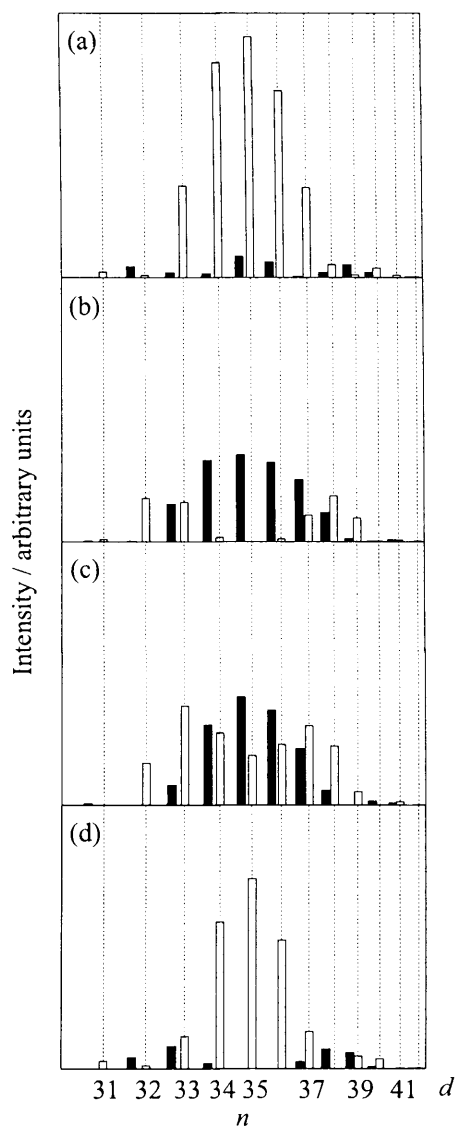


Figure 3.23 Calculated s and d Rydberg state populations for the most significant phase angles between the two wave packets. (a) Putting the d series exactly in phase maximises the d population at the expense of the s . All other phase angles are measured relative to this zero. (b) Shifting the phase angle by π minimizes the d population. (c) and (d) show respectively maximization and minimization of the s population, achieved by a phase differences of 0.7π and -0.3π .

In addition to comparing the wave packet and frequency resolved SSFI data to understand the coherent control, we have attempted to understand the shapes of the SSFI traces themselves. Some of the traces in figure 3.17a are broad and others sharply peaked. Some SSFI work reported in the literature has included calculated traces and the agreement between them is very good [21]. The state-of-the-art approach to this

problem is to solve directly the time-dependant Schrödinger equation for the atom including the applied external electric field as it rises [29]. The Hamiltonian is,

$$H(t) = H_1 + \hat{z}F(t), \quad (3.40)$$

where H_1 is the atomic Hamiltonian and $F(t)$ is given by equation (3.38). The wave function is a sum of products of radial wave functions $R_l(r, t)$ and spherical harmonics $Y_{lm}(\theta, \phi)$,

$$\psi(t) = \sum_l R_l(r, t) Y_{lm}(\theta, \phi) \quad (3.41)$$

evaluated on a radial grid equally spaced in the variable $s = r^2$ at time intervals $dt = T_{cl}/100$ [30]. The outgoing electron flux is absorbed by a complex potential whose imaginary part is zero for $r < 5800$ a.u. and increases to the edge of the radial range at $r = 8800$ a.u. These calculations, kindly carried out for us by Francis Robicheaux at Auburn University using the same electric field parameters as our experiment, gave SSFI traces shown in figure 3.24a, along with the experimental frequency resolved SSFI traces. Clearly the agreement is not as good as we would have hoped for.

The calculation gives the flux of electrons very close to the atom ($r < 10^4$ a.u.) and does not include the flight time that electrons in our experiments experience. An attempt was made to account for flight time and time-varying acceleration field in the hope of matching better the experimental and calculated SSFI traces. Flight times were calculated for electrons ejected and accelerated by the ramped field. The calculation was carried out assuming that an electron ionised by a particular field would instantly feel the force of that field and all subsequent fields until it left the interaction region, and would be accelerated by the integral of the instantaneous accelerations during that time. This was done by iteratively evaluating the instantaneous velocity in small time steps for electrons ionised at small increments of an applied field used in the experiment until the electron had travelled out of the interaction region. This gave a final velocity from which the flight time could be calculated. The calculated SSFI traces were then ‘corrected’ by multiplying by the flight times (figure 3.24b). This approach could not reproduce in the calculated traces either the spacing or profile seen in the experiment.

The interaction volume between the lasers and the sodium beam discussed in section 3.2C is very small, approximately 22 μm in diameter, so it seems unlikely that electrons formed at its upper and lower edges (i.e. nearer or further from the detector)

would have substantially different flight times. This suggests some as yet unidentified process was shaping the SSFI traces.

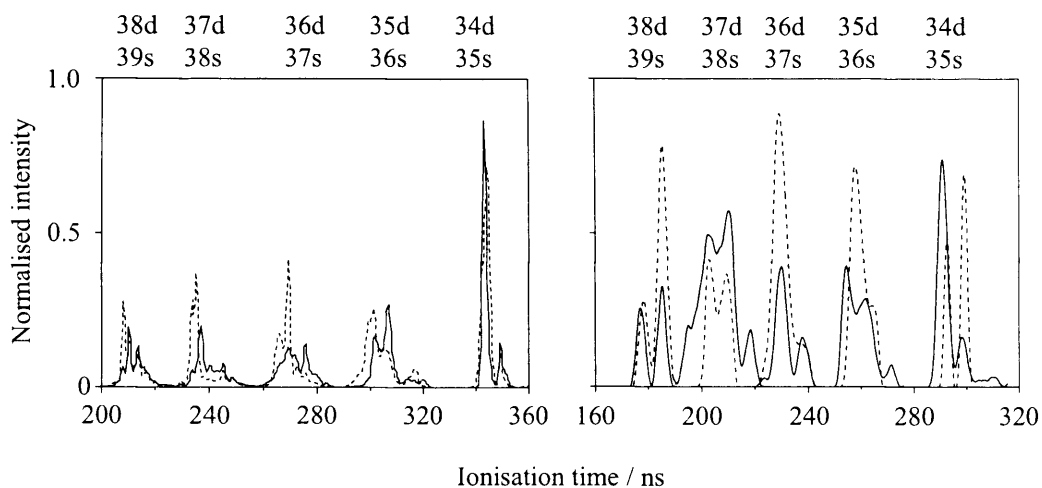


Figure 3.24 Comparison of calculated (a) and experimental (b) SSFI traces for individually excited Rydberg states. The calculation modelled the experimental external electric field and laser excitation parameters, but excluded the flight time to the detector. The experimental traces are a composite of traces from Rydberg states excited individually by a narrow linewidth ns laser and ionised by a ramped electric field. *s* and *d* states are shown by dashed and solid lines respectively. The peak intensities have been normalised to the highest in each trace.

SSFI experiments in the literature that match calculated values well were carried out with the electron detector just outside the interaction region. It would be interesting to reposition the detector region and repeat these experiments to see the effect on the SSFI trace shapes.

Finally, one feature of figure 3.20 that has so far been neglected is the slight phase shift between the maxima of adjacent states, which leads to the sloped appearance of the figure. Since this is present in both the experimental and calculated spectra it is unlikely to be an experimental artefact, such as a chirp in the laser pulses, so it is most likely due to higher order dispersion in the wave packet.

D. WAVE PACKET INTERFEROMETRY

Where SSFI directly measures the Rydberg state populations, an entirely equivalent way to observe the results of control is to monitor changes in the dynamical behaviour of the wave packet, and from that infer the populations.

These experiments require three identical laser pulses, time-delayed and phase-locked by the stabilised three-arm Michelson interferometer. The first pulse created a wave packet, which was allowed to evolve for $1.5T_{cl}$ before a second wave packet was launched. The system was then allowed to evolve until the second order partial revival before being probed by the third wave packet using the optical Ramsey method. Having set the coarse delay between the first and second wave packets, the initial phase difference between them is unknown. To be sure we have generated the correct relative phases between the wave packets to achieve control, it is necessary to step the phase between them for at least 2π in small increments, typically around $\pi/10$.

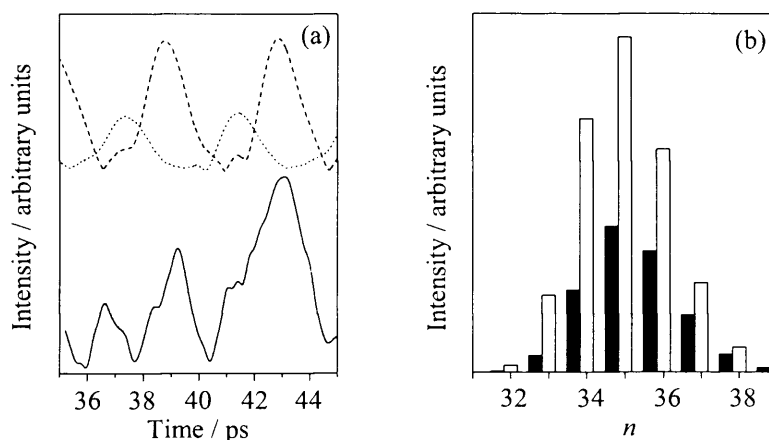


Figure 3.25 (a) Experimental (lower) and calculated (upper) recurrence spectrum of a single wave packet around the time of the second order partial revival. The s component is shown dotted and the d is dashed to emphasise the separation of the angular parts due to their different quantum defects, which reproduced in the experimental data. The wave packet was excited around $n = 35$ by a 0.7 ps (21 cm^{-1} bandwidth) laser pulse centred at a wavelength in vacuum of 410.1 nm. The population of Rydberg states is shown in (b); d states are white, s states are black. The overall envelope of the wave packet reflects the Gaussian laser energy profile and the relative intensities arise from the oscillator strengths.

At each phase step the resultant wave packet was probed at the second order partial revival using the optical Ramsey method. The requirement for a doubly stabilised Michelson interferometer is evident: the optical Ramsey method requires a phase-locked pulse pair (the 2nd and 3rd pulses), and during each detection period the relative phases of the first and second wave packets must be locked. If at any time during an experimental run the phase locking between the wave packets was lost, the experiment had to be restarted. Figure 3.25 shows experimental recurrence spectra around the second order partial revival for two interfering wave packets separated by time $t = 3T_{cl}/2 + t_\phi$ for a series of phase steps t_ϕ for wave packets excited around $n = 35$ by 0.7 ps (21 cm^{-1} bandwidth) laser pulses.

Recurrence spectra were modelled by evaluating the time autocorrelation function for three wave packets formed at $t = 0$, $1.5T_{cl} + \phi$ and around $t_{probe} = T_{rev}/2$,

$$\left| \langle \Psi(t_{probe}) | \Psi(1.5T_{cl} + \phi) + \Psi(0) \rangle \right|, \quad (3.42)2$$

where $\Psi(0)$ is the first wave packet formed, $\Psi(1.5T_{cl} + \phi)$ is the control wave packet and $\Psi(t_{probe})$ is the probe wave packet. Comparison of the modelled and experimental data allows us to find the zero phase difference case. It is then possible to identify key phase difference spectra for coherent control. For this system these are when the two wave packets are separated by time $t = 3T_{cl}/2 + t_\phi$, where $\phi = -\pi/2$ (upper plot) and $\phi = +\pi/2$ (lower plot) and these results are shown in figure 3.26 along with modelled data and calculated Rydberg state populations. The populations were calculated by evaluation of equation (3.39) for excitation of the second wave packet at $1.5T_{cl}$. The figure indicates that we have indeed been able to selectively remove one of the two sub-wave packets at the second order partial revival to leave either just the s or just the d angular momentum component, although this is clearer in the time domain spectra than in the calculated Rydberg state populations.

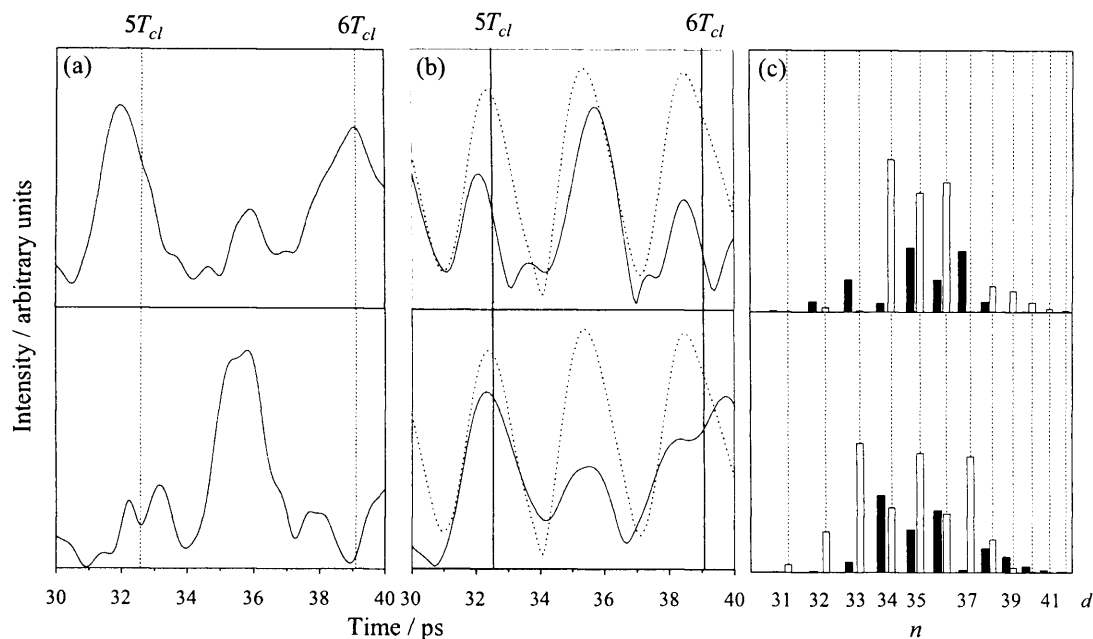


Figure 3.26 Experimental (a) and calculated (b) recurrence spectra around the time of the second order partial revival resulting from excitation of two wave packets excited around $n = 35$ and separated by $t = 3T_{cl}/2 + t_\phi$, for $\phi = -\pi/2$ (upper) and $\phi = +\pi/2$ (lower). The recurrence spectrum of a single wave packet is shown as a dashed line in (b) and the classical orbit times are indicated in (a) and (b) by vertical lines. Plot (c) shows the calculated Rydberg state population for a wave packet pair with these relative phases.

It is clear from the upper and lower traces of figure 3.26(a) and (b) that we can select which sub-wave packet to keep by shifting the phase of the second wave packet by $\pm \pi/2$ compared to the first. This detection method cannot discriminate between the angular momentum components of the remaining sub-wave packet, so this experiment effectively generates a full revival at the time of the second order partial revival, as shown by the removal of every other peak from the single wave packet spectrum (panel (b) dashed line).

3.4 CHIRPED WAVE PACKET INTERFEROMETRY

The coherent control discussed above in terms of wave packet interferences can also be viewed in an entirely equivalent way in the frequency domain because of the Fourier transform relationship between optical pulses in the time domain and their

spectral content in the frequency domain. This equivalence was noted by both Noel and Stroud [7] in their seminal ‘Shrödinger’s cat states’ paper, by Noordam *et al.* in their description of the optical Ramsey technique [13], and by Scherer *et al.* [31] who used the spectrum to stabilise the pulse phase, but it has been explored very little. The frequency picture of the coherent control described above offers significant insight into correlations between the characteristics of the light field and the atomic system with which it interacts.

For two laser pulses, separated by time τ , the total electric field experienced by the atom can be written,

$$E(t) = f(t)e^{i\omega t} + f(t - \tau)e^{i\omega(t - \tau)} \quad (3.43)$$

where E_0 is field amplitude, ω is the central wavelength of the laser pulse. The temporal profile of the laser pulse is assumed to be Gaussian with the form $f(t) = \exp\left[-2 \ln 2 (t/\tau_p)^2\right]$, where τ_p is the temporal full-width-at-half-maximum (FWHM). Since our experiment operates in the weak field limit, excitation only occurs at resonant frequencies contained in the *spectral* profile of the pulse pair. The spectrum of the pulse pair can be found from their Fourier transform,

$$g(\omega) = \frac{1}{\sqrt{2\pi}} \int_{-\infty}^{\infty} E(t)e^{-i\omega t} dt, \quad (3.44)$$

which can be evaluated analytically or numerically. For its flexibility we used a fast Fourier transform (FFT) algorithm [32]. Calculated spectra for pairs of time-delayed transform-limited laser pulses with duration and bandwidth used in our experiments are shown in figure 3.27.

It is clear from the figure that when the first and second pulses arrive simultaneously the spectrum is that of a single transform-limited pulse of 0.7 ps duration. As the delay between the pulses increases the frequency comb develops more peaks. The relationship between temporal and spectral phase can be seen clearly between spectra (c) and (d). A π shift in the time domain gives rise to a π phase shift in the spectrum.

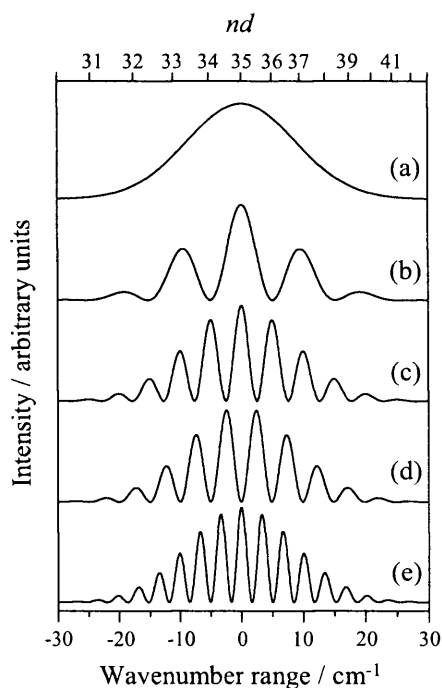


Figure 3.27 FFT of a pair of transform-limited 0.7 ps laser pulses centred at the $35d \leftarrow 3^2P_{3/2}$ transition frequency of sodium and separated by times (a) 0, (b) $T_{cl}/2$, (c) T_{cl} , (d) $T_{cl} + \omega/\pi$, and (e) $3T_{cl}/2$. The Principal quantum numbers of the corresponding d Rydberg states are shown along the top.

The pulse spectra offer an alternative perspective on the Rydberg state populations in our coherent control calculations and SSFI data. When the spectral peaks of the pulse pair correspond to selected Rydberg states, the state populations are altered compared to those excited by the full bandwidth of a single pulse or pulse pair (figure 3.27(a)). Figure 3.27(b) suggests that by separating the pulses by $T_{cl}/2$ only alternate Rydberg states in the d series will be excited. Figure 3.27(c) and (d) show that by shifting the optical phase the states which are excited, and those which are not, can be chosen. Finally figure 3.27(e) shows that it is possible to excite, for instance, the d series intensely while the interleaved s series, lying in the spectral troughs, will be excited with smaller amplitude. This is exactly our objective: to selectively excite either the s or d components using broad bandwidth laser pulses.

This frequency domain perspective suggests that if the spectral peaks the pulse pair could be made to better coincide with resonances we wish to excite, and the troughs coincide with states we wish not to excite, then the degree of control would be improved. Chirped laser pulses appear to offer a way to achieve this so, to test its

feasibility, a coherent control experiment was modelled using either one chirped and one transform limited pulse.

Laser chirp describes a shift in the frequency of the pulse with time, or a shift in the spectral phase with time. Experimentally laser pulses are usually chirped by a phase modulation in frequency space introduced by passing through a dispersive medium, such as a fibre or prism. In this case the bandwidth of the transform limited pulse is preserved but the pulse is stretched in time [33]. The chirp can be understood by expanding the frequency content of the pulse about the central frequency ω_L ,

$$\phi(\omega) \approx \phi(\omega_L) + \phi'(\omega_L)(\omega - \omega_L) + \phi''(\omega_L)(\omega - \omega_L)^2. \quad (3.45)$$

The electric field of the chirped pulse can then be written,

$$E_C(t) = E_0(t) \exp[i\phi(\omega_L)] \exp\left[-\frac{(t - \phi'(\omega_L))^2}{\tau_c^4}\right] \exp\left[-i(\omega_L t + \delta(t - \phi'(\omega_L))^2)\right] \quad (3.46)$$

where

$$\tau_c = \tau_L \sqrt{1 + 4 \frac{\phi''^2(\omega_L)}{\tau_L^4}} \quad (3.47)$$

is the duration of the (stretched) chirped pulse, and

$$\delta = 2\phi''(\omega_L) \left\{ \tau_L^4 \left(1 + 4 \frac{\phi''^2(\omega_L)}{\tau_L^4} \right) \right\}^{-1} = \frac{2\phi''(\omega_L)}{(\tau_L \tau_c)^2} \quad (3.48)$$

is the chirping parameter. The first exponential in equation (3.47) is a phase shift introduced to all the frequency components. The second exponential gives the shift of the pulse envelope and depends on the laser frequency. The quadratic phase shift associated with frequency chirp is given by the term $\delta(t - \phi'(\omega_L))^2$ in the last exponential. Both the pulse stretching and the chirp depend on the group velocity dispersion (GVD) $\phi''(\omega_L)$. The duration of the transform-limited pulse τ_L is related to the measured pulse duration by $\tau_L^2 = \tau_p^2 / 2 \ln 2$.

Writing the chirped Gaussian pulse (equation (3.46)) in a simpler form [33],

$$E(t) = E_0 \exp\left[-\frac{(t - t_0)^2}{2\sigma^2}\right] \exp\left[-i\left(\omega_0(t - t_0) + \frac{\alpha}{2}(t - t_0)^2\right)\right], \quad (3.49)$$

where σ is the temporal deviance, ω_0 is the carrier frequency and α is the chirp parameter, allows for a simple analytical form for its Fourier transform,

$$\tilde{E}(\omega) = \tilde{E}_0 \exp\left[-\frac{(\omega - \omega_0)^2}{2\gamma^2}\right] \exp\left[-i\frac{\alpha'}{2}(\omega - \omega_0)^2\right], \quad (3.50)$$

which is a linearly chirped Gaussian in the frequency domain. The correspondence between the terms in time and frequency domains are then,

$$\begin{aligned} \sigma^2 &= \frac{1}{\gamma^2} + (\alpha')^2 \gamma^2, \\ \sigma^2 \alpha &= \gamma^2 \alpha', \text{ and} \\ \sigma |E_0|^2 &= \gamma |\tilde{E}_0|^2. \end{aligned} \quad (3.51)$$

Correlation of the chirp with the Rydberg system follows from the quadratic term in equation (3.45). It is often defined as the *pulse broadening per unit bandwidth* $\phi''(\omega_0) = \Delta t / \Delta \omega$ [34]. This can be rewritten,

$$\phi''(\omega_0) = \frac{\partial t}{\partial n} \times \frac{\partial n}{\partial \omega}, \quad (3.52)$$

which for a Rydberg system with $t_n = 2\pi n^3$ and $\omega_n = -1/2n^2$, gives

$$\phi''(\omega_0) = 6\pi n^5, \quad (3.53)$$

which shows the relationship between the chirp parameter and the Rydberg states we wish to excite. Since we have considered so far a single chirped pulse, it is convenient to continue so the pump probe experiment is modelled with a transform-limited pump and a chirped probe, the opposite arrangement to [35]. Frequency spectra calculated using a FFT for such a pulse pair centred at the $35d \leftarrow 3^2P_{3/2}$ transition frequency are shown in figure 3.28.

The transform-limited pulse duration was $\tau_p = 0.7$ ps, and the chirped pulse derived from it had $\delta = 0.5793$ ps² and $\phi_c = 0.2020\pi$. The pulses were separated in time and phase shifted by $xT_{cl} + (\phi + \phi_c)/\omega_L$ where ϕ the phase shift of central frequency (as for the TL pulse pair experiments).

Values of x were chosen to correspond to the experiments reported above for TL pulse pairs. Thus for $x = 1$ the first wave packet makes one round trip and is back at the core when the second is excited and they interfere directly. If $\phi = 0$ the d states are maximised and the s minimised (a), for $x = 1$ and $\phi = 0.3\pi$ the s states are maximised (b). Extending the utility of this approach, a more exotic wave packet can be created. If

$x = 0.5$ the first wave packet is at the outer turning point when the second is formed and they do not interfere directly. Nonetheless if $\phi = 0.175\pi$ a wave packet is created that is composed predominantly of odd d states and even s states.

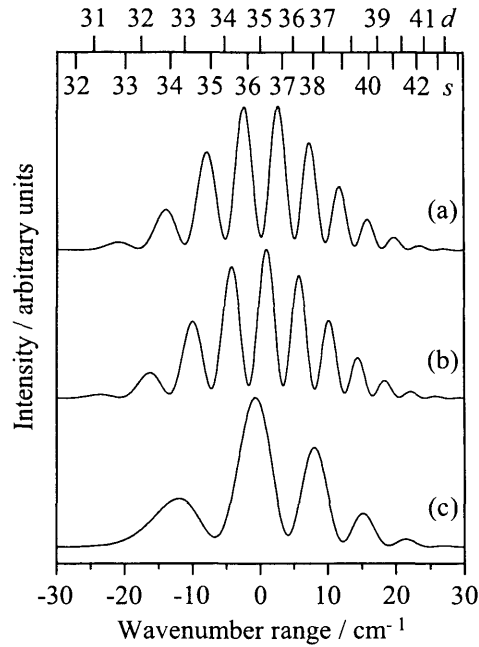


Figure 3.28 FFT frequency spectra of TL-pump-chirped-probe pulse pairs centred at the $35d \leftarrow 3^2P_{3/2}$ transition frequency for different time delays and phases given by $xT_{cl} + (\phi + \phi_c)/\omega_L$. The first is a transform-limited Gaussian pulse with a time FWHM of 0.7 ps. The second is identical to the first but chirped by $\alpha = 0.5793 \text{ ps}^2$ and $\phi_c = 0.2020\pi$. (a) $x = 1$ and $\phi = \pi$ to minimise the d state Rydberg population. (b) $x = 1$ and $\phi = 0.3\pi$ to minimise the s population. (c) $x = 0.5$ and $\phi = 0.175\pi$, which corresponds to excitation of predominantly d states with odd n and s states with even n . The topmost axes show the positions of the ns and nd Rydberg states.

It is clear from the figure that the peaks in the spectrum can indeed be selected to coincide with the Rydberg states better with a chirped pulse than two TL pulses. The use of chirped pulses has, in this case, allowed the coherent control to be refined to better match the fundamental scaling in the system.

3.5 CONCLUSION

Coherent control of the angular momentum composition in radial Rydberg electronic wave packets has been demonstrated. This control exploits the phase evolution of a wave packet arising from the difference in the quantum defects between two Rydberg series, and that due to its motion in an anharmonic potential. The results of control have been observed in two different, but complementary ways. In the frequency domain, state-selective field ionisation allows us to directly measure the changes brought about in the populations of individual Rydberg states in the wave packet. In the time domain we can see altered wave packet dynamics by the optical Ramsey method.

Analysis of the frequency spectrum of the pulse pair used in our coherent control experiments has been found to be a useful tool in understanding the mechanisms involved, and is complimentary to the more familiar time-domain approach taken in wave packet interferometry.

The use of chirped laser pulses in wave packet interferometry has been investigated computationally and shown to be a useful extension to the experimental approaches shown in this chapter. The laser chirp can be arranged to compensate for the dispersion of the wave packet to achieve better control over the Rydberg state populations than is possible with transform-limited pulses. We have been able to relate the chirp rate of the pulse to the energy levels of the system in such a way as to allow prediction of the pulse details required to achieve particular control outcome. It is anticipated that experiments utilising chirped pulses in Rydberg wave packet coherent control will be carried in this group in the future.

3.6 REFERENCES

1. W.C. Martin and R. Zalubus, *J. Phys. Chem. Ref. Data* **10** (1), 153-196. (1981).
2. T.F. Gallagher, *Rydberg Atoms*. Cambridge Monographs on Atomic, Molecular, and Chemical Physics 3, ed. A. Dalgarno, *et al.* 1994, Cambridge: Cambridge University Press.
3. M. Ciocca, C.E. Burkhardt, J.J. Leventhal, and T. Bergeman, *Phys. Rev. A* **45** (7), 4720-4730. (1992).

4. J. Parker and C.R. Stroud, *Phys. Rev. Lett.* **56** (7), 716-719. (1986).
5. I.S. Averbukh and N.F. Perelman, *Phys. Lett. A* **139** (9), 449-453. (1989).
6. M.W. Noel and C.R. Stroud, *Phys. Rev. Lett.* **75** (7), 1252-1255. (1995).
7. M.W. Noel and C.R. Stroud, *Phys. Rev. Lett.* **77** (10), 1913-1916. (1996).
8. I.S. Averbukh and N.F. Perelman, *Uspekhi Fiz. Nauk* **161** (7), 41-81. (1991).
9. J.R.R. Verlet, V.G. Stavros, R.S. Minns, and H.H. Fielding, *J. Phys. B (At. Mol. Opt. Phys.)* **36** (17), 3683-3696. (2003).
10. J.R.R. Verlet, V.G. Stavros, R.S. Minns, and H.H. Fielding, *Phys. Rev. Lett.* **89** (26), 263004. (2002).
11. R.S. Minns, J.R.R. Verlet, L.J. Watkins, and H.H. Fielding, *J. Chem. Phys.* **119** (12), 5842-5847. (2003).
12. D.S. Bethune, *Appl. Optics* **20** (11), 1897-1899. (1981).
13. L.D. Noordam, D.I. Duncan, and T.F. Gallagher, *Phys. Rev. A* **45** (7), 4734-4737. (1992).
14. L.D. Noordam and R.R. Jones, *J. Mod. Opt.* **44** (11-12), 2515-2532. (1997).
15. H. Fielding, *Ann. Rev. Phys. Chem.* **56**, 91-117. (2005).
16. J.F. Christian and B. Broers, *Phys. Rev. A* **52** (5), 3655-3660. (1995).
17. M. Nauenberg, *J. Phys. B (At. Mol. Opt. Phys.)* **23** (15), L385-L390. (1990).
18. A. Gurtler and W.J. van der Zande, *Phys. Lett. A* **324** (4), 315-320. (2004).
19. T.F. Gallagher, L.M. Humphrey, R.M. Hill, and S.A. Edelstein, *Phys. Rev. Lett.* **37** (22), 1465-1467. (1976).
20. T.H. Jeys, G.W. Foltz, K.A. Smith, E.J. Beiting, F.G. Kellert, F.B. Dunning, and R.F. Stebbings, *Phys. Rev. Lett.* **44** (6), 390-393. (1980).
21. F. Robicheaux, C. Wesdorp, and L.D. Noordam, *Phys. Rev. A* **6204** (4), 043404. (2000).
22. T.C. Weinacht, J. Ahn, and P.H. Bucksbaum, *Phys. Rev. Lett.* **80** (25), 5508-5511. (1998).
23. J.H. Hoogenraad, R.B. Vrijen, and L.D. Noordam, *Phys. Rev. A* **57** (6), 4546-4552. (1998).
24. S.N. Pisharody and R.R. Jones, *Phys. Rev. A* **65** (3), 033418. (2002).
25. R.B. Watkins, W.M. Griffith, M.A. Gatzke, and T.F. Gallagher, *Phys. Rev. Lett.* **77** (12), 2424-2427. (1996).

26. J. Ahn, D.N. Hutchinson, C. Rangan, and P.H. Bucksbaum, *Phys. Rev. Lett.* **86** (7), 1179-1182. (2001).
27. R.A.L. Smith, J.R.R. Verlet, E.D. Boleat, V.G. Stavros, and H.H. Fielding, *Faraday Discuss.* (115), 63-70. (2000).
28. R.A.L. Smith and H.H. Fielding, *Abstr. Pap. Am. Chem. Soc.* **223**, 135-PHYS. (2002).
29. F. Robicheaux, E. Oks, A.L. Parker, and T. Uzer, *J. Phys. B (At. Mol. Opt. Phys.)* **35** (22), 4613-4618. (2002).
30. F. Robicheaux, *Personal Communication*, 2004
31. N.F. Scherer, R.J. Carlson, A. Matro, M. Du, A.J. Ruggiero, V. Romero-Rochin, J.A. Cina, G.R. Fleming, and S.A. Rice, *J. Chem. Phys.* **95** (3), 1487-1511. (1991).
32. W.H. Press, B.P. Flannery, S.A. Teukolsky, and W.T. Vetterling, *Numerical Recipes in FORTRAN 77: The Art of Scientific Computing: Vol 1*. Vol. 1. 1992: Cambridge University Press.
33. Z. Shen, I. Boustani, M. Erdmann, and V. Engel, *Chem. Phys. Lett.* **339** (5-6), 362-368. (2001).
34. P.M.W. French, *Rep. Prog. Phys.* **58** (2), 169-262. (1995).
35. M.A. Bouchene, C. Nicole, and B. Girard, *J. Phys. B (At. Mol. Opt. Phys.)* **32** (21), 5167-5177. (1999).

CHAPTER 4 OPTICAL CONTROL OF VIBRATIONAL WAVE PACKET DYNAMICS IN THE SODIUM DIMER

ABSTRACT

This chapter describes progress towards a novel experiment for optical coherent control of vibrational wave packet dynamics in the sodium dimer. A coherent superposition of high-lying Rydberg states of Na_2 is excited by the broad bandwidth of a femtosecond laser pulse. The Rydberg states converge to several vibrational ionisation limits of the dimer, so the excitation effectively forms a vibrational wave packet in the $X^+ \ ^2\Sigma_g^+$ ionic potential. Excitation of several wave packets by a series of phase-locked transform-limited pulses allows for control over the composition and dynamics of the wave packet, and its detection using a combination of the optical Ramsey method and pulsed-field ionisation techniques adapted from ZEKE-PFI spectroscopy.

4.1 INTRODUCTION

The objective of this project was the construction of a novel apparatus, comprising a molecular beam, laser system and data collection electronics, to study the time resolved dynamics of molecular cations on the ionic potential surface with femtosecond resolution. Most molecular dynamics studies to date have focussed on neutral species, either on the potential surface or by monitoring product formation, but the role of cations in aqueous, combustion and interstellar chemistry makes them an important target for study [1], as well being of fundamental interest.

The novel experimental method combines the techniques of zero-electron-kinetic-energy spectroscopy with pulsed-field ionisation (ZEKE-PFI) and phase sensitive detection using ultrafast (femtosecond) pulses from a titanium sapphire laser. This will be used to characterise the vibrational dynamics of the Na_2^+ ion – a process that will also test its validity. The objective is to control these dynamics using interference between multiple wave packets using sequences of phase-locked laser pulses. Ultimately, specially designed sequences of laser pulses (analogous to radio-frequency sequences used in magnetic resonance experiments) will be used to control the molecular dynamics of the ion

A. SODIUM DIMER SPECTROSCOPY

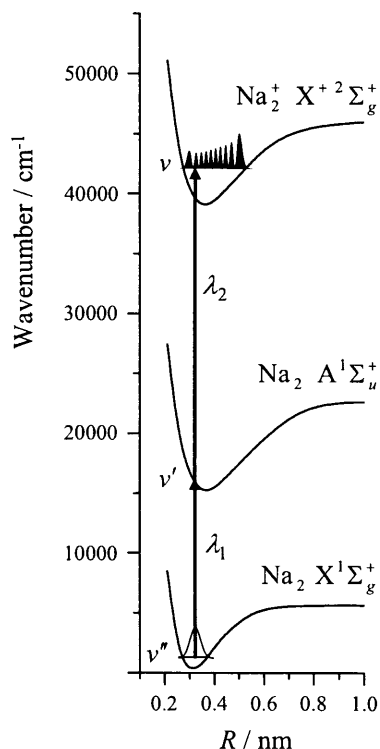


Figure 4.1 The excitation scheme used in the experiment showing the potential energy curves of the sodium dimer excited by two laser systems. From the $X^1\Sigma_g^+$ ground state a continuous wave (CW) laser at $\lambda_1 \approx 565$ nm excites a single rovibrational level of the $A^1\Sigma_u^+$ state. From this intermediate an approximately 50 fs laser pulse at $\lambda_2 \approx 400$ nm excites a wave packet in the Rydberg states converging to several vibrational levels of the $X^+ 2\Sigma_g^+$ state of the Na_2^+ ion.

We excite Na_2 in a molecular beam from the $X^1\Sigma_g^+$ ground state to specific rovibrational states of the $A^1\Sigma_u^+$ state using a narrow linewidth dye laser. From there high-lying Rydberg states will be excited which converge to rovibrational states of the $X^+ 2\Sigma_g^+$ Na_2^+ ion. This excitation, shown in figure 4.1, is made using a transform limited pulse of a frequency-doubled femtosecond titanium sapphire laser.

The rotational and vibrational energy levels of the states can be found using experimental or theoretical spectroscopic constants in the Dunham expansion

$$T_{i,k} = \sum_{i,k} Y_{i,k} (\nu + 1/2)^i J^k (J + 1)^k \quad (4.1)$$

where i and k are the powers raising the vibrational and rotational quantum numbers ν and J respectively, and the $Y_{i,k}$ are related to the spectroscopic constants:

$$Y_{1,0} = \omega_e, \quad Y_{2,0} = \omega_e x_e, \quad Y_{0,1} = B_e, \quad Y_{0,2} = D_e, \quad Y_{1,1} = \alpha_e, \quad (4.2)$$

The frequency of a transition between a lower rovibrational level $v''J''$ and an upper one $v'J'$ can then be written

$$\nu(v''J'', v'J') = T_e + [G(v') - G(v'')] + [F_{v'}(J') - F_{v''}(J'')], \quad (4.3)$$

where T_e is the energy difference between the minima of the two potential energy curves,

$$G(v) = \omega_e(v + 1/2) - \omega_e x_e(v + 1/2)^2 + \omega_e y_e(v + 1/2)^3 + \omega_e z_e(v + 1/2)^4 + \dots \quad (4.4)$$

gives the vibrational contribution, and

$$F_v(J) = B_v[J(J+1) - \Lambda^2] - D_v[J(J+1) - \Lambda^2]^2 + \dots \quad (4.5)$$

is the energy difference between the rotational sub levels of each vibrational state. Λ is the magnitude of the projection of the electronic angular momentum onto the molecular axis. $\Lambda = 0$ for Σ states and is not considered further. The constants B_v and D_v are given by,

$$B_v = B_e - \alpha_e(v + 1/2) + \gamma_e(v + 1/2)^2 + \dots \quad (4.6)$$

and

$$D_v = D_e - \beta_e(v + 1/2) + \delta_e(v + 1/2)^2 + \dots \quad (4.7)$$

B. VIBRATION WAVEFUNCTIONS

The potential energy curves, as figure 4.1 shows, of electronic states of a diatomic molecule have the approximate form of a Morse potential [2],

$$V(r) = D_e [1 - \exp(-\beta(r - R_e))]^2 \quad (4.8)$$

where r is the internuclear distance, R_e is the equilibrium bond length, D_e is the well depth and β is a constant. Vibrations of a diatomic molecule are therefore those of an anharmonic oscillator. Within the Born-Oppenheimer approximation the molecular Schrödinger equation is separable into electronic and nuclear parts so the radial Schrödinger equation for a diatomic can be written,

$$-\frac{\hbar^2}{2\mu r^2} \frac{d}{dr} r^2 \frac{dR(r)}{dr} + \left(V(r) + \frac{\hbar^2 J(J+1)}{2\mu r^2} \right) R(r) = E_{v,J} R(r), \quad (4.9)$$

since the equation is separable from the angular terms and dependent only on r . This can be rewritten for the vibrational wave functions $\psi(r) = rR(r)$ by substitution,

$$\frac{-\hbar^2}{2\mu} \frac{d^2\psi}{dr^2} + \left(V(r) + \frac{\hbar^2 J(J+1)}{2\mu r^2} \right) \psi = E_{v,J} \psi \quad (4.10)$$

where μ is the reduced mass, J is the rotation quantum number and $E_{v,J}$ is the energy. The term in brackets is the potential energy and, because of its dependence on J and r , prevents vibrational and rotational motion being separable. There are no analytical solutions to this equation as $V(r)$ contains nuclear repulsion energy and electronic energy [3]. It can be solved numerically by, for example, the Level program by R. LeRoy [4].

To gain some insight into the form of the vibrational wavefunctions, the radial (vibration) and rotational contributions can be separated by approximating the system as a rigid rotor [5]. In this case $r^2 = R_e^2$, the equilibrium bond length and equation (4.10) becomes,

$$\frac{-\hbar^2}{2\mu} \frac{d^2\psi_v}{dr^2} + V(r)\psi_v = E_{vib}\psi_v \quad (4.11)$$

since $E_{v,J} \equiv E_{nuc} = E_{rot} + E_{vib}$, which is the Schrödinger equation for the harmonic oscillator if we substitute $\rho = r - R_e$ and take $V(\rho) = \frac{1}{2}k_e\rho^2$, where k_e is the force constant. Solutions of equation (4.11) are [2]

$$\psi_v = N_v H_v(y) \exp(-y^2/2) \quad (4.12)$$

which is a Gaussian multiplied by the v^{th} Hermite polynomial, $H_v(y)$ with $y = 2\pi\rho\sqrt{\mu\nu_e/\hbar}$, and N_v is a normalisation constant. The corresponding vibrational energy levels are

$$E_{vib} = E(v) = \left(v + \frac{1}{2}\right)\hbar\nu_e \quad (4.13)$$

where $\nu_e = \frac{1}{2}\sqrt{k_e/\mu}$ is the classical vibration frequency.

C. VIBRATIONAL WAVE PACKETS

Vibrational wave packets are formed by coherent superposition of vibrational wavefunctions,

$$\Psi(t) = \sum_v a_v g_v \psi_v \exp(-iE_v t/\hbar), \quad (4.14)$$

where the sum goes over the number of vibrational levels ν with energy $E_\nu = \hbar\omega_\nu$ under the Gaussian spectrum of the laser pulse $g_\nu = \exp\left[-2\ln 2(E_\nu - E_L)^2/\Delta E^2\right]$ weighted by the Frank-Condon factors, $a_\nu = \int \psi_{\nu'} \psi_\nu dr$. E_L is the central energy of the laser spectrum and ΔE its FWHM. ν' and ν'' indicate upper and lower vibration levels respectively.

The wave packet evolves over time in a way that can be understood by expansion of the energy term about its central value, $\bar{\nu}$,

$$E_\nu = E_{\bar{\nu}} + \hbar\omega(\nu - \bar{\nu}) + \frac{\hbar^2}{2} \frac{\partial\omega}{\partial E_\nu} (\nu - \bar{\nu})^2 \omega + \dots \quad (4.15)$$

since $E_\nu = \hbar\omega_\nu$, where the angular frequency $\omega = 2\pi/T_{cl}$ and T_{cl} is the classical vibration period for state ν . From this can be established the temporal behaviour of the wave packet, shown in figure 4.2. Substitution of equation (4.15) back into equation (4.14) gives,

$$\begin{aligned} \exp\left(\frac{-iE_\nu t}{\hbar}\right) &= \exp\left[\frac{-it}{\hbar} \left(\hbar \frac{2\pi}{T_{cl}} (\nu - \bar{\nu}) + \frac{\hbar}{2} \frac{2\pi}{T_{cl}} (\nu - \bar{\nu})^2 \frac{\partial\omega}{\partial E_\nu} + \dots \right)\right] \\ &= \exp\left[-2\pi i \left(\frac{(\nu - \bar{\nu})t}{T_{cl}} + \frac{\hbar^2 (\nu - \bar{\nu})^2 t}{2T_{cl}} \frac{\partial\omega}{\partial E_\nu} + \dots \right)\right] \end{aligned} \quad (4.16)$$

The classical period of the wave packet, analogous to the classical vibration of the molecule, is then given by

$$T_{cl} = \frac{2\pi\hbar}{E'(\bar{\nu})} = \frac{2\pi\hbar}{\hbar\omega} = \frac{2\pi}{\omega} \quad (4.17)$$

Anharmonicity of the potential means that components of the wave packet evolve at different rates and the wave packet spreads out over the whole vibrational coordinate. As its evolution continues some components come back into phase as a fractional revival, then all the components rephase as a full revival. The revival time T_{rev} is the time taken for wave packet to return to its initial localised state given by,

$$T_{rev} = \frac{2\pi\hbar}{E''(\bar{\nu})} = \frac{2\pi\hbar}{\hbar \left(\frac{\partial\omega}{\partial E_\nu} \right) \omega} = \frac{2T_{cl}}{\hbar \left(\frac{\partial\omega}{\partial E_\nu} \right)}, \quad (4.18)$$

Fractional revivals occur at times given by,

$$t = 2T_{rev} \frac{p}{q} \quad (4.19)$$

where p/q is an irreducible fraction of integers [6].

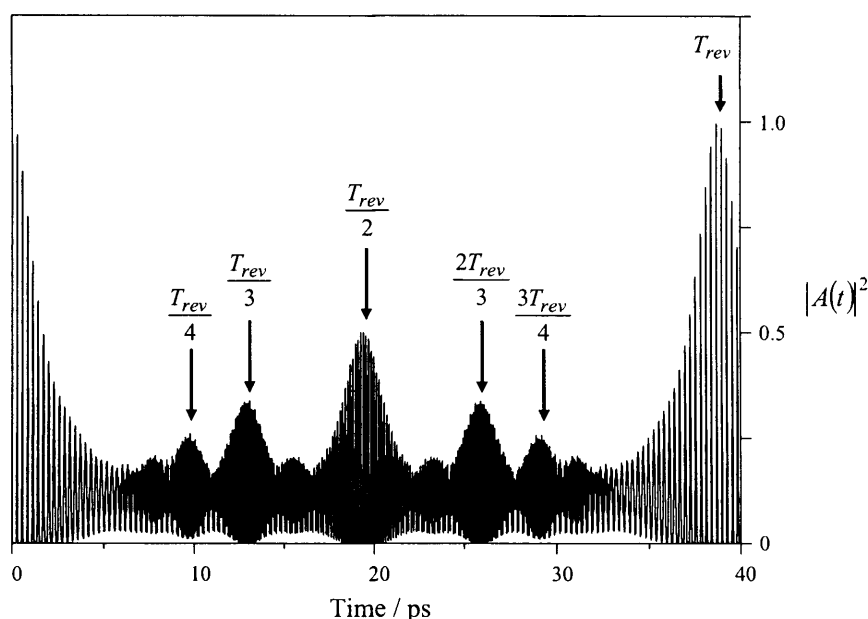


Figure 4.2 Calculated recurrence spectrum of a vibrational wave packet in the $X^+ 2\Sigma_g^+$ state of Na_2^+ excited by a 30 fs pulse around $\nu = 9$ showing partial revivals (up to fourth order) and a full revival at approximately 40 ps [7]. The fine structure is the classical oscillation of the wave packet and has an initial period of approximately 290 fs.

D. FORMATION AND DETECTION OF VIBRATIONAL WAVE PACKETS IN THE $X^+ 2\Sigma_g^+$ STATE OF Na_2^+

The broad energy bandwidth of a 50 fs laser pulse centred at around 400 nm excites a coherent superposition of Rydberg states in many series converging to different vibrational states of the ion – a wave packet. The wave packet evolves in the vibrational and electronic coordinates in a complex way but the classical periods of each are so different that it should be possible to distinguish them experimentally. The Rydberg states are less than 0.5 cm^{-1} apart so the classical period of the electronic wave packet motion will be $> 650 \text{ ps}$. The vibrational states of the ion are separated by approximately 120 cm^{-1} giving a classical period of $\sim 250 \text{ fs}$. If we observe the molecular dynamics in a time period short compared to the electronic wave packet motion we will effectively filter out the electronic dynamics, and select only the vibrational motion of the $X^+ 2\Sigma_g^+ \text{Na}_2^+$ ion.

To detect the wave packet we have been working towards a modified version of the optical Ramsey method discussed in chapter 3. Following formation of the wave packet, a second identical wave packet is excited that is time-delayed and phase-locked to the first. The wave packets interfere depending on the extent of their spatial overlap. Thus if the wave packets are formed at the inner turning point of the potential well, and the first wave packet has made an integer number of roundtrips, it will overlap and interfere with the probe wave packet. When the pump and probe wave packets interfere constructively the total Rydberg population is enhanced, whereas it is diminished when they interfere destructively. Thus the interference between the first (pump) and second (probe) wave packet leads to a phase-dependant oscillation in the total Rydberg population. In order to observe the oscillating Rydberg population, a pulsed electric field will be applied a short time after the laser excitation. If the pulsed electric field is small enough, just a few V cm^{-1} , only the highest Rydberg states, lying just below threshold, will be ionised. In this way it should be possible to isolate beating in the electron signal between bunches of Rydberg states converging to different vibrational ionisation limits from beatings between Rydberg states.

The formalism of the optical Ramsey method (ORM) can be modified to include these ideas. Assuming that the molecular Rydberg states of Na_2 are unperturbed and hydrogenic (i.e. their energies $E_n = -1/2n^2$ a.u.), and that the Condon approximation (the dipole transition moments are independent of internuclear separation) pertains, then the autocorrelation function central to the ORM can be rewritten to sum over Rydberg states converging to vibrational ionisation limits,

$$\langle \psi(\tau) | \psi(0) \rangle = \sum_{n(v^-)} a_{n(v^-)}^2 g_{n(v^-)}^2 \exp[-iE_{n(v^-)}\tau/\hbar] \quad (4.20)$$

where $\psi(\tau)$ is the initial wave packet, $\psi(0)$ is the probe wave packet.

$$a_{n(v^+)} = a_{v^+} \int_0^\infty \psi_{ns,nd}(r) r^3 \psi_{3p}(r) dr \quad (4.21)$$

accounts for the one-electron transition moments for hydrogenic orbitals from the intermediate A-state, and $g_{n(v^+)}^2$ is the Gaussian amplitude factor. $E_{n(v^+)}$ is the energy of each Rydberg series converging to a particular ionisation limit, v^+ . Fielding and Stavros [1] performed calculations using these expressions for $n = 150 - 200$, corresponding to field ionisation with a field of around $1.5 - 0.5 \text{ V cm}^{-1}$, for excitation

with a 30 fs pulse in a one-photon transition from the ground state to form a wave packet centred around vibrational state of the ion $\bar{v}^+ = 7$. The results were compared to an analogous calculation that treated only the vibrational states of the ion and found to be dynamically identical, but with slightly diminished amplitudes in the Rydberg result at long time delays. Knowing this, the authors were able to treat the vibrational wave packets in the ionic potential alone. Thus the wave function for a pump and probe wave packet pair can be written,

$$\psi(\tau) = \sum_{v^+} a_{v^+} g_{v^+} \psi_{v^+}, \text{ and} \quad (4.22)$$

$$\psi(0) = \sum_{v^+} a_{v^+} g_{v^+} \psi_{v^+} \exp[-iE_{v^+} + \tau/\hbar] \quad (4.23)$$

which give an ORM autocorrelation,

$$\langle \psi(\tau) | \psi(0) \rangle = \sum_{v^+} a_{v^+}^2 g_{v^+}^2 \exp[-iE_{v^+} + \tau/\hbar]. \quad (4.24)$$

The experimental observable is, as always with the optical Ramsey method, the modulus of the autocorrelation function,

$$S(t) = |\langle \psi(\tau) | \psi(0) \rangle| \quad (4.25)$$

It would be possible to treat the states excited in this way with multi-channel quantum defect theory (MQDT), which has been applied to the frequency spectra of Na₂ [8, 9] and to wave packet dynamics in argon [10] and xenon [11, 12], but this has yet to be attempted.

The states excited in these experiments are sometimes known as ZEKE states as they are amenable to zero-kinetic energy pulsed-field ionisation (ZEKE-PFI) spectroscopy. This high resolution spectroscopic technique was developed by Muller-Dethlefs and Schlag [13]. High-lying Rydberg states are excited optically then ionised by a small pulsed electric field. The technique depends on the anomalous longevity of the high Rydberg states. MQDT calculations suggest that the ZEKE states of Na₂ have lifetimes of the order of nanoseconds [14], easily long enough for our pump – probe experiments, which have delays of a few tens of picoseconds. Time-resolved ZEKE-PFI has been implemented before to study vibrational dynamics [15, 16] but in a quite different way to this.

In summary, this approach should allow measurement of vibrational wave packet dynamics in the $X^+ \ ^2\Sigma_g^+ \text{Na}_2^+$ potential well by excitation of wave packets in the

high-lying Rydberg states of Na_2 followed by pulsed-field ionisation, and offers a convenient theoretical tool for modelling the proposed coherent control experiments.

4.2 PROPOSED COHERENT CONTROL SCHEME

The work of Fielding and Stavros [1] forms the basis of the coherent control scheme we have attempted to implement [1], and is discussed here. Two vibrational wave packets are excited in the $X^+ \ ^2\Sigma_g \text{Na}_2^+$ ion with a well-defined phase difference between them. The first wave packet is allowed to evolve to $\tau = \tau_{cl}/2$, at which time it can be written,

$$\psi(\tau_{cl}/2) = \sum_{v^+} a_{v^+} g_{v^+} \psi_{v^+} \exp[-iE_{v^+}(\tau + \tau_{cl}/2)/\hbar] \quad (4.26)$$

At this time, which we call $t = 0$, a second wave packet is excited by the same laser pulse separated in time and phase from the first by a Michelson interferometer. This second wave packet is given by,

$$\psi(\vartheta) = \sum_{v^+} a_{v^+} g_{v^+} \psi_{v^+} \exp[-iE_{v^+}(\tau + \vartheta)/\hbar] \quad (4.27)$$

A variable time later, after the first two wave packets have been allowed to evolve and interfere, the probe pulse forms a third wave packet given by,

$$\psi(\tau) = \sum_{v^+} a_{v^+} g_{v^+} \psi_{v^+} \quad (4.28)$$

The autocorrelation function measured by the optical Ramsey method is then,

$$\begin{aligned} \langle \psi(\tau) | \psi(\tau_{cl}/2) + \psi(\vartheta) \rangle &= \sum_{v^+} a_{v^+}^2 g_{v^+}^2 \exp[-iE_{v^+}(\tau + \tau_{cl}/2)/\hbar] \\ &+ \sum_{v^+} a_{v^+}^2 g_{v^+}^2 \exp[-iE_{v^+}(\tau + \vartheta)/\hbar] \end{aligned} \quad (4.29)$$

where τ_{cl} is the classical vibration period, ϑ is the phase difference between the two wave packets at $t = 0$.

As in the coherent control in the sodium atom Rydberg wave packets (section 3.1D), the approach here exploits phase evolution in the partial revivals. Around the time of the second order partial revival the total wave function for the wave packet can be written,

$$\psi(R, \tau) = \frac{1}{\sqrt{2}} [\exp(-i\pi/4) \psi_{cl}(R, \tau) + \exp(i\pi/4) \psi_{cl}(R, \tau + \tau_{cl}/2)] \quad (4.30)$$

where R is the internuclear distance, and $\psi_{cl}(R, \tau)$ and $\psi_{cl}(R, \tau + \tau_{cl}/2)$ are the two sub wave packets of the second order partial revival, separated in time by half the classical vibration period. These components are out of phase by $\pi/2$ (figure 4.3).

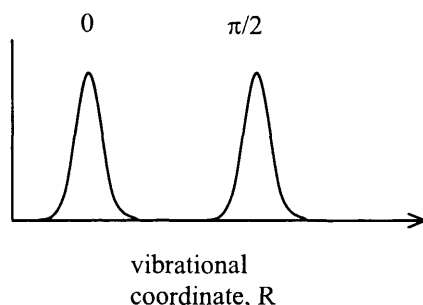


Figure 4.3 A cartoon showing the phase of the sub wave packets of the second order partial revival resulting from evolution of a single vibrational wave packet for time $T_{rev}/2$.

If a second wave packet is excited $\tau_{cl}/2$ after the first, at $T_{rev}/2$ they will have relative phases shown in figure 4.4.

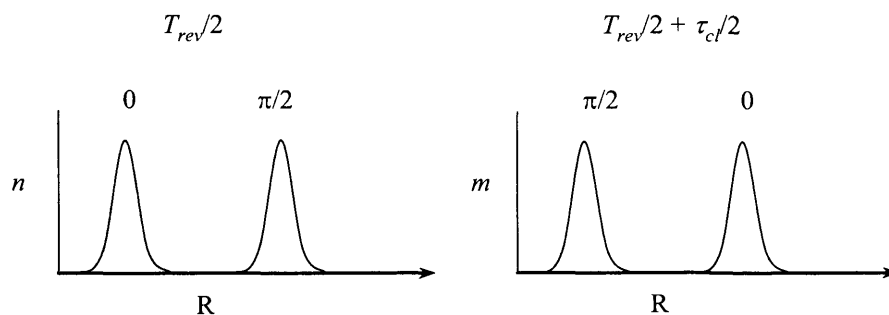


Figure 4.4 A cartoon showing the relative phases of two second order partial revivals of two wave packets n and m . The second wave packet n is formed $\tau_{cl}/2$ after m .

Now if the initial phase of the second wave packets n is changed with respect to the phase of m , the sub wave packets of the second order partial revival (localised at the inner and outer classical turning points) will interfere (figure 4.5).

When the phase difference is $-\pi/2$ the inner little wave packets of m and n are exactly out of phase and interfere destructively. The outer little wave packets interfere constructively to form a single wave packet localised at the outer turning point. A phase difference of $\pi/2$ gives rise to single wave packets localised at the inner turning point by the same argument. The π phase difference does not give completely constructive or

destructive interference so two wave packets are formed, one at each classical turning point.

These ideas have been extended to the 4th and 8th order partial revivals, each time using interference between two identical wave packets to manipulate the vibrational dynamics [1]. More recently, and in conjunction with experimental efforts discussed here, Boléat and Fielding have made further theoretical investigations of coherent control in the $X^+ 2\Sigma_g^+$ potential [7].

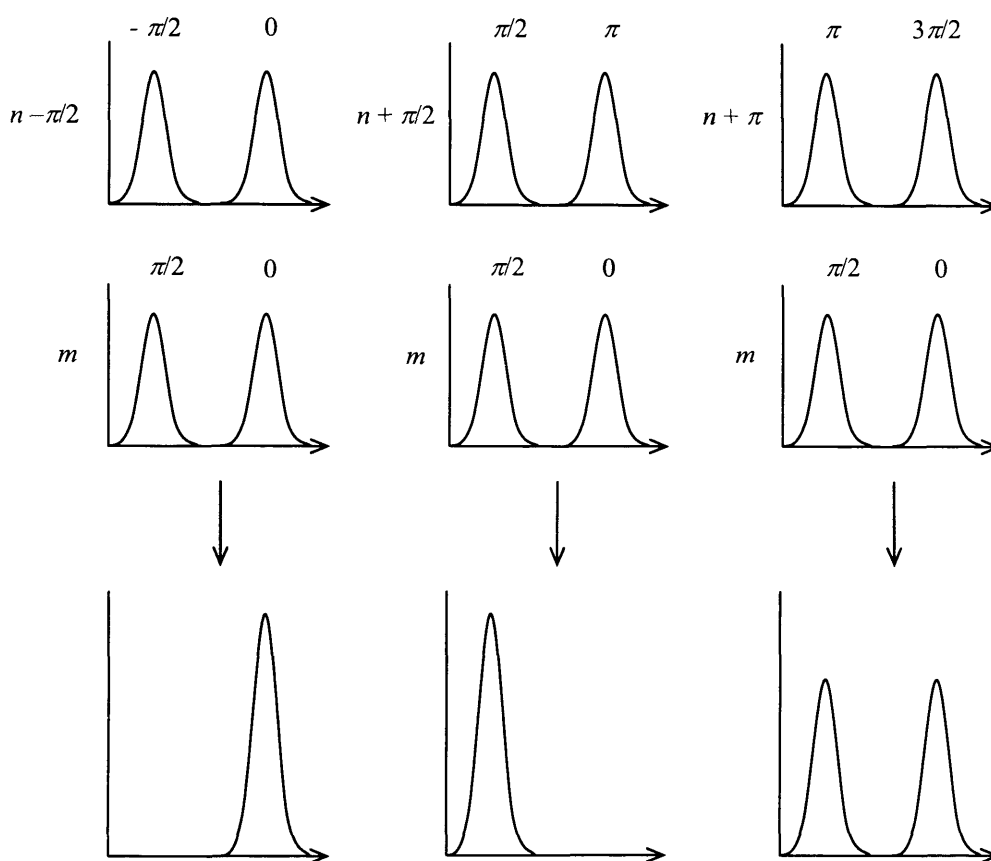


Figure 4.5 Cartoons showing the effect of phase differences between two wave packets, m (middle row) and n (top row), resulting from interference between them around the time of the second order partial revival, $T_{rev}/2$. Wave packet n is excited $\tau_{c}/2$ after wave packet m with a phase shift indicated on the y -axes in the top row. A phase shift of wave packet n by $-\pi/2$ leads to constructive interference at the outer turning point and destructive interference at the inner turning point (left column), whereas a $\pi/2$ phase shift (middle column) reverses the positions of constructive and destructive interference. When wave packet n is phase shifted by π , neither completely constructive nor completely destructive interference occurs (right column).

In that work the ideas of interference between wave packets leading to selective quantum state population control was extended to an arbitrary number k of identical time-delayed and phase-shifted transform-limited laser pulses. In this case the autocorrelation function leading to the observable is,

$$\langle \psi(0) | \psi(t) \rangle = \sum_{\nu} a_{\nu}^2 g_{\nu}^2 \exp(-i\omega_{\nu}t) \left[1 + \sum_k \exp(-i\omega_{\nu}t_k) \right] \quad (4.31)$$

Assuming that the A state population is not depleted, the population of vibrational states following such excitation is given by

$$b_{\nu} = -\frac{i}{2} \Omega_{\nu} g_{\nu} \left[1 + \sum_k \exp(-i\Delta_{\nu}t_k) \exp(i\omega_L t_k) \right], \quad (4.32)$$

where Ω_{ν} is the Rabi frequency between the A state and the ionic state, and $g_{\nu} = \exp\left[-2 \ln 2 (E_{\nu} - E_L)^2 / \Delta E^2\right]$ is the Gaussian spectral profile of laser with FWHM ΔE centred at E_L . The detuning $\Delta_{\nu} = \omega_L + \omega_{\nu'} - \omega_{\nu}$, where ω_L is the central laser frequency, $\omega_{\nu'}$ is the vibrational frequency of the A state and ω_{ν} is the that of the ionic state.

Careful analysis of the calculated spectra allowed the authors to derive expressions that can be used to predict the populations for such a sequence of pulses. Thus to depopulate a specific vibrational quantum state ν in the wave packet the optical phase would need to be

$$\phi_{\nu}^{-} = (2n + 1)\pi - (\omega_{\nu} - \omega_{\nu'}) (p/q) T_{cl} \quad n = 0, \pm 1, \pm 2, \dots \quad (4.33)$$

and to enhance its population,

$$\phi_{\nu}^{+} = 2n\pi - (\omega_{\nu} - \omega_{\nu'}) (p/q) T_{cl} \quad n = 0, \pm 1, \pm 2, \dots \quad (4.34)$$

where the superscripts ‘-’ and ‘+’ indicate depopulation and enhancement respectively. The phase shift corresponds to a small time shift $t_{\phi} = \phi_{\nu} / \omega_L$ made in addition to the coarse delay of pulse k given by $(p/q)T_{cl}$, where (p/q) is an irreducible fraction of integers.

The phases required to achieve a particular control result in the two wave packet coherent control experiment could then be easily found. Thus two pulses separated by $T_{cl}/2$, i.e. where $p/q = 1/2$ allow selection of only odd vibrational states from a Gaussian wave packet if the phase of the second pulse is shifted by $\phi_{\nu}^{-} = 0.804\pi$, which

is equivalent to a time shift of $t_\phi = 0.804\pi/\omega_L$. At the same coarse delay a π phase shift from there gives $t_\phi = -0.196\pi/\omega_L$ in the second pulse and leaves only even states in the wave packet.

4.3 EXPERIMENTAL

A narrow bandwidth continuous-wave (CW) dye laser excites sodium dimers in a molecular beam from the $X^1\Sigma_g^+$ ground state to the $A^1\Sigma_u^+$ intermediate. Vibrational wave packets formed by coherent superposition of high Rydberg states converging to several vibration states of the $X^+2\Sigma_g^+ Na_2^+$ ion are then excited by 100 fs pulses at around 400 nm generated from the pulse-picked and frequency-doubled output of a Kerr-lens modelocked titanium sapphire laser. Figure 4.6 shows the layout of the laser table. Following the formation and evolution of one vibrational wave packet another identical wave packet is excited as described above. Finally a third identical (probe) wave packet is formed followed by field ionisation of the molecules (optical Ramsey method). The timing of these three wave packets is controlled using a nested Michelson interferometer. A short time after formation of the third wave packet a ramped electric field ionises the molecules. Either the electrons or ions formed are accelerated along the time-of-flight tube to a suitably biased multi-channel plate detector. The signal from the detector is amplified, filtered and recorded as time-resolved spectrum of the wave packet behaviour.

A. LASERS

Both the CW and femtosecond laser were pumped by a Coherent Verdi V8 diode-pumped Nd:YVO₅ laser producing up to 8.5W CW at 532 nm. It is generally operated at 8.0 W output power. The CW laser, a Coherent 599, is pumped by the approximately 3 W of the Verdi beam. To operate at 637 nm to 656 nm DCM dye was used dissolved in ethylene glycol solution in ethanol (2 g L⁻¹).

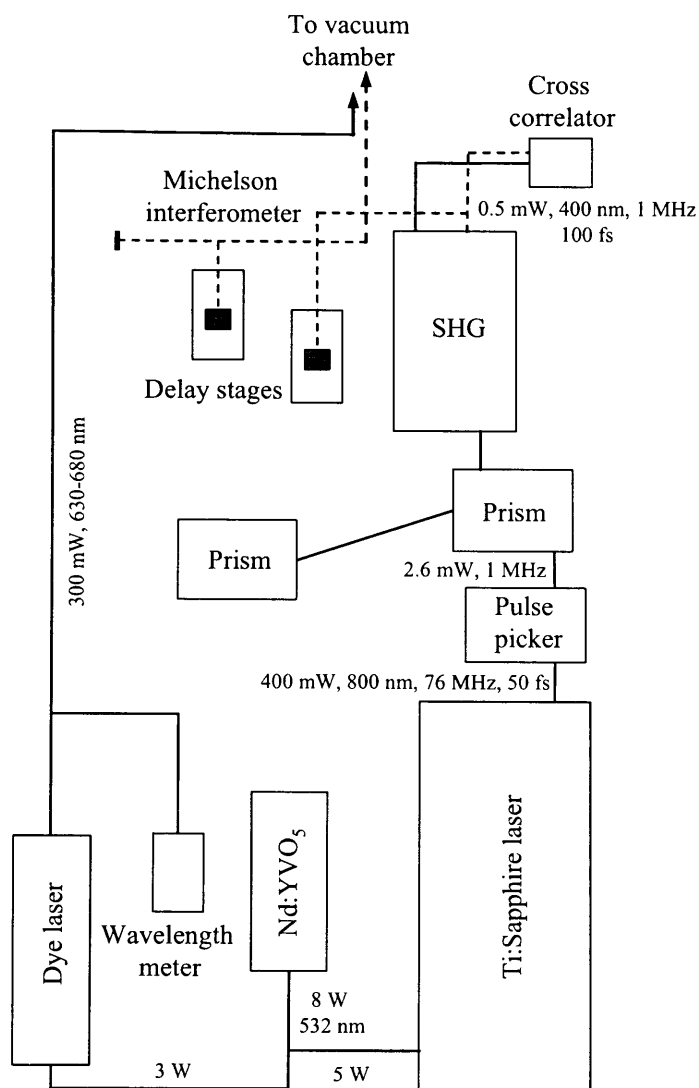


Figure 4.6 The layout of the femtosecond laser table. A diode-pumped Nd:YVO₅ CW laser pumps a CW dye laser and a titanium sapphire femtosecond oscillator operating at around 800 nm. The repetition rate of the femtosecond pulse train is reduced from 76 MHz to 1 MHz by a pulse-picker. The beam then passes through a prism pair compressor, and is then frequency-doubled by second harmonic generation (SHG). The SHG beam passes through a nested Michelson interferometer to generate phase-locked pulse sequences. After the interferometer the ultraviolet femtosecond beam is combined with the CW dye laser beam at a dichroic mirror and they are directed into the vacuum chamber collinearly. The lasers and molecular beam interact between two electric-field plates forming one end of the ion (electron) time-of-flight mass spectrometer.

The cavity was equipped with two Fabry-Perot etalons and a 3-plate BRF ostensibly to narrow its output linewidth. However this laser proved unsuitable for the task of exciting single rovibrational states of the $A^1\Sigma_u^+ \leftarrow X^1\Sigma_g^+$ transition as its

linewidth was not particularly narrow and its output wavelength and power were very unstable. A more suitable laser, a Coherent 699 ring-dye laser, was kindly lent to us by Prof. Tony McCaffrey from Sussex University but there was insufficient pump power to operate it in conjunction with the femtosecond laser.

The remaining 5 W of the Verdi beam was used to pump a Kerr-lens modelocked titanium sapphire ($\text{Ti:Al}_2\text{O}_3$) laser (Coherent Mira Seed). This produced a train of pulses of ~ 50 fs duration with a repetition rate of 76 MHz and around 400 mW power. The output pulse bandwidth was monitored using a spectrum analyser (IST-Rees E200). Figure 4.7 shows a typical spectral profile for this laser operating at around 800 nm.

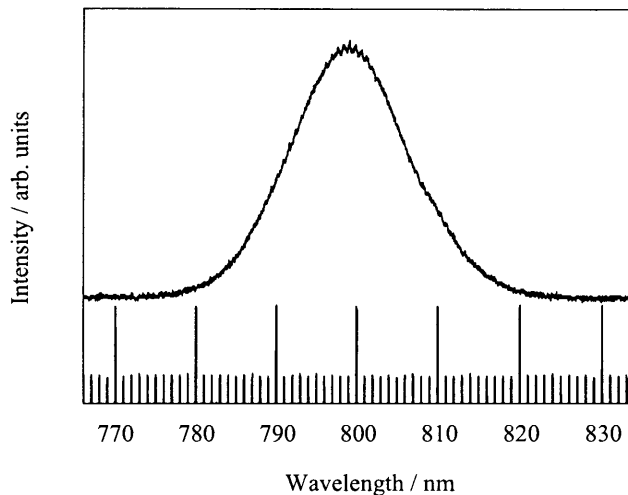


Figure 4.7 Spectrum of the output pulse train from the titanium sapphire laser as displayed on a digital oscilloscope. The horizontal scale is generated by the spectrum analyser and displayed simultaneously on the oscilloscope.

The output wavelength of the titanium sapphire laser can be tuned between 780 nm and 820 nm by altering the angle of a birefringent filter. The 76 MHz repetition rate of this laser was too high for the electronics needed to ramp the electric field in the interaction region, so it was reduced to 1 MHz by an acousto-optic pulse picker (Coherent 9200 Pulse-Picker). Removing 75/76 pulses from the train reduced the power from around 400 mW to 5.2 mW. The device was only about 50 % efficient so the output power further reduced to around 2.6 mW. The 1MHz pulse train is sent into prism pair compressor. The purpose of the compressor was to compensate for the chirped output of the titanium sapphire laser and dispersion suffered by the pulses in the

pulse-picker, as well as to pre-compensate for dispersion encountered in the second harmonic stage, Michelson interferometer, steering optics and vacuum chamber windows. The transmission efficiency of the compensator was $> 95 \%$, so typically the beam power was around 2.5 mW after compression. The femtosecond pulses were then frequency-doubled by passing through an Inrad 5-050 Harmonic Generator containing a thin (*ca.* 1 mm) LBO crystal. The output power was typically around 500 μW at 1 MHz around 400 nm, giving a pulse energy of 500 pJ. The fundamental and SHG beams of the titanium sapphire were either passed into a cross-correlator (Angewante Physik und Electronic (APE) PulseCheck Autocorrelator [sic]) or separated by a dichroic mirror so the UV beam could be used directed into the Michelson interferometer and vacuum chamber. This optical arrangement is not ideal and it would be better to have the cross-correlator measuring all the time.

B. DATA COLLECTION

After SHG the beam passes into a double Michelson interferometer. A schematic of the double interferometer intended for this experiment is shown in figure 4.8. It is similar to the interferometer discussed in chapter 3 but differs sufficiently to warrant inclusion here.

The inner interferometer (comprising paths 1 and 3), used to separate the first- and control wave packets, was identical to the feedback-stabilised digital system discussed in chapter 3. Indeed it was our intention simply to duplicate or borrow it – hence the appeal of building the stabilisation circuit from off-the-shelf components rather than bespoke electronics.

The larger interferometer (paths 1 and 2) sets the delay and phase of the probe laser pulses. Its variable length arm comprises two moving parts. Coarse adjustments are made with a linear translation stage (Physik Instrumente P510.12). The linear translation stage has a carriage that travels along a worm shaft turned by a DC electric motor. The position of the shaft, and therefore the carriage, is monitored by a rotary encoder. This generates 1000 counts per revolution, giving the carriage position a calculated resolution of 17 nm count^{-1} .

The stage is controlled using National Instruments LabView programs via an ISA card (Physik Instrumente C842) in a PC. Fine adjustments are made with a

piezoelectric actuator (Physik Instrumente P780) bolted on top of the translation stage. The moving mirror is mounted on top of the piezo. The quoted resolution of this device is < 1 nm, it can travel through a distance of $80 \mu\text{m}$. It is powered by a X10 voltage and current amplifier (Physik Instrumente E501). Voltage amplification means that a small signal (less than ± 10 V) can be used to control the actuator, which requires 100 V for full deflection. A pulse/function generator (Hewlett Packard 8116A or Stanford Research Systems DS345) drives the amplifier to control the actuator.

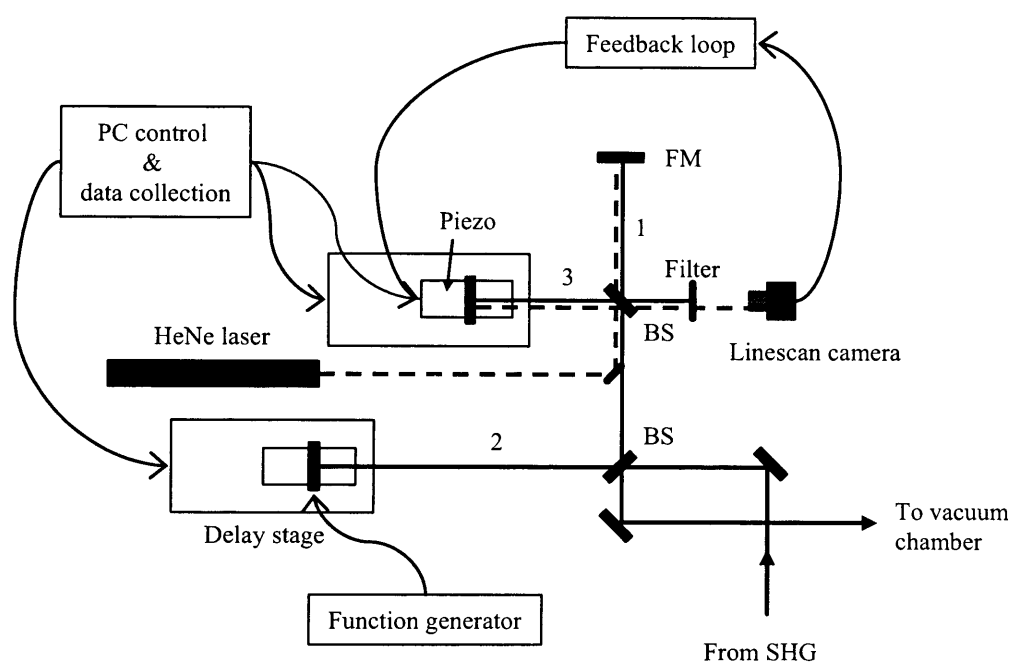


Figure 4.8 The nested Michelson interferometer designed to generate pump-probe pulse delays and phase-locked pulses for multiple wave packet excitations. Beams are shown as straight lines, electrical connections are curved. Path 3 gives the first pulse, path 1 the control pulse and path 2 the optical Ramsey probe pulse. Both moving arms have a motor driven delay stage for coarse adjustments. Arm 3 has a feedback stabilised piezo stage for fine positioning and is position-stabilised with reference to HeHe (dashed line) fringes by a lab-built feedback loop. The mirror at the end of the probe arm 2 is dithered by a piezo driven by a function generator to sweep the phase of the probe pulse.

In contrast to the data collection arrangements discussed in chapter 3, where the phase of the probe wave packet was stepped to give Ramsey fringes in the ion or electron signal, here we wanted to continuously sweep its phase. The idea is that the sweeping phase is adequately sampled by the high repetition rate of the laser. To collect wave packet recurrence spectra we would sweep the phase by, for instance, ten optical

cycles (approximately 4000 nm) at each large time step made by the motor stage, giving 10 Ramsey fringes in the electron signal. The moving mirror therefore has to sweep through 2000 nm. Since the frequency of the fringes derives from the wavelength and the sweep rate it is then possible to filter that signal with a bandpass filter. The amplitude of the interference fringes would depend on the overlap between the pump and probe wave packets so the recurrence spectrum could be recovered by taking the RMS of the fringes at each coarse time step.

The interrelated signal processing instruments are shown in figure 4.9. All timing is based on the repetition rate of the titanium sapphire laser (76 MHz reduced to 1 MHz by the pulse picker). A photodiode signal from the femtosecond laser pulses triggers the pulse picker and trigger pulses from there can be used readily to synchronise other devices. Delays can be introduced into the timing network by the use of a digital delay generator (Stanford Research Systems DG535).

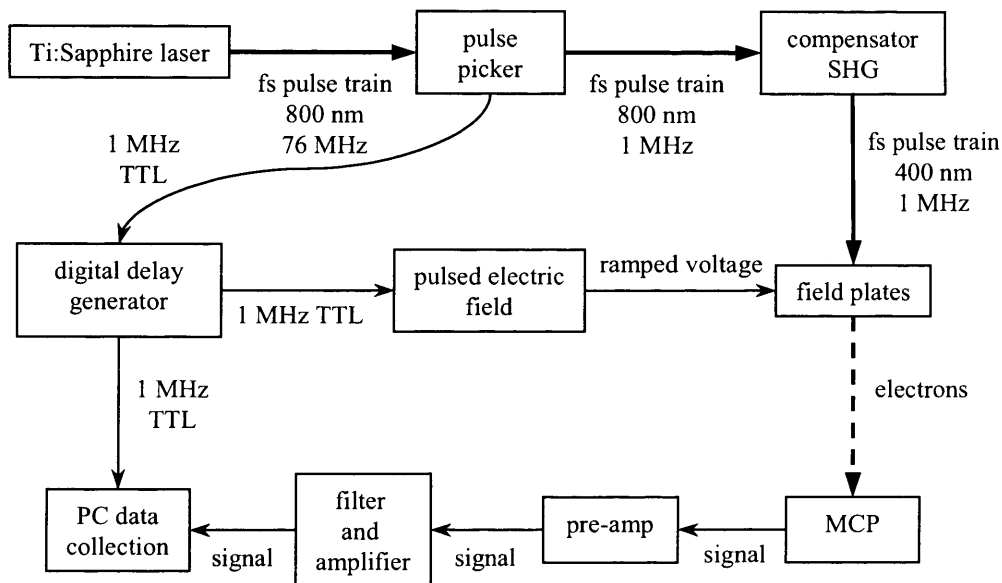


Figure 4.9 Timing in the experiment is derived from the repetition rate of the titanium sapphire laser, recorded by a photodiode sampling a small fraction of the output. The pulse-picker driver outputs TTL pulses synchronised to, and frequency-divided from, the fs pulse train. The digital delay generator allows timing of the ionising of the electric field ramp to be synchronised with the laser pulses, and triggers the data collection hardware in the PC. A fast digital oscilloscope can be used to capture the filtered signal in place of the analogue input card in the PC. In that case the waveform is transferred to the PC via GPIB.

For our wave packet dynamics experiments, ionisation of the ZEKE states comprising the wave packet would have been achieved using a programmable signal generator (Stanford Research Systems DS435). This is triggered from the pulsed laser, as it has to ramp the electric field in the ionisation region of the time-of-flight for every laser pulse. This device allows us to apply stepped or ramped fields as required. In initial experiments a high electric field (2000 V cm^{-1}) was applied to the field plate to ensure that any Rydberg molecules would be ionised. This was done to facilitate finding the ion signal on the oscilloscope.

The electron or ion signal produced by the detector will be modulated by several frequencies. Firstly there is the repetition rate of the laser (1 MHz), then there is the oscillation rate of the piezoelectric translator changing the phase between the wave packets, and finally there is the modulation of the signal due to the interference of the vibrational wave packet(s) and the probe wave packet – the optical Ramsey signal that we want. The signal from the detector will be sent into a programmable digital filter amplifier (Stanford Research Systems SR650). This device has one high- and one low-pass filter. The filter thresholds of each can be varied between 1 Hz and 99.9 kHz. Both input channels have a 60 dB variable amplifier and both outputs have a 30 dB variable amplifier. These will be used to isolate the wave packet signal from the others.

Once the filtering is set up correctly the data (output from the filter) will be digitised by a 16-bit analogue-to-digital converter (ADC) or a 500 MHz digital oscilloscope (LeCroy LT372 Waverunner). The ADC is a PCI expansion card (National Instruments PCI-6032E) that can be externally triggered and has a maximum data acquisition rate of 200 kHz. The oscilloscope can download data to a PC via a GPIB connection. Once on the PC the data will be reduced and written to disk by a lab-written LabView data collection program which also controls the position of the delay stage(s).

C. EXPERIMENTAL ARRANGEMENT FOR FREQUENCY RESOLVED SPECTROSCOPY OF Na_2

With a view to characterise the molecular beam temperatures and velocity and identify suitable rovibrational states of the A state intermediate we performed frequency resolved spectroscopy using narrow linewidth nanosecond lasers. It was our intention to extend this to the high-lying Rydberg states of Na_2 , however that was not possible.

Two configurations of the lasers were used. The first attempted to excite the A – X transition with the fundamental of a dye laser and use the frequency-doubled output to photoionise. A Sirah PrecisionScan dye laser with DCM dye in DMSO (0.34 g L⁻¹ in the oscillator and pre-amp, 0.11 g L⁻¹ amplifier) was pumped by a Continuum Powerlite II 8000 Nd:YAG operating at 10 Hz giving 400 mJ pulse⁻¹ at 532 nm. The dye laser output was 8 – 10 mJ pulse⁻¹ around 656 nm and was frequency-doubled in KDP to give ~0.4 mJ pulse⁻¹. The fundamental and SHG beams were combined with a dichroic mirror and directed into the vacuum chamber to excite the sodium molecular beam. The SHG pulses were delayed slightly (< 1 ns) with respect to the fundamental pulses. In some experiments the two beams were focussed using a 250 mm lens, in others no lens was used in an attempt to eliminate ionisation via excitation paths other than the desired one.

The second approach, intended to make the excitation more selective and reduce the excitation of competing pathways to ionisation, used two different dye lasers so that the ionisation wave length was independent of the scanning wave length. The output of the 10 Hz Nd:YAG laser (400 mJ pulse⁻¹ at 532 nm) was split equally to pump a Continuum ND6000 dye laser and the Sirah PrecisionScan. DCM dye in methanol (270 mg L⁻¹ in the oscillator and pre-amp, 90 mg L⁻¹ for the amplifier) gave 3 mJ pulse⁻¹ from the ND6000 with a bandwidth specified at 0.05 cm⁻¹. Styryl 9M dye in ethanol (0.13 g L⁻¹ in the oscillator and pre-amp, 0.04 g L⁻¹ for the amplifier) was frequency-doubled in KDP to give around 6 μJ pulse⁻¹ at 410 nm from the PrecisionScan with a bandwidth specified at 0.1 cm⁻¹. The two beams entered the vacuum chamber after combination at a dichroic mirror. As above, the blue pulse train was retarded slightly.

Data was collected with exactly the same instrumentation as for the frequency resolved sodium atom spectroscopy described in sections 3.2B and 3.2C. The pre-amplified electron or ion signal from the MCP was captured on a digital oscilloscope. From there the waveform was transferred to a PC running a dedicated LabView (National Instruments LabView 5.1) program via a GPIB connection.

4.4 RESULTS AND DISCUSSION

A. PROGRESS IN THE PROPOSED DATA COLLECTION METHOD

Suitable sweep rates, amplitudes and functions to continuously sweep the probe wave packet timing were established without relying on excitation of sodium dimers. An experiment was set up where the output of a one-arm interferometer was directed either onto a black surface overlooked by a photomultiplier tube (Hamamatsu R1463) or a fast photodiode (ThorLabs DET210). Once the interferometer was correctly aligned it was possible to monitor the optical interference fringes as the two pulses swept through each other. Figure 4.10 shows a sample of optimised fringes generated by sweeping the probe pulse completely through the other.

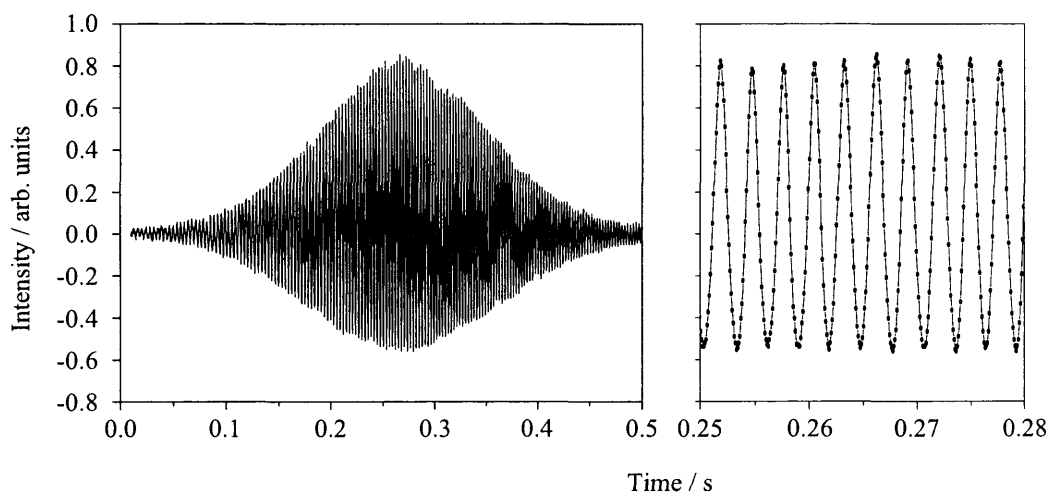


Figure 4.10 Left panel: Optical fringes generated by 400 nm \approx 100 femtosecond laser pulses by dithering the path length of one arm of a single Michelson interferometer. The signal was generated by a PMT and recorded on a digital oscilloscope (LeCroy LT372 Waverunner). The piezo was driven by a 1 Hz 2.5 V sine wave with a duty cycle of 50 %. A 50 V offset was also applied so that the piezo moved around its central displacement. Right panel: a close-up of the fringe pattern from near the centre of the interferogram. The data points indicate that the fringe is well sampled by at this scanning speed.

The function applied to the piezo was generated by a programmable function generator (Hewlett Packard 8116A) outputting a 1 Hz sine wave of 2.5 V and 50 % duty cycle). Other functions were tested but this one gave the smoothest fringes with the

most consistent frequency. The frequency is significant as the signal would be passed through a filter.

Sweeping the phase of the probe wave packet was never achieved for sodium dimers, however the experiment was carried briefly in sodium atoms as a test of principle. Similar approaches have been used in high repetition rate experiments before [17], but we wanted to see if it would work with our system.

The $3^2P_{3/2} \leftarrow 3^2S_{1/2}$ transition in atomic sodium was excited by the CW dye laser at 589.158 nm followed by direct photoionisation by the 76 MHz pulse femtosecond pulses train at around 400 nm, bypassing the pulse-picker to increase the power. A single interferometer was used with the phase dithered by the piezo over a few optical cycles. Shown in figure 4.11 are the fringes observed when the resulting electron signal was output to a digital oscilloscope.

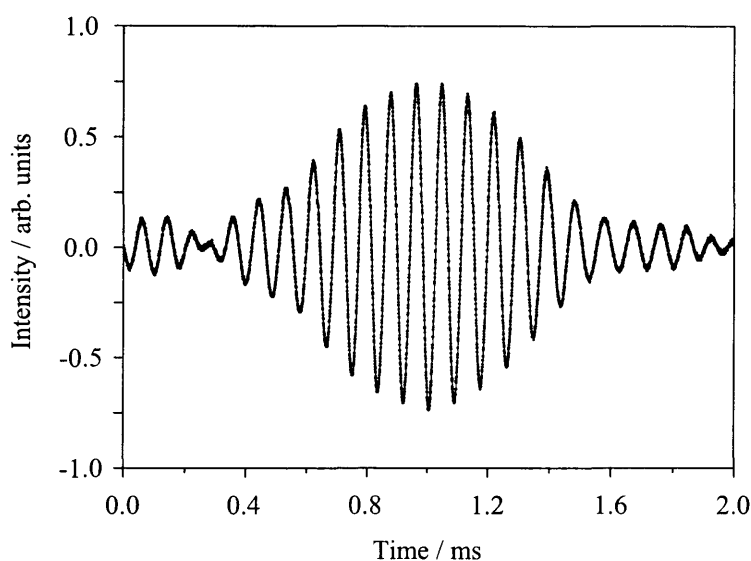


Figure 4.11 Optical interference fringes from photoelectrons from atomic sodium. Sodium atoms in the atomic beam were excited from the ground state $^2S_{1/2}$ to the $^2P_{3/2}$ by a CW dye laser at 589.158 nm and from there photoionised by a pair of interfering 100 fs pulses at around 400 nm. The pump-probe delay was dithered at 150 Hz with a triangle wave of 400 mV amplitude applied by the SRS DS345 function generator, giving a time sweep of approximately 20 fs. Photoelectrons were detected by a MCP (Hamamatsu F4655.12). The signal passed through a 100 Hz bandpass filter set at 12.25 kHz and captured by the digital oscilloscope. The data points indicate that the fringes were sampled more than adequately.

This experiment showed that sweeping the piezo could generate Ramsey fringes in the photoelectron signal. It also indicated that we would require long collection times to see the signal in sodium dimers as they would be excited below the ionisation threshold, they were less numerous in the molecular beam and the probability for both optical transitions is probably smaller than in atomic sodium. Also, since the path only changed by about 20 fs the pump and probe pulses only swept partially through each other. It is not clear why in that case the signal should have the shape it has. Presumably the piezo velocity was not linear and the fringe frequency changed near the end of its travel. If the frequency went outside the band pass of the filter it would be blocked.

B. Na₂ A – X FREQUENCY SPECTRA

These experiments, carried out with the lasers described in section 4.3C, utilised the same data collection hardware and software as the frequency-resolved experiments presented in chapter 3. Briefly, approximately 70 ns after the laser pulses a fast-rising (< 25 ns) 2000 V pulse was applied to the field plate to ionise and repel ions to the detector. Ions were detected on a MCP (Hamamatsu F4655-10), pre-amplified (Ortec EG&G VT 120) and sampled on a digital oscilloscope (LeCroy Waverunner LT372). Signal waveforms for each laser shot, shown in figure 4.13 were downloaded via GPIB to a PC running a lab-written LabView data collection program. A wavelength meter (Angstrom WS-7) simultaneously recorded the wavelength of the scanning laser to the data collection PC.

Figure 4.12 would indicate sodium dimers are certainly present in the beam. The flight-times are correct for the narrow peak at 1.8 μs to be Na⁺ and the broader smaller peak at 2.6 μs to be Na₂⁺. The relative peak areas are 4:1 Na⁺:Na₂⁺, but this may not reflect truly their relative intensity in the beam as the laser was much nearer resonant with Na₂ than Na. It should therefore have been possible to obtain frequency-resolved, and indeed time-resolved, spectra of Na₂.

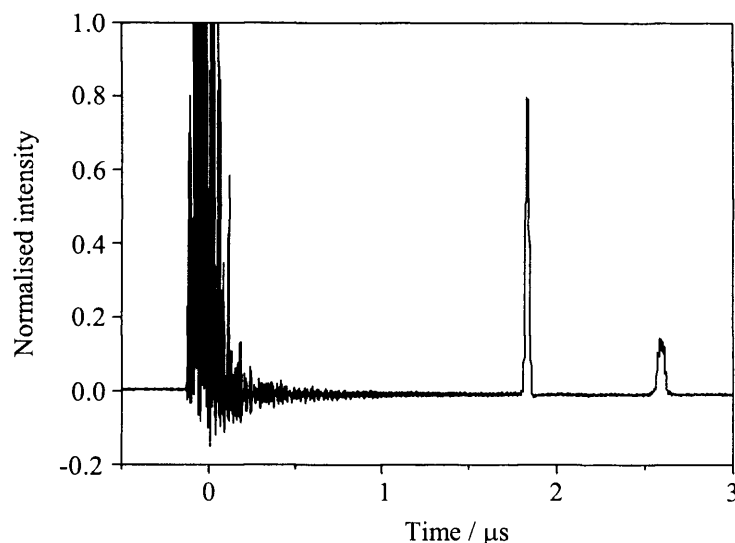


Figure 4.12 Sample signal waveform recorded by the oscilloscope for excitation of the sodium beam by a ns dye laser at 637 nm. The narrow peak at 1.8 μs is due to Na^+ and that at 2.6 μs from Na_2^+ . The noisy peak at $t = 0$ is from RF interference generated by the high-voltage switching electronics. The peak areas are 4:1 $\text{Na}^+ : \text{Na}_2^+$, but this probably does not reflect their intensities in the beam as the laser was much nearer resonance with Na_2 than Na.

However despite many attempts with different sodium source conditions (temperatures and carrier gas (Ar) flows), different laser configurations, focusing and power variations and high-voltage pulse values, no reproducible, assignable spectra were ever found. Indeed most scans of the wavelength of the A – X transition simply yielded no signal *at all*. One exception is shown below. The source conditions were $T_{\text{oven}} = 495\text{ }^\circ\text{C}$, $T_{\text{nozzle}} = 650\text{ }^\circ\text{C}$ with Ar carrier gas at 4 bar fed through a needle valve (Nupro/Swagelok bellows-sealed metering valve SS-4BMW-TSW) such that the pressure in the source chamber was approximately 1×10^{-4} mbar. Two ns dye lasers were used, as in the second arrangement discussed in section 4.3C. The beams were not focused, leading to an interaction volume (limited by the 4 mm diameter of the sodium beam) of approximately 2×10^{-5} m³, and a power density of approximately 7 MW cm^{-2} for a laser beam with a diameter of 6 mm, and the pulse energy and duration were 10 mJ and 5 ns respectively. For other scans the beams were focused as discussed in section 3.2C for the sodium atom experiments, giving a maximum power density of approximately 5×10^{11} W cm⁻². It was felt that focusing lead to enhanced multiphoton ionisation as the signal was larger but independent of wavelength.

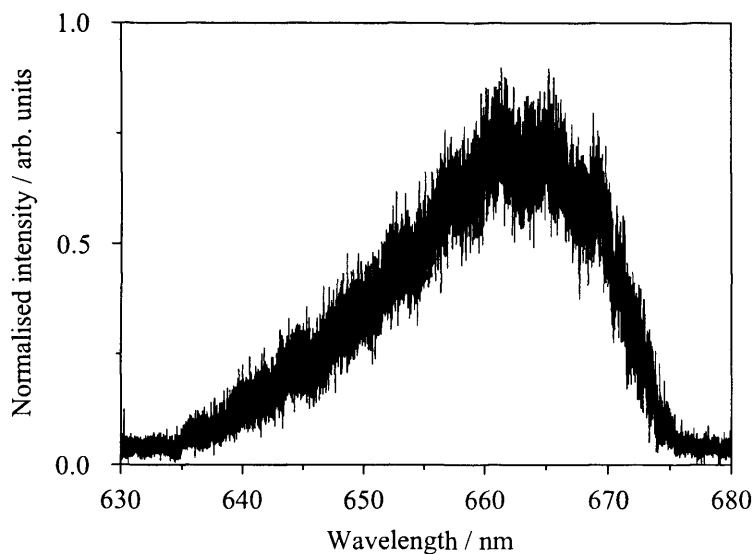


Figure 4.13 Trace of the wavelength dependent ion signal recorded during attempts at A – X frequency spectra for Na₂. Experimental conditions are recorded in the text.

Clearly this is not the expected spectrum, which is shown below for transitions from $v'' = 0$ and 1 to $v' = 0$ to 20 calculated over the same wavelength range for rotational and vibrational temperatures of 50 K and 100 K respectively, reasonable temperatures for a sodium dimer beam [18].

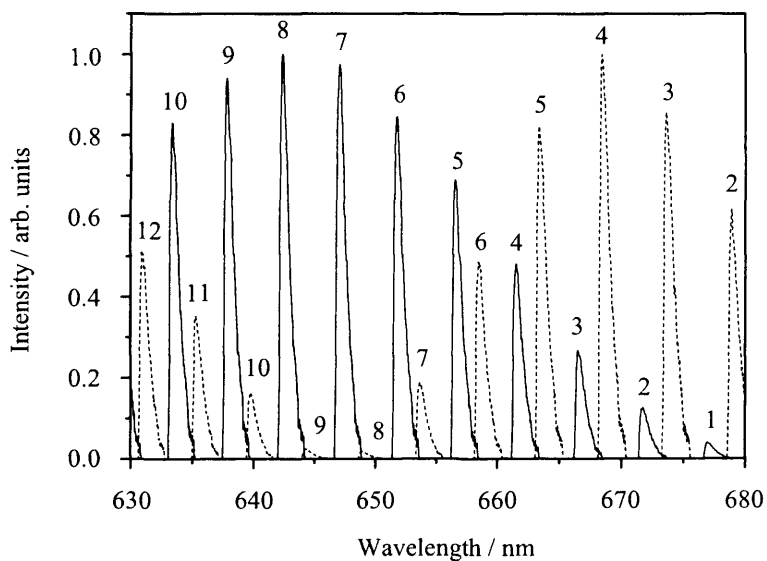


Figure 4.14 Calculated A($v = 0-20$) ← X($v = 0$ (solid) and $v = 1$ (dashed)) spectrum for Na₂ at a rotational temperature of 50 K and a vibrational temperature of 100 K over the wavelength range 630 nm to 680 nm. The spectrum was simulated using X. Tan's program Diatomic [19, 20] with a laser linewidth of 0.1 nm to smear out individual rotational states.

The most likely reason for the disparity between the recorded and simulated spectra is that the beam was rotationally and vibrationally hot. This implies that the molecular beam was behaving effusively rather than being formed in a supersonic expansion. This is supported by fluorescence spectra of Na₂ in heat pipe experiments where vibrational states populated according to a Maxwell-Boltzmann distribution[21, 22].

4.5 CONCLUSION

A novel experiment has been described which combines wave packet interferometry from the study of Rydberg wave packets and pulsed-field ionisation techniques from ZEKE-PFI spectroscopy to create and monitor vibrational wave packets in the X⁺ ²Σ_g⁺ potential of Na₂⁺.

The objective was to use this technique to perform coherent control experiments that interfere wave packets generated by trains of phase-locked femtosecond laser pulses and then observe the altered dynamics and quantum state amplitudes that result.

Some progress has been made towards implementing the intended experiment, however it was ultimately thwarted by the molecular beam, which failed to generate a suitable source of ground state sodium dimers. It is hoped that in the near future we can modify the molecular beam apparatus and make it work so that this rather elegant experiment can be demonstrated.

4.6 REFERENCES

1. V.G. Stavros and H.H. Fielding, *J. Chem. Phys.* **112** (21), 9343-9352. (2000).
2. J. Brown and A. Carrington, *Rotational Spectroscopy of Diatomic Molecules*. Cambridge Molecular Science Series, ed. R.J. Saykally, A.H. Zewail, and D.A. King. 2003, Cambridge: Cambridge University Press.
3. N.J.B. Green, *Quantum Mechanics 1: Foundations*. Oxford Chemistry Primers, ed. R.G. Compton. Vol. 48. 1997: Oxford University Press. 92.
4. R.J. LeRoy, *Level*. 1996, University of Waterloo: Waterloo.
5. M. Karplus and R.N. Porter, *Atoms and Molecules*. 1970, Menlo Park: Benjamin Cummings.

6. I.S. Averbukh and N.F. Perelman, *Phys. Lett. A* **139** (9), 449-453. (1989).
7. E.D. Boléat and H.H. Fielding, *Mol. Phys.* **103** (4), 491. (2005).
8. G. Jalbert, P. Labastie, P.F. Brevet, C. Bordas, and M. Broyer, *Phys. Rev. A* **40** (2), 784-794. (1989).
9. P. Labastie, M.C. Bordas, B. Tribollet, and M. Broyer, *Phys. Rev. Lett.* **52** (19), 1681-1684. (1984).
10. J.A. Ramswell and H.H. Fielding, *J. Chem. Phys.* **108** (18), 7653-7661. (1998).
11. J.R.R. Verlet, V.G. Stavros, R.S. Minns, and H.H. Fielding, *Phys. Rev. Lett.* **89** (26), art. no.-263004. (2002).
12. J.R.R. Verlet, V.G. Stavros, R.S. Minns, and H.H. Fielding, *J. Phys. B (At. Mol. Opt. Phys.)* **36** (17), 3683-3696. (2003).
13. L.A. Chewter, M. Sander, K. Muller-Dethlefs, and E.W. Schlag, *J. Chem. Phys.* **86** (9), 4737-4744. (1987).
14. C. Bordas, P.F. Brevet, M. Broyer, J. Chevaleyre, P. Labastie, and J.P. Perrot, *Phys. Rev. Lett.* **60** (10), 917-920. (1988).
15. I. Fischer, D.M. Villeneuve, M.J.J. Vrakking, and A. Stolow, *J. Chem. Phys.* **102** (13), 5566-5569. (1995).
16. M.J.J. Vrakking, I. Fischer, D.M. Villeneuve, and A. Stolow, *J. Chem. Phys.* **103** (11), 4538-4550. (1995).
17. N.F. Scherer, R.J. Carlson, A. Matro, M. Du, A.J. Ruggiero, V. Romero-Rochin, J.A. Cina, G.R. Fleming, and S.A. Rice, *J. Chem. Phys.* **95** (3), 1487-1511. (1991).
18. M.P. Sinha, A. Schultz, and R.N. Zare, *J. Chem. Phys.* **58** (2), 549-556. (1973).
19. X. Tan, *Diatomic: A powerful spectral simulation program for diatomic molecules*, in *57th International Symposium on Molecular Spectroscopy*. 2002, Ohio State University: Columbus, Ohio, USA.
20. X. Tan, *Diatomic, a spectral simulation program for diatomic molecules on Windows platforms*. 2004.
21. A.G. Astill, A.J. McCaffery, S.C. Taylor, B.J. Whitaker, and M.J. Wynn, **89** (1), 184-191. (1988).
22. A.G. Astill, A.J. McCaffery, and B.J. Whitaker, **142** (1-2), 1-6. (1987).

CHAPTER 5 DEVELOPMENT OF A GENETIC ALGORITHM TO OPTIMISE SIMPLE COHERENT CONTROL IN RYDBERG WAVE PACKETS IN ATOMIC SODIUM

ABSTRACT

A simple genetic algorithm has been implemented to investigate the suitability of this type of optimisation procedure in simulations of Rydberg electronic wave packet coherent control in atomic sodium. The operation of the algorithm is described in detail. It is then tested against known solutions for two experimental scenarios: coherent control based on pairs of transform-limited laser pulses; and transform-limited first pulse followed by a chirped second pulse. The behaviour of the algorithm is discussed in detail for each of these cases. Finally, the potential for application of the algorithm to unknown problems is briefly discussed.

5.1 INTRODUCTION

Genetic algorithms were developed by J. Holland in the early 1970s in an attempt to harness the power of optimisation exhibited by biological evolution in computer software. This power derives from the ability to efficiently search a large parameter space in which there are local minima that might ensnare a gradient search method without finding the optimum solution. Genetic algorithms have been used extensively to optimise multi-parameter problems in mathematics, computer science and engineering. Their appearance in experimental chemical physics followed the development of ultrafast lasers and pulse-shaping technology.

The general idea of a genetic algorithm is simple: individuals in a group are compared for their ability to achieve some objective, and based on their ability are used to generate (breed) a new population. The process of comparison and breeding iterates until the objective is satisfied to within some limit. There are many implementations of genetic algorithms in the literature and on the internet. Most of them operate in a broadly similar way, which is illustrated in figure 5.1.

The GA starts with a population of individuals with random genes. The fitness of each individual is established by its suitability for the problem at hand. If one of the

individuals has reached the objective the GA stops. It is undesirable to have the GA stop at the end of the first cycle as no optimisation can have occurred. If the objective has not been reached a new population is generated.

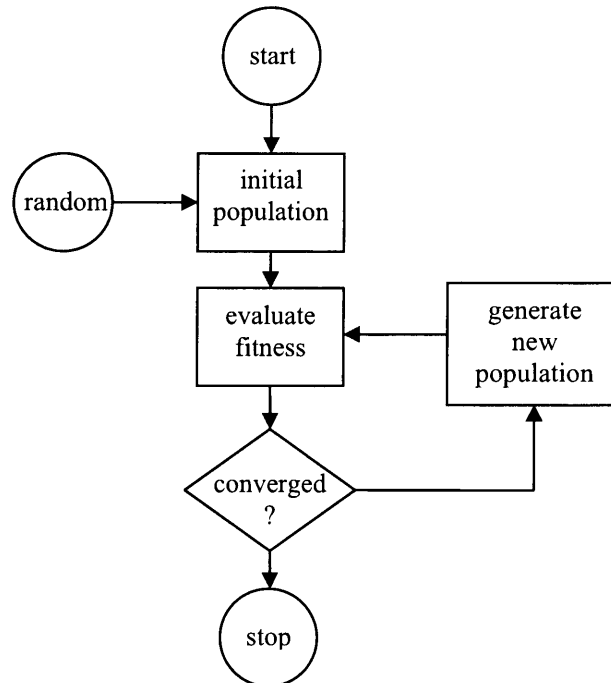


Figure 5.1 Schematic operation of a genetic algorithm. The initial population is generated randomly. Each individual is evaluated against an objective to measure its fitness. If one of the individuals has achieved the objective the GA stops. If not, a new population is generated from the previous one in a way that conserves characteristics from the fittest individuals. Each generation should therefore always be fitter, on average, than the previous one.

Generation of the new population involves generating new individuals from individuals from the previous generation. This is normally done in a way analogous with biological sexual reproduction. Two ‘parent’ individuals are selected from which to ‘breed’. Parents are selected at random but fitter individuals have to be represented more highly in the next generation than less fit ones. This can be done on a grey scale or by selecting a subset of fit individuals from the original population and breeding from them randomly. Generating a new individual from the parents can be achieved in any number of ways, but it has been found that some ‘crossover’ is essential. Crossover describes conservation of parts of the parents in their offspring. Crossover is thought to be the most efficient way for beneficial ‘genes’ or characteristics of an individual to be

passed to the next generation. For example, if each parent has a beneficial characteristic and their offspring inherits both, those benefits accumulate in the population much faster than if an individual with one of them has to evolve the other by mutation alone. In this way fitness accumulates in the population at each generation. At some point during the generation of a new individual it is common to introduce some mutation by randomly changing a gene. The role of mutation is to allow the population to avoid becoming stuck in local minima in the search space. The effect of mutation is to suddenly create an individual that explores a radically different region of the search space than its parents. The complete cycle, from a new population, through assessment of fitness, to the convergence test and generation of the next population corresponds to one generation of the genetic algorithm.

5.2 THE USE OF GENETIC ALGORITHMS IN CHEMICAL PHYSICS

Motivation to utilise genetic algorithms in chemical physics arose from attempts to use optimal control theory to design *a priori* laser pulse sequences to achieve particular outcomes from photoexcitation. The required calculations are complex and the Hamiltonians of chemical systems can have many linked degrees of freedom with only approximate solutions. This uncertainty, combined with experimental errors in generating the optimal laser pulses, might render such schemes impracticable. To circumvent this problem Judson and Rabitz [1] simulated an experiment to excite KCl preferentially from rotational state $j = 0$ to $j = 3$ using an arbitrarily shaped microwave field. The genetic algorithm manipulated either the electric field or its spectral components. The optimal outcome from each could then be compared with the other by Fourier transform. Although that paper simulated a microwave experiment, the authors intended the ideas to be applied to laser excitation. The concept was realised for many systems by the combination of genetic algorithms with the ultrafast pulse shaping techniques discussed in chapter 1.

The power of genetic algorithms in coherent control is clear from the wide range of systems they have been applied to (see chapter 1). There are two features of their use that warrant further discussion. The optimal pulse shapes are often very complex and, at least initially, it was not obvious how those pulse shapes achieved control. The other issue concerns the genetic algorithm itself. How can it be optimised for the particular

role of coherent control using laser pulse shaping, and does it offer any insights into coherent control?

Most implementations of genetic algorithms in coherent control provided insights into the physics underlying the laser-matter interaction, and the role of different features of optimal shaped pulses. Indeed in one of the earliest experiments, maximising either the efficiency or efficacy of excitation to the first excited state of the laser dye IR125 in methanol [2], found that these objectives required quite different optimal laser pulses. High efficiency (defined as excited population / laser power) was achieved by a low power pulse with narrow bandwidth at the absorption maximum of the dye. An effective pulse (defined by high total excited state population) had higher power, broad bandwidth and a strong positive chirp. This process was attributed to the ‘molecular π pulse’ effect discussed in chapter 1.

Maximising 2-photon absorption by atomic rubidium revealed interesting phase effects. The best shaped pulses showed a π phase shift between the resonant and non-resonant components, which was explained by a modified classical absorption model [3]. Selection of harmonic orders in coherent XUV generation from argon [4] was also attributed (tentatively) to a phase phenomenon. In this case the optimised laser pulse phase-matched the wavefunction of the ionised electron and later cycles of the electric field of the pulse.

The results of studies in diatomics are diverse but some patterns can be discerned. Finding optimally shaped pump plus transform-limited (TL) probe to maximise Li_2^+ yield [5] at particular delays appeared to require two processes: one for short delays and another for long delays. The predominant mechanism at short delays (pump and probe pulses overlap) involved matching the phases of frequency components in both pulses to maximise multiphoton ionisation. For long delays the amplitudes of resonant frequencies were maximised with phases that generated constructive interference at the desired delay. Motzkus and co-workers [6] made a detailed study control of vibrational wave packet dynamics for different degenerate four wave mixing (DFWM) arrangements in K_2 . They compared the results of excitation by two TL DFWM pulses and a single TL pulse, a train of 3 TL pulses, phase-locked pulse pairs and chirped pulses. Surprisingly, this apparently wide range of excitation schemes could all be modeled in terms of incoherent sums of TL pulses. A similar result pertains for maximisation of multiphoton NaK^+ and Na_2K^+ yields [7]. The optimal pulse

contained three sub-pulses whose effects were analysed in terms of vibrational wave packet dynamics. The first sub pulse was chirped and counteracted wave packet dispersion. The second was delayed by half the classical period of the wave packet, and the third by 1.5 times the classical period. These delays occurred because the maximum Franck-Condon overlap to the ionic potential was at the outer turning point of the wave packet.

In polyatomics, stimulated Raman scattering experiments in methanol and benzene suggested that the shaped pulse redistributed energy spread among a population of vibrational modes to a single mode [8]. In CpMn(CO)_3 [9] selection between photoionisation products CpMn(CO)_2^+ and CpMn(CO)_3^+ also lead to a shaped pulse with three sub-pulses, which were found to be resonant with different Mn-CO bond potential surfaces. Even in a huge bacterial light harvesting complex [10], the pulses preferentially exciting intra- and intermolecular energy transfer channels reduced to a train of equally spaced phase-coherent pulses.

The most interesting outcome is that for a range of molecules, K_2 , NaK and Na_2K , CpMn(CO)_3 and a bacterial light harvesting complex, the optimally shaped pulses reduced effectively to a train of simpler sub-pulses. In some cases the sub-pulses were transform-limited and phase-locked, in others transform-limited and phase incoherent and, in one case, chirped. Despite this variation, it is clear that the apparently complex pulse shapes generated by feedback optimisation experiments using genetic algorithms can give rise to relatively simple physical processes, which can be identified.

In addition to realisations of the 'traditional' genetic algorithm, several studies have investigated the nature of the genetic algorithm itself, and how it can be improved and used to decipher the physics involved. Bucksbaum and co-workers [8] developed a sophisticated GA that evaluated different breeding and search strategies while optimising pulses for several targets. Their GA could bring to bear two-point crossover, average crossover, mutation and creep (where genes move in the genome and thus acquire new meaning) to generate new individuals. Individuals could be modified by moving-window averaging (over three genes), time domain crossover (which involved making a FFT, a 2-point crossover followed by an inverse FFT), polynomial phase mutation (where several adjacent genes were replaced by values from a polynomial), and additional search methods such as simulated annealing.

Several workers have attempted to reduce the size of the parameter space the GA has to search. For LC-SLM shapers this has been done by linear interpolation [10], or by applying regular functions to the pixels of the pulse shaper instead of allowing them to be arbitrary. The GA searches only among parameters of the function. Examples include sine functions [10, 11] and binary masks [12]. For example, Moztkus *et al.* [11] used a cosine phase function of the form $\phi(n) = a \cos(bn + c)$ where n is the SLM pixel number, and a , b and c are the only freely variable parameters available to the genetic algorithm. AOM pulse shapers can be used in a way that requires only four [2] parameters, as opposed to 2×128^n for a double stacked LC-SLM with 128 pixels with n -bit resolution for the applied voltage. Weinacht *et al.* [13] have identified sets of basis functions which reduce the parameter space required to represent the pulse phases to an AOM to one or two.

Attempts to extract physical information from the GA have focussed on finding optimised pulses that comprise only the required features. One way this has been achieved is by adding a cost function that penalises pulses for departing from transform-limited [13]. Another uses co-variance analysis of many optimal pulses to identify common features, which are assumed to be essential [14], and feeds that information into the fitness assessment.

5.3 A GENETIC ALGORITHM FOR SIMPLE COHERENT CONTROL SCHEMES

Our approach to using genetic algorithms forms part of our wider efforts to understand the details of simple coherent control schemes in simple systems. In this it is highly complementary to other current work in the area. We have applied the genetic algorithm to two test cases, both of which complement and extend the work of the previous chapters. To test the applicability of genetic algorithms to pulse sequencing, as opposed to pulse shaping, experiments we have attempted to optimise the delay and phase difference between two transform limited laser pulses to selectively minimise or maximise s and d Rydberg state angular momentum components of an atomic Rydberg electron wave packet. In the same system we then investigated the use of a genetic algorithm in the simplest of pulse shaping, namely chirping. The algorithm had to optimise the pulse delay, phase and chirp in order to achieve control over the wave

packet composition. In both cases the algorithm was highly constrained in terms of the number of parameters available for evolution. In this way we hope to be able to learn more from its results.

A. OVERVIEW OF OUR GENETIC ALGORITHM

The GA we have developed is similar to many others, but differs sufficiently to warrant proper discussion. Operation of the GA is shown schematically in figure 5.2.

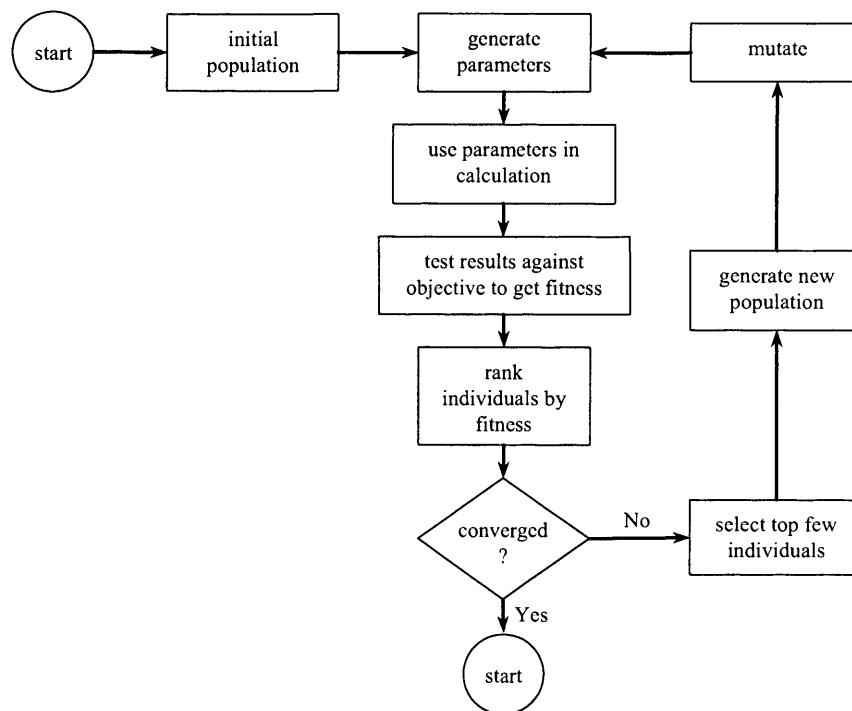


Figure 5.2 Schematic of the current genetic algorithm. Details of the operations carried out by each step are discussed in the text.

B. STEPS IN THE GENETIC ALGORITHM

The following paragraphs detail how our genetic algorithm operates. The Fortran code for the algorithm and objective functions is listed in the appendix.

I. GENERATION OF THE INITIAL POPULATION.

The population comprises a number of individuals, typically 50, each of which in turn comprises one or more sets of many elements (or genes). The number of genes was varied between as few as 5, to around 100, but typically 50. Each gene is a double precision number. In practice the population is a three dimensional array, as illustrated in figure 5.3. One dimension counts the individuals, the second is the number of parameters each individual must generate, and the third is the number of genes used in making the parameter. If just one parameter is required the population reduces to an array of individuals, each comprising a one-dimensional array.

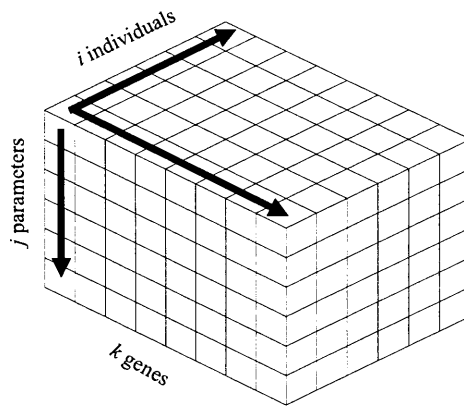


Figure 5.3 Representation of the GA population as a three dimensional array. The population comprises i individuals of j parameters derived from k genes. Each gene is a double precision number.

II. EXTRACTION OF OUTPUT PARAMETERS

To reduce the genes to parameters for use in a calculation, the first step is to take the average of each gene. The value is stored in the $(k + 1)^{\text{th}}$ element of each parameter array, like an extra gene (see figure 5.4). Using the genes in this way is a departure from the approach outlined by Davis [15] where each individual is a one-dimensional binary array. The binary array of Davis is evaluated as a decimal number so the significance of each element of the array depends on its position. This presumably enables the GA to rapidly change the value of its parameters by mutation of a highly significant digit. We felt the expedience of coding double precision arrays outweighed

the benefits of binary ones. However it would be interesting to make a comparison between the search paths of the two systems. After storing the parameter, the range of the number is then altered to make a useful parameter. For example the delay time of the second laser pulse is input into the calculation as a time in picoseconds, so this parameter might be scaled to have a range between 0.5 ps and 1.5 ps.

III. PERFORMING THE CALCULATION

Details of the two calculations performed in our GA modelling are given in the following section. The parameters derived from each individual are used in the calculation and the result passed to a subroutine for comparison with the objective.

IV. EVALUATING THE FITNESS

The outcome of the calculation performed with parameters from each individual has to be compared to an objective in order that their relative fitness can be established. Each problem to which a GA is applied requires a particular method to evaluate the fitness. Developing suitable methods turned out to be the key problem of implementing our GA.

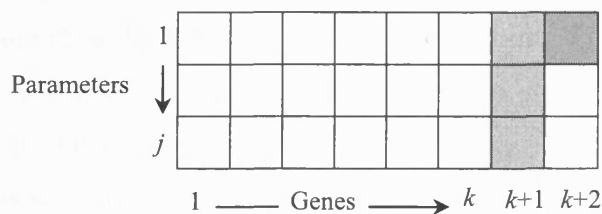


Figure 5.4 Storage of the output parameters and fitness parameter for an individual in the GA population. One individual comprising j parameters and k genes is shown with the storage locations for output parameters (grey) used in the objective calculation and the fitness parameter (hatched) used in ranking.

Details of the objectives and comparisons used are given in sections 5.3C. Whatever fitness assessment was made the fitness parameter of the i^{th} individual is stored in element $(i, j = 1, k + 2)$ of the population array (see figure 5.4), i.e. the $(k + 2)^{\text{th}}$

element of the $j = 1$ parameter for each individual. Storing the fitness parameter with the individual it refers to makes keeping track of the data easier during coding.

V. RANKING THE INDIVIDUALS

The next step is to rank the individuals on the basis of their fitness parameters. Clearly, the closer a spectrum is to the objective the smaller will be the variance, so the individual that generated the spectrum will be ascribed a smaller fitness parameter. Ranking the individuals involves sorting the population by fitness parameter, putting the smallest first, using a simple 'selection sort' algorithm. Selection sorting is not the most efficient (pivot sorting is) but it is straightforward to code.

VI. CONVERGENCE TESTING

Having sorted the population, it is necessary to test whether the objective has been achieved. Two convergence tests are employed. If the fitness parameter for the fittest individual is less than some arbitrary value the algorithm is considered to have reached the objective. The exact value of the convergence criterion has to be optimised by a few trial runs of the GA. For each iteration of the GA, the fitness parameter can also be tested against the previous one. If they differ by less than a predetermined arbitrary amount then the GA has reached an end point. Of course this does not mean the objective has been reached, indeed it is there to stop the algorithm in those cases where the objective is never reached. There are two cases which can stop the GA reaching its objective: it has become stuck in a local minimum in the search space, or the objective has been set at an unreachable level. If either of the convergence criteria are met the GA stops and presents the fittest individual (which triggered the cessation) as the optimum solution.

VII. SELECTING THE BREEDING SET

If neither stopping condition is met the GA generates a new population by breeding from the top individuals of the last. The first step in this operation is to decide which individuals to breed from. Davis [15] discusses a 'roulette wheel' method in

which fitter individuals tend to be chosen for breeding more than less fit ones. This is elegant but a little complex and a sufficient alternative is simply to select the top few individuals and breed from them. In the present implementation we have taken the latter approach and it appears to work satisfactorily.

The number of individuals selected for breeding itself requires some optimisation. If too few are selected there is insufficient variety and a population of identical clones rapidly develops. If too many are selected there is essentially no selection. For a population of 50 individuals taking the 8 fittest to breed from was found to work well.

VIII. BREEDING

Breeding a new population involves several steps. Firstly, for each new individual two parents are selected from the breeding set at random. The only stipulation is that the two parents are different. The new individual is then generated by copying genes from one or other parent. The genes maintain their position from the parent in the new individual. Which parent is chosen for each gene is again random, so each new individual will, on average, inherit 50 % of its genes from each parent. This process effects crossover with a variable and random crossover rate.

IX. MUTATION

The final stage of generating a new population is to introduce some mutation. In our GA mutation is achieved by performing a predetermined number of random substitutions to the genes. The number of mutations is typically referred to as a percentage mutation rate. The mutation rate is usually small (a few percent) and has to be tweaked to get the best results from the GA. In the current work, a mutation rate of 1% was found to be effective.

C. RUNNING THE GENETIC ALGORITHM

We have applied the genetic algorithm to two problems for which we already knew the solutions. The objective was to compare the results of our GA with the

solutions found analytically to assess the suitability of the GA for this problem. Both problems involve the same optimisations as in chapter 3: to selectively populate s and d angular momentum states in Rydberg electron wave packets in atomic sodium. In the first problem the delay and phase of a pair of transform-limited picosecond laser pulses was optimised. The second problem modelled excitation by a transform-limited pulse followed by chirped pulse and found the delay, phase and chirp of the second pulse. The following paragraphs describe the objective functions we employed, and compare the GA and analytical results.

1. OPTIMISATION OF THE DELAY AND PHASE OF A PAIR OF TRANSFORM-LIMITED PICOSECOND LASER PULSES

The first target for the GA was to selectively maximise either the s or d angular momentum character of a Rydberg electron wave packet in the sodium atom. The problem is cast in exactly the same way as the calculations in Chapter 3. Briefly, a radial Rydberg electronic wave packet is created using a transform-limited picosecond laser pulse. The angular momentum composition of the wave packet is determined by the oscillator strengths of the s and d Rydberg series and the Gaussian profile of the laser. After approximately one classical orbit of the wave packet, a second identical wave packet is excited. The two wave packets interfere and the precise delay and phase difference between them determines the composition of the resultant wave packet.

The objective function evaluated the expression for the population, resulting from double wave packet excitation, of the n quantum states in the wave packet,

$$a_n(t) = -\frac{i}{2}\Omega_n g(\omega) \left[1 + \sum_k e^{i\Delta_n t_k} e^{i\omega t_k} \right] \quad (5.1)$$

where $\Omega_n = eE_0 \langle n|z|g \rangle / \hbar$ is the Rabi frequency for a laser, with electric field E_0 , coupling a ground state g and a Rydberg state n , where the transition has dipole moment z . The Gaussian frequency profile of the picosecond laser pulses is $g(\omega)$. $\Delta_n = \omega_n - \omega_g - \omega$ is the laser detuning, ω is the excitation frequency, and the summation runs over k laser pulses. The value of t_k was a parameter derived from each individual in the GA population. The fitness parameter was found by calculating the ratio of total s population to total d population or *vice versa*. Because the GA sorts the

population from the smallest fitness parameter to the largest, to maximise the d population the ratio (s population / d population) was taken as the fitness parameter. Initially, the value of t_k was made by summing separate delay and phase parameters from the GA. This approach was unsuccessful because, in this case, phase is simply a part of the delay. For a 400 nm laser pulse, a 2π phase shift is equivalent to a delay change of 1.33 fs, which corresponds to a change in the third decimal place for a delay expressed in picoseconds. The GA found multiple solutions derived from many combinations of delay and phase. The t_k value was subsequently derived from a single GA parameter from which the phase can be extracted. The results from running the GA with this simple objective are remarkably consistent. Figure 5.5 shows the result of five consecutive runs of the GA with the objective to maximise separately the d and s components of the wave packet. These results indicate that the GA is effective and consistent. The extent of the optimisation can be seen by comparing the optimised output (figure 5.5) to a sample of the initial, random, population from one run of the GA (figure 5.6).

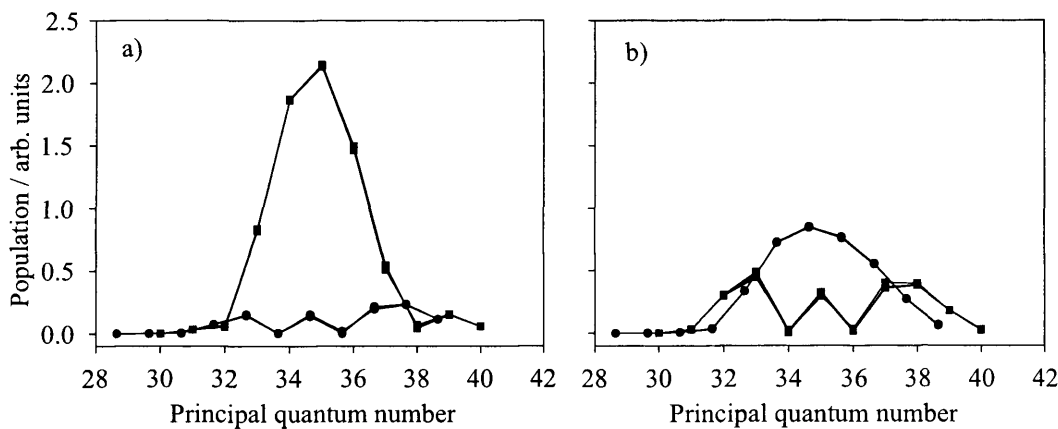


Figure 5.5 The outcome of five consecutive runs of the GA attempting to maximise (a) the d , or (b) the s component of a radial Rydberg electronic wave packet in sodium with two transform-limited laser pulses separated by approximately one classical period of the wave packet. d and s state populations are indicated by squares and circles respectively. Lines between points are for clarity and have no numerical meaning.

Having seen that the GA works it is worth investigating some of its operating characteristics. It seems a little paradoxical, but the GA has to be optimised itself before it can effectively optimise a problem. The parameters determining the behaviour

of the GA are the number of individuals in the population, the number of genes each individual comprises, the convergence value and the mutation rate, and of course the objective function. The following paragraphs address optimisation of each of these parameters.

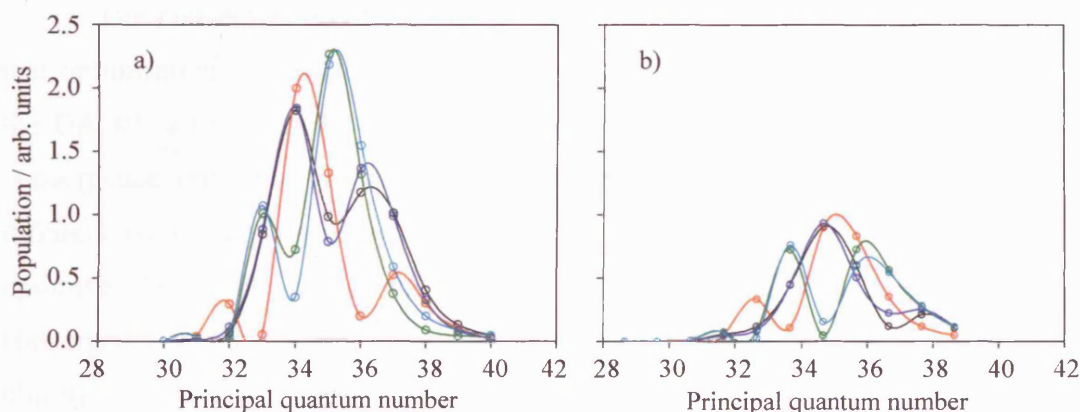


Figure 5.6 Rydberg state populations, d in (a) and s in (b), for wave packets calculated with output parameters from the first five individuals of the initial GA population (prior to any optimisation), each arbitrarily assigned a different colour. Identical colours in (a) and (b) show s and d populations from the same run of the GA. The genes of each individual are random numbers between 0 and 1, giving random time parameters for the wave packet calculation with values between 0 and $2.75 t_{cl}$. The lines interpolated between points link data from each individual but do not contain any numerical information.

The number of individuals in the population can be expected to impact in two areas of GA operation. Firstly, it will determine the diversity of parameters fed into the calculation and thence the variation between the top few individuals used in breeding. Secondly, the more individuals there are, the longer each generation will take. Execution time is really a minor issue compared to that for the Fourier transform objective functions. For this GA, it appears that decreasing the number of individuals simply increases the number of generations required to reach the objective. This trend continues until a large proportion of the population is being used to generate the new population for the next generation. At this point the GA fails to reach the objective as there is effectively no selection of fitter individuals.

The number of genes used to derive an output parameter (for example, a delay time of the second laser pulse), affects the influence each gene has on that parameter. If

there are 10 genes and one of them is changed from its maximum (1) to its minimum (0) the parameter will undergo at least a 10% change. On the other hand if one gene in 100 changes by the same amount, the parameter will change by at least 1%. Populations with more genes tend to converge more smoothly. A practicable number was found to be 50.

The convergence criterion (the value of the fitness parameter taken to indicate that optimisation is complete) also has a pronounced effect on how many generations the GA takes to reach the objective. The sensitivity of the optimisation rate to the convergence criterion was explored by performing sets of 1000 GA runs for four different convergence values and recording how many generations each run took to optimise. The results are shown as bar charts in figure 5.7. Obviously, by making the convergence criterion less stringent, the number of generations taken to reach the objective decreases. However this also means that the outcome is less consistent.

While using the GA it was necessary to make several trial runs that performed a set number of generations to see what kind of values the fitness parameter would take. Having found an approximate value, it was fine tuned by making several more runs with slightly different convergence criteria until a suitable one was found. The final value must ensure that the GA requires more than one generation to reach the objective, otherwise no optimisation has taken place, and that the objective is actually attainable. Typically a threshold is chosen so that the GA takes between 10 and 100 generations. Once a suitable value was obtained the GA would behave like those in figure 5.8, converging rapidly to a value close to the objective, then oscillating slightly before reaching the objective.

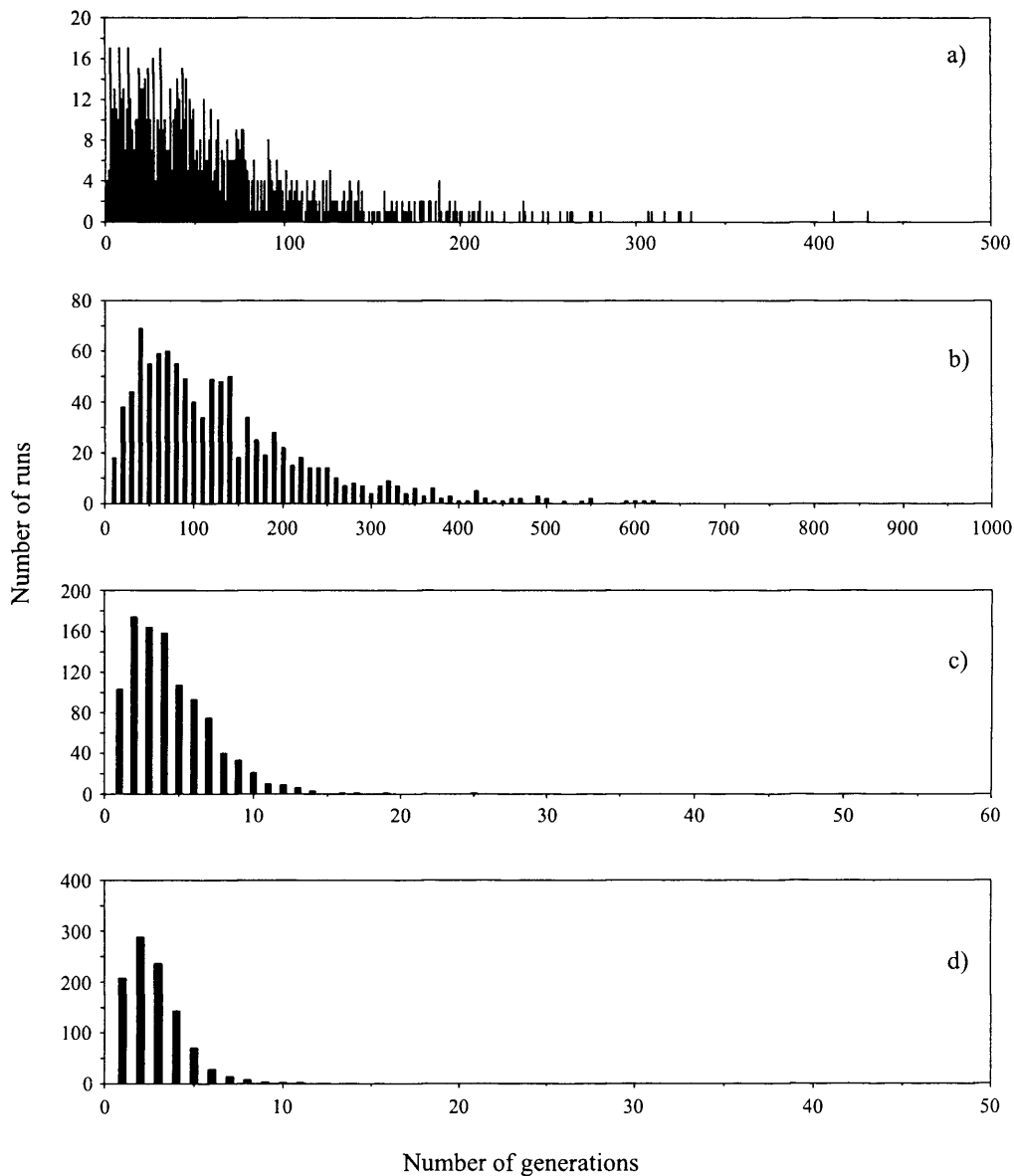


Figure 5.7 Plots showing the dependence of the optimisation rate on the convergence criterion. The plots show the number of times (ordinate) out of 1000 runs that the GA took a particular number of generations (abscissa) to converge. The objective in each case was the same: to maximise the d component of the wave packet by minimising the ratio, s population / d population. The convergence criteria were (a) 0.130, (b) 0.132, (c) 0.135 and (d) 0.14

It seems likely that the behaviour shown in figure 5.8 can be understood as follows. The rapid improvement in the fitness parameter in the first few generations is brought about by selection of, and breeding from, the best individuals. Once this phase is over

the whole population is essentially equivalent and it is only mutation that allows the objective to be reached.

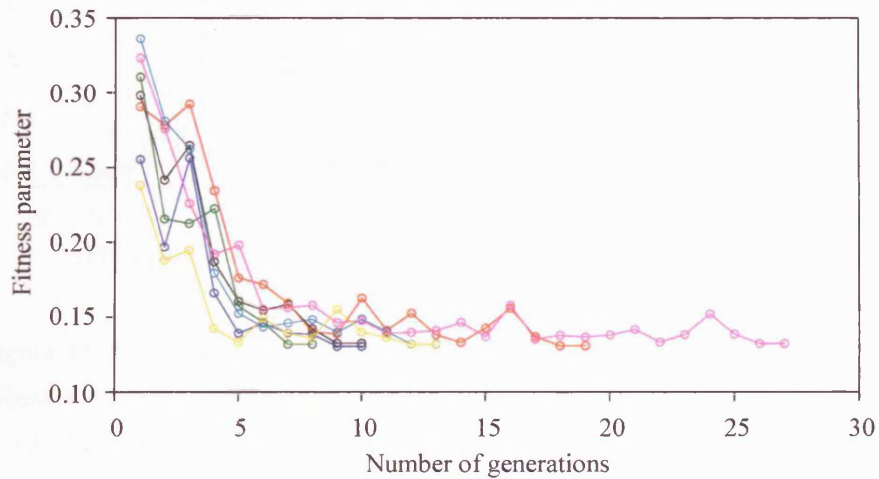


Figure 5.8 Convergence of the GA. The plot shows the best fitness parameter for each generation for 7 runs of a GA (each arbitrarily assigned a different colour for identification) with 50 individuals, 50 genes and a mutation rate of 1 per individual. The objective was again maximisation of the d state population of a Rydberg electron wave packet by minimisation of the s population : d population ratio. The convergence criterion was set at 0.133. It is clear that for any initial fitness the GA rapidly converges towards the objective, then wanders up and down until finally reaching the objective.

The mutation rate is small – usually one mutation per individual per generation – and can have a positive or negative effect on the fitness, which oscillates until it randomly reaches the convergence criterion. This is borne out by examination of the non-optimal individuals from the final, optimised population (figure 5.9). The objective function affects the operation of the GA differently than the features discussed above. The GA cannot tell whether the objective function is suitable for the problem. This is because the GA is guided by the fitness parameter, whereas the objective function generates the fitness parameter. The issue therefore is whether the objective function is an appropriate measure of the fitness.

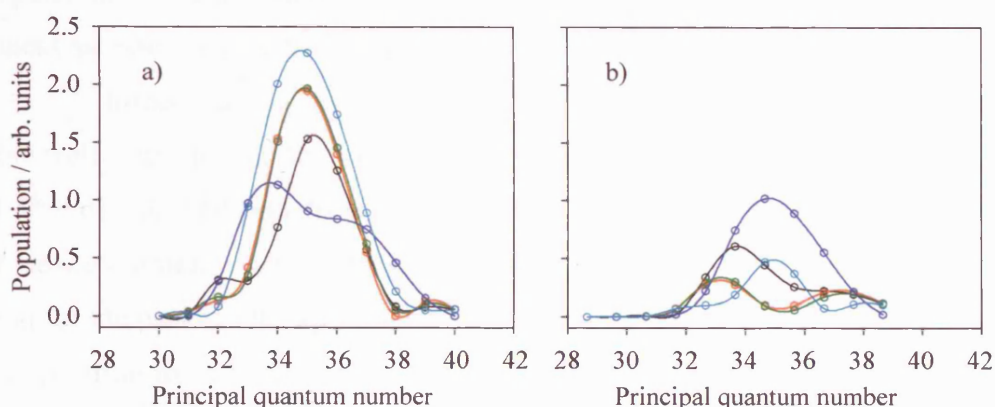


Figure 5.9 Population of (a) d Rydberg states, and (b) s Rydberg states in wave packets generated from output parameters from five non-optimal individuals (each arbitrarily assigned a different colour) in the final population of a GA run where the objective was to maximise the d component. Identical colours in (a) and (b) identify s and d populations from the same run of the GA. Compared to figure 5.5a, these wave packet populations are clearly not optimal, but they are noticeably better than the Rydberg state populations generated by random numbers in figure 5.6. The best-fit lines between points are shown to indicate sets of points and contain no numerical information.

II. OPTIMISATION OF THE DELAY, PHASE AND CHIRP OF A PAIR OF PICOSECOND LASER PULSES

In the previous section we showed that the GA works and that we have gained, by attempting to optimise a very simple problem, some insight into its behaviour. In this section the objective is a slightly more taxing one. The aim was exactly as in the previous section: to maximise either the s or d angular momentum components of a Rydberg electron wave packet in sodium using two laser pulses separated in time by approximately one classical orbit period of the wave packet. In this case however, in addition to the delay and phase of the second laser pulse, its chirp must also be optimised.

In order to incorporate the laser chirp, the code to generate the spectra of two interfering light pulses used in chapter 3 was written into the GA. The time, phase and chirp of the first laser pulse were all set to zero, and its duration and wavelength were held constant. The delay (comprising the coarse delay and phase) and chirp of the second laser pulse were parameters extracted from each individual in the GA

population. For each pulse pair the spectrum was generated using a FFT routine and its fitness assessed against the objective.

It turned out that the simplest way to evaluate the fitness of the spectrum, i.e. how well it maximised the s or d components of the wave packet, was to find energies of all the peaks and troughs in the spectrum and see how closely they lie to the energies of desired states. For instance, maximising the d components of the wave packet requires the peaks in the spectrum to lie close in energy to the d states and the troughs in the spectrum to lie close to the s states. The fitness parameter was then enumerated as the variance, s^2 , of the spectral peak positions from the objective peak positions, where,

$$s^2 = \sum (x - x_{obj})^2, \quad (5.2)$$

where x is the energy of a spectral peak or trough, x_{obj} is the objective Rydberg state energy, and the sum is over all the spectral peaks and troughs. The GA then minimised the fitness parameter, leading to pulse pairs that exhibit the desired spectral components. In order to mimic accurately the analytical optimisation process, the errors in the peak positions were weighted by their intensities. This ensured that the central Rydberg states contributed more than outer ones to the fitness assessment.

Figure 5.10(a) shows the spectrum of an optimised pulse pair where the objective was to maximise the d component. The peak positions match the energies of the d states extremely well. Since the s states were not minimised by the GA there is a slight disparity between its values of the phase and chirp and those from manual optimisation. The GA gave an average (from 10 runs) time delay of $1.00 T_{cl}$, a phase of 0.26π and a chirp of 0.63 ps^2 , compared with a delay of $1.00 T_{cl}$, a phase of 0.20π and a chirp of 0.58 ps^2 derived analytically.

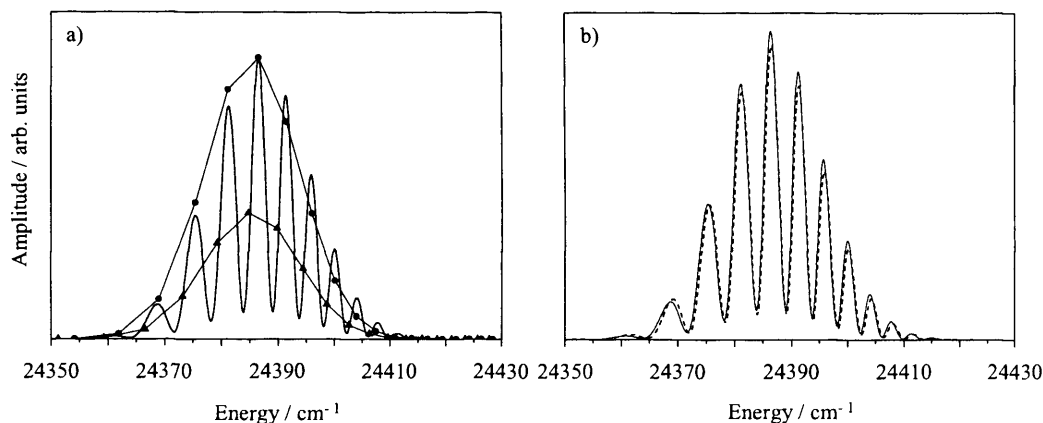


Figure 5.10 (a) An optimised spectrum for a pair of laser pulses compared to the objective Rydberg state populations. The spectrum was generated from the average values of delay, phase and chirp for 10 runs of the GA. The objective of the GA was to maximise the d components of the wave packet (solid diamonds). The relative proportions of the Rydberg states are those of a single wave packet excited by a transform-limited laser pulse. (b) A comparison between the derived solution (solid line) and GA-optimised spectra (dashed line).

The results between runs are quite consistent. The values of delay, phase and chirp for 10 optimisations are plotted in figure 5.11. On the assumption that these values all lie close to a global minimum in the search space, their averages were used to plot the spectra in figure 5.10. Although it is not explored here, the variation in the optimised parameters, and how the convergence threshold affects that variation, may well offer insights into the search space and the physics of the problem

It is clear that the GA can find the desired laser pulse parameters. If the objective function is suitable, the GA will find the solutions. Such sensitivity can be seen in first computational application of GAs to chemical physics in the Judson and Rabitz paper.[1] Their cost function scrutinised only the population of the target rotational state. Any features of the optimal field which had no effect on the target exerted no selective pressure on the population and could not be removed.

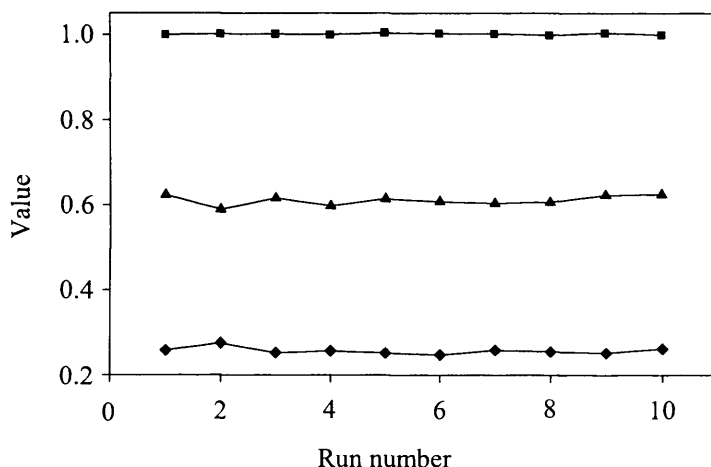


Figure 5.11 Values of delay (squares), phase (diamonds) and chirp (triangles) for 10 runs of the GA attempting to maximise the population of the d Rydberg states. The averages of these values were used to calculate the spectra plotted in figure 5.10.

The result was a spectrally broad, noisy field that had only to contain *at least* the required spectral components to achieve the objective. The key issue in computational GAs, therefore, is to make a suitable objective function. For instance, an attempt to use the method employed for the chirped pulse, namely to minimise the errors of the spectral peak positions, failed when applied to a pair of transform-limited pulses like section 5.3C, yet simply comparing the total s and d populations was successful.

III. APPLICATION TO OTHER PROBLEMS

An obvious extension of this work is to match the optical spectrum to the Rydberg energy level spacing by incorporating higher orders of chirp, where perhaps the analytical optimisation becomes increasingly difficult. Likewise, the inclusion of larger and variable numbers of control pulses would rapidly become intractable as an analytical problem, but could be addressed numerically using a genetic algorithm. Both of those approaches promise greater levels of control than have been shown here.

5.4 CONCLUSION

The genetic algorithm discussed above has been developed as a proof-of-principal investigation into the use of such systems in coherent control in Rydberg systems. It is a relatively unsophisticated implementation of a GA and it continues to be developed in this group. Nonetheless, it is clear that from the results of these simulations that genetic algorithms represent a useful tool in our efforts to elucidate control mechanisms, both from a computational perspective and experimentally.

5.5 REFERENCES

1. R.S. Judson and H. Rabitz, *Phys. Rev. Lett.* **68** (10), 1500-1503. (1992).
2. C.J. Bardeen, V.V. Yakovlev, K.R. Wilson, S.D. Carpenter, P.M. Weber, and W.S. Warren, *Chem. Phys. Lett.* **280** (1-2), 151-158. (1997).
3. T. Ando, T. Urakami, H. Itoh, and Y. Tsuchiya, *Appl. Phys. Lett.* **80** (22), 4265-4267. (2002).
4. R. Bartels, S. Backus, E. Zeek, L. Misoguti, G. Vdovin, I.P. Christov, M.M. Murnane, and H.C. Kapteyn, *Nature* **406** (6792), 164-166. (2000).
5. J.B. Ballard, H.U. Stauffer, Z. Amitay, and S.R. Leone, *J. Chem. Phys.* **116** (4), 1350-1360. (2002).
6. T. Hornung, R. Meier, R. de Vivie-Riedle, and M. Motzkus, *Chem. Phys.* **267** (1-3), 261-276. (2001).
7. A. Bartelt, S. Minemoto, C. Lupulescu, S. Vajda, and L. Woste, *Eur. Phys. J. D* **16** (1-3), 127-131. (2001).
8. B.J. Pearson, J.L. White, T.C. Weinacht, and P.H. Bucksbaum, *Phys. Rev. A* **6306** (6), 063412. (2001).
9. C. Daniel, J. Full, L. Gonzalez, C. Lupulescu, J. Manz, A. Merli, S. Vajda, and L. Woste, *Science* **299** (5606), 536-539. (2003).
10. J.L. Herek, W. Wohlleben, R.J. Cogdell, D. Zeidler, and M. Motzkus, *Nature* **417** (6888), 533-535. (2002).
11. T. Hornung, R. Meier, D. Zeidler, K.L. Kompa, D. Proch, and M. Motzkus, *Appl. Phys. B (Lasers Opt.)* **71** (3), 277-284. (2000).

12. M. Comstock, V.V. Lozovoy, I. Pastirk, and M. Dantus, *Opt. Express* **12** (6), 1061-1066. (2004).
13. D. Cardoza, F. Langhojer, C. Trallero-Herrero, O.L.A. Monti, and T. Weinacht, *Phys. Rev. A (At. Mol. Opt. Phys.)* **70** (5), 053406. (2004).
14. J.L. White, B.J. Pearson, and P.H. Bucksbaum, *J. Phys. B (At. Mol. Opt. Phys.)* **37** (24), L399. (2004).
15. L. Davis, *Handbook of Genetic Algorithms*, ed. L. Davis. 1991.

CHAPTER 6 SUMMARY AND OUTLOOK

6.1 ATOMIC AND MOLECULAR BEAM SOURCE

A sodium atomic and molecular beam source and experimental vacuum chamber containing a time-of-flight mass spectrometer has been designed, built and operated. The source functioned well for sodium atoms, but less well for sodium dimers. Ongoing improvements to the design of the atomic/molecular beam source, in particular better nozzle heating, thermal insulation of the oven and cold-trapping of sodium (as discussed in chapter 1) should make the dimer source operational in the near future.

In the mean time the vacuum chamber has been refitted for photochemical coherent control experiments. Initially these will focus on benzene so the source is being altered to expand benzene with a helium or argon carrier. The experimental chamber is also being substantially remodelled. It will soon incorporate an ion/electron imaging detector and suitable ‘Eppink and Parker’ type ion optics [1].

6.2 COHERENT CONTROL IN SODIUM ATOMIC RYDBERG ELECTRONIC WAVE PACKET DYNAMICS

Coherent control of the angular composition of a radial Rydberg electronic wave packet by interference has been demonstrated with pairs of wave packets separated by T_{cl} and $1\frac{1}{2}T_{cl}$. The control outcome – selectively altered angular momentum quantum state populations – was monitored in two ways. For wave packets separated by T_{cl} state-selective field-ionisation was used to measure directly the relative populations. This is the first time the angular components of a Rydberg wave packet in sodium have been resolved in this way. For wave packets separated by $1\frac{1}{2}T_{cl}$ the optical Ramsey method was used to monitor the effect on the dynamics of the interference around the time off the second order partial revival, where the contributions to the dynamics from the two angular components, s and d , can be seen.

Calculations were performed to model an extension of interfering wave packet pairs to include one wave packet excited by a chirped laser pulse. The chirp can be chosen to counteract exactly the natural dispersion of the wave packet. The role of the

chirp was analysed from the frequency domain perspective, where interference between the pulses leads to a spectrally chirped pulse. The chirp and phase can be arranged so that dips and peaks of the spectrum coincide with particular angular states of the wave packet, leading to selective excitation.

Atomic sodium is really an ideal experimental system – it can be easily generated in the gas phase, and easily excited by lasers with wavelengths that are readily available. There are most likely many more coherent control tricks that could be played in this simple atomic system, in addition to the ones modelled.

6.3 VIBRATIONAL WAVE PACKET COHERENT CONTROL IN Na_2

A novel experimental technique for observing vibrational wave packets in the sodium dimer ion, Na_2^+ was described, and progress towards its realisation was presented. A coherent control scheme based on sequences of phase-locked time-delayed transform-limited laser pulses and using this detection method was introduced.

Modifications to the molecular beam apparatus underway in the laboratory will soon make the sodium dimer source operational. Once this happens there are many potential targets for coherent control experiments, in addition to the one we initially set out to do. The sodium dimer is an excellent prototype molecule and has many potential energy wells in which, even though they have been extensively studied in the past, certainly offer further opportunities. This is especially so because of the recent installation of a pair of tuneable amplified femtosecond lasers (Coherent Opera), coupled with pulse shaping capability.

The theoretical developments made in coherent control in this system [2] incorporating sequences of arbitrary numbers of pulses have suggested that it is possible, given a sufficient number of pulse, to achieve arbitrary vibrational quantum state populations. In a very elegant demonstration of its power, the authors give an example of a wave packet excited by transitions $\text{Na}_2^+(\nu^+ = 5-15) \leftarrow \text{Na}_2(\nu' = 9)$ from the A state. The Frank-Condon overlap from the ground state diminishes the transition amplitude to $\nu' = 9$, which leads to unusual dynamics. These were made into regular Gaussian wave packet dynamics by increasing the $\nu' = 9$ state amplitude while *simultaneously* reducing that of $\nu' = 8$ by 50 % *and* of $\nu' = 10$ by 33% by application of five laser pulses timed at half-integer multiples of the classical vibrational period and

phase shifted in accordance with equations (4.31) and (4.32). Clearly the use of wave packet interference has been advanced from simple cases of completely constructive or destructive interference to subtle manipulation of the amplitudes. Such an experiment would certainly not be possible with nested Michelson interferometers as the loss of optical intensity would be too severe. However it may be possible with using the pulse-shaper soon to be brought into the lab. Pulse shapers can be set up to generate trains of transform-limited pulses in a way that has been shown to be equivalent to pulses delayed interferometrically [3].

6.4 DEVELOPMENT AND USE OF GENETIC ALGORITHMS COMBINED WITH ULTRA FAST PULSE SHAPING

Our work on genetic algorithms has really only just started. The algorithm itself can be improved by including, as others have done, more sophisticated breeding and search strategies, and analysis of the evolutionary path the GA makes, as well as new features we feel are appropriate for the systems we study. In Rydberg electronic wave packet coherent control there are a number of systems where constraining the variation the shaped pulses to relatively simple functions might be a fruitful approach. In particular, systems where there is complex coupling between Rydberg series, such as H_2 . Experimentally we have yet to implement a GA plus pulse shaping experiment, but once this is done there is enormous potential for coherent control studies. Constraining the shapes a pulse shaper is allowed to make promises to be a powerful tool in unravelling the complex interactions between the light field and vibrational and electronic dynamics in molecular systems, and work is currently underway in our laboratory to build an experiment to exploit that power.

6.5 REFERENCES

1. A.T.J.B. Eppink and D.H. Parker, *Rev. Sci. Instrum.* **68** (9), 3477. (1997).
2. E.D. Boleat and H.H. Fielding, *Mol. Phys.* **103** (4), 491-499. (2005).
3. A. Prakelt, M. Wollenhaupt, C. Sarpe-Tudoran, and T. Baumert, *Phys. Rev. A* **70** (6), 063407. (2004).

A1 INTRODUCTION

This appendix lists the Fortran code (mostly Fortran90 but with one Fortran77 subroutine) for the genetic algorithm discussed in chapter 5. For brevity, only the code used to optimise the laser parameters in the chirped-pulse problem are included. The listing is divided into subroutines in the same way as the calling hierarchy within the program, which is shown in outline below. Preceding each listing is a short introductory paragraph.

```

na_ga_fft
  ga
    popgen (for the first generation only)
    breed
    mutate
  compete
    make_var
    do_calc
      chirpfft
      cf_obj
        energies
        peak_pos
        peak_err
    popsort
  converge
  out_var

```

Figure A1 An outline of the calling hierarchy for subroutines comprising the genetic algorithm described in chapter 5. This particular implementation was used to optimise the delay, phase and chirp of a laser pulse to maximise the d Rydberg state population of atomic sodium following excitation by a transform-limited pulse.

A2 CODE LISTING

The first listing is the main program and acts as the interface between the genetic algorithm (GA) and the particular problem of maximising the d Rydberg population in a

APPENDIX

wave packet excited by a transform-limited laser pulse and a chirped pulse. Variables controlling the GA are read in from an external text file called `ga_data.txt`. Their meanings are explained in the comments in the code below. Since this subroutine encompasses all the other subroutines, it can be used to control how many optimisations are carried out.

```
program na_fft_ga

! nindiv    Number of individuals in population.
! nelem     Number of elements in each individual (the +1 element is
used to
!           store the variables derived from each gene. The +2
element is
!           used to store the fitness parameter.
! ndata     Number of parameters needed in the problem eg time delay,
chirp,
!           phase, etc.
! rmut      Mutation rate.
! numtop    Number of top individuals used in breeding the next
population.
! pop       The population of individuals.
! topfew    The top few individuals selected for breeding the next !
            population.
! ngen      Number of generations.
! conv      Convergence threshold.
! istop     Integer set to 1 to indicate convergence

!ga variables
implicit double precision (a-h,o-z)
integer :: nindiv,ndata,nelem,numtop,ngen,istop
double precision,dimension (:,:,),allocatable :: pop
double precision,dimension (:,:,),allocatable :: topfew

!read in ga data
open (1,file='ga_data.txt')
read (1,*) nindiv,ndata,nelem,numtop,rmut,conv
close(1)

allocate (pop(nindiv,ndata,nelem+2))
```

APPENDIX

```
allocate (topfew (numtop, ndata, nelem+2))

do j=1,5 !number of optimisations to run
    ngen=1 !incremented inside ga() subroutine
    istop=0 !value set to 1 inside converge() when calculation has
converged,
    do
        call ga (pop, nindiv, ndata, nelem, numtop, topfew, rmut, ngen)
        call compete (pop, nindiv, ndata, nelem, numtop, ngen)
        call popsort (pop, nindiv, ndata, nelem, numtop, topfew)
        call converge (pop, numtop, ndata, nelem, topfew, &
            & conv, istop, ngen, bestlast)
        call out_var (pop, nindiv, ndata, nelem)
        if (istop == 1) then
            call out_var (pop, nindiv, ndata, nelem)
            exit
        end if
        ngen=ngen+1
    end do
!end do
end program na_fft_ga
```

As its name suggests, this subroutine controls operation of the genetic algorithm. In the first iteration a new population is generated by `popgen`. In subsequent generations, the breeding population is selected and the new population bred by calls to `popsort`, `breed` and `mutate`.

```
subroutine ga (pop, nindiv, ndata, nelem, numtop, topfew, rmut, ngen)

implicit double precision (a-h, o-z)
double precision, dimension (nindiv, ndata, nelem+2) :: pop
double precision, dimension (numtop, ndata, nelem+2) :: topfew
integer :: nindiv, ndata, nelem, numtop

print*, "generation ", ngen

if (ngen == 1) then
    call popgen (pop, nindiv, ndata, nelem)
else
```

APPENDIX

```
        call breed(pop,nindiv,ndata,nelem,numtop,topfew)
        call mutate(pop,nindiv,ndata,nelem,rmut)
end if

end subroutine ga
```

The `popgen` subroutine generates the first population, and so runs only once for each run of the genetic algorithm. It uses the intrinsic Fortran functions `RANDOM_SEED` and `RANDOM_NUMBER` to generate an initial population comprising a 3D array of double-precision random numbers. The range of these numbers is between 0 and 1, but can be moved by the parameters `SHIFT` and `SCALE`.

```
subroutine popgen(pop,nindiv,ndata,nelem)

implicit double precision (a-h,o-z)
integer :: i,j,nindiv,ndata,nelem
double precision,dimension(nindiv,ndata, nelem+2) :: pop
parameter SHIFT=0.0D0
parameter SCALE=1.D0

!Random_seed ensures that each time random_number() is called a
different
!set of random numbers is generated
call RANDOM_SEED
call RANDOM_NUMBER(pop)

!Shift the random number range (eg -0.5 to +0.5 instead of 0 to 1)
pop = pop + SHIFT

!Scale the random number range
pop = pop * SCALE

!Set element for variable & fitness parameter storage (nelem+1 and
nelem+2)
!to zero
do i=1, nindiv
    do j=1,ndata
        pop(i,j,nelem+1) = 0.D0
        pop(i,j,nelem+2) = 0.D0
    end do
end do
```

APPENDIX

```
        end do
end do

end subroutine popgen
```

This subroutine sorts the individuals according to their fitness parameter, which is stored in element $(i, 2, 1)$ of the population array, `pop`. Since the objective is to minimise the error in the peak positions of a spectrum, sorting is to smallest first. The sorting algorithm keeps looping through the fitness parameters, comparing values and swapping them, until it makes no swaps. At each swap the whole pair of 2D arrays is exchanged. The best few individuals are copied into an array called `topfew`, which is then used in the `breed` subroutine.

```
subroutine popsort(pop, nindiv, ndata, nelem, numtop, topfew)

implicit double precision (a-h,o-z)
integer :: nindiv, ndata, nelem, nswaps
double precision, dimension(nindiv, ndata, nelem+2):: pop
double precision, dimension(numtop, ndata, nelem+2):: topfew

nswaps=0
!Sort population by decreasing fitness parameter
do
    do i=1, nindiv-1
        !Compare the fitness element (pop(i,1,nelem+2)) of each
        !individual
        if (pop(i,1,nelem+2) > pop(i+1,1,nelem+2)) then
            nswaps = nswaps + 1
            !loop through individuals' elements to swap them
            do j=1, ndata
                do k=1, (nelem+2)
                    temp = pop(i+1,j,k)
                    pop(i+1,j,k) = pop(i,j,k)
                    pop(i,j,k) = temp
                end do
            end do
        end do
    end if
end do
```

APPENDIX

```
        if (nswaps == 0) exit !exit if no swaps made: sort complete
        nswaps = 0 !reset
end do

!Put best 'numtop' individuals in array topfew
do i=1,numtop
    do j=1,ndata
        do k=1,nelem+2
            topfew(i,j,k)=pop(i,j,k)
        end do
    end do
end do

print*, 'top variables'
print*, 'delay = ',topfew(1,1,nelem+1)
print*, 'phase = ',topfew(1,2,nelem+1)
print*, 'chirp =' ,topfew(1,3,nelem+1)

end subroutine popsort
```

The `breed` subroutine produces a new population from the best individuals from the previous population. Pairs of individuals from the `topfew` population are selected at random to be bred together. Elements from each individual are then randomly used to create a new individual. In this process, elements keep their place, i.e. the 20th element of one parent becomes the 20th element of the offspring.

```
subroutine breed(pop,nindiv,ndata,nelem,numtop,topfew)

implicit double precision (a-h,o-z)
integer :: nindiv,ndata,nelem,numtop
double precision,dimension(nindiv,ndata,nelem+2):: pop
double precision,dimension(numtop,ndata,nelem+2):: topfew

call RANDOM_SEED
!loop to generate new population
do i=1,nindiv
!randomly select 2 individuals from topfew array
    do
        call RANDOM_NUMBER(who1)
        call RANDOM_NUMBER(who2)
```

APPENDIX

```
!rescale whoN to number of top individuals, NUMTOP (NUMTOP-1 so
! adding does not go out of range)
    who1 = who1 * numtop
    who2 = who2 * numtop
    iwho1 = int(who1)
    iwho2 = int(who2)
    iwho1 = iwho1 + 1 !add 1 because arrays start at 1 not 0
    iwho2 = iwho2 + 1

!check they are not the same
    if (iwho1 .NE. iwho2) then
        exit
    else
        cycle !call RANDOM_NUMBER(who2)
    end if
end do

!loop through new individual's elements filling from parents
do j=1,ndata
    do k=1,nelem
        call RANDOM_NUMBER(aorb)
        !select which parent to take element from
        if (aorb <= 0.5) then
            pop(i,j,k) = topfew(iwho1,j,k)
        else !aorb must be > 0.5 and <=1
            pop(i,j,k) = topfew(iwho2,j,k)
        end if
    end do !k
end do !j
end do !i

!set the auxiliary elements to 0 to stop previous fitness parameters
etc.
!carrying to new generation
do i=1,nindiv
    do j=1,ndata
        pop(i,j,nelem+1) = 0.D0
        pop(i,j,nelem+2) = 0.D0
    end do
end do
```

APPENDIX

```
end do
```

```
end subroutine breed
```

The `mutate` subroutine makes a number of random changes to the elements of the new population generated by `breed`. The extent of mutation is controlled by `rmut`, a value read from the `ga_data.txt` file. Mutation is achieved by replacing a randomly selected element (gene) by a randomly generated number.

```
subroutine mutate(pop,nindiv,ndata,nelem,rmut)

implicit double precision (a-h,o-z)
integer :: nindiv,ndata,nelem
double precision,dimension(nindiv,ndata,nelem+2) :: pop

!Calculate how many mutations to make to each individual
dnmut = rmut*nelem
inmut = int(dnmut)
call RANDOM_SEED

!Loop through population
do i=1, nindiv
  do j=1,ndata
    !Perform inmut mutations
    do k=1, inmut
      call RANDOM_NUMBER(elem)
      !scale to number of elements
      elem = elem * nelem
      ielem = int(elem)
      ielem = ielem + 1
      call RANDOM_NUMBER(dmut)
      !replace an element in the ith individual
      pop(i,j,ielem)=dmut*1.d0
    end do !i
  end do !j
end do !i

end subroutine mutate
```

APPENDIX

The `compete` subroutine marshals competition between the individuals by calling the subroutine `make_var` to make useful variables from the genes and then calling `do_calc` to use the variables.

```
subroutine compete(pop,nindiv,ndata,nelem,numtop,ngen)

implicit double precision (a-h,o-z)
integer :: nindiv,ndata,nelem,numtop,ngen
double precision,dimension(nindiv,ndata,nelem+2):: pop
double precision,dimension(numtop)::topfew
!double precision,dimension(2,50) :: swp,dwp

!call subroutine to make useful variables out of ga population
call make_var(pop,nindiv,ndata,nelem)
!use variables in calculation
call do_calc(pop,nindiv,ndata,nelem)

end subroutine compete
```

`make_var` generates useful variables from the genes of each individual. For each variable, the average value of the genes is calculated, then scaled and shifted into a suitable range. The variable is then stored in element `(nelem+1)` of the `pop` array for use by the `do_calc` subroutine.

```
subroutine make_var(pop,nindiv,ndata,nelem)

implicit double precision (a-h,o-z)
integer :: nindiv,ndata,nelem,ngen
double precision,dimension(nindiv,ndata,nelem+2):: pop

del=3.0d0 !scale range for delays
del_sh=0.d0 !shift the time delay
phs_sc=5.d0 !scale range for phases
phs_sh=-2.5d0 !shift the phase
chp_sc=5.d0 !scale range for chirps
chp_sh=-2.5d0 !shift range for chirps

!elements are summed and stored in the 'nelem+1'th element
```

APPENDIX

```
do i=1,nindiv
  do j=1,ndata
    sum=0
    do k=1, nelem
      sum=sum+pop(i,j,k)
    end do
    sum = sum/nelem
    pop(i,j,nelem+1)=sum
  end do
end do

!scales and shifts the sum to make it a useful variable for do_calc
do i=1,nindiv
  pop(i,1,nelem+1)= (pop(i,1,nelem+1)*del)+del_sh
  pop(i,2,nelem+1)= (pop(i,2,nelem+1)*phs_sc)+phs_sh
  pop(i,3,nelem+1)=(pop(i,3,nelem+1)*chp_sc)+chp_sh
end do

end subroutine
```

The `do_calc` subroutine runs through the current population, sets up the laser pulse parameters used to calculate the spectrum and calls the subroutines to calculate the spectrum. It also instigates comparison of the spectrum with the objective

```
subroutine do_calc(pop,nindiv,ndata,nelem)

implicit double precision (a-h,o-z)
integer :: nindiv,ndata,nelem,numtop
double precision,dimension(nindiv,ndata,nelem+2) :: pop
double precision,dimension(2,5000) :: spect !result of current calc
double precision,dimension(20):: delay,phase,phi
!double precision,dimension(2,50):: swp, dwp

do i=1,nindiv
  ithis = i
  !get variables from pop(i,j,k) array
  !and build arrays delay(i), phase(i) and phi(i)
  delay(1) = 0.d0 !pop(i,1,nelem+1)
  phase(1) = 0.d0 !pop(i,2,nelem+1)
```

APPENDIX

```
phi(1) = 0.d0 !pop(i,3,nelem+1)
delay(2) = pop(i,1,nelem+1)
phase(2) = pop(i,2,nelem+1)
phi(2) = pop(i,3,nelem+1)

!chirp fft calc
call chirpfft(delay,phase,phi,spect)
call cf_obj(spect,ithis,fit)
!write the fitness parameter for this individual to pop() array
pop(ithis,1,nelem+2) = fit
end do

end subroutine
```

This Fortran77 subroutine, `chirpfft`, calculates the spectrum of the laser pulses with the delay, phase and chirp for one individual. The laser wavelength is determined from the spectroscopic details for the excitation being modelled. In this case, a two-colour excitation of the Rydberg states of atomic sodium lying around $n = 35$. The subroutine calls a FFT routine, `four1`, from ref. [1], the text of which is not included.

```
subroutine chirpfft(delay,phase,phi,spect)

implicit double precision (a-h,o-z)
dimension tfield(10000000),field(10000000),data(10000000)
dimension delay(10),phase(10),tdelay(10),phi(10),a(10)
dimension alpha(10),tp(10),chirp(10),addphs(10)
dimension spect(2,5000)

c Assign values to spectroscopic variables and pulses.
c Ionisation potential, launch state and system-specific Rydberg
constant in
c wavenumbers.
xip = 41449.45
xlaunch =16973.368
Ryd =109734.5
c Average n in wave packet, pulse width (NOTE: this is without the
2ln2 factor).
xn = 35.0
pulse = 0.595
```

APPENDIX

```
c Total number of pulses.
npulse = 2
c FT parameters: tstep = time stepsize; array size is 2^npower.
tstep = 0.0005
npower = 19

autime=2.418884326505d-5
au=0.5d0/109737.3156852573d0
dln2=0.69314718d0
fact=2.0d0*dln2
pi=3.141592654d0

c Set the initial pulse parameters (atomic units).
do i=1,npulse
    chirp(i)=pulse*dsqrt(1.0d0+4.0d0*phi(i)**2/pulse**4)
    alpha(i)=2.0d0*phi(i)/(pulse*chirp(i))**2
    alpha(i)=alpha(i)*autime**2
c tp is the pulse duration assuming Gaussian. NOTE that tp^2 is
defined as
c (FWHM^2)/2ln2
    tp(i)=dabs(chirp(i))/autime
end do
omega=(xip-xlaunch-Ryd/xn**2)*au

c addphs accounts for the energy term
do i=1,npulse
    tau=delay(i)*2.0d0*pi*xn**3
    phasen=(omega*tau)/(2.0d0*pi)
    addphs(i)=2.0d0*(dint(phasen)-phasen)
    tdelay(i)=delay(i)*2.0d0*pi*xn**3 +
(phase(i)+addphs(i))*pi/omega
end do

c Set up time grid so that the number of points is 2^npower as
required by FFT
tmin=-5.0d0*chirp(1)
tmax=(2.0d0**npower)*tstep + tmin

c Generate the complex Gaussian electric field pulse sequence
k=0
```

APPENDIX

```

do t=tmin/autime,tmax/autime,tstep/autime
  k=k+1
  do i=1,npulse
    a(i)=dexp(-((t-tdelay(i))/tp(i))**2)
    field(2*k-1)=field(2*k-1)+
    cos(omega*(t-tdelay(i))+alpha(i)*(t-tdelay(i))**2)*a(i)
    field(2*k)=field(2*k)-
    sin(omega*(t-tdelay(i))+alpha(i)*(t-tdelay(i))**2)*a(i)
  end do
  data(2*k-1)=field(2*k-1)
  data(2*k)=field(2*k)
  if(k.eq.2**npower) exit
end do

c Fourier transform
call four1(data,k,1)

c Set wavenumber scale
fstep=1.0d0/(tstep*1.0d-12*(2.0d0**npower))
wavstep=fstep/2.99792458d10

c Extract the absolute values and the argument (i.e. the phase)
unwrap=0.0d0
oldarg=0.0d0
j=1
do i=1,k/2
  x=data(2*i-1)
  y=data(2*i)
c   The absolute value of the FT
  ft=dsqrt(x**2+y**2)
c   The phase of the FT in units of pi
  arg=datan2(y,x)/pi
  if(arg+unwrap.lt.oldarg) unwrap=unwrap+2.0d0
  arg=arg+unwrap
  oldarg=arg
  wavenum=dfloat(i)*wavstep
  wid=40.0d0
  if((wavenum.gt.(omega/au-wid)).and.(wavenum.lt.(omega/au+wid)))
then
  ft=1.0d-6*ft**2

```

APPENDIX

```
c          Note that the square of the FT is written out over a
limited
c          frequency range
          spect(1,j)=wavenum
          spect(2,j)=ft/20.d0
          j=j+1
        end if
end do

c Reset all variables to zero to prevent propagation of values
tfield=0.d0,field=0.d0,
      dat=0.d0,delay=0.d0,phase=0.d0,tdelay=0.d0,phi=0.d0
a=0.d0,alpha=0.d0,tp=0.d0,chirp=0.d0,addphs=0.d0,wavenum=0.d0

end subroutine
```

Subroutine cf_obj controls comparison of the calculated spectrum from each individual to the objective in order to generate the fitness parameters.

```
subroutine cf_obj(spect,ithis,fit)

implicit none
integer :: i, ithis, nryd, nerr
double precision :: fit, err
double precision,dimension(2,5000) :: spect
double precision,dimension(2,50) :: swp, dwp
double precision,dimension(2,50) :: peaks,trofs

!generate sodium energies
call energies(swp,dwp)

!find the peaks in the spectrum from the fft
call peak_pos(spect, peaks,trofs)
call peak_err(peaks,trofs,dwp,err) !only compares d peaks

!assign the fitness parameter for this individual
fit = err

!reset the whole fft array to zero ready for next individual
```

APPENDIX

```
spect = 0.d0
swp=0.d0
dwp=0.d0

end subroutine
```

This subroutine calculates the energies of the *s* and *d* states relative to the intermediate. The corresponding oscillator strengths and transition intensities are then calculated. These values form the objective against which are measured the spectra generated for each individual.

```
subroutine energies(swp,dwp)

implicit double precision (a-h, o-z)
double precision,dimension(20) :: s_en, d_en, s_intens, d_intens, os,
od, double precision,dimension(20) :: s_trans, d_trans
double precision,dimension(2,20) :: en, trans, swp, dwp
parameter c=2.99792458002e10, pi=3.141592654
real n_av

iryd = 20
! Set up in spectroscopy data
n_av=35, wint=16973.368, fwhm_t=0.75, nmin=30, nmax=40, nstep=1,
tmin=30, tmax=45, tstep=0.01, wip=41449.451, ryd=109734.697, qds=1.35,
qdd=0

fwhm=((8065.465*0.441)/(241.79659*fwhm_t))

! Calculate tcl, pi in ps, revival time and excitation energy
tcl=2*pi*(n_av**3)*2.4188843d-5
av_en=wip-wint-(ryd/(n_av**2))
t_rev=(n_av*tcl)/3

! Calculate energies, oscillator strengths and transition intensities
do 99 n=1,iryd
  nq = nmin + n - 1 !move nq since n starts at one
  s_en(n)=wip-wint-(ryd/((nq-qds)**2))
  os(n)=(1.0d0*s_en(n))/(nq**3)
```

APPENDIX

```

        s_intens(n)=dexp((-4*(dlog(2.0d0))*(s_en(n)-
av_en)**2)/(fwhm**2))
        s_trans(n)=os(n)*s_intens(n)
        d_en(n)=wip-wint-(ryd/((nq-qdd)**2))
        od(n)=(2.0d0*d_en(n))/(nq**3)
        d_intens(n)=dexp((-4.0*dlog(2.0d0)*(d_en(n)-
av_en)**2)/(fwhm**2))
        d_trans(n)=od(n)*d_intens(n)
        !put energies and intensities in arrays for return to calling
program
        swp(1,n)=s_en(n)
        swp(2,n)=s_trans(n)
        dwp(1,n)=d_en(n)
        dwp(2,n)=d_trans(n)
99    continue

end subroutine energies

```

This subroutine finds all the peaks and troughs in the spectrum calculated by the `chiptfft` subroutine. Peaks are located by calculating the gradient between adjacent pairs of data from the spectrum (which is sufficiently smooth to allow this to work), then finding where, and in which direction, the gradient passes through zero. The peak positions are then compared to the objective peak positions in the `peak_err` subroutine.

```

subroutine peak_pos(spect,peaks,trofs)

implicit none
integer :: i,j,k,npks,ntrf
double precision :: grad, prev
double precision,dimension(2,50) :: peaks,trofs
double precision, dimension(2,5000) :: spect
double precision, parameter :: threshold=0.01d0

k=1
j=1
prev=0.d0

do i=1,2751-1

```

APPENDIX

```

grad = spect(2,i+1)-spect(2,i)
!find peaks
if ((grad .lt. 0.d0) .and. (prev .gt. 0.d0))then
    if(spect(2,i) .ge. threshold)then
        peaks(1,j) = spect(1, i)
        peaks(2,j) = spect(2,i)
        j=j+1
    end if
end if
!find troughs
if ((grad .gt. 0.d0) .and. (prev .lt. 0.d0))then
    if(spect(2,i) .ge. threshold)then
        trofs(1,k) = spect(1, i)
        trofs(2,k) = spect(2,i)
        k=k+1
    end if
end if
prev = grad
end do

npks=j-1
ntrf=k-1

end subroutine peak_pos

```

The `peak_err` subroutine calculates the difference between the positions of the spectral peaks and the d Rydberg states. The total error is calculated from the sum of the squares of the differences for all the peaks. The error in each peak position is weighted by the peak intensity so that central states, $n = 34, 35$ and 36 , contribute more strongly to the total error. The total error becomes the fitness parameter for each individual.

```

subroutine peak_err(sp_pks,sp_tfs,wp_pks,err)

implicit none
integer :: i,j,filestat,idxs,idxw
double precision :: maxs,maxw,err,nerr,perr
double precision,dimension(2,50) :: wp_pks, sp_pks,sp_tfs

```

APPENDIX

```
perr = 0.d0, nerr = 0.d0, err = 0.d0 !set all errors to zero

!find maximum height in each array
maxs = sp_pks(2,1)
maxw = wp_pks(2,1)
idxs = 1
idxw = 1
do i=1,50
    if (sp_pks(2,i) > maxs)then
        maxs = sp_pks(2,i)
        idxs = i
    end if
    if (wp_pks(2,i) > maxw) then
        maxw = wp_pks(2,i)
        idxw = i
    end if
end do

!add difference in energy of maximal peaks to the error
err=(sp_pks(1,idxs)-wp_pks(1,idxw))**2

!move outward from maxima, adding up errors
j=1
do
    if((idxs+j .le. 30) .and. (idxw+j .le. 30) .and. &
        & (wp_pks(2,idxw+j) .ge. 0.01))then
        perr = sp_pks(1,idxs+j)-wp_pks(1,idxw+j) !peaks at higher
energy
        if(abs(perr) .ge. 100.d0) then !no peak in one array
            perr = 0.d0
        else
            perr = perr**2
            ! weight error to favor central lines
            perr = perr * wp_pks(2, idxw+j)
            err = err + perr !15/12/4
            perr = 0.d0 !15/12/4
        end if
    end if
end do
if ((idxs-j .ge. 1) .and. (idxw-j .ge. 1) .and. &
    & (wp_pks(2,idxw-j) .ge. 0.01))then
```

APPENDIX

```
nerr = sp_pks(1,idxs-j)-wp_pks(1,idxw-j) !peaks at lower
energy
if (abs(nerr) .ge. 100.d0) then !no peak in one array
    nerr = 0.d0
else
    nerr = nerr**2
    nerr = nerr * wp_pks(2, idxw-j)
    err = err + nerr !15/12/4
    nerr = 0.d0 !15/12/4
end if
end if
if(.not.((idxs+j .le. 30) .and. (idxw+j .le. 30)) .and. &
    &.not.((idxs-j .ge. 1) .and. (idxw-j .ge. 1))) exit
j=j+1
end do

wp_pks = 0.d0, sp_pks = 0.d0

end subroutine peak_err
```

Subroutine `converge` applies two tests to ascertain if the population has reached the objective. Firstly, whether the convergence threshold (read from a text file) has been reached, and secondly, whether the best individual from the current generation differs from the previous one by more than an arbitrary value. The second test turned out to be less useful than the first and was often disabled.

```
subroutine
converge (pop, numtop, ndata, nelem, topfew, conv, istop, ngen, bestlast)

! conv = the convergence criterion
! nstop = should I stop, yes or no? i.e. has it converged yet?
!
implicit double precision (a-h,o-z)
integer :: numtop, ndata, nelem, istop
double precision, dimension(numtop, ndata, nelem+2):: topfew

!see if the fitness value is less than the convergence criterion
if ( topfew(1,1,nelem+2) .lt. conv )then
    istop = 1
```

APPENDIX

```
        print*, "best is better than conv"
else if(ngen .gt. 1) then
    test = topfew(1,1,nelem+2) - bestlast
    test = dabs(test)
    if (test .le. 0.001)then
        istop = 1
        print*, "values less than 0.0001 different"
    end if
end if

bestlast=topfew(1,1,nelem+2)

end subroutine converge
```

out_var simply writes to file the laser parameters and fitness parameter of the fittest individual for each generation. This allows the progress of the optimisation to be followed easily.

```
subroutine out_var(pop,nindiv,ndata,nelem)

implicit double precision (a-h,o-z)
double precision,dimension (nindiv,ndata,nelem+2) :: pop
integer :: nindiv,ndata,nelem,numtop

open (1,position='append',file='cverg.csv')
write(1,21) pop(1,1,nelem+1), pop(1,2,nelem+1), pop(1,3,nelem+1)
close(1)
21 format (f7.5,',',f7.5,',',f7.5)

print*, 'best indiv (out_var) = ',pop(1,1,nelem+2)

open (2,position='append', file='topman.csv')
write(2,*) pop(1,1,nelem+2)
close(2)

end subroutine
```

A3 REFERENCES

1. W.H. Press, B.P. Flannery, S.A. Teukolsky, and W.T. Vetterling, *Numerical Recipes in FORTRAN 77: The Art of Scientific Computing: Vol 1*. Vol. 1. 1992: Cambridge University Press.